DISSERTATION

4D Printing of Programmable Polymers

Christoph Alexander Spiegel

2023

DISSERTATION

zur

Erlangung der Doktorwürde (Dr. rer. nat.)

der

Gesamtfakultät für Mathematik, Ingenieur- und Naturwissenschaften

der

Ruprechts-Karls-Universität Heidelberg

vorgelegt von

Christoph Alexander Spiegel

aus Dornbirn

Tag der mündlichen Prüfung

17. März 2023

4D Printing of Programmable Polymers

Gutachter

Prof. Dr. Eva Blasco

Prof. Dr. Christine Selhuber-Unkel

„*I know not all that may be coming, but be it what it will, I'll go to it laughing.*"

Hermann Melville, Moby-Dick (1851)

ACKNOWLEDGEMENTS

Looking at this work, it is important to mention that this thesis could have never been written in the way it is present now without the contribution, support, and help of numerous individuals, whom I would like to thank here.

First and foremost, I would like to express my gratitude to Prof. Dr. Eva Blasco for trusting in me and giving me the opportunity to be a starting member of the Blasco research group at KIT and the continuous faith in me and my work and the patience – even when the results were not present in the desired quality immediately. Thank you for project related guidance helping me – a trained organic chemist – to find my way in the world of 3D/4D printing and polymer chemistry. But I also want to thank you for your personal guidance showing me how to do science – efficiency over quantity –, how to manage large workloads, how to communicate scientifically – written, orally and visually – in an appealing way for reader and listener, and your representation as role model showing me how to handle difficult situations emerging in scientific and personal life in a professional way.

In addition, I would like to thank you Prof. Dr. Christine Selhuber-Unkel for agreeing to be the second assessor for my thesis and the upcoming defense.

Furthermore, I want to thank all the present and former members of the Blasco research group. To do science meaning to put theoretical ideas and assumptions into practice, a motivating and inspiring work environment must be present, and this was the case for me in the Blasco team. Starting with the initial members, I would like to thank Dr. Joël Monti, who started his PhD a few days before me, for his warm welcome and the nice Friday evenings we spent discussing personal, organizational and scientific topics in Karlsruhe. I would like to thank Li-Yun Hsu for being a good friend and motivator during the PhD time at KIT and Heidelberg University and for the introduction into Taiwanese food and sweets. Furthermore, thank you Li-Yun for allowing me to celebrate my first Chinese New Year together with you and experiencing the exquisite food prepared by you. It was soothing to figure out with you, Joël and Li-Yun, the initial questions and issues we have all at the beginning of our PhDs. A year after my PhD start Britta Weidinger joint after successfully conducting her master thesis with Prof. Dr. Blasco our research group and was immediately from the beginning my office buddy – a state that never changed even after the groups moving to Heidelberg University. Thank you for your good advices in science and personal questions and for helping me through sometimes difficult situations, where I lost trust in myself. After the group's relocation to Heidelberg, we experienced a quite rapid growth in team members starting with Samantha Catt and Marcus Dodds. I would like to thank you Samantha for always staying calm, quickly doing orderings of chemicals outside initially agreed timeframes and

for your large support keeping the Nanoscribe Photonic GT2 microprinter running. I also would like to thank Marcus for being a good friend, nice colleague and for all the support especially when I had questions about organizational things at the beginning of my time in Heidelberg – Marcus as experienced member of the Ruprechts Karls University knew always what to do. Later in this year Clara Vazquez-Martel, the group's Spanish sunshine from the Canary Islands joined the team. It is, was, and will always be a pleasure to talk and work with you, motivating me by your positive personality and helping me in this way through several hard times. Furthermore, help me and the group by giving us insight in your enormous knowledge in Material science and providing us with the views of an Engineer towards measurements and characterizations (DIN-A norms) plus your excellent feeling for visualization and design supporting me – an excellent stickman drawer. The latest PhDs joining our research groups were Philipp Mainik and Niklas Schwegler. Philipp I would like to thank you for being a good friend and "Rewe" partner, your project collaboration with me, and all the nice discussions about science and non-scientific topics. Furthermore, it is always a treasure to revert to your knowledge about liquid crystalline elastomers and biomaterials. I also would like to thank Niklas for all the nice discussions we had. Concluding my gratitude towards the Blasco group members I would like to thank Dr. Guangda Zhu, the group's newest post-doctoral researcher. I always enjoy conversations with you about scientific topics including your enormous amounts of new ideas and off-topic about Chinese food and culture. Thank you for giving me insight into new culinary world of China. I want to thank you all again. It is inspiring, motivating and enjoyable to work together with such a team.

I also would like to thank all the students and interns I was allowed to train and supervise, including Khrystyna Pelenska, being my first intern and giving me first experience in supervision, Viktoria P. Bothe, who was figuring out together with me shape memory ink design and printing process using a light-based macroprinter during her internship and the beauty and challenge of stable radicals at macroscale printing later in her master thesis, Niclas Krupp, for being an excellent student astonishing me with his scientific independence and his creativity and precision in lab work and subsequent writing, Lukas Herold, for his synthetic assistance in oligomer preparation and his positive character, and finally Hoang Bao Duc Tran – short Duc – conducting his master thesis under my supervision, suprising me all the time with his exceptional commitment and his fast way of solution finding.

Moreover, I would like to thank all the other students and visitors being temporarily part of our group including Pia Klee, Moritz Hopp, Mehran Amanpur, Tamara Unterreiner, Claudius Zimmer, Lotta Tölke, Julius Schwieger, Lukas Becker, Ann Kathrin Bergmann, Dr. Miriam Abad and Ian Mac Lean for adapting to the groups mentality and keeping the work environment within it great.

I wish all of you a great future in industry or academia – in our group or another one – and a lot of success and hope you enjoyed working with me.

I also would like to thank my collaboration partners for their support in measurements and characterization and the final production of the publication. Here, I want to express my gratitude towards Prof. Dr. Joachim P. Spatz and Dr. Maximilian Hackner for their support in mechanical characterization of our materials, their professionalism and their reliability. I also would like to thank Dr. Manuel Tsotsalas and Dr. Yixuan Jia for the efforts they spend to finish our common publication. Furthermore, I want to thank Dr. Ignazio Roppolo and Dr. Matteo Gastaldi for the nice experience to conduct science and write a paper together with them.

Further on I would like to thank Prof. Martin Wegener and his team at KIT. Here especially Dr. Liang Yang, for helping me with technical issues with the two-photon laser printing setup at KIT Campus North and Dr. Vincent Hahn, Dr. Marc Hippler, Dr. Alexander Münchinger, Pascal Kiefer, Tobias Messer and Sebastian Kalt for the nice discussions about two-photon printing from a physicist's perspective, giving me insight into the topic not take-for-granted for a chemist.

Finally, I would like to thank my family including my father Manfred Spiegel, my mother Erika Spiegel and my sister Julia Spiegel. You gave me the opportunity to study chemistry and to continue with my PhD. You were always there during good and bad times, strengthening me, if it was necessary and most importantly you always believed in me and persuaded me to do the same, when I lost this belief.

Thank you to all of you!

ABSTRACT

3D printing has experienced a tremendous development in recent decades on the technological as well as material side. However, most 3D printable materials are restricted in one aspect: They produce static 3D geometries, unable to respond or adapt to their environment – limiting in this way their applicability for smart technologies where a dynamic behavior is needed. To overcome this issue, the concept of "4D printing" emerged, where the incorporation of time as fourth dimension in 3D geometries enables new features such as responsiveness or adaptivity towards external stimuli. The simplest strategy to access such 4D structures is the utilization of smart polymeric materials for ink design, which can respond to external stimuli on-demand. In particular, the use of shape memory polymers (SMP) – one of the promising materials investigated in this thesis – is suitable for this purpose. Although the concept (and use) of SMP has already been investigated at the macroscale, the microscale is only scarcely explored. Taking one step further, this work presents – in the first part - a novel SMP ink system offering printability of thermoresponsive structures at macro- and microscale using light-based techniques namely digital light processing (DLP) and two-photon laser printing (2PLP). In particular, formulations based on designed SMP ink system are designed and adapted to fulfill requirements of each technique. At both size regimes (macro and micro) excellent printability as well as shape memory properties are demonstrated. Especially the microformulation is considered as promising system for applications in future fields such as microrobotics, biomedical therapies or smart microsensors. In a further work, push-pull azo dye species are incorporated into the SMP formulation giving access to light responsive 4D architectures fabricated at high resolution using DLP. By exploitation of the dyes' photothermal effects, new features are achieved. Translation towards light as stimulus allows excellent spatial control during shape recovery and access to a multiplicity of intermediate shapes. Last, investigating another aspect of 4D printing, "living" radical polymerization features are incorporated in 3D microstructures permitting the generation of 3D geometries, enabling precise setting of their properties for customized applications. In particular, dormant alkoxyamine bonds were integrated during 2PLP fabrication, allowing postmodification by network decrosslinking via nitroxide exchange reaction (NER) and by chain extension with styrene via nitroxide-mediated polymerization (NMP). Remarkable changes in mechanical properties and size are achieved, giving in this way access to precisely manufacturable and adjustable microscopic geometries –relevant for areas and fields where customized precise architectures are of highest necessity.

KURZFASSUNG

3D Druck hat in den letzten Jahrzehnten sowohl auf der technologischen Seite als auch auf der Seite der anwendbaren Materialien eine ungeheure Entwicklung erfahren. Die meisten 3D-druckbaren Materialien sind jedoch in einem Aspekt limitiert. Sie erzeugen statische 3D-Geometrien, die nicht in der Lage sind, auf ihre Umgebung zu reagieren oder sich an sie anzupassen – was ihre Anwendbarkeit für intelligente Technologien, bei denen ein „intelligentes“ oder „lebensechtes“ Verhalten erforderlich ist, einschränkt. Um dieses Problem zu überwinden wurde das Konzept des „4D-Drucks“ entwickelt, das den Einbau der vierten Dimension Zeit in 3D-Geometrien beschreibt und so 4D-Objekte erzeugt, die auf äußere Reize reagieren, indem sie ihre Form, Eigenschaften und Funktionen ändern. Die einfachste Strategie zur Herstellung solcher 4D-Strukturen ist die Nutzung intelligenter, polymerer Materialien bei der Tintenentwicklung, die bei Bedarf auf externe Reize reagieren können. Insbesondere die Verwendung von Formgedächtnispolymeren (SMP) – eines der in dieser Arbeit untersuchten vielversprechenden Materialien – eignet sich zu diesem Zweck. Obwohl das Konzept (und die Anwendung) von SMP bereits auf der Makroskala untersucht wurde, ist der Bereich der Mikroskala nur wenig erforscht. Diese Arbeit geht einen Schritt weiter und stellt im ersten Teil ein neuartiges SMP-Tintensystem vor, das die Druckbarkeit von thermoresponsiven Strukturen auf Makro- und Mikroebene unter Verwendung lichtbasierter Techniken, nämlich der digitalen Lichtverarbeitung (DLP) und des Zwei-Photonen Laserdrucks (2PLP), ermöglicht. Im Speziellen wird eine Makro- und eine Mikroformulierung auf Basis dieses konzipierten SMP-Tintensystems entwickelt – angepasst an die Anforderungen der jeweiligen Technik. In beiden Größenregimen wurden ausgezeichnete Druckbarkeit sowie hervorragende Formgedächtniseigenschaften erreicht. Insbesondere die Mikroformulierung wird als vielversprechendes System für Anwendungen in zukünftigen Bereichen wie der Mikrorobotik, biomedizinischen Therapien oder intelligenten Mikrosensoren angesehen. In einer weiteren Arbeit werden Push-Pull Azofarbstoff-Verbindungen in die SMP-Formulierung integriert, was den Zugang zu lichtresponsiven 4D Architekturen ermöglicht, die mit hoher Auflösung mittels DLP hergestellt werden. Durch Ausnutzung der photothermischen Effekte der Farbstoffe werden neue Eigenschaften erreicht. Die Verlagerung auf Licht als Stimulus ermöglicht auszeichnete räumliche Kontrolle während der Formwiederherstellung sowie Zugang zu einer Vielzahl von Zwischenformen. Zuletzt wird ein weiterer Aspekt des 4D Drucks untersucht: Merkmale „lebender“ radikalischer Polymerisierungen werden in 3D Mikrostrukturen eingebaut und ermöglichen so die Erzeugung von nachträglich modifizierbaren 3D Geometrien, wodurch deren Eigenschaften für individuelle Anwendungen präzise eingestellt werden können. Im Speziellen wurden ruhende Alkoxyaminbindungen während der 2PLP Herstellung eingebaut, die eine nachträgliche Modifizierung

durch Entvernetzung des Netzwerks mittels Nitroxid-Austauschreaktion (NER) und durch Kettenerweiterung mit Styrol via Nitroxid-vermittelter Polymerisation (NMP) ermöglichen. Der Einsatz beider Verfahren ermöglicht bemerkenswerte Änderungen der mechanischen Eigenschaften und der Größe und bietet dadurch Zugang zu präzisen herstellbaren und einstellbaren mikroskopischen Geometrien – relevant für Bereiche und Gebiete, in denen maßgeschneiderte, präzise Architekturen von höchster Notwendigkeit sind.

ABBREVIATIONS

2PLP	two-photon laser printing
2P PI	two-photon photoinitiator
3D	three dimensional
4D	four dimensional
ABS	acrylonitrile butadiene styrene
ATR-FTIR	attenuated total reflection-fourier transform infrared spectroscopy
ATRP	atom transfer radical polymerization
BAPO	phenylbis (2,4,6-trimethylbenzoyl)phosphine oxide
CAL	computed axial lithography
CAMs	covalent adaptable microstructures
CAN	covalent adaptable network
CLIP	continuous liquid interface production
cw	continuous wave
DCC	dynamic covalent chemistry
DEF	diethyl formamide
DETC	diethylamino-3-thenoyl coumarin
DIW	direct ink writing
DLP	digital light processing
DLW	direct laser writing
DMA	dynamic mechanical analysis
DMAc	dimethylacetamide
DMD	digital mirror device
DMF	dimethyl formamide
DMSO	dimethyl sulfoxide
DnMA	dynamic nanomechanical analysis
DOC	double bond conversion
D_p	penetration depth
DSC	differential scanning calorimetry
EBM	electron beam melting

E_c	exposure dose/critical energy
FDM	fused deposition modelling
FRP	free radical polymerization
FTIR	fourier-transform infrared
HexA	hexyl acrylate
IsobA	isobornyl acrylate
LCE	liquid crystalline elastomer
LCST	lower critical solution temperature
LSMP	light activated shape memory polymers
NER	nitroxide exchange reaction
NIR	near-infrared
NMP	nitroxide-mediated polymerization
NMP2	nitroxide-mediated photopolymerization
NMR	nuclear magnetic resonance
NTI-RAFT	Norrish type I photoinduced -RAFT
OLED	organic light emitting diode
OPA	one-photon polymerization
PEGDA	poly(ethylene glycol) diacrylate
PETG	polyethylene terephthalate glycol
PET-RAFT	photoinduced electron / energy-transfer-RAFT
PI	photoinitiator
PRE	persistent radical effect
RAFT	reversible-addition-fragmentation chain transfer polymerization
RDRP	radical-deactivation radical polymerization
R_f	shape fixity ratio
RPC-RAFT	radical-promoted cationic RAFT
R_r	shape recovery ratio
R^2	coefficient of determination
SEM	scanning electron microscopy
SLA	stereolithography
SMP	shape memory polymer

SME	shape memory effect
SLS	selective laser sintering
STED	stimulated emission depletion
TcddA	tricyclo [5.2.1.$0^{2,6}$]decanedimethanol diacrylate
TEMPO	2,2,6,6-tetramethylpiperidine-1-oxyl
TEMPO-methacrylate	4-methacryloxyloxy-TEMPO
T_g	glass transition temperature
TGA	thermogravimetric analysis
T_m	melting point /temperature
TME	temperature memory effect
TMPTA	trimethylolpropane triacrylate
ToF-SIMS	time of flight-secondary ion mass spectrometry
TPA	two-photon absorption
TPP	two-photon polymerization
UV	ultraviolet
VIS	visible

Contents

List of Publications and Conference contributions:

The results described in this thesis were published and additionally presented in conferences. The published work of the author as first coauthor (and shared first coauthorship, marked here with a "§") includes:

Peer-reviewed articles:

- **C. A. Spiegel[§]**, M. Hippler[§], A. Münchinger[§], C. Barner-Kowollik, M. Wegener, E. Blasco, *Adv. Funct. Mater.* **2020**, *30*, 1907615. IF = 19.924
- **C. A. Spiegel**, M. Hackner, V. P. Bothe, J. P. Spatz, E. Blasco, *Adv. Funct. Mater.* **2022**, *32*, 2110580. IF = 19.924
- Y. Jia[§], **C. A. Spiegel[§]**, A. Welle, S. Heißler, E. Sedghamiz, M. Liu, W. Wenzel, M. Hackner, J. P. Spatz, M. Tsotsalas, E. Blasco, *Adv. Funct. Mater*, **2022**, 2207826. IF = 19.924
- M. Gastaldi[§], **C. A Spiegel [§]**, C. Vazquez-Martel[§], C. Barolo, I. Roppolo, E. Blasco, *Mol. Sys. Des. Eng.* **2023**, Advance Article. IF = 4.920

Conferences:

- **C. A. Spiegel**, E. Blasco, "4D Printed Programmable Structures", 2022 MRS Spring Meeting SF14.06.03 "New Materials and Technologies III" (online conference), May 2022**.**
- **C. A. Spiegel**, E. Blasco, "4D Printed programmable microstructures: from macro- to microscale", 4D Materials Design and Additive Manufacturing Conference 2022 (online conference), September 2022. Awarded with the best oral contribution prize.
- **C. A. Spiegel**, E. Blasco, "Towards covalent adaptable microstructures by combination of two-photon laser printing and alkoxyamine chemistry", 4D Materials Design and Additive Manufacturing Conference 2022 (online conference), September 2022.
- E. Blasco, **C. A. Spiegel**, L.-Y. Hsu, "4D microprinting of programmable polymers: towards "living" behaviours", SPIE Photonic West 2023, January 2023. Awarded with the 3D Printing Best Paper Award.

In addition, I have contributed to further work including:

Peer-reviewed articles

- D. Schauenburg, M. Divandari, K. Neumann, **C. A. Spiegel**, T. Hackett, Y. Dzeng, N. D. Spencer, J. W. Bode, *Angew. Chem. Int. Ed.* **2020**, *59*, 14656.

  G. Zhu, H. A. Houck, **C. A. Spiegel,** C. Selhuber-Unkel, Y. Hou, E. Blasco, *Adv. Funct. Mater* **2023**. submitted (Invited review).

Book Chapter

- L. Y. Hsu, **C. A. Spiegel,** E. Blasco, 4D printing Principles and Fabrication, Smart Materials in Additive Manufacturing (Eds.: M. Bodaghi, A. Zolfagharian), Vol. 1, Elsevier, Amsterdam, the Netherlands **2022**, pp. 231 – 263.

Chapter 1

Introduction

Additive manufacturing, also known as 3D printing, offers a great number of opportunities to our society. Above all, the freedom in the rapid design and creation of personalized products to satisfy our necessities. One recent example of a challenge in our society was the necessity of a large amount of protection and medical equipment in a very short period of time to fight against the COVID-19 Pandemic. 3D printing has been established as one of the modern key technologies allowing fabrication of any arbitrary 3D design with a nowadays wide range of materials including most prominently polymeric materials, but also metals, ceramics, glass, paper or even food components. Furthermore, the concept 3D printing is not limited to on specific size scale but can be performed at a size regime ranging from microscale in the range of dozens and hundreds of nanometers to the macroscale featuring printings in meter scale due to the presence of a multiplicity of methods for 3D fabrication. Exactly this versatility in material and size variables for manufacturing is the key advantage of 3D printing rendering this technology to a present and future key player in a multiplicity of application sectors including the health and biomedical sector, the engineering and prototyping sector, electronics and robotics, the construction sector, the food industry, aircraft and aerospace industry, but also the protective and defense sector.

Despite of its versatility one main limitation of most present 3D fabricated materials is their lack of capability to be programmed or be adjustable in properties. Employing the novel concept of 4D printing the 3D/4D printing community approaches to react towards this, developing new smart materials permitting fabrication of “dynamically programmable” and “living” 4D structures with established 3D printing methods. Incorporating such dynamic and responsive behavior allows the fabricated 4D part to react to its environment, being responsive to changes of surrounding conditions such as light, temperature or present chemicals. Furthermore the “living” feature gives access to property adaptability of a 3D printed part approaching the opportunity for fabrication of entirely individually customizable 3D/4D architectures within a minimal amount of processing steps associated with all its advantages – faster production of the “right”, “fitting” parts for the specific process, less environmental impact due to minimum of processing steps and fully automatic generation of customized parts offering the opportunity to fast scale up production.

Both discussed features offered by 4D printing – the programmability and “living” behavior – were subjects of enormous research efforts in the recent decade. However, most of the reported 4D systems are still based on macroscale structures limiting the range of usage especially for smart applications within the technological trend towards miniaturization in today’s world.

To overcome these limitations, this thesis will concentrate on design of smart 4D materials employable for precise macro- and microscale 3D fabrication. On one hand, several different systems including smart polymeric materials such as shape memory polymers responsive to temperature and light are

investigated. In addition, a new system allowing precise microfabrication of “living” 3D objects adjustable in their size and mechanical properties by simple postprinting modification procedures is demonstrated.

The current thesis is separated in six chapters. In the following each chapter will be described in brief as well as its function and value for the reader:

Chapter 2 “General and theoretical background” will introduce history, theory and state of the art of the main topics of the current thesis. In particular, concepts of 3D printing in regard of technologies and their progress as well as of 4D printing with a focus on employed materials and their successful applications will be introduced. Moreover, the idea of “living” polymerization techniques and its application in “living additive manufacturing” will be presented. Here the focus will lie on the introduction of different “living” polymerization techniques as well as dynamic covalent networks as well as their implementation in 4D printing to achieve adaptable features.

Chapter 3 “4D Printing of Shape Memory Polymers: From Macro to Micro” will introduce my results on the design and 4D printing of shape memory polymer (SMP) structures at the macro and micro size regimes. In particular, a versatile SMP ink system is presented that can be employed with minimal modifications for 4D printing at both size regime: at the macroscale as well as at the microscale. In addition to printability at both regimes, excellent programmable and responsive features will be shown.

In Chapter 4 “4D Printing of Light Activated Shape Memory Polymers with Organic Dyes” the author demonstrates the simple design of SMP 4D macrostructures featuring responsivity toward light irradiation in the visible range. Making use of photothermal features offered by specific organic dyes and the SMP macroformulation introduced in chapter 3, 4D light activated shape memory polymers (LSMP) are developed offering the advantage of spatial control in shape memory response – extending in this way the materials applicability due to higher versatility in smart actuation.

Chapter 5 “Combining Two-Photon Laser Printing and Alkoxyamine Chemistry: Toward Living 3D Microstructures” introduces a novel 4D material allowing the precise fabrication of “living” microstructures that can be adjusted in their mechanical properties and their size by performance of simple postmodification procedures. In particular, the system was developed in the spirit of the concepts of “living additive manufacturing” and “covalent adjustable networks” combining chemistries of both approaches towards dynamic materials.

Chapter 6 “Experimental Section” will contain a detailed description of all performed experiments and characterization processes to design, fabricate and characterize all 4D systems presented in chapter 3, 4, and 5.

Chapter 7 “Conclusion and Outlook” will conclude the main body of this thesis by summarizing the most important results and findings of the experimental work. Furthermore, an outlook will be provided by the author showing next design steps necessary to take to extend the functionality and applicability of presented functional systems. Thereby, a more general outlook including possible pathways to 4D geometries of higher programmability, versatility and thus applicability will be provided by the author.

Chapter 2

General and Theoretical Background

Standing on the shoulders of giants

In this chapter, I will introduce the general concepts and terms of the topics relevant for this thesis. The goal is to provide the reader with general and theoretic information about 3D printing technology, the 3D fabrication process and current techniques applied within my doctoral thesis. Vat photopolymerization, and here particularly digital light processing (DLP) and two-photon laser printing (2PLP), both main techniques employed will be discussed in more detail. Subsequently, I will describe the transition from 3D towards 4D printing, going from the concept to the main applied material classes and their 4D mechanism and applications. Here a special focus will lie in shape memory polymers (SMP), one of the main material classes used in this work. Last, I will describe the concept of living additive manufacturing based on living polymerization techniques.

2.1. 3D Printing

3D printing, also termed "additive manufacturing"[1-4] or "rapid prototyping"[5,6] refers to fabrication technologies allowing the generation of three dimensional (3D) structures with high shape complexity.[1-6] The main advantage of this technological platform for industry is the accessibility towards customized 3D parts made from a manifold library of diverse materials including different kinds of polymers, ceramics, metals, food or glass.[1,7-11] Combining this flexibility in printable materials with the versatility in the 3D objects' size scales offered by the different fabrication techniques included in the term "3D printing", 3D geometries of high complexity can be fabricated from microscopic scales in the range of hundreds of nanometers up to macroscopic scales in the centimeter or meter regime – more tangible for humans.[1,12,13] Exactly this versatility in material and size enriches technological progress in various areas of industry or science such as medicine[14,15], (micro)robotics[16,17], electronics[18,19], the construction sector[13,20], or art and design[21] to name a few – leading to the reasonable conclusion that 3D printing is one of the important technologies at presence becoming even more influential for science, industry and society in general in the next decades.

The general workflow[1] to produce 3D geometries via 3D printing starts for all included fabrication techniques with the design of a virtual 3D model. In the next step this 3D model is digitally sliced by appropriate software and a file readable for the corresponding printing device is generated. The printer used the geometric information included in this file to build – 3D print – the final structure in the third step with the ink employed. Due to the layer-by-layer fabrication manufacturing process of most 3D printing techniques, overhanging structural features are often supported by digitally incorporated supporting structures, allowing defect free structure-fabrication.[1] Such auxiliary structures can be added manually or automatically using the slicing software and will be automatically incorporated into the printing file data and printed during the 3D fabrication process. In the final step a postprocessing

routine is applied on the 3D printed structure. Depending on the technique postprocessing can include, removal of auxiliary structures, removal of unreacted – not printed – chemical moieties such as monomers or dye and solvent molecules by development in an appropriate solvent, a post-curing step under suitable temperature or irradiation conditions, or additional manufacturing steps such as grinding or polishing. After this step the 3D fabrication workflow is finished and the generated structure can be used for the intended purpose.[1]

As mentioned beforehand the term 3D printing includes a multiplicity of different techniques distinct in achievable size scale of the fabricated 3D structure and the applied printable material. Based on defined terms by the ASTM International Committee F42 on Additive Manufacturing Technology[22] in 2009 3D printing techniques are generally classified in seven distinct categories including:

1) "Material Extrusion" a 3D fabrication process in which the printable materials are dispensed through a nozzle called extruder building the 3D structures line-by-line in the x-y plane and layer-by-layer along the z-axis.[1,23] Techniques included in this category are fused deposition modelling (FDM)[24], direct ink writing (DIW)[25], 3D dispensing or bioplotting[26]. Typical materials applied are thermoplasts such as polylactic acids, acrylonitrile butadiene styrene (ABS) or polyethylene terephthalate glycol (PETG).

2) "Material jetting" defines a 3D printing technological class, that builds 3D objects by selective deposition of droplets of printing material based on photopolymer or thermoplasts.[1,27] Inkjet printing[28], a technique applied in printable electronics, is part of this technological category. As reasonable from its name this class can be imagined as adding the third dimension to a 2D ink jet printer.

3) "Binder jetting" uses a liquid bonding agent, termed binder, to form stable connections in between powder particles – to fuse powder.[1,29] In the process binder is selectively added to powder to fuse a layer of defined geometry. Subsequently, another layer of powder is added and the binder addition is conducted for the next sliced layer forming in this way the final 3D geometry. Materials for powders include sand, metals, polymers or ceramics. Typically, water- or organic binders are applied. Importantly this class permits complex structure fabrication without the necessity of auxiliary structures, because the surrounding powder itself acts in this role.

4) "Vat photopolymerization" is a class of 3D printing techniques in which a liquid or solid photosensitive species is selectively irradiated with suitable light to induce selective curing by light-initiated polymerization or selective dissolution of monomer depending on the type of ink.[30] This class comprised several different techniques starting with

stereolithography (SLA), digital light processing (DLP), two-photon laser printing (2PLP)[12], light sheet-based approaches[31] and continuous printing approaches[32] as well as volumetric printing approaches[33]. Typical materials fabricable are photopolymerizable polymers as well as ceramics, glass or in some cases metals.[1]

5) "Powder bed fusion" another 3D printing class fabricates 3D structures by selective binding of powder particles, in a layer-by-layer manner such as binder jetting.[1] In contrast to this technique powder bed fusion uses thermal energy to selectively fuse regions of the powder bed. Source for this thermal energy is thereby a laser or electron beam. Selective laser sintering (SLS)[1,34] and electron beam melting (EBM)[1,35] are techniques that fall in this 3D printing category. Powder materials employed are usually based on metals as well as polymers.

6) "Directed energy deposition" uses a focused thermal energy source such as an electron or laser beam to melt the printing material in the same time as it is deposited by a nozzle.[1,36] Main materials used in this category are metal powders or metal filaments.

7) "Sheet lamination" is a 3D printing process in which sheets of materials are stacked or laminated on each other to generate the final 3D geometry.[1,37] In principle a large variety of material sheets including paper, polymers and ceramics can be 3D processed utilizing this method.[1] In the process the choice of a suitable binder depends on the printing material applied.

In the following section, I will focus on the 3D printing class of vat photopolymerization and here especially on SLA/DLP and 2PLP.

2.2. Vat photopolymerization

As previously described, vat photopolymerization is a 3D printing technology class in which a photoreactive chemical species – the photoresist respectively ink – is irradiated selectively by light of suitable wavelength and intensity to fabricate desired 3D geometries.[1] Applied light sources are LEDs[1,38,39,] or laser[1,40] ranging from ultraviolet (UV) over to visible (VIS) to near-infrared (NIR) wavelengthts.[1,38-40] Importantly, after fabrication a development step in suitable solvent is necessary to remove soluble residues (unreacted monomers, dyes, solvents, soluble residues of the ink) from the generated structures. Usually this is followed by a post-curing step inside a UV-chamber to reduce the number of unreacted reactive moieties on the structure's surface and for homogenization and improvement of mechanical properties within the 3D geometry.[41]

Generally, photoresists employed in 2D lithographic techniques are divided in positive or negative photoresists depending on their response to light irradiation.[1] Translating this concept to 3D printing, inks of both kind of behaviors are employed. Inks behaving as positive photoresists will become more soluble in response to light irradiation, rendering them the perfect material for direct generation of channels inside a prefabricated structure for example via 2PLP.[42] In contrast inks acting as negative photoresists are initially a mixture of low molecular weight monomers or oligomers in a liquid state. Upon light irradiation with light of suitable wavelength the liquid ink becomes insoluble due to formation of insoluble polymeric networks via chemical reaction.[38,39,43,44] All inks presented in this thesis are based on negative photoresist behavior. Thus, only this type of 3D printable inks will be treated in the following.

2.2.1. Ink components and curing mechanisms

Typical inks suitable for vat photopolymerization consist of several core components including a photopolymerizable moiety being mainly mono- or bifunctional chemical compounds, a photoinitiator (PI), if necessary photoabsorbing dyes and solvents. Importantly the type of PI and photopolymerizable moiety decide about the chemical curing mechanism and final mechanical and functional properties of the 3D printed geometry.[1] Most popular photopolymerizable moieties in vat photopolymerization are acrylate- respectively methacrylate-based monofunctional and multifunctional compounds.[1,44] Inks containing this type of photopolymerizable groups are cured via the mechanism of free radical polymerization[45] depicted in Scheme 2.1. The first step – termed initiation – starts with a radical formation step including the generation of initiating radicals by irradiation of the PI with light of suitable wavelength leading to homolytic generation of radical moieties. In the following these radicals react with the photopolymerizable groups, in the present case the double bond moiety of the methacrylate and the acrylate compounds. Forming a first stable bond towards the ß-carbon of compound species a radical is formed at position α in respect of the carbonyl group due to resonance stabilization and in case of methacrylates the stabilizing electron donating effect generated by the adjacent methyl group. This radical species will conduct in the next step - the chain propagation - a carbon-carbon bond formation to another monomer species generating chain end radicals again. This chain growing process is repeated until the chain growing process is stopped by radical recombination or disproportionation during the termination step. During recombination two chain end species will recombine forming a carbon-carbon single bond at the cost of two chain end radicals, quenching in this way the propagation process. At disproportionation one chain end radical abstracts an H atom from another propagating species resulting in quenched C-C single bond species and a double bond

species. Additional typical quenching agents leading to termination are oxygen[46,47] or inhibitors such as nitroxides[48] featuring a stabilized radical.

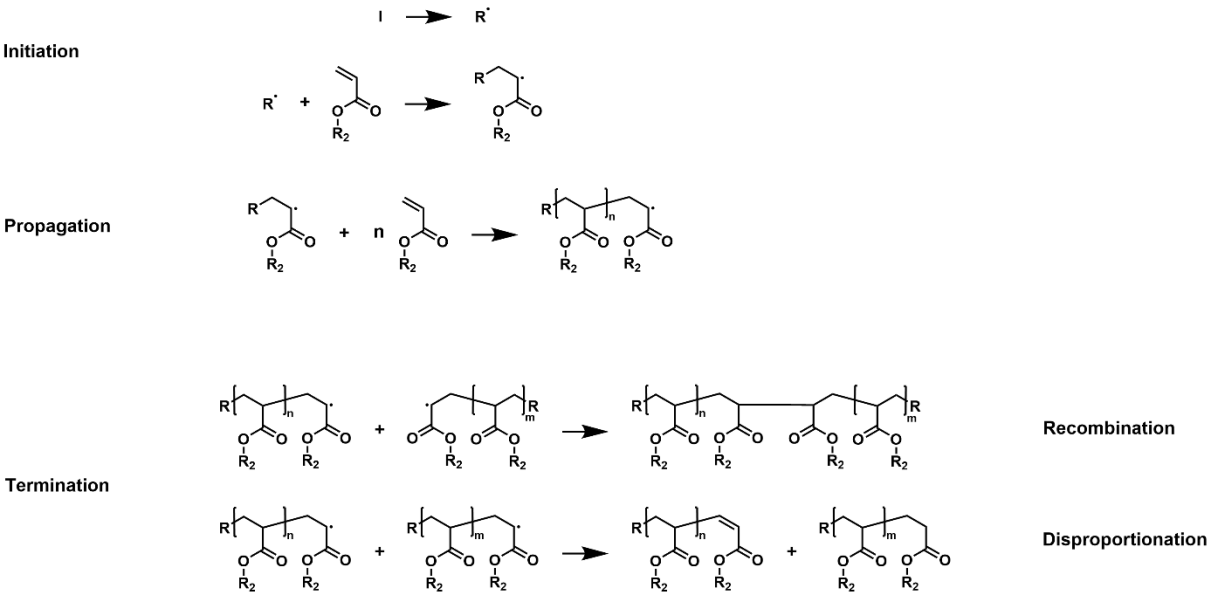

Scheme 2.1: General mechanism of free radical polymerization including i) initiation, ii) propagation and iii) termination steps.

Further on in case of presence of solvent chain transfer the abstraction of an H atom by the active chain end leads to termination and generation of a solvent radical. Importantly vat photopolymerization is applied for both monomer types, acrylates and methacrylates, whereas acrylate-based monomers are in general preferred due to faster reaction times.[1]

Besides, vat photopolymerization is also reported for thiol-based monomers in combination with acrylates or other species offering double bonds, enabling 3D printing of geometries via the thiol-ene mechanism.[1,48] A prominent example of a 3D ink – used in 2PLP – labelled SU8 includes epoxide-based

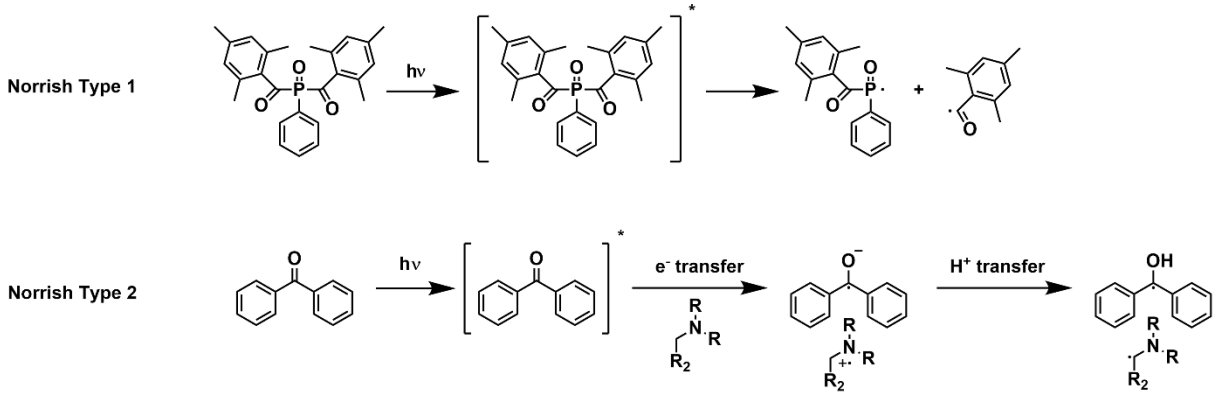

Scheme 2.2: Photoinitation mechanisms. Norrish type 1 (above) and type 2 (below) mechanism are depicted.[1]

monomers and works via a cationic polymerization mechanism.[1,49,50] In this case the initiation is not based on a radical photoinitator but on a photoacid generator[51] providing the necessary proton to initiate the subsequent chain growing process.

As stated, the PI as the pivotal role of efficiently converting the energy of the stimulus light towards the generation of reactive species allowing the initiation and successive chain propagation step. In case of this thesis, I will discuss mainly radical photoinitiators due to their relevance for all presented systems in this work. Generally radical photoinitiators produce initiating radicals via two mechanisms named Norrish Type 1 and Norrish Type 2 (see Scheme 2.2).[1,52] Photoinitator systems working via a type 1 mechanism consist of a single photoreactive molecule, splitting homolytically in response to light irradiation of suitable wavelengths (see Scheme 2.2). Prominent examples of type 1 photoinitiators are benzil ketals or acyl phosphine oxides, whereby especially commercially available examples of the later named TPO or BAPO (see Scheme 2.3) are often employed for inks in vat photopolymerization.[1,53-56] The process of radical generation via photocleavage starts for both cases with the excitation of the n to π* transition. The transition itself is located in the energy regime of 350 to 360 nm for benzil ketals and even lower in the region of 400 nm for acyl phosphine oxides. Main

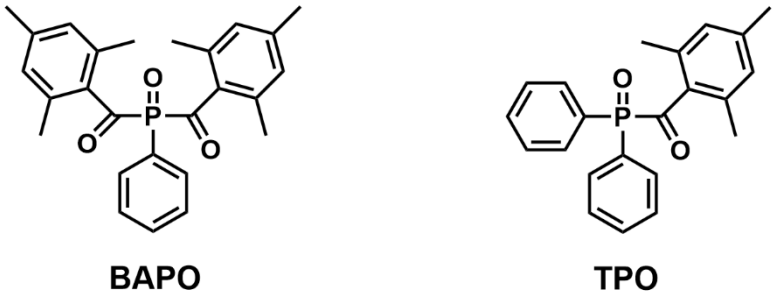

Scheme 2.3: Representation of chemical formulas of prominent Norrish Type 1 photoinitiators BAPO and TPO.

reason for the energetic redshift is the lowering of the π* state due to the presence of the phosphorus atom adjacent to the carbonyl group.[1] This rather low energy transition render both types of molecules ideal for controlled photochemical generation of radicals especially due to the avoidance of harsh UV irradiation, reducing the amount of possible side reactions within a 3D printable resin as well as exposure to less dangerous conditions for the 3D printer operator. After excitation the formed excited singlet state can either cleave directly forming radicals or form this reactive species after an intersystem crossing transition to an excited triplet state and successive homolytic bond fission (see Scheme 2.2 in case of BAPO). In case of Norrish type two photoinitiators a two-component system is applied composed of a light absorbing molecule called sensitizer together with a co-initiator labelled synergist.[1,52] In response to irradiation with suitable wavelengths the sensitizer enters an excited state, accepting a hydrogen atom donated by the synergist. The synergist forms in this process a radical, that acts as initiating species in the successive free radical polymerization. Reported synergists are tertiary amines with at least one alkyl substituents. Examples for sensitizers are benzophenone or isopropylthoxanthone.[57,58] Scheme 2.2 depicts the mechanism of Norrish type two radical generation in case of a tertiary amine acting as synergist and a benzophenone being the sensitizer. After light induced excitation of benzophenone an electron transfer occurs from the amine towards the

benzophenone forming a radical cation amine species and a radical anion sensitizer species. Subsequent proton transfer from the radical cation towards the racial anion produces the initiating radical synergist species.

Additionally, ink formulations usually contain a photoabsorber, representing chemical species that absorb in the regime of the applied photoinitating wavelength reducing in this way the penetration depth D_p – the depth of light penetration into the resin at which its initial intensity is lowered to the factor e^{-1} – of the curing irradiation.[59] Including effects of photoinitiator and photoabsorber the penetration depth D_p can be described by the equation 2.1:

$$D_P = \frac{1}{2.3\ (\varepsilon_1[PI]+\varepsilon_2[A])} \qquad \textbf{(Equation 2.1)}$$

Where D_P is dependent on the extinction coefficient (ε_1) and concentration of the photoinitiator (PI) and on the extinction coefficient (ε_2) and concentration of the photoabsorber (A).[1,59] As deducible from equation 2.1 higher concentration of photoabsorber inside the resin reduces D_P and consequently axial length – the thickness – of the cured layer in SLA and DLP, meaning an improvement in axial resolution.[1] Furthermore, the whole polymerization process appears to be more controlled. Depending on the applied curing wavelength a selection of commercially available photoabsorbers is applicable. For standard wavelengths in DLP at 385 nm or 405 nm azodye species Sudan I is often used as absorber of first choice as visible in a range of SLA and DLP based publications[60,61] (see Scheme 2.4).

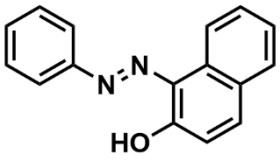

Sudan I

Scheme 2.4: Chemical structure of prominent photoabsorber Sudan I.

As it is sometimes necessary solvent is added as component to the ink aiming complete dissolution of monomer, photoinitiator or additional additive.[62,63] In general addition of solvent is not beneficial in 3D printing due to several reasons: I) addition of solvent leads to inevitable dilution of polymerizable components within the ink, being the reason for poor curing respectively insufficient curing during the printing/polymerization process, resulting in non-printability of inks respectively poor printing results.[62] II) Solvent within the 3D printed structures will be removed during the development process after 3D structure fabrication, because no chemical inclusion into the polymeric network has occurred. This "empty" space inside the 3D structures leads to issues in regard of mechanical and structural stability. The appearance of cracks within the 3D structures is often a consequence due to shrinkage.[64] Levkin *et al* showed recently an DLP approach where non photopolymerizable solvent was used

actively to generate microporous structures.[65] Stability of the final 3D structures was achieved by development via supercritical drying. III) Solvent molecules can in principle lead to chain transfer events during the polymerization process prematurely terminating in this way the chain propagation leading to poor polymerization results.[45,66] Consequently, structural instabilities or non-printability as described in point I can be a possible outcome.

To avoid these obstacles generated through the use of solvents, many commercial and published resins try to use solvent free formulations, if possible. In case of absolute necessity due to dissolution of monomer or PI components or to lower the viscosity of an ink a reactive diluent is sometimes utilized meaning a low viscosity monomer that allows dissolution and viscosity decrease.[63] This concept of reactive diluent is often reported for inks used in macroscale vat photopolymerization methods. A special role is taken at this point by hydrogels. In case of this material class the solvent water is in addition part of the chemical structures of the polymeric network stabilizing it.[67] Further on hydrogels are usually stored in aqueous environment preventing them from desiccating and consequential structural damage. 3D printing appeared here to be possible with higher solvent (water) content in general.[68]

In addition to all main components discussed already, functional additives can also be added to a liquid ink to incorporate additional properties to finally 3D printed structures, extending in this way the library of accessible functionalities. Such composite 3D printed structures can be achieved by inclusion of magnetic nanoparticles, piezoelectric barium titanate nanoparticles, oxide nanoparticles, quantum dots, carbon nanotubes, proteins, biological cells to name a few. Combining this units with polymer inks allows access towards additional functionality such as magnetism, conductivity, electrochromism, thermoresponsivity, photoresponsivity, biodegradablility as well as enhancement and tunability of mechanical properties.[69]

In the following paragraphs the two main vat photopolymerization methods employed in this thesis will be discussed in more detail starting first with digital light processing (DLP) for macroscale 3D printing and afterwards two photon laser printing for structure generation at the microscale regime.

2.2.2. Digital light processing (DLP)

Starting the discussion of DLP 3D printing first comments must be made about 3D stereolithography (SLA). SLA is one of the first origin 3D printing technologies and one of the first one using light as medium/stimulus to achieve controlled and selective curing in terms of spatial solidification to fabricate 3D geometries from initially digitally generated files.[1,59] The first appearance of SLA in history was in a patent of 1986 by Chuck Hull[70], describing the layer-by-layer lithographic fabrication of solids

being seen today as the ground work of commercial 3D printing giving rise to the first commercially available SLA 3D printers in the late 1980s by Chuck Hull's company 3D Systems. Figure 2.1 shows the general setup of an SLA apparatus described in Hull's patent. Core of the device is the coherent wavelength source – in most cases a laser in the UV range – inducing polymerization and thus structure fabrication in a layer-by-layer manner onto an axially movable platform, lowering itself after each finalization of each layer, so that the laser can start fabrication of the next one. Importantly the velocity of the 3D fabrication process depends on the speed of the laser focus that sequentially scans point-by-point through the area of each layer always located at the working surface of the ink inside the vat. Hereby achievable resolution as well was minimal feature size is determined by the size of the focal volume of the laser. Lateral control of the laser is achieved by use of galvano mirrors, optical devices directing the laser beam in the x-y plane depending on their position.

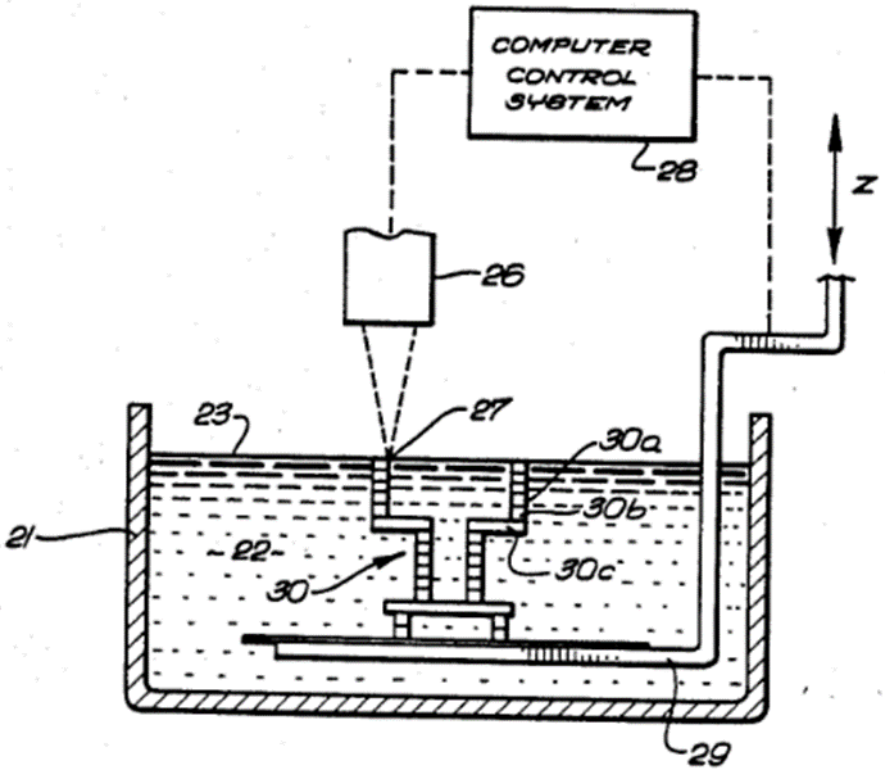

Figure 2.1: Image of SLA setup, described in Chuck Hull's patent of 1984. Image adapted from U.S. Patent 4575330, Hull.[70]

Digital light processing can be seen due to its similarity to SLA as a progression of the initial technique. The general setup is depicted in Figure 2.2. Differently from SLA technique DLP uses a LED lamp emitting in the ultraviolet respectively visible range as light and curing source – standard commercial devices are available with LEDs featuring wavelengths in the UV and visible range.[1,68,71,] Importantly curing will also occur in a layer-by-layer fashion, however the instead of the point-by-point curing process in SLA the sliced object plane will be illuminated at once by selectively masking the light source, making the curing process via DLP technique much faster than in SLA structure fabrication. To explain

the 3D structure fabrication process in more detail we need to consider the DLP setup in Figure 2.2. The UV LED light source produces a beam of desired intensity and wavelength directed towards a digital micromirror device (DMD). At the DMD each sliced layer of the 3D structures is transformed to a black and white image that is projected towards the transparent bottom of the vat containing the ink onto a vertically movable build platform also termed build head, curing in this process the sliced layer. After fabricating a layer on this build platform, the build head moves upwards, often out of the ink, so that new photopolymerizable material can flow in between the space of previously printed layer and the bottom of the vat container. After moving downwards again the next layer will be polymerized onto the previous layer. This process is repeated until the fabrication of the 3D structure is finished.

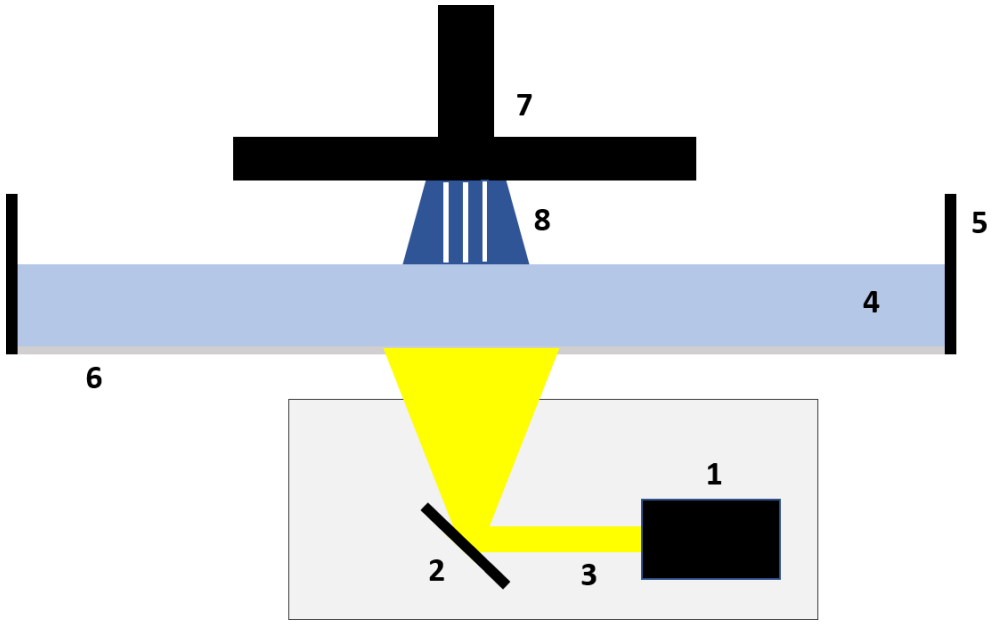

Figure 2.2: Schematic representation of a DLP setup. Numeration corresponds to the following components: (1) the curing light source, (2) the digital mirror device, (3) curing beam, (4) ink, (5) tray, (6) foil transparent for curing light, (7) vertically movable print head, (8) fabricated structure.

2.2.2.1. Resolution, minimum structure size and ink parameters

In terms of DLP, SLA and all other 3D printing technologies the printing resolution defines the minimum distance two separately printed lines or objects can still be distinguished as two individual moieties.[73] The minimum structure size is a quantity describing the smallest possible structural unit manufacturable via the printing method. Both quantities make in principle a statement about the quality of a printing process respectively a 3D fabricated object in terms of fabrication precision. In DLP and SLA we can distinguish between the lateral and axial resolution.[74] Whereas both values are defined in SLA by the size of the focal volume of the curing focus, the values in DLP systems are dependent on different properties of the 3D printer. In terms of fabrication precision, the achievable resolution as well as minimum structure size in axial direction is dependent on the step size the motor

can heighten or lower the build platform defining the minimum possible layer thickness from the side of the device.[1,73,74] The maximum lateral resolution as well as minimum structure size in lateral direction are defined by the x-y dimensions of the pixel projected onto the ink vat.[1,73,74] In case of axial precision layer thicknesses in the range of some micrometers can theoretically be achieved. The same is valid for the pixel sizes – the lateral dimensions. Here current DLP technology allows sizes far below 100 µm, giving in theory access to fabrication of objects of very high precision.[75] Importantly main limitations in terms of lateral and axial resolution as well as accessible minimum structure sizes are defined by the properties of the ink itself and values offered by the printer can be seen as theoretical maxima accessible with the "perfect" ink system. Important parameters describing the quality of an 3D ink are the previously discussed penetration depth D_P and the critical exposure E_c. D_P describes the pathlength of the curing wavelength into the ink leading to a decrease of intensity down to a value e^{-1} (~ 37%) of the initial curing intensity giving a good estimate of the possible layer thickness and the sensitivity of the ink towards irradiation. Main factors influencing D_P are the concentration of PI and photoabsorber within the ink visible in Eq. 1 before. E_c another ink intrinsic parameter is defined as the exposure necessary to reach the gel point of the ink. Below E_C the ink remains liquid, above E_C at least partial polymerization is observed.[59] The critical energy itself depends on the amount of photoinitiator and the amount of possible radical inhibitor within the ink system. Evidently increase of PI to a certain point allows general lowering of the critical energy rendering the curing process more efficient due to lower necessary LED power.[76] Considering simply the increase of the probability to reach the necessary level of initiation events with subsequent propagation for network formation even at lower intensity respectively photon density makes this behavior plausible. However, to large increase in photoinitiator concentration can have the effect of inhibiting the initiation process of propagation process due to dominant premature self-termination caused by the high density of active radical species rendering the curing process during 3D printing inefficient.[77] Furthermore, too high PI concentration usually leads to decrease in control of fabrication during 3D printing – meaning loss in structural precision of the finally fabricated 3D object. Thus, the optimal amount of PI must be evaluated experimentally. As addressed radical inhibiting species for example stable radicals like nitroxides result in higher critical exposure dose values compared to inks without inhibitor.[76] Higher doses are necessary because many generated radicals respectively radical chain ends will be quenched in the presence of the inhibiting species thus making it necessary to generate a higher number of initiating radicals respectively reactive chain ends for successful polymerization and generation of solid non-dissolvable 3D structures.

Both quantities D_P and E_c can be easily accessed via experimental evaluation and plotting of the Jacob's working curve.[59] To generate such a curve the curing depths C_d of an ink at different irradiation time intervals at constant curing intensity are measured and plotted semilogarithmic against the applied

energy dose. Conduction of the linear regression allows access to the immediate evaluation of E_c and D_p as visible in equation 2.2 being the mathematical description of the working curve.

$$C_d = D_p \, ln\left(\frac{E_{max}}{E_c}\right) \qquad \textbf{(Equation 2.2)}$$

Where E_{max} corresponds to maximum energy dose. Apparently from equation 2.2 the critical energy dose E_C can be determined from the x-intercept (energy dose) and D_p is equivalent to the slope of the working curve. In this way Jacobs working curves offer an easy visualization for quality description and comparison of different ink formulations (Example of schematic Jacobs working curve depicted in Figure 2.3).

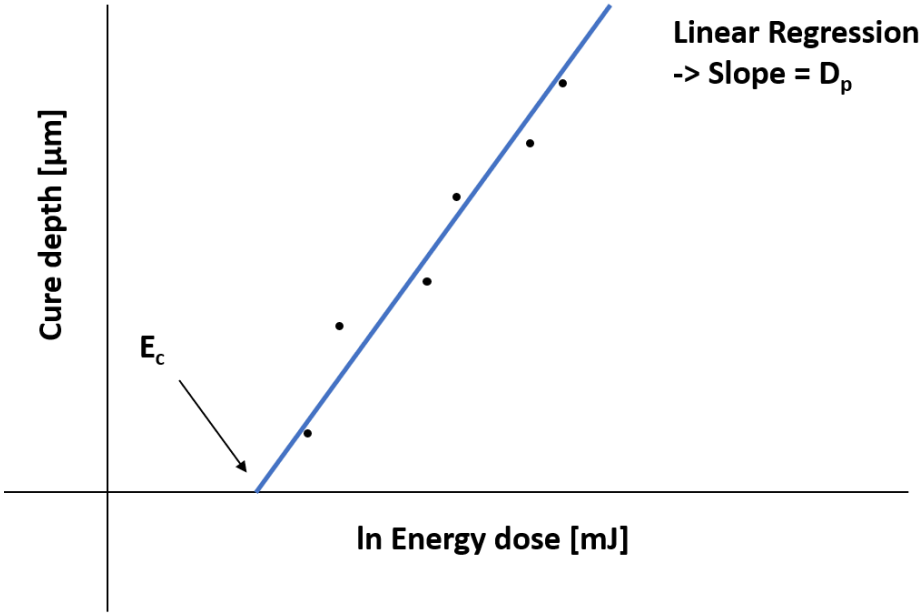

Figure 2.3: Representation of Jacobs working curve. Cure depths at different energy doses are measured and are represented semilogarithmic. A linear regression will be performed on obtained measurement points. The slope of the linear regression corresponds to the penetration depth D_p, the x-axis intercept to the critical energy dose E_c.

2.2.2.2. Current developments:

Although DLP based 3D printing has been established as valuable fabrication tool for precise 3D manufacturing in range of different industries emphasizing here dentistry[78] or jewelry[79], the method shows weak spots in practical application, causing especially challenges in its commercial application. First 3D fabrication via DLP is not a smooth continuous manufacturing process allowing preparation of a 3D object in a non-disruptive solidification process. After curing each layer, the build head with the structure on it has to move outside of the ink, so that ink can flow again back to the space, where the previously cured layer was. In this way enough curable material is present for curing of the next layer. This necessary recoating step has two consequences for DLP fabrication. On the one hand the recoating step appears to be relatively time-consuming, representing a large portion of time during structure

fabrication – especially for structures with high axial dimension meaning many curing steps.[1,32], On the other hand, the homogeneity of the structure along printing direction is disturbed due to discontinuous fabrication process. Interlayer connection is one of the main weak spots in DLP fabricated geometries, rendering them mechanical stable along the lateral dimensions but much more fragile axially.[41] To lower axial discontinuity, homogenize and improve the mechanical properties, postcuring under UV irradiation is necessary.

To overcome these issues continuous liquid interface production – abbreviated as CLIP – was developed by DeSimone *et al.* in 2016.[32,80] This vat photopolymerization method uses an oxygen permeable film to inhibit polymerization at the surface close to the UV source allowing in this way exclusion of the time-consuming recoating step for each curing layer rendering the structure fabrication continuous with less interlayer defects and much faster in axial direction.

Another study carried out by Walker and coworkers make use of a fluorinated oil as mobile liquid interface at the bottom of the ink vat, reducing in this way adhesive forces between the interface and the printed objects, allowing for a continuous rapid printing process.[81] In this process, unlike in CLIP, where the size of the printing area is restricted by thermal limitation, the flowing oil enabled direct cooling across the entire printing area giving access to vertical printing rates of more than 430 millimeters per hour and a volumetric throughput of 100 liters per hour. Using this technique, a variety of materials can be utilized for 3D structure fabrication including hard plastics, ceramic precursors, and elastomers. In a similar approach Wu and coworkers introduced a slippery surface for DLP printing to reduce the vertical solid-solid interfacial adhesion increasing the refilling speed of liquid ink and further improve the printing speed.[82] Moving away from layer-by-layer printing approach – in its discontinuous (DLP) and continuous form (CLIP) – volumetric 3D printing approaches have recently been developed.[33,83-85] Here, 3D printing is performed by curing inks in 3D space, giving access to the fabrication of complex and highly detailed shapes. First successful developments were performed by Kelly *et al.* designing a volumetric 3D printing technique termed computed axial lithography (CAL).[83] 3D structure fabrication is performed by concurrent printing of all points of a 3D object by illumination of a rotating volume inside the ink with a dynamically evolving light pattern. Using this approach features as small as 0.3 millimeters were printable using acrylate-based inks. Furthermore, soft structures with excellent surface quality were fabricable into a gelatin methacrylate hydrogel. Importantly, fast 3D structure generation in the centimeter scale within printing times between 30 s and 120 s were achieved. Further progress was made by Regehly and coworkers presenting a volumetric approach using a projection light system in combination with a novel dual-color photoinitiator enabling dual-color photopolymerization.[84] This process offers rapid and high-precision

printing, visible in the ten times higher values for resolution compared to state of the art volumetric printing methods such as CAL without feedback optimization.

2.2.3. Two-photon laser printing (2PLP)

Two-photon laser printing (2PLP), often also termed "direct laser writing" (DLW)[43], "multiphoton laser lithography"[86] or simply "direct laser lithography"[87] is a nonlinear light-based 3D printing technique predestined for the precise fabrication of 3D and 4D structures at the micro- and nanoscale (few hundreds of nanometers to dozens of micrometers). First time reported, Maruo *et al.* demonstrated in 1998 generation of 3D microhelices, hinting towards the various opportunities this technique will open to the scientific community in the next decades.[88] By scanning a tightly focused femtosecond pulsed laser of wavelength 790 nm into a photopolymerizable ink, solidification along the focus pathway was achieved, allowing real 3D structure generation without the restrictions of the layer-by-layer fabrication process employed in many other additive manufacturing techniques. Solidification of the liquid resist – 3D geometry generation – occurs in this process by two-photon polymerization (TPP) a process based on two-photon absorption (TPA), meaning initiating the polymerization process via prior simultaneous absorption of two or more photons by a photo initiating species, starting the network formation process in case of a negative photoresist-like 3D ink[44] respectively dissolution process for a positive photoresist-like 3D ink[42]. Specifically, the physical requirements and properties leading to a successful TPA event – described in the following section – are the basis for the main advantages of 2PLP, the structure formation below diffraction limit, and generation of microstructural geometries such as woodpile structures[89] inaccessible by other microfabrication techniques such as electron beam deposition or conventional lithographic techniques.

2.2.3.1. Two-photon absorption (TPA):

Two-photon absorption (TPA), a nonlinear absorption process, was first predicted by Maria Göppert-Mayer in 1931 in her doctoral thesis, where she defined the process as "an absorption event caused by the collective action of two or more photons, all of which must be present simultaneously to impart enough energy to drive a transition"[90]. Experimental validation of Göppert-Mayer's hypothesis happened 30 years later by Kaiser and Garret by exciting $CaF:Eu^{2+}$ [91] via two-photon absorption.

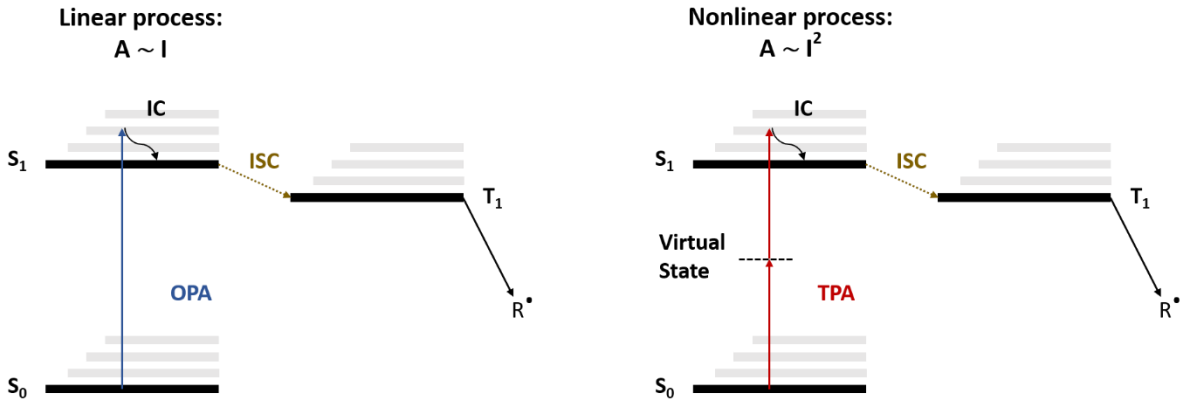

Figure 2.4: Simplified Jablonski diagram comparing the absorption and radical generation process in case of linear one-photon absorption (OPA) and nonlinear two-photon absorption (TPA).

In the process of TPA the absorbing species – in most cases of 2PLP a photoinitiator molecule – is excited from its ground electronic state S_0 to an excited electronic state S_1 by simultaneous absorption of two photons via a short lived (fs) virtual state. Hereby, S_2 has the energy roughly equal to twice the value of the excitation laser wavelength. Due to the extremely low probability of this nonlinear absorption event to happen, a sufficiently high concentration of photons must be present.[1] This is achieved by tightly focusing a femtosecond pulsed laser, providing in this way the necessary photon density to drive the excitation. Successive internal conversion towards the ground vibrational state of S_1 is followed by intersystem crossing towards the excited triplet state T_1. Deexcitation back to the ground state is accompanied by generation of the radical by the photoinitiator molecule starting the polymerization process.[12] The whole process is illustrated and compared to a linear one-photon absorption (OPA) process in the simplified Jablonski diagram depicted in Figure 2.4. Owing to its nonlinearity, the probability of TPA is unlike linear OPA not directly but rather proportional to the square of the light intensity.[1,12] Consequently, successful initiation and successive polymerization events will most probably happen in the center of the laser focus – the spatial volume with highest photon density –, decreasing in its likelihood by departure from the focus center, confining in this way the spatial volume where successful polymerization – solidification – of the material can happen. This volume entity is termed voxel, the 3D equivalent of the two- dimensional “pixel”. The dimensions of a voxel are due to prior presented physical features below the diffraction limit of light allowing polymerization of features in the range of hundreds of nanometers. Dimensions of this voxel are in general dependent on applied laser power, employed objectives as well as the level of nonlinearity. Exemplary, increase of laser power during writing will lead to an increased voxel size due to increased likelihood of successful polymerization within a larger volume of focal space.[92] Optical properties of the employed focusing objective – the numerical aperture – have a direct effect on the voxel size, consequently allowing to simply select the level of end structure precision or polymerization

throughput by simple choice of the right objective.[92, 93] Increase of the level of nonlinearity, meaning change towards a multiphoton process including three or n photons decreases the voxel size due to the process probability proportionality towards n^{th} power of intensity. However, processes above n=3 are less likely to be employed due to the high necessary intensity densities and associated energy costs.[94] Properties of the ink components such as the two-photon efficiency of the photoinitator (PI) or the general viscosity of the resin further affect the shape and accuracy of finally fabricated structures. Highly efficient PI allow generation of stable structures at low energy doses, meaning low laser intensities and high scanning velocities, generating minimal linewidth.[95] Viscosity of the resin, principally set by the monomers respectively crosslinkers, affects the size and the stability and efficiency of the printing process at large extent.[96] Both optimizing the ink materials and the optical components for the 3D fabrications process allows highly efficient microstructure generation with high scan speed close to the 1 m s^{-1} regime.[44]

Unlike many processes in the ink during structure fabrication by TPP are yet not fully understood, for example reaction-diffusion kinetics[97-99], polymerization behavior and its associated precise 3D structure generation by TPP can be explained by two theoretic models: i) the threshold model, ii) the accumulation model.[44]

The threshold model makes a statement about the minimal dose necessary for successful – meaning stable 3D microstructure generation. Concentrating on the irradiated focal space there is a certain exposure dose, necessary – the energy threshold dose E_{th} – allowing the ink to sufficiently crosslink generating in this way stable 3D microstructures in general comparable with the critical exposure dose E_c in SLA/DLP macroscale fabrication. Below this dose irradiated material is in a state of insufficient crosslinking, forming soluble entities, that can be washed away during the development step. In this way the threshold model "digitizes" the exposure dose to material or "no material". Furthermore the model includes no restriction in minimal voxel respectively feature size allowing in principle printability of arbitrary small features or voxels.[98,100,101] There is in principle no limit for the linewidth imposed by the diffraction of light.[100] Furthermore, an upper energy dose threshold termed the burning threshold E_{damage} is defined, marking the upper limit in regard of energy dose for structure fabrication.[1] At this dose or above structures will be damaged due to occurrence of microexplosions, caused by heat accumulation due to occurrence of multiphoton absorption processes. The fabrication window in between E_{th} and E_{damage} is termed dynamic range of an ink and is a parameter for the general printing quality of an microink.[96] The larger the dynamic range of the ink the higher the fabrication stability provided by the ink system rendering it more suitable for general application in industry and science.

In contrast the accumulation model describes the effect on multiple exposure on a given ink volume element. This is especially valuable in explaining instability effects due to overpolymerization[44]

respectively the advantage of TPA based processes over one OPA processes in terms of resolution.[44] It implies that if an ink is subjected to two or more point exposures at the same location or at different, the ink integrates the corresponding exposure doses respectively "remembers" prior exposure events regardless if they are above or below the polymerization threshold. Important consequences of the accumulation model are i) the minimal separation distance between two features is defined by the Sparrow criterion[2] and ii) due to integration over all exposures at different positions it is impossible to use OPA a linear absorption process to fabricate complex 3D structures.[44]

2.2.3.2. Ink requirements for TPA:

Similar to other vat photopolymerization based 3D printing techniques TPA inks are made of basic ink components including a two-photon (2P) photoinitiator (PI) being efficient in the wavelength regime of the laser for TPA, a photopolymerizable monomer species, if necessary a solvent or additives to include additional functionalities.[44,62,69,102-104] However, in contrast to OPA based 3D printing techniques, restrictions in terms of applicability towards these components are in general narrower and will be treated in the following.

In regard of the 2P PI several properties respectively physical quantities define the quality and suitability of molecule for the 2PLP process. Important parameters deciding about the effectiveness of compound as a 2P PI are its two photon cross section σ_{TPA}, its fluorescence quantum yield Φ_{fl} , the intersystem crossing efficiency and its solubility.[105] The two-photon cross section σ_{TPA} is a direct measure describing the probability of a two-photon absorption from the ground electronic state towards an excited electronic state via virtual short lived intermediate state.[106] In honor to Maria Goeppert Mayer the unit used for this quantity is GM (equivalent to 10^{-50} cm^4 s $photon^{-1}$ $molecule^{-1}$). After successful TPA the PI will undergo an intersystem crossing process transforming the excited singlet state to an excited triplet state, whereby the probability is governed by the PI's intersystem crossing efficiency.[105] Successive decay from this state by forming radical species will provide the initiation species. Hereby competing process such as fluorescence, phosphorescence or thermal decay must be taken in account too.[12] In addition, initiator and radical quenching can also play a role in the final process in the ink. Good solubility within the monomeric component or by addition of solvent is another requirement for good PI molecules.[105] Microparticles, due to undissolved PI residues can be additional sources for instabilities during the 3D microfabrication process, leading to 3D structural damage or non-printability. Although standard one photon PI such as BAPO, Irg 369 or LAP have been demonstrated to offer sufficient efficiency in terms of σ_{TPA} and two-photon initiation efficiency[40,107,108], much effort was done in the recent decades to design 2P PIs with large σ_{TPA} and radical generation efficiency.[105] Investigation in the recent decades concluded that molecules with

extended planar pi-conjugated cores that connect electron accepting and donating groups have in general excited states of lower energy and large dipole transitions, both factors that increases the probability of multiphoton absorption. For example, TPA of dipolar, quadrupolar or octapolar chromophores featuring these D-π-A-π-D motifs was found to be multiple orders of magnitude better than TPA of traditional photoinitiators.[1,105] Nowadays several excellent systems suitable for organic inks and water-based microinks are known.[109-113] Major critic point is their difficult accessibility to the community due to necessary synthetic effort for producing them.

In terms of monomer, inks based on acrylate, methacrylate, utilizing free radical polymerization, epoxides fabricable via cationic polymerization and thiol-ene systems are applied in 2PLP, mirroring the polymerization chemistry offered at the macroscale partly. However, most systems applied nowadays are acrylate based or hybrid acrylate – methacrylate inks, due to the fast reaction kinetics offered by these moieties.[1,12,44] Furthermore the photopolymerizable species must be transparent in the curing wavelength regime, not disturbing the PI excitation process in this way. Due to the restrictions of 2PA based initiation in terms of probability of radical generation the successive propagation process must exhibit high efficiency visible in fast solidification of stable structures respectively a gel point at low conversion. To achieve this, factors improving efficient network formation at a low amount of reaction events must be achieved, favored especially by multiple presence of photopolymerizable moieties in one monomeric unit. Multifunctional monomers such as PETA, TMPETA, etc. show excellent printability.[44] In addition to its multifunctional character monomers and final inks should feature in general higher viscosities than SLA/DLP inks (10 mPa s to 10^3 mPa s).[96] Especially high viscosity inks show larger dynamic ranges, rendering the printing process more stable and generation of highly complex 3D structural features for example overhangs or sub micrometer lines possible at high scan speeds possible. However, increasing the viscosity too much results in decrease of the achievable structural resolution, due to diminution of mass diffusion of oxygen, the natural quencher in 2PP resins preventing uncontrolled polymerization outside the voxel.[96]

In a simple 2PLP ink PI and monomer are sufficient to generate a complete ink system visible in highly efficient 2PLP formulation containing PETA and DETC allowing superfast microstructure formation.[44] To included additional “exotic” features often additives are incorporated into the ink. Thereby the type of additives included is decided by the final properties desired to be incorporated into the fabricated microstructures. Starting from simple incorporation of fluorescent moieties into 3D hydrogels to allow confocal microscopy as accessible analytical technique[114], to magnetic[115] as shown in a variety of magnetic microrobots in recent years or just the inclusion of chemical species allowing postprinting modification after 3D microstructure fabrication as separate step[62,116] a large variety in terms of

additive induced functionalization has been achieved. Usage of inhibitors or quenching reagents is in general less common in 2PLP due to the inherent high resolution provided by the method itself. Usage of nitroxides was reported in case of high-resolution printing approaching the lower optimum linewidths accessible through 2PLP.[117]

In case of additional additives and sometimes due to insolubility of the PI in the monomer, the use of solvent is necessary. Here it is important to use solvents featuring high boiling points to prevent evaporation during the microprinting process and no absorption at the curing wavelength, not inhibiting in this way the initiation process.[62,118] Typical solvents applied are DMSO, DMF, DMAc. In general solvents are tried to be avoided in 3D ink formulations. As nonpolymerizable component solvents do not contribute or improve structural fabrication and can also act as possible chain transfer reagent during the radical propagation process leading to immature termination of a reactive chain end. Furthermore it "dilutes" the monomer and PI density in the volume of the voxel, leading to less efficient polymerization and consequently defective 3D structure fabrication. Another challenge in solvent containing inks is the enormous 3D structure shrinkage after the development step, diminishing the advantages in terms of structural precision offered by 2PLP.

2.2.3.3. Current developments:

In recent years 2PLP based methods have undergone distinct development in terms of technical and materials (ink) aspects. In 2017 major challenges were defined to improve its potential for future applications[119] including technical aspects such as increase of fabrication speed and parallelization to improve 3D microgeometry output, writing below diffraction limit, as well as progress in ink formulations allowing inclusion of adaptive, biocompatible or electrical functionality in 3D microstructures.

In terms of technical progress in 2PLP drastic increase of fabrication output was recently demonstrated by the Wegener group. In 2020 they reported a method allowing the parallelization of microstructure fabrication. By separating on focus into 9 single spots, microstructure fabrication was possible simultaneously in a 3 times 3 array with a total voxel printing rate of 10^7 voxels s^{-1}. Illustrating the advantages of this multifocus approach fabrication of a sample containing 108000 3D unit cells was demonstrated occupying a total volume of 2.4 x 2.4 x 9.6 mm^3.[120]

Several successful attempts have been conducted on implementing the principles of stimulated-emission depletion (STED) to further improve the possible minimal feature size of fabricable 3D microstructures. Based on the Nobel Prize winning principle introduced by Stefan Hell a second laser with a special focus shape is applied to confine the volume of activated photo-excitated fluorescent

molecules by deactivating them via STED, in fluorescence microscopy.[121,122] Translating this concept to 2PLP approaches were developed including the stimulated emission-depletion of two-photon excited photoinitiator molecules[123], depletion by excited state absorption[124,125] as well as usage of photoinihibitor lithography[126,127]. However, the richness in publications using STED for applications is rather low, comprising examples in invisible cloaks operating at visible wavelengths, phontonic crystal featuring complete 3D photonic band gaps in the visible spectral region, and chiral metamaterials based on linear rod and triple helices.[119]

Recently Hahn *et al.* reported a paradigm change in two-photon based 3D fabrication. He proposed a method using sequential two-step absorption for radical initiation instead of typical simultaneous two photon absorption via a virtual transition state.[128] Using this approach issues of 2PLP based on TPA, such as the necessity and consequences of higher order absorption processes, the high costs of femtosecond pulsed lasers, the reliability and the size of the microprinting systems can be circumvented, still retaining the desired quadratic nonlinearity feature. With respect to the ink formulation a suitable two step photoinitators was found in benzil. In the process of two-step absorption benzil was first excited from its ground state to its first electronic excited state by absorption of the first photon. After intersystem crossing to the excited triplet state T_1, bond scission and immediate radical generation is rather improbable for benzil, a "reluctant" PI. In this type of PI the triplet state energy is lower than the bond energy, rendering radical generation via homolytic bond cleavage unlikely, enabling absorption of the second photon allowing access to an high energy triplet state T_n from where the initiating radical are generated. Additionally, bis(2,2,6,6-tetramethyl-4-piperidyl-1-oxyl) sebacate (BTPOS) was added as quencher and scavenger, suppressing undesired H-abstraction and associated radical generation starting a polymerization based on a linear photon absorption process. Using these components in a multifunctional acrylate-based ink it was possible to fabricate structures with minimum grating periods below 150 nm, outperforming best values obtained with STED-based 2PLP at fundamental wavelengths at around 800 nm. Furthermore, scan speed can be improved up to three orders of magnitude compared to comparable systems for light-based microfabrication allowing highly efficient and precise microstructure fabrication at low equipment costs (continuous-wave (cw) laser with sub-milliwatt optical output at 405 nm wavelength), democratizing in this way 3D microprinting.

Continuing on this work Hahn *et al.* reported recently a light-sheet based 3D microprinting method based on two-color two-step absorption, using a cw laser diodes at 440 nm wavelength for projection and a cw laser at 660 nm for the generation of the light-sheet.[32] Using this approach peak printing rates of 7×10^6 voxels s^{-1} at a voxel volume of 0.55 μm^3 were achieved. Combining multifunctional acrylates with biacetyl as PI and TEMPO as quencher and scavenger fabrication of complex 3D

microstructures such as buckyballs, knot-like structures, benchies or five stacked unit cells of a mechanical metamaterial were demonstrated.

As visible from state of the art 2PLP technologies and methodic, 2PLP has made enormous progress improving technical aspects such as achievable resolution or fabrication speed as well as material aspects here especially the development of new photoinitiators allowing highly efficient two-photon absorption based structure fabrication as well as more recent progress in design of suitable two-step absorption systems.

2.3. 4D printing:

Structures fabricated by conventional 3D printing are usually static meaning nondynamic or nonresponsive. In 2013 Skylar Tibbits introduced and conceptualized the idea termed “4D printing” in his TED talk.[129] He presented a printed dynamic geometry based on stimuli responsive hydrogel structures. Referring to Tibbits’ original definition of 4D printing the concept describes the combination of 3D printing together with the fourth-dimension time.[130-133] To be more precise it describes the process of generating 3D structures that are able to change their shape over time in response to a certain external stimulus in a controlled manner postprinting. With ongoing research in the subsequent years, the field becomes more and more interdisciplinary including engineering, physics, biology, material science, medicine and thus gains in richness of potential applications. Consequently, the initial definition was extended to include all newly discovered variants summarized in the term 4D printing. Nowadays using a more popular definition 4D printing can be summarized as follows: “the shape, property, and functionality of a 3D printed structure is able to evolve with time when it is exposed to a predetermined stimulus, such as heat, water or solvents in general, light, pH or magnetic or electric fields among others”.[134-136] Importantly 4D printing itself has made a fruitful development since its initial conceptualization in 2013 leading to a multiplicity of potentially, possible applications in a variety of research areas for example (micro)robotics[137] and (micro)actuators[138], biomedicine[139], sensors[140], and aerospace engineering[140] to highlight a few. To achieve such dynamic features in printed geometries the most straightforward way is the combination of current 3D printing technologies with smart polymeric materials including shape memory polymers (SMP)[142], liquid crystalline elastomers (LECs)[143] or stimuli responsive hydrogels[144]. Furthermore, the usage of composite materials and multimaterial structures further extends the material library accessible for generation of 4D structures.[145] Depending on the printing technique employed – extrusion or light based – these smart materials must be adapted to the specific requirements of the technology to generate fabricable inks: rheometric behavior in terms of extrusion-based techniques and crosslinkability via light induced polymerization in case of light-based 3D printing technologies.

Continuing I will focus in the next part more on the material aspects and the 4D mechanisms of the smart materials applied to transfer dynamic, responsive – often called "living" properties into otherwise static 3D structures.

2.3.1. Stimuli responsive hydrogels:

Hydrogels are defined as hydrophilic polymer networks in which the swelling agent is water.[67] Hydrogels offer several advantages such as low cytotoxicity, presence of water as inherent biocompatible medium, mechanical properties close to human tissue as well as easy adjustability in their stiffness. Thus, main applications of this material class are envisaged in biomedical areas.[145-147] Previously presented properties in combination with their ability to mimic the extracellular matrix of connective tissue render them to perfect candidates for cell culturing samples. Introducing stimuli responsive hydrogels 4D structures can be fabricated allowing to adapt to changes in cells mimicking the natural cell environment present in living organisms. Another promising field for 4D hydrogels is soft robotics as visible by a variety of designed applications at macro and microscale featuring (micro)grippers or (micro)actuators.[114,148-152]

Generating 4D hydrogel-based geometries, the transfer of stimuli responsive behavior to finally fabricated structures is achieved by careful selection of suitable monomers. In regard of ink design usually monomers responsive to a temperature stimulus such as NIPAm or a pH stimulus such as acrylamide and acrylic acid are applied together with crosslinkers such as bisacrylamide facilitating the network formation process.[145] Importantly the responsive monomer component is in its network incorporated form responsible for the 4D functionality. The crosslinker is used to improve the 3D fabricability and enable the generation of stable structures. In case of light-based fabrication techniques, macroprinting as well as microprinting is typically performed in water as solvent. In case of 2PLP, microprinting is sometimes performed in polar organic solvents featuring high boiling points such as ethylene glycol, stabilizing in this way the printing process by reduction of structural damage due to solvent evaporation and microexplosions.[114] Furthermore, these types of solvents are selected due to their favorable properties in regard of crosslinker and PI solubility. Subsequent solvent exchange with water after printing allows introduction of biocompatible environments if required for the later application.[114] Importantly, water as solvent requires a water soluble efficient PI. Especially in case of PI's suitable for 2PLP the range of accessible compounds is still limited to a few commercially available ones such as LAP.[114,154] Otherwise, PIs offering a suitable two photon cross section must be prepared synthetically. At macroscale DLP printing one fruitful approach developed recently is the usage of an organic PI together with detergents in aqueous conditions enabling successful light-based 3D macrofabrication.[55] being in principle a potential option at the microscale too.

Giving a closer look at the physical mechanism behind the 4D actuation in printed hydrogels, one needs to differentiate working mechanisms dependent on the applicable stimulus, temperature, pH or solvent exchange. However, in all cases isotropic swelling respectively shrinkage is the main background drive for the 4D shape change.[145] In case of temperature responsivity the lower critical solution temperature (LCST) of the hydrogel network play the key role in the actuation behavior. LCST describes the mixing respectively demixing behaviour of a two-component system in relation to temperature.[154] Below LCST the two-component system is present as one phase, above in form of two phases due to demixing. In case of thermoresponsive hydrogels such as PNIPAm, they show miscibility with water below LCST and immiscibility above LCST. Due to the hydrophobic effect and a net increase in entropy of the system PNIPAm undergoes simultaneously a coil-to-globule transition by temperature increase above LCST. Thus, the polymer chain exhibiting shrinkage visible as shape change in a 4D structure. Lowering the temperature again below LCST allows dissolution of the polymeric component in water and recovery of the initial shape.[114] Using this mechanism several 4D examples were demonstrated at the macroscale.[134] Transferring this to microscale 2PLP several actuators were fabricated.[145] One PNIPAm based system was designed by Hippler *et al.* in collaboration with our group, allowing efficient actuation by direct temperature increase above LCST or with spatial selectivity by laser induced heating.[114] Further insight into the response behavior of this system and its dependence on the size scale was provided by recent study published by Spratte et al. together with our research group.[155]

Other hydrogel related 4D mechanisms using pH responsivity or response towards different solvents controlling in this way the swelling respectively shrinkage behaviour of hydrogels. Macroscale examples are represented in form of a variety of different actuators.[134] At the microscale interesting 4D examples are shown by a range of different microactuators or microgrippers.[145]

2.3.2. Liquid crystalline elastomers:

Liquid crystals are a state of matter exhibiting properties in between crystalline and fluid phases. Liquid crystalline phases termed mesophases appear in a variety of different types. They can be characterized by their type of long-range order, that can either be positional or orientational. One of the most common phases is the nematic phase, consisting of stiff rod-shaped molecules that are randomly distributed in space, but aligned along a common direction termed director.[156]

Liquid crystalline elastomers (LCEs) are class of smart polymeric material composed of a crosslinked liquid crystalline network, combining the entropic elasticity of elastomers with the self-orientation of liquid crystal phases exhibiting a long-range order.[157]

In terms of 4D printing LCEs allow in contrast to responsive hydrogels anisotropic reversible shape change due to their ability to change their order parameters by reorientation of the molecules in response to a certain stimulus, achieving in this way large mechanical actuation. In case of a nematic mesophase this shape transformation is induced by changing from the nematic to the isotropic state utilizing a temperature or light stimulus. Hereby the direction of the alignment, the director, plays a key role. In the course of a phase transition a volume change will occur along the direction of the alignment – visualized for example in case of single crystal LCE in a shrinkage along the alignment direction and an expansion orthogonally to the direction of the director. By introducing more complex director distributions into a 4D printed moiety complex shape changes can be achieved, for example bending.[158]

In recent years extensive progress was made in the 4D fabrication of liquid crystals at the macro and microscale.[159,160] Here especially micro- as well as macro-applications in the field of soft robotics as well as optics can be pointed out as areas of high potential for applications. However, at the process of 4D fabrication several challenges must be met to successfully fabricate and actuate LCE based 4D structures: I) a fabrication method allowing fixation of the director field inside the polymeric network during the printing process to program the desired motion of the final 4D object, II) a suitable easy applicable stimulus.

Nowadays 4D LCE structures can be prepared by three printing techniques including DIW, DLP at the macroscale and 2PLP for microscale objects.

As explained previously DIW fabricates 4D LCE structures by extrusion of a viscous LCE ink layer-by-layer building up the 3D geometry with feature sizes in the range of hundreds of micrometers. More importantly the main advantage is the possibility to directly align the director along the print path due to shear forces acting on the LCE ink during the fabrication process. Main challenge here is the production of a DIW suitable ink offering the right viscosity in the nematic phase achieved for example by chemical modification of the mesogenic unit. Utilizing this technique several macroscopic actuators for example a gripper, or an artificial hand as well as folding structures or simple adaptive optics were reported.[158,161-163] All presented examples use a temperature stimulus as trigger for the nematic to isotropic transition and associated actuation.

DLP fabricated LCE structures correspond to the minority of existing 4D printed LCE systems, due to the rather complex technical challenge to incorporate alignment in final fabricated objects. Nevertheless, several examples of DLP fabricated 4D LCE structures were reported recently. One first example published in 2019 by Tabrizi *et al.* describes an approach utilizing the anisotropic magnetic susceptibility of the liquid crystalline monomer ink components in a reorientable magnetic field

allowing to define their molecular orientation in a voxel-by-voxel fashion in situ during the photopolymerization process. Using this approach several LCE based 4D structures featuring light and/or heat response were successfully produced.[164] In a more recent work Li *et al* introduced a DLP based 4D printing approach permitting automatic orientation of mesogenic oligomers by shear flow - induced alignment via a built-in shear separation mechanism. By shear aligning the LC mesogens layer-by-layer they could achieve high orientational order in fabricated photocrosslinked structures. Employing this approach, they printed actuators able to do soft robotics' tasks such as reversible grasping, untethered crawling and weightlifting.[165]

For 4D LCE microstructure generation via 2PLP inks usually contain an acrylate functionalized liquid crystalline monomer, a diacrylate containing mesogen as crosslinker and a suitable 2PLP photoinitiator. To include light as applicable stimulus to trigger actuation of 4D microstructures often a few weight percent of azodye are included in designed LCE microinks.[145] By irradiation with light of suitable wavelength the azo dye can switch from trans to energetically higher cis conformation and subsequently relax back by thermal process inducing a temperature increase and change to the isotropic state of the LCE.[166] Beside printability main challenge is here to achieve the alignment of the director to obtain the desired microstructural actuation. The usual pathway to achieve alignment is by pretreatment of the glass substrates which are used as components for a sandwich cell to encapsulate the LCE ink. During 4D fabrication the alignment is transferred from the glass substrate surface to the ink, giving the method the name surface-mediated alignment. Pretreatment of glass substrates includes coating it with thin layers of polyimide or polyvinyl alcohol that are subsequently rubbed with a cotton cloth to create in this way necessary microgrooves allowing to create alignment parallel to the substrate.[167] Vertical alignment is achieved by special PI coating or treatment of the glass surface with silanes.[168-170] Using this methods it is possible to achieve a homogeneous vertical[168,170], horizontal[172] or splayed director field[169] in the bulk of the ink. A more advanced alignment method was reported by Tartan *et al.* comprising of a combined surface mediated alignment and alignment using an electric field.[173] Using this combination both spatial as well as temporal control of the director was obtained during 3D structure formation within the whole sandwich cell.

Utilizing 2PLP several kinds of actuators especially in the field of microrobotics and microoptics were designed and fabricated. One notable example in the fied of microrobotics is a microwalker presented by Zeng *et al.* allowing light controlled motion in the forward direction.[172] Another promising example was demonstrated by the same group reporting a optically controlled microhand, where the fingers featuring a splayed director field can be bent by illumination with green light.[169] In terms of microoptics LCEs were successfully applied to generate tunable optical devices, for example whispering gallery mode resonators[168] enabling the shifting of the resonance frequency utilizing an optical

stimulus. Furthermore, tunable gratings offering adjustability of the diffracted orders by tuning of the grating constant by laser induced heating, giving access to simple manipulation of the polarization state of the diffracted light.[174-176] Recently Münchinger *et al.* presented in collaboration with our group a new approach to align the direction of LCE in situ during microfabrication for each voxel in three dimensions by application of a quasi-static electric field with variable orientation. A sample cell with variable height based on optically transparent electrodes allowed to apply arbitrary electric field vectors in three dimensions. By addition of a variable optical phase plate combined with a pivotable half-wave plate a single well-defined laser focus was guaranteed for almost all quasi static electric field vectors, circumventing in this way the presence of two spatially separated laser foci, an ordinary and an extraordinary, generated by the optical birefringence due to the alignment of the liquid crystal director via the quasi-static electric field.[177] Concentrating more on the facile introduction of additional stimuli in 4D LCE microstructures our group recently reported a simple two-step protocol for generation of multi-photoresponsive LCE microstructures. In the first step temperature responsive LCE microactuators were fabricated by 2PLP using conventional surface-mediated alignment methods. In the second step a multitude of dyes absorbing over the complete visible regime (400 to 700 nm) were incorporated by simple exchange process giving access to light responsivity. By combination of dyes featuring orthogonal absorptions, wavelength selectivity in terms of actuations was demonstrated.[178] Combining the two-step procedure developed in our group with the in situ alignment approach via quasi-static electric fields Münchinger *et al.* was able to generate optomechanic metamaterial geometries with remarkable switching behavior in terms of Poisson ratio and twisting.[179]

2.3.3. Shape Memory Polymers:

Shape memory polymer (SMPs) the main type of smart materials used in this thesis, are a class of stimuli responsive polymeric networks capable to be transformed and fixed into one or more additional shapes termed temporary shapes. Showing the shape memory effect (SME) these materials can memorize their initial shape also called permanent shape and recover it upon exposure to a suitable stimulus.[142,180,181] Thereby, the nature of the stimuli applied is quite diverse, including most prominently temperature, but also light or effects of solvents, pH changes or effect of magnetic fields.[142] Featuring this beneficial memory behavior SMPs offer additional advantages for scientific and industrial application:

i) **Versatility in programmable shape:** There is no real limitation regarding choice of the temporary shape. Every arbitrary temporary shape deformable out of the initial shape is in principle accessible resulting in a large variety of possible programmable motions

and shapes during recovery. The opportunities offered by SMPs in terms of actuation are in strong contrast to the deformation/actuation behavior of stimuli responsive hydrogels or LCE.[142] Responsive hydrogels just allow simple shape change by swelling or shrinkage, giving rise to only limited amount of accessible shapes and associated actuation motions. To achieve more complex actuations respectively shapes combination with non-responsive material is necessary. In case of LCEs the necessity to prior program the director alignment is the main limiting factor to achieve complex and versatile actuator behavior. To generate actuators having access to complex movements respectively shapes highly complex director programming must be performed associated with large technological, temporal and financial effort. Furthermore, only additional shapes included in the programming are accessible in the final LCE structure.

ii) **Versatility in terms of environment:** The SME of shape memory polymers is independent of their environment. They can be actuated in water, air, solvents and vacuum. This versatility is especially visible when considering aerospace and space applications.[142,182-86]] Contrarily, hydrogels are in need of an aqueous surrounding, otherwise collapse of the polymeric network and structural degeneration wouldconsequently occur.[187,188] Importantly the 4D actuation behavior is solvent – in most cases water - based too, when considering for example shape changes due to LCST or pH change, rendering stimuli responsive hydrogels useless in all environments outside water. LCEs share this flexibility in application environments of SMPs.

iii) **Excellent mechanical properties:** SMPs have superior mechanical properties compared to LCEs or stimuli responsive hydrogels. Young moduli in the range of hundreds of MPa to GPa are typical.[142,180,181] Young moduli of LCEs are due to their elastomeric characteristics in the range of a few MPa. For hydrogels they are even lower in the range of kPa. Because of that SMPs can be useful materials for applications in soft robotics or in the field of engineering, where stiff but intelligent materials are necessary.

Based on these properties SMPs have established a status as remarkable useful and promising smart material class in the community of functional polymer engineers, in a large variety of industrial fields and in the academic world in general.[142] Possible and future applications are for example located in the fields of aerospace technology[189,190], biomedical devices[191,192], flexible electronics[193] or soft robotics[194,195].

Although in recent decades a large library of SMPs has been reported featuring SMEs induced by a variety of different stimuli, I will focus the discussion in this thesis on SMPs showing a thermally induced SME that is based on a transition temperature. The transition temperature can be either a glass transition temperature (T_g) in case of amorphous polymer networks or a melting point (T_m) for SMP networks based on semicrystalline polymers.[180,181] Describing the thermally induced shape memory cycle in more detail starting point is in all cases the permanent or initial shape – in case of 4D printed SMPs the printed 3D geometry. Upon heating above the transition temperature, the SMP structure converts from a hard, brittle state to a soft, deformable state. This drastic change in material properties can be explained by inspecting changes of the polymeric network at a microscopic level. In case of an amorphous network, heating above T_g converts the glassy state to rubbery state rendering the structure malleable in terms of shape. If the SMP networks contains crystalline domains as so-called switching phase heating above the T_m leads to their melting, resulting in the macroscopic hard-to-soft transition of the SMP structure. In the next step termed programming the SMP object is mechanically transformed into a new shape termed temporary shape while keeping the temperature above transition temperature. This new shape is fixed by maintaining the shape deformation stress and lowering the temperature below transition temperature. For amorphous SMPs the polymeric network will return to its glassy state, while in case of semicrystalline polymers, the crystalline domains will solidify again. In both cases network mobility is lowered resulting in "freezing" the temporary shape. Importantly this temporary shape is higher in energy compared to the initial shape due to internal stored stress and energy. The initial, permanent shape can be accessed again by heating above transition temperature. Amorphous SMPs as well as thermoplastic elastomeric SMPs will enter the soft state again and associated increased network mobility will lead to transformation back to the energetically lower initial shape, releasing in this way the stored internal stress and energy. This process is termed shape memory recovery.[142,180,181] The described SME is valid for SMPs exhibiting a one-way SME, characterized by the ability to store only one shape in each SME cycle and the irreversibility in regard of recovery.[142,80,180] Adding multiple transition temperatures into a SMP network one-way multiple SMPs are accessible featuring a multi-shape SME[142], defined by a multiplicity of shapes storable at different temperatures and accessible by targeted irreversible recovery at distinct temperatures. Such SMPs can be prepared by inclusion of several transition temperatures into the polymeric network by incorporation of multiple defined polymeric phases into the network. For example, polymeric phases exhibiting melting points at different temperatures can be incorporated or phases exhibiting different glass transition temperatures or combinations of both types of transitions. Importantly the presence of two distinct glass transitions requires sufficient phase separation within the network otherwise both transitions will contribute to one final glass transition

exhibited by the polymeric network. The latter behavior can be estimated in case of copolymers containing two components by the Gordon-Taylor equation (see equation 2.3).[196,197]

$$T_{g,mix} = \frac{w_1 T_{g,1} + k w_2 T_{g,2}}{w_1 + k w_2} \qquad \textbf{(Equation 2.3)}$$

where $T_{g,mix}$ is the final T_g of the copolymer network, w_1 and w_2 the mass fractions of both components and $T_{g,1}$ and $T_{g,2}$ the glass transitions of both monomer component exhibited in their homopolymeric form, k corresponds to the Gordon-Taylor-constant a dimensionless quantity that can be determined experimentally at different mass fractions. Importantly, the Gordon-Taylor equation is valid for statistical copolymers having weak intermolecular interactions.

The glass transition temperature of a copolymer network can further be quickly estimated by the Fox equation (see equation 2.4).[197]

$$T_{g,mix} = T_{g,1} w_1 + T_{g,2} w_2 \qquad \textbf{(Equation 2.4)}$$

where $T_{g,mix}$ is the resulting T_g of the copolymer, $T_{g,1}$ and $T_{g,2}$ the glass transition temperature exhibited by each monomer component in its homopolymeric form and w_1 respectively w_2 the mass fractions of each monomer component in the network.

In case of stronger intermolecular interactions the glass transition estimation can be performed using the Kwei-equation.[198]

Another interesting type of multi-shape memory effect is the temperature-memory effect (TME).[199] A SMP exhibiting a TME can store a multiplicity of shapes as a function of temperature. Requirement for such SMP behavior is the presence of a broad glass transition temperature. In the process of a TME cycle distinct shapes are programmed at defined temperatures within the temperature range of the glass transition. Sequential accessibility of these different shapes is possible by reaching each of the programming temperatures during the recovery process. In this way a multiplicity of programmed shapes is accessible although only one glass transition is present in the polymeric network. Recently SLA printed 4D TME structures were fabricated and investigated by Inverardi *et al.*[199,200]. They demonstrated multiple shape memory effects for a printed bar-shaped specimen based on commercially available Clear ink and demonstrated its promising features for controlled thermally triggered sequential shape variation.

All types of SME described before show one-way behavior due to irreversible recovery restricting in this way potential applicability. To overcome this limiting factor much effort was spent to design two-way respectively reversible shape memory polymers.[142] Apart from LCE which show in principle such reversible shape memory behavior, but require complex alignment methods, Lendlein *et al.* reported

a first example of reversible shape memory polymer based on two crystalline domains, the high temperature skeleton domain (poly (ω-pentadecalactone)), also called geometry defining domain, and the low temperature switching domain (polycaprolactone), also termed actuator domain.[201] By heating first up to a temperature T_{Reset}, a temperature above T_m of the geometry defining domain, the permanent shape is first reshaped to shape A and fixed by cooling down to T_H, a temperature between the crystallization temperature of the geometry defining domain and the melting point of the switching domain. Subsequently shape A is deformed to shape B and fixed by cooling down to T_L, a temperature below the crystallization temperature T_c of the switching domain. Heating up again to T_H allows access to Shape A, subsequent cooling to T_L permits regeneration of shape B. This actuation can be performed reversibly multiple times until all information is "deleted" by heating up to T_{Reset} enabling a new programming process. Since its discovery only a limited amount of reversible SMPs were reported.[142]

2.3.3.1. Thermomechanical theory of SMP

For proper theoretical description of the thermally induced SME two theoretical models are applied: the thermoviscoelastic theory model and the phase transition model.[142]

Thermoviscoelastic theory model:

The thermoviscoelastic theory model enables a thermodynamic explanation of SMP behavior. Within the model the molecular chains are considered as springs. These springs are assumed to be small in diameter but large in length and are entangled with each other. At room temperature the SMP has high entropy because the springs are randomly arranged. By rising the temperature, molecular mobility is increased and the polymer gains thermoviscoelasticity. Applying an external force, the springs can be stretched and reoriented in this state, leading to a decrease in entropy of the polymer. Reducing temperature leads to decrease of molecular mobility and loss of thermoviscoelasticity. Thus, the springs are not able to return to their initial shape and orientation. The stress applied during deformation and reorientation of the springs is stored thereby as elastic potential energy within the springs. Increasing the temperature afterwards – equivalent to shape memory recovery – enables the springs to gain thermoviscoelasticity again and thus molecular mobility. This permits reorientation and conversion to their initial shape by release of the stored elastic potential energy. During the whole process the elasticity of the system stores the work done by the external force, the viscosity of the system consumes the work done by the external force. Irreversible viscosity deformation of the SMP, causing incomplete recovery is explained by heat generated by friction between the springs, consuming parts of elastic potential energy that cannot be stored anymore within the springs. Furthermore, is important that no excessive slippage is present between the springs. This would lead to macroscopic deformation without entropic change. Using the thermoviscoelastic theory the

mechanical behavior of SMPs can be explained, however, it shows weaknesses in explanation in storage and release of enthalpy energy.[142]

Phase transition theory:

Another theory the phase transition theory allows to explain the phase transition behavior during a SME cycle from a thermomechanical point of view.[202-204] Within the model the SMP network is composed of frozen and an active phase. The frozen (hard) phase is present when enthalpy energy changes inside the SMP material without change of internal structure. This is ensured in the frozen phase by stretching and rotation of molecular chains within the material. Any further conformational motion is not possible. The active (soft) phase consisting of dynamic bonds allows rotation, elongation and compression of the molecular chains meaning deformation is allowed compared to the frozen phase. At the glassy state below transition temperature the frozen phase is the dominant phase in the material. By changing from the glassy state towards rubbery state by increasing the temperature above transition temperature, parts of the frozen phase transform to the active phase, leading to a change in the ratio between active and frozen phase. In the subsequent programming process after heating above transition temperature the conformational movements generated by deformation are stored in the active phase. By temperature decrease during fixation the active phase transforms back to frozen phase including stored stress caused by prior conformational motion. Importantly, this stress cannot be released in the frozen phase. Heating up again above transition temperature leads to conversion of the frozen phase back to active phase. The previously stored stress can be released now due to the permission of conformational motions at this state, inducing the shape recovery process.[142]

Both the thermoviscoelastic theory and the phase transition theory can be combined to generate constitutive model describing the shape memory behavior more accurately.[205,206] Theoretical description of the multi-shape memory effect and the corresponding phase transition behavior was reported by Leng *et al*. combining thermoviscoelastic theory and phase transition theory in one general model, where mechanical, storage and thermal expansion strains were main model factors.[207]

2.3.3.2. Analytical methods for SMP characterization:

Typical methods for characterization of SMP concentrating on the evaluation of the transition temperature include differential scanning calorimetry (DSC) or dynamic mechanical analysis (DMA).[142,180,181] DSC, a popular method in the material science community, permits direct access to thermal properties such as 1st order phase transitions such as melting points or crystallization temperatures of semicrystalline polymers or 2nd order phase transitions like the glass transition, rendering this technique ideal for characterization of SMPs. To measure such transitions several

milligram of a sample will be added together with a reference into a heating chamber. During the measurement the difference in the amount of heat necessary to increase the temperature of the sample and the reference is evaluated as a function of temperature. Depending on the phase transition the sample undergo a higher or lesser amount of heat that is necessary to keep the sample at the similar temperature like the reference. In case of endothermic processes like melting transitions more heat is necessary in contrast for exothermic behavior visible during crystallization less heat must be transferred to the sample. Result of the measurement is a DSC curve showing positive peaks for melting transitions during heating, negative peaks for crystallization during cooling and changes in the slope for glass transitions for heating and cooling processes. Another method often employed for SMP characterization is DMA allowing access to viscoelastic data of SMPs. To evaluate the glass transition of a specimen a small-amplitude linear oscillation is applied on a sample while increasing the temperature, giving access to storage modulus (E'), loss modulus (E'') and loss factor also termed tangent delta (tan δ). Evaluating the T_g from the resulting DMA curve is possible in several ways defined in ISO 6721-11[208]: i) the onset of the storage modulus (E'), ii) the peak value of the loss modulus (E'') or iii) the peak value of tan δ. All three measurement procedures result in different numbers due to different physical meaning. T_gs evaluated from the onset of the storage modulus appear at the lowest temperatures, being a good indicator for the temperature a material starts to fail mechanically especially important for determination of the usable range for a load bearing element. T_g determined from the peak of the loss modulus E'' appear in the temperature region between T_gs measured from storage modulus and tangent delta. The physical meaning behind this T_g corresponds directly to the molecular motion in a material. Upon reaching the peak of the loss modulus large segments of the polymer specimen are able to move cooperatively and the polymer becomes easier deformable. T_gs evaluated from the peak value of the tangent delta curve appear at higher temperature than T_gs determined from previous two methods. At the peak of tan delta, the material has highest viscous response. Generally, all three methods can be used to determine the glass transition temperature and are valid results.

Both methods DSC and DMA are more appropriate for macroscopic SMP samples. Changing to the microscale the method of choice is performance of DMA like measurements via nanoindentation termed dynamic nanomechanical analysis (DnMA).[209] By selection of the right experimental parameters such as indenter tips, oscillation frequency, indentation depth etc. similar insight in viscoelastic behavior like in case of DMA can be achieved. Evaluation of transition temperature via nanoindentation was successfully employed for thin films including SMPs and microfabricated SMP structures.[210,211]

2.3.3.3. Quality parameters for SMP quality

To evaluate the quality of the SME of a SMP two quantities, both accessible via a cyclic thermomechanical test, have been defined: i) the strain fixity rate, ii) strain recovery rate. The strain fixity rate $R_f(N)$ describes the ability of a SMP specimen to fix the mechanical deformation applied during programming.[180] It describes how the specimen can fix a stretched shape after its deformation to the maximum strain ε_{max}. The final temporary length achieved after stress release concluding programming is thereby never equivalent to the shape reached by deformation under stress loaded conditions. In equation 2.5 the strain fixity rate R_f is determined by the ratio between the strain in the stress-free state after programming in the N^{th} cycle $\varepsilon_u(N)$ and the maximum strain ε_m under stress loaded conditions.

$$R_f(N) = \frac{\varepsilon_u(N)}{\varepsilon_m} \qquad \textbf{(Equation 2.5)}$$

The strain recovery ratio R_r is a quantification of the ability of a SMP to memorize its permanent shape.[180] Further on it is a measure to which extent a strain that was applied in course of programming $\varepsilon_m - \varepsilon_P(N-1)$ is recovered in the following shape memory transition. To calculate this comparison the strain that occurs upon programming in the N^{th} cycle $\varepsilon_m - \varepsilon_p(N-1)$ is conferred to the strain occurring with the shape memory effect $\varepsilon_m - \varepsilon_p(N)$ as shown in equation 2.6.

$$R_r(N) = \frac{\varepsilon_m - \varepsilon_p(N)}{\varepsilon_m - \varepsilon_p(N-1)} \qquad \textbf{(Equation 2.6)}$$

where $\varepsilon_p(N\text{-}1)$ and $\varepsilon_p(N)$ represent the strain of the specimen in two successively passed cycles in the stress-free state before application of stress during programming.

Another method to quantify the quality of a SME is the shape memory bending test.[180] Here a sample is bent at a given angle at temperatures above transition temperature, maintained in this shape and cooled below transition temperature for fixation. Subsequent release of the deforming stress give access to the bent temporary shape. By heating up to a temperature above transition temperature recovery is initiated. The recovery rate R_b is determined from ratio of the different angles before and after recovery as shown in equation 2.7

$$R_b = \frac{(\theta_i - \theta_f)}{\theta_i} \qquad \textbf{(Equation 2.7)}$$

where θ_f is the deformation angle and θ_i the deformation angle in the temporary shape.

2.3.3.4. Thermal stimuli and other suitable stimuli types

Obvious from the term thermally induced shape memory effect the main external stimulus for programming and fixation and recovery is temperature. However, the stimulus temperature can also be translated to other stimuli, that enable generation of high temperatures inside the SMP polymeric network overcoming in this way the transition temperature. Such translated stimuli are for example light[212], electric field[213] or magnetic fieds[214], incorporable by inclusion of suitable functionalities into the shape memory network respectively the SMP ink in case of 4D printing. All of these translated stimuli have the advantage to allow spatial as well as temporal control at the shape recovery step, allowing structural recovery of parts of the programmed temporary shape increasing in this way the number of accessible shapes in a one-way SME cycle and enhances the versatility in terms of applicability. In contrast recovery by application of a thermal stimulus -meaning increase of temperature of surrounding atmosphere or of a water bath – recovery occurs rather unspecific – usually recovery of the whole structure.[210,211]

Light irradiation is on promising stimulus to achieve high levels of spatial and temporal control in the SME process, as visible in a range of reported examples. Due to several advantages light offers such as: tunability of intensity, irradiation, irradiation time, polarization direction and wavelength, it appears particularly attractive for this purpose.[215-217] Simplest way to achieve translation of the temperature stimulus to a light stimulus is incorporation of inorganic fillers, acting as photoabsorbers, into the SMP network respectively the 4D ink. In particular, gold[218], silver[219], titanium nanoparticles[220], as well as carbon fibers[221], or carbon black[222] have been incorporated in shape memory systems allowing light activated recovery. Such particles are able to convert absorbed light energy into thermal energy. Other promising strategies include the incorporation of organic dyes as additional component into the SMP network. One attractive class of dyes are azo-dyes, a compound class offering several advantages: I) straightforward preparation and functionalization and II) possibility to fine-tune absorption properties by chemical modification as well as III) their advantageous photostability.[223] This class of compounds has been extensively investigated and applied as functional dyes in polymers, especially in the field of liquid crystalline materials. Recent years have produced a variety of potential actuators among them photoactuators, photonic elements or biomedical devices.[160,169,172] As explained before azo-dyes have been extensively employed as additive in light based 3D printing techniques, noticeably in SLA or DLP. The main role of the azo-dyes such as Sudan I is here their interaction with curing light in form of absorption of excessive photons improving the actual polymerization reaction, permitting higher precision, higher resolution and smaller minimal feature sizes, giving access to the fabrication of more complex structural designs.

Furthermore, these types of dyes were recently employed to impart functional properties to 3D printed components.[224]

2.3.3.5. Examples of SMPs in 4D printing

Since its first conceptualization by Tibbits in 2013[129,131], SMPs have been established as one of the most employed material classes in 4D printing.[134,225,226] Reason for that are their advantageous properties especially in view of the fabrication process. They offer caused by their higher values in Young Moduli mechanical stability during 3D structure fabrication process and furthermore, there is no inherent necessary of solvent such as water or humid environments like for hydrogels, facilitating the 3D printing process from a technological point of view. Consequently, a rich library of 4D printable inks have been established at the macroscale in equal measure for extrusion-based techniques and light-based techniques.[134,225,226] Focusing on light-based techniques especially the advantage of applying inks with low crosslinker content due to the more probable photoinitiation event and the longer curing times, facilitated development of highly efficient 4D SMP systems. This is especially visible in the fact that first macroscopically printed SMPs were just reported within short time after conceptualization of 4D printing.[130,134] At the microscale the development of 2PLP printable SMP systems required a much higher amount of effort. First examples were reported in 2021, eight years after advent of the concept 4D printing.[211,227] Reason for this are the high restrictions in terms of printability for a 4D printable ink via 2PLP. Due to the low probability of the nonlinear absorption event and the necessity of fast polymerization kinetics a large amount of photopolymerizable group density must be present for successful 3D structure fabrication – meaning a high crosslinker content in the ink and consequently a high crosslinking density within the fabricated 4D object. However, too high crosslinking density within a stimuli responsive structure prevents successful incorporation of dynamic features such as the SME. Result is in this case a static object not featuring any controlled response to an external stimulus.[145]

In the following an overview of light-based SMP systems at the macro- and microscale will be presented. In case of the macroscale a selection of examples will be provided. In case of microscopic 2PLP fabricated SMPs all examples known to the author by the time of thesis writing will be summarized with respect to the ink components employed, structures fabricated as well as potential applicability.

2.3.3.5.1. 4D printed examples of SMPs at the macroscale

As stated above macroscopic light based 4D printing of SMP using SLA or DLP have appeared to be highly prosperous. Ge *et al.* for instance used microstereolithography to fabricate a range of structures

including an Eiffel Tower, a microgripper or a stents envisioning potential biomedical application using a methacrylate based ink formulation.[228] Later Zarek *et al.* fabricated cardiovascular and tracheal stents as well as smart SMP electrical circuits.[229,230] Recently Maity *et al.* fabricated tracheal stent structures based on DLP polymerizable inks composed of polypropylene glycol/polycaprolactone triblocks.[231] By surface functionalization with polyethylene glycol the authors were able to minimize biofilm formation. Further ciprofloxacin, a drug, was added to the ink, allowing postprinting in vitro release of it from the fabricated structure over time, transferring antibacterial activity towards the stent. Zhang *et al.* developed an impressive acrylate-based ink system. Utilizing *tert*-butyl acrylate and aliphatic urethane diacrylate as ink components, fabricated 4D structures allowed stretching of up to 1240% at the programming temperature while simultaneously demonstrating excellent shape fixity and good shape recovery.[232] Recently Meurer *et al.* presented SLA printable shape memory polymers, that were based on supramolecular halogen bond acting as switching phase during the SME cycle, whereas covalently formed crosslinks formed the stable phase stabilizing the permanent shape.[233] Another recent study by Paunovic e*t al.* reported a DLP printable composite SMP composed of gold nanorods embedded in in polyester copolymer.[234] The authors demonstrated near infrared light-triggered SME for facilitated insertion and expansion of a 3D fabricated stent ex vivo by exploiting the photothermal effect incorporated by the gold nanoparticles. Another interesting DLP printable SMP system exhibiting autonomous off-equilibrium morphing pathways was designed by Peng *et al.*.[235] The authors designed covalently crosslinked SMPs with supramolecular ureidopyrimidinone moieties endowing the SMP with a strong time-temperature dependency giving access to autonomous shape shifting pathways.

Additionally, to previously described one-way shape memory polymers Cavicchi et al. reported a DLP printable triple shape memory polymer allowing for one-way sequential shape recovery.[236] The functional ink was composed of acrylate-based monomers and an ion pair comonomer. By polymerization induced microphase separation during DLP fabrication, ion-rich and ion-poor domains were produced within the polymeric network. Excellent phase separation of both domains resulted in two well defined glass transition regions, giving access to the triple shape memory effect.

In regard of two-way respectively reversible SMPs the number of designed systems is still limited. Based on the findings of Lendlein *et al.*[201] Shi *et al.* developed a photocurable ink composed of acrylated poly(ω-pentadecalactone) and poly(caprolactone) offering the two crystalline domains required for a reversible SME. By 4D fabrication of a humanoid object the authors were able to demonstrate remarkable reversible shape memory behavior.[237]

Beside above reported systems, additional SMP formulations featuring promising functionalities such as self-healing ability[238-240] or recyclability[241-242] were recently described.

2.3.3.5.2. 4D printing of SMPs at the microscale

In contrast to the macroscale, microscale 4D printing of SMP is still in its infancy, visible in the limited number of designed systems. In 2021 Zhang *et al.* reported one of the first 2PLP-printable systems using an ink formulation based on commercially available Vero Clear mixed together with a elastomer consisting of 2-hydroxy-3-phenoxypropyl acrylate and bisphenol A ethoxylate dimethacrylate.[227] 2PA based initiation was achieved by diphenyl (2,4,6-trimethylbenzoyl) phosphine oxide, a known commercial available PI typically used for SLA or DLP printing. Applying the resulting formulation in 2PLP printing SMP structures providing a T_g-based one-way SME featuring a transition temperature at approximately 40°C were achieved. In particular, 3D color filters composed of a base layer and a submicron grid were generated. Interaction of incident light with the printed nanostructures via scattering and interference processes enabled preferential transmittance of certain wavelengths in dependence of the geometric parameters of the grid. By transforming the grid to a compressed temporary shape via programming und fixation, the 4D structure loses its color filter effect and appeared to be transparent. Upon recovery by application of a temperature stimulus the permanent shape associated with the color filter effect was reobtained. In another early example, Elliot *et al.* have designed an acrylate/methacrylate-based microink system.[211] To be more precise the ink formulation comprised benzyl methacrylate as first chain builder, an amine-functionalized methacrylate as second chain builder as well as chemically modified pentaerythritol triacrylate as crosslinker and 7-Diethylamino-3-thenoylcoumarin (DETC) as multiphoton PI. Employing this functional ink the authors demonstrated microfabrication of flowers, cubic lattices, and cylindrical pillars. Characterization via dynamic nanomechanical analysis using a nanoindentation setup, revealed a glass transition region occurring in the range of 60°C. The authors envision for their systems potential applications ranging from miniaturized deployable biomedical devices for example stents to smart mechanical metamaterials. In 2022, one year after the first two examples, Jeske e*t al.* reported a 2PLP printable functional SMP ink system using radical mediated thiol -vinyl hydrothiolation instead of common used free radical polymerization as curing mechanism.[243] The thiol-ene based ink was composed of pentaerythritol tetrakis(3-mercaptopropionate) as multifunctional thiol component, 1,3,5-triallyl-1,3,5-triazine-2,4,6(1*H*,3*H*,5*H*)-trione as multifunctional ene-component and 2-benzyl-2-(dimethylamino)-4-morpholino-butyrophenone as PI component, whereby all used compounds were commercially available. Importantly, the thiol-ene based mechanism produces inherently lower crosslinking density and more network uniformity caused by its step growth curing mechanism, facilitating preservation of responsive features of finally fabricated 4D microstructures. Employing this material, the authors printed twisted woodpile structures with circular dichroism demonstrating the systems potential applicability for generation of optical metastructures. In the same year Minnick *et al.* published a novel SMP microink system, allowing fabrication of free-hanging fibers, utilized by the

authors to develop a new mechanical characterization method for tensile testing in liquid environments.[244] The microfibers featuring shape memory properties were printed using commercially available microink IP-Visio composed of 7,7,9 (or 7,9,9)-trimethyl-4,13-dioxo-3,14-dioxa-5,12-diazahexadecane-1,16-diyl bismethacrylate as monomer and phenyl bis(2,4,6-trimethylbenzoyl)-phosphine oxide as PI. Important to note, the SME property was only accessible in liquid conditions, limiting applicability of this ink system and printed SMP devices thereof.

2.4. "Living" Polymerization and its use in Additive Manufacturing:

As previously mentioned typically inks applied for photo-based 3D printing produce static, nondynamic polymeric structures. Recently, the concept of 4D printing was introduced, enabling incorporation of dynamic and "living" features into 3D printed structures. The inclusion of stimuli responsive properties into 3D printed structures gave them access to dynamic behavior over time – the 4th dimension – in response to a stimulus. Simplest way was the before described strategy of combining smart polymeric materials with the 3D printing technology. Although the emergence of 4D printing was a large step towards "living" respectively "life-like" intelligent materials, it suffers in most reported examples on one similar issue as conventional 3D printing. Materials are general based on uncontrolled photopolymerization mechanisms like free radical polymerization or cationic polymerization. One mechanistic consequence of such uncontrolled polymerization techniques is that their resulting polymeric networks in which chain propagating units, reactive chain ends radicals in case of free radical polymerization, are irreversibly terminated during the curing and network forming process – creating dead ends – allowing no effective reactivation to incorporate other functionalities. This issue limits the range of properties featured by one printed material dramatically, because postprinting fine-tuning of properties such as mechanical, optical, or responsive ones is not possible anymore. In other words, the monomer and crosslinker employed in the ink finally determines physical and chemical features of the fabricated structures, limiting in this way ability to property fine-tuning, on demand printing and thus customized 3D fabrication.

A new approach that emerged in the community of 3D and 4D printing is the concept of "Living Additive Manufacturing". The term was first conceptualized by Johnson *et al.* in their publication in 2017 explaining it as the possibility to incorporate spatiotemporally monomers and/or crosslinkers directly into an already printed polymeric network – the "parent" network – to convert it into new structurally modified network – the "daughter" network – exhibiting altered shapes, composition and properties.[245] To prepare such "living" networks the network forming reaction has to fulfill special conditions: it must be a highly regulated, light controlled living polymerization technique within

dynamic covalent polymer networks without the occurrence of side reactions or substation irreversible termination events.[246-250]

As illustrated by Johnson *et al.* and later employed in a multiplicity of studies, a pathway to living networks was the change from uncontrolled free radical polymerization to controlled reversible-deactivation radical polymerizations (RDRP), often termed controlled or "living" radical polymerizations. In the following different types of RDRP reactions including atom transfer radical polymerization (ATRP), reversible-addition-fragmentation chain-transfer polymerization (RAFT) and nitroxide-mediated polymerization (NMP) will be introduced generally and mechanistically, whereby the focus will be on NMP and related alkoxyamine based chemistry, methods employed in this work.

2.4.1. Reversible-deactivation radical polymerizations:

Conventional free radical polymerization (FRP) suffers in general from limited control during the chain growth process and thus a rather undefined final polymeric network structure. This loss in network control is mainly caused by the lack of control in molar mass of the polymer strands. The resulting high polydispersity, originating from slow initiation events compared to fast chain propagation and uncontrolled termination by recombination respectively chain transfer, is mirrored by the heterogeneity of the final polymeric network.[251] Furthermore due the lack of reactivatable reactive chain ends – radicals – pathways to possible postmodification by successive thermal or photoinitiated chemistry – organic reactions or chain extending polymerizations – is locked, rendering this materials unsuitable for on demand adjustment of properties or property fine tuning after network generation.[251]

Progress in development of more controlled polymerization methods at the end of the 20th century resulted in the development of reversible-deactivation radical polymerizations (RDRP) techniques. RDRP often termed controlled radical polymerization respectively "living" radical polymerization due to their similarities in features with real living polymerization methods like anionic polymerization such as high control of molar mass and low polydispersity due to fast initiation compared to rather slow propagation, constant concentration of reactive chain ends during the reaction or the possibility to produce block copolymers.[252] Importantly, RDRP techniques are just "living" polymerizations techniques because termination events are possible in contrast to methods such as living anionic polymerization having real living character without termination occurring. However, by keeping the concentration of chain end radicals very low through smart use of reaction equilibria, self-termination by recombination can be reduced drastically in its probability, allowing generation of polymer chains of low polydispersity – meaning high control in molar mass within the resulting material. In particular RDRP methods apply an equilibrium between a dormant species, not able to propagate, and an active

propagating species. Here in general a fast equilibrium is employed that is located on the side of the dormant species.[252] Especially this feature of the equilibrium can be exploited for further post-printing-modification of printed living networks by reactivation of the propagating species by suitable conditions – temperature or light – within a structure containing dormant species as later described.

Summarizing the RDRP methods developed three prominent examples can be mentioned including nitroxide-mediated polymerization (NMP)[253], atom-transfer radical polymerization (ATRP)[254] and reversible-addition-fragmentation chain-transfer polymerization (RAFT)[255]. The key element of their "livingness" the reversible equilibrium has for all three methods different origins (see Scheme 2.5): In case of NMP it is based on the dissociation-combination mechanism featured by the alkoxyamine bonds and stable nitroxide radical species as reactive chain end control agent. ATRP employs an alkyl-halogen or alkyl-pseudohalogen bond and an inorganic transition metal halide complex as deactivators. For RAFT polymerization a degenerative chain transfer mechanism based on the alkyl-sulfur bond integrated in chain transfer agents such as dithioester, dithiocarbamate, trithiocarbonate or xanthate acts.[252]

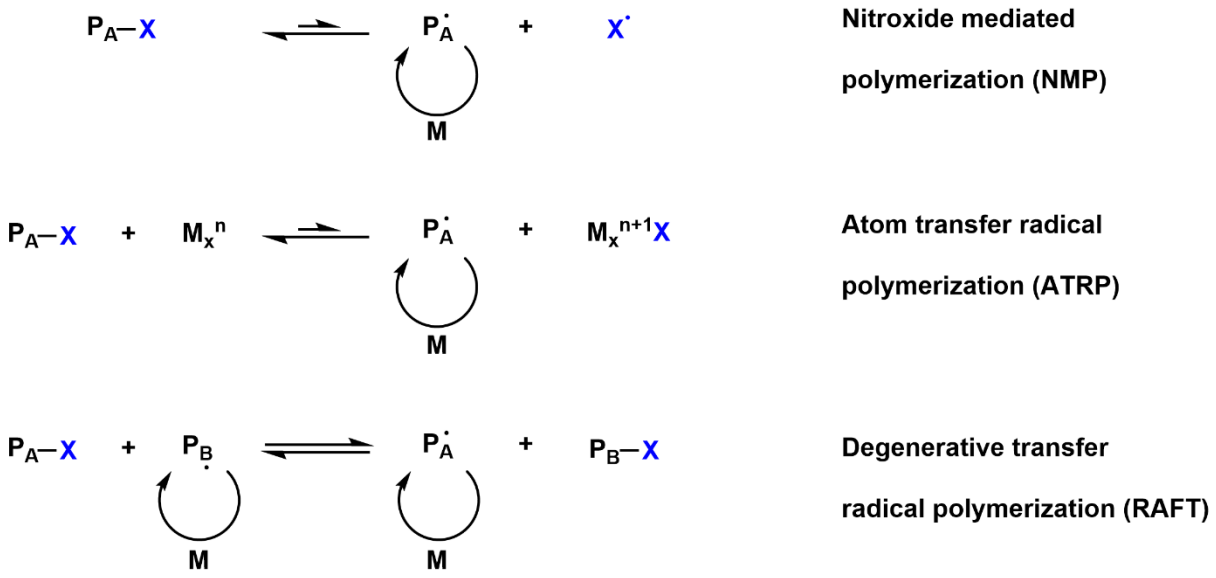

Scheme 2.5: Scheme describing the origin of the polymerization control for each of the CRP methods including: NMP, ATRP and RAFT.[252]

The following discussion will focus on NMP technique, as it is the RDRP technique employed in this thesis. Focus will lie first on general mechanism, described in more detail, a possible side reaction the nitroxide exchange reaction – applied in this thesis too as well as its application in dynamic polymeric networks adaptable in their properties – termed covalent adaptable networks (CAN).

2.4.2. Nitroxide-mediated Polymerization (NMP):

Nitroxide-mediated Polymerization (NMP) was historically seen the first type of CRP observed.[256] Since its emergence it has found utilization as synthetic method for generation of materials for a multiplicity of applications such as lithium batteries, organic electronics including organic photovoltaic devices, organic light emitting diodes (OLEDs) and organic thin film transistors, or nanoparticles for drug delivery or antimicrobial materials.[257]

As previously explained, the superior features of NMP compared to FRP are based on the reversible termination mechanism between the active growing chain end radical and a nitroxide component, recombining with the chain end by formation of alkoxyamine bond, the dormant species, unable to perform chain propagation but either termination by recombination or chain transfer. The active species, a reactive carbon centered radical can be formed by homolytic dissociation – either induced thermally or by suitable irradiation – and propagates until the next deactivation event. Beside the maintenance of this fast equilibrium the persistent radical effect (PRE) is another key element providing the foundation of the high control in NMP. PRE a kinetic feature in polymerization chemistry divides the radicals present in a transient one able to perform chain propagation or self-termination, in case of NMP the carbon centered radical chain end, and a persistent radical – the nitroxide species – not able to recombine with other persistent radicals, only recombinable with the growing chain end radical, the transient species. At the beginning of the polymerization process fast initiation resulted in the dominant presence of transient radicals, that tend to self-terminate, while simultaneously leading to an accumulation of persistent species with every self-termination event. As a consequence, the probability of a transient radical to self-terminate decreases with ongoing time. Along with that their concentration is reduced leading to their prevailing reaction with the persistent species.[258,259]

Importantly the nitroxide, taking the role of the persistent species, must not actively take part in the chain propagation and must not tend to self-termination. This is in case of nitroxides guaranteed by the high stability of the radical species based on the high delocalization energy offered by the $\pi_{N\text{-}O}$ three-electron bond, being in the region of 23-30 kcal mol^{-1}. Dimerization – self termination – is actually disfavored considering the energy gain obtained by generation of a O–O in the range of 35 kcal mol^{-1} being by far lower than the loss in resonance energy by sacrificing two aminoxyl groups.[253]

In general, the mechanism of NMP can be induced via a i) bicomponent initiating system, including first initiation of by a thermal- or photoinitiator and formation of a carbon centered radical of the primary reacted monomer species joining the reversible equilibrium with the nitroxide species or via ii) an monocomponent system consisting of a unimolecular initatior being an alkoxyamine activated to form the chain propagating species by energy influx (see Scheme 2.6).

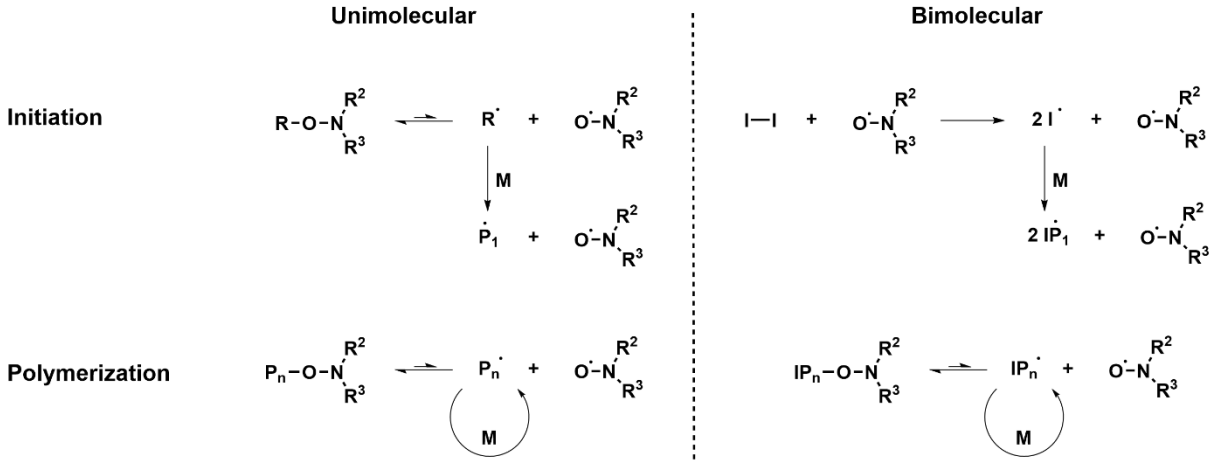

Scheme 2.6: Schematic representation of unimolecular and bimolecular pathways for initiation and subsequent polymerization process.[253]

Discussing the scope of NMP in terms of applicable monomers, large progress has been made in recent decades. Initially NMP was reported for polymerization of styrene and a limited range of acrylate monomers. With the passing of time a large library different nitroxide compounds including complex variations such as TIPNO[269], DEPN[270], Et-TEMPO[271] and ^{t}Bu-Piperazin[272] to name a few (see Scheme 2.7), extensively broaden the scope of compatible monomers and functionalities for NMP. Nowadays, successful NMP is reported for styrenes, acrylates, methacrylates, acrylamides, dienes and vinyl acetate. Furthermore, performance of NMP is possible in organic as well as aqueous conditions, permitting controlled polymerization of hydrophilic monomers via this technique.[253]

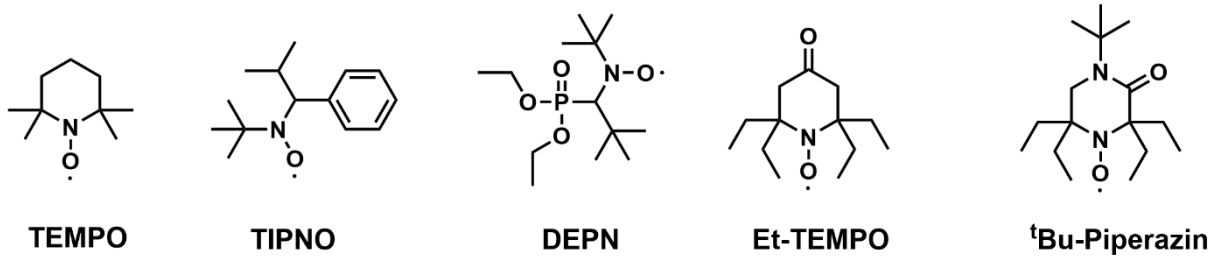

Scheme 2.7: Selection of nitroxides employed for nitroxide-mediated polymerization.

As stated in the beginning of this section NMP found remarkable usage as synthetic design medium for variety of applications. A more interesting application of NMP and alkoxyamine chemistry in general is its application in covalent adaptable networks, a type of dynamic polymeric network that will be introduced in the next section, focusing first on their general concepts and subsequently on examples of these network type based on alkoxyamine chemistry.

2.4.3. Covalent Adaptable Networks:

In general, polymeric networks can exist in form of a thermoset or a thermoplastic crosslinked system, differing in the nature of their crosslinks. Thermosets are covalently crosslinked systems usually superior in their thermal and mechanical integrity. Due to the “fixed” character of the covalent bonds and its irreversible formation, thermoset networks can be seen as “set” after network generation. Consequently, networks of thermoset character are not-meltable, insoluble and are fixed in one permanent shape – decided during their production - which they always remember and try to maintain. Although these rather “static” characteristics are on the one hand accompanied by excellent mechanical strength, higher chemical and temperature resistance and larger moduli, highly favored properties, several undesired features are accompaniments including the absence of recyclability, and the lack of variability in permanent shape – remolding of the first permanent shape is not possible.[273] Thermoplastic networks on the other side are characterized by the absence of any permanent covalent crosslinks between chains, having a large impact on the material’s final properties and behavior. Thermoplastics appear deformable and remoldable after overcoming a certain transition integrated into the polymeric network, including glass transitions or crystalline transitions respectively both. Overcoming these transitions increases chain mobility providing the material with the ability to perform plastic deformation corresponding to the change of the permanent shape – the equilibrium shape – of the material. Thus, thermoplastics are reprocessable and offer recyclability.[273]

Concluding, it would be advantageous to have a kind of polymeric network including advantages of both previously described polymer types, meaning the excellent mechanical and thermal integrity as well as chemical resistance of thermosets and the recyclability and reshapability of thermoplastics. Incorporating features of both types into one network, covalent adaptable networks (CANs) were conceptualized and introduced by Bowman *et al.* in 2010.[274] In particular CANs are based on reversible dynamic covalent crosslinks, permitting reversible network rearrangement in response to suitable stimuli. In this way, plasticity is accessible due to possible stress relaxation at the molecular level by rearrangement of the network topology, permitting change in permanent shape. By coupling the activation of such network rearrangements to an external stimulus smart responsive materials can be generated.[273-275] Such stimuli comprise thermal, light or chemical stimuli, permitting the material adaption towards environmental changes, thus smart behavior. In recent decade a range of dynamic covalent chemistries (DCC), displaying reversible bond formation and breakage behavior, was applied for fabrication of CANs. Based on the employed DCC two subclasses of CANs can be distinguished comprising associative ones, in case of temperature responsive network behavior termed vitrimers, and dissociative ones (see Scheme 2.8).[276] The first class is based on associative DCC featuring strict maintenance of crosslinking density within the polymeric network during rearrangement reactions.

Constant crosslinking density is guaranteed by the mechanistic progress of an associative exchange reaction, starting with formation of a new bond before cleavage of the former one – an addition/elimination pathway. Typical DCC displaying associative mechanistic behavior are transesterification reactions, disulfide metathesis, transamination.[277-280] The latter CAN type is based on dissociative DCC. Here a change in crosslinking density during network rearrangement of CANs, in particular a reduction, is observed. Reason for this is the presence of a dissociative covalent reversible reaction mechanism, where bond breakage occurs before bond formation – an elimination/addition pathway. Representative examples of this type of bond exchange chemistry are Diels-Alder cycloaddtions, boronic ester cycloaddition, thio-/aza- Michael addition or silanol bond rearrangements.[276,281-284]

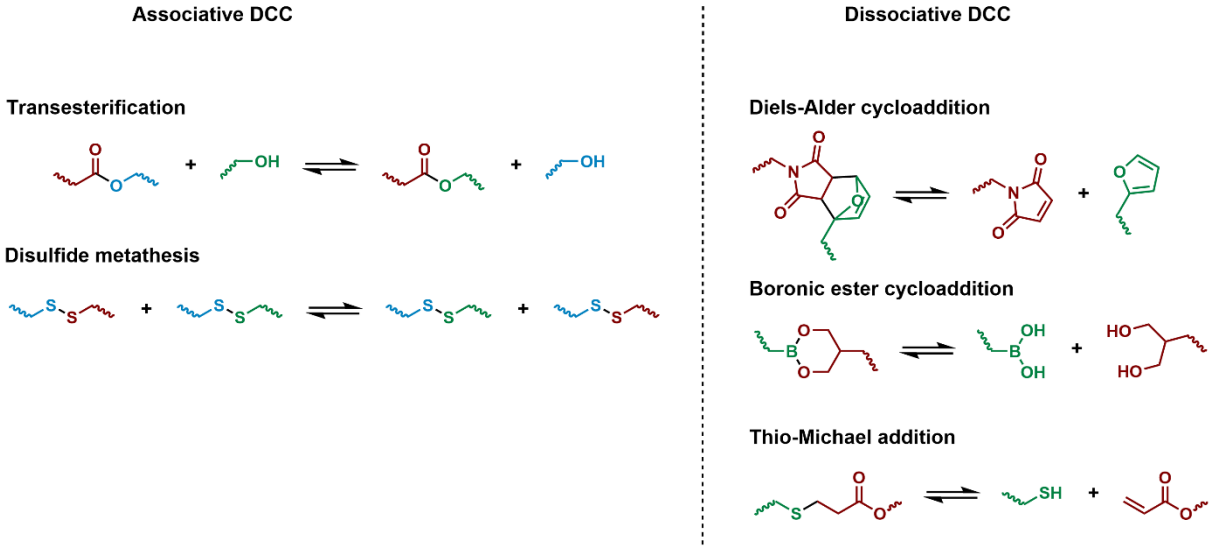

Scheme 2.8: Depiction of a selection of DCC sorted by their exchange mechanism. Transesterification and disulfide exchange exhibit an associative mechanism, whereas Diels-Alder cycloaddition, boronic ester cycloaddition or thio-Michael addition work via a dissociative mechanism.

Recapitulating the advantages offered by CANs a large range of possible applications can be imagined. Especially in regard of 3D printable systems investigations in recent years resulted in several publications employing this material class for 3D fabrication of smart materials showing self-healing features, reprocessable and recyclable materials, or even functional materials such as thermadapt shape memory polymers.[273,274,276,285]

Being one chemistry treated in this thesis, alkoxyamine chemistry and its applications in CANs will be discussed in the following section.

2.4.3.1. Alkoxyamine bonds in CANs:

From prior discussion about NMP, which is based in its original form on the thermally bond dissociation/reformation mechanism of alkoxyamines, it is obvious that alkoxyamine bonds could be appropriate candidates for generation of CANs.

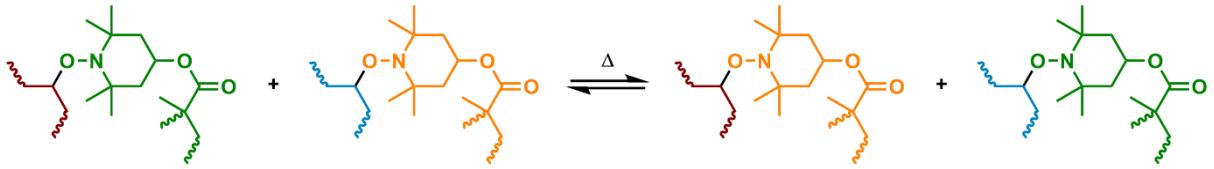

Scheme 2.9: General mechanism of nitroxide exchange reaction.

Indeed, alkoxyamine offer the possibility for network rearrangement via nitroxide exchange reaction, initiated by a suitable temperature stimulus (see Scheme 2.9). This dynamic covalent rearrangement reaction follows a dissociative mechanism meaning thermal homolysis into nitroxide and carbon centered radicals occurs before successive alkoxyamine bond formation. In addition, each dynamic alkoxyamine crosslinks offers the potential to be used as starting point for NMP, permitting the inclusion of network extrinsic monomers, incorporating tunability of properties.[286]

Using above mentioned reactions a variety of alkoxyamine based system was developed in last years. First example employing alkoxyamine chemistry was demonstrated by Takahara *et al.* in 2009.[284,287] Here, NMP as well as NER was employed on a tunable network generated by free radical polymerization using a styrene and bifunctional crosslinker featuring an alkoxyamine bridging unit. Using NER decrosslinking was achieved, whereas by application of NMP conditions employing styrene network extension was performed increasing in this way the mesh size. In 2016 Torkelson *et al.* designed recyclable and reprocessable polymeric networks based on alkoxyamine chemistry via an one-step strategy.[288] Impressively, multiple melt-reprocessing cycles were performed while observing excellent property recovery concerning Young's modulus, elongation at break and tensile strength. Another example featuring self-healing and recyclability based on the integration of alkoxyamine bonds into a network was reported by Zhang *et al.* in 2016.[289] In analogy to the work of Takahara, Tsotsalas *et al.* reported in 2019 an alkoxyamine based CANs with tunable crosslinking degree and mechanical properties.[290] The CAN itself was constructed out of discrete molecular building blocks featuring multiple alkoxyamine groups. Networks were formed, tuned and recycled by application of NER. Extending this concept, the group produced in a follow up work 2020 an alkoxyamine based CAN exploiting NER and NMP modification.[291] By NER prepared CANs were tunable in their crosslinking degree as well as rendered from initial insolubility to complete solubility – making them highly

attractive for recycling purpose as stated by the authors. Furthermore, application of NMP as postmodification network properties such as glass transition or mesh size were altered.

Important to mention is that alkoxyamine CANs are not solely limited to temperature as stimulus as it might appear from previous summary of examples. Recent developments in photo-dissociable alkoxyamines offer the feature of light responsivity towards alkoxyamine-based CANs too.[286] One example published by Telitel *et al.* comprised a CAN based on photosensitive alkoxyamine bonds giving access to self-healing of the network in response to light irradiation.[292] Dissociation of initial bonds by UV irradiation and subsequent radical recombination allows this feature to occur.

Although photoresponsive CANs have been less investigated yet the ground research performed on photo-based alkoxyamine chemistry provided an excellent basis for further development of such systems as well as implementation of alkoxyamine chemistry into 3D printing or living additive manufacturing.

Closing the loop, starting point of the discussion was a general introduction about living additive manufacturing. Successive focus was pointed towards different RDRP methods with a focus on NMP, which was treated in addition to implement the topic of CANs. Concluding, several examples and developments in living additive manufacturing will be treated in the next section.

2.4.4. Examples of Living Additive Manufacturing:

In recent years several systems have been successfully designed allowing fabrication of “living” materials based on RDRP methods. Especially in case of macroscale light-based printing a fruitful development is recognizable by a multitude of systems employing RAFT polymerization. The microscale, by contrast, using 2PLP has only been scarcely explored. As stated prior in the SMP example section, the author suspected main reasons for it in the delicate requirements – treated exhaustively in former sections – for an ink to be appropriate for two photon absorption-based fabrication techniques. However, in the following system design approaches successfully applied for DLP printing at the macroscale will be presented. Furthermore, currently reported microinks for 2PLP comprising the concept of living additive manufacturing will be treated too.

2.4.4.1. Living Additive Manufacturing at the Macroscale:

Employing light-based macroscale techniques, living additive manufacturing was mainly investigated in terms of RAFT systems, mirrored by the number of publications. Here inks based on different RAFT mechanisms were designed including photoinduced electron/energy transfer-RAFT (PET-RAFT) polymerization[293-298], photoiniferter RAFT polymerization[299,300], Norrish type I photoinitiated RAFT

polymerization (NTI-RAFT)[301-307], and photoinduced radical-promoted cationic RAFT (RPC-RAFT)[308] polymerization.

PET-RAFT polymerization is based on a photocatalyst that activates the RAFT agent, starting and mediating in this way the polymerization process and thus 3D structure fabrication.[293-298] Notably the proposed mechanisms vary depending on the applied reaction components and conditions. First step is in all cases the photoexcitation of the photocatalyst by irradiation of light of appropriate wavelength. In one exemplary mechanism the excited photocatalyst performs an electron or energy transfer towards a dormant RAFT species. Successive β-scission of the C-S bond generates a carbon centered radical, initiating the chain propagation process. In another mechanism proposed for the presence of electron donors, such as tertiary amines, the excited photocatalyst is first reduced, performing in the next step an electron transfer to the RAFT agent. Similar to the first version a β-scission of the C-S bond occurs and the carbon centered radical is formed inducing chain propagation. In both cases the catalytic cycle is closed by final recombination of the RAFT fragment – the thiocarbonylthio fragment – and the propagating radical, letting the reactive chain end return to the dormant state (see Scheme 2.10). During the network forming process, growth is controlled by degenerative chain-transfer as typical for RAFT. Working via second displayed mechanism, Boyer *et al.* designed ink formulations, that employ an initiation system composed of erythrosine B as photocatalyst and triethanolamine representing the electron donating tertiary amine to induce RAFT photoactivation by generation of a thiocarbonylthio stabilized anion and the chain propagating carbon centered radical. Importantly the reaction is rendered oxygen tolerant by the reduction of present oxygen to superoxide during the catalytic process. Employing this system, the authors were able to achieve building speeds up to 12 mm h^{-1}. Another system employed utilizes eosin Y as photcatalyst and triethylamine as electron donor.

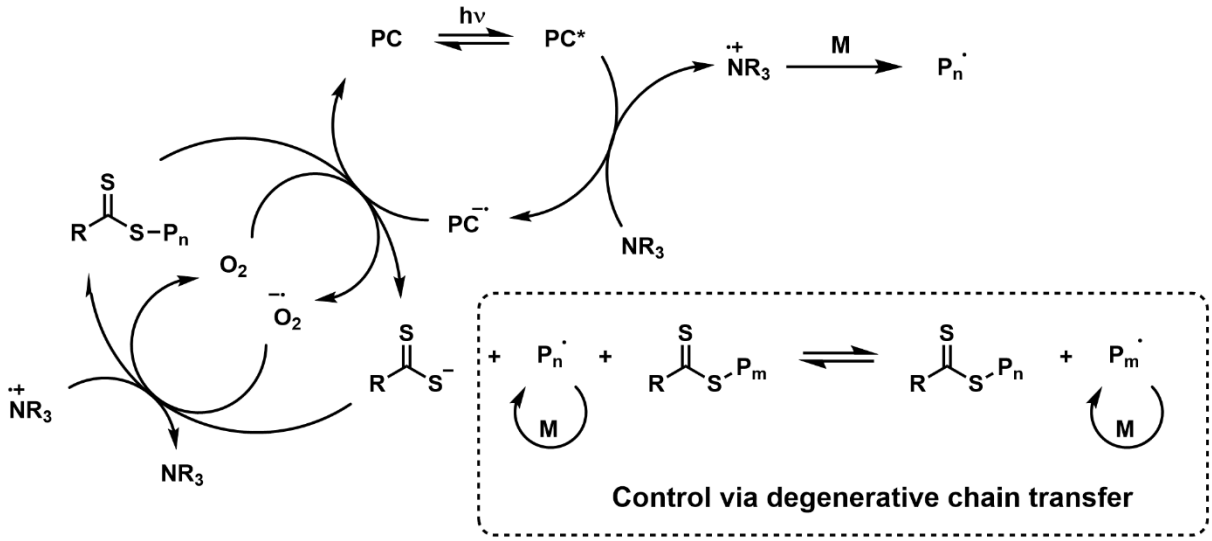

Scheme 2.10: Proposed mechanism of PET-RAFT. Mechanism is drawn based on mechanistic explanation and illustration of reference [293].

Although it allowed 3D fabrication at visible light curing conditions, fabrication speed was rather low. A further system employed a zinc based photocatalyst permitting fabrication using red light. However inert reaction conditions were necessary during 3D printing.[309]

In contrast to PET-RAFT, photoiniferter RAFT mechanism is based on the direct photolytic bond cleavage of RAFT agents.[299,300] Summarizing the mechanism RAFT agents undergo β-scission of the C-S bond initiated by irradiation with light in the visible or UV range, producing a thiocarbonylthio radical, the persistent species, and the transient carbon centered radical. Chain propagation is stopped – return to dormant state – by recombination with mentioned persistent species or by typical RAFT degenerative chain-transfer mechanism (see Scheme 2.11). Application of this type of RAFT method in DLP printing was performed by Bagheri *et al.* employing trithiocarbonates at visible curing wavelengths of 405 nm. Beside very low build speeds, 3D printing under inert conditions was required rendering the fabrication process unsuitable for general application. Overcoming these issues, Zhang *et al.* employed a xanthate RAFT agent achieving build speeds in the range of 12 mm h^{-1} at ambient conditions.[309]

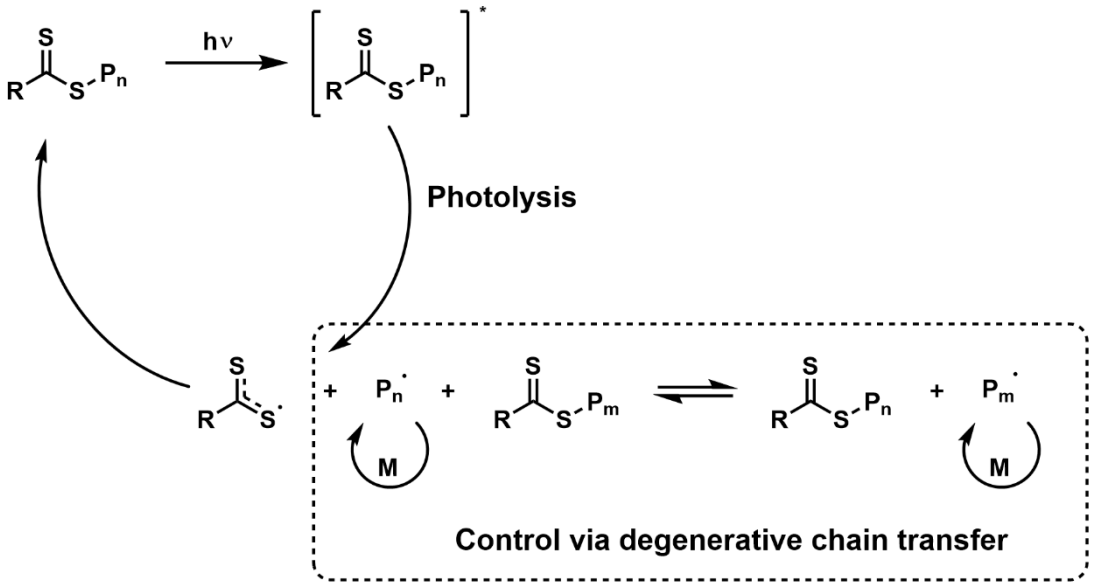

Scheme 2. 11: Proposed mechanism of photoiniferter RAFT. Mechanism is illustrated based on the explanation and illustration in reference [309].

In NTI-RAFT polymerization a Norrish Type 1 photoinitator such as TPO is employed, forming initiating radicals upon irradiation of suitable wavelengths.[301-307] Formed radicals induce the chain propagation process by reaction with vinylic monomers. Control is provided by degenerative chain transfer via RAFT (see Figure 2.12). Employing TPO in combination with a RAFT agent a library of DLP printable inks were

designed, permitting efficient 3D fabrication under ambient conditions with build speeds up to 91 mm h^{-1}.[309]

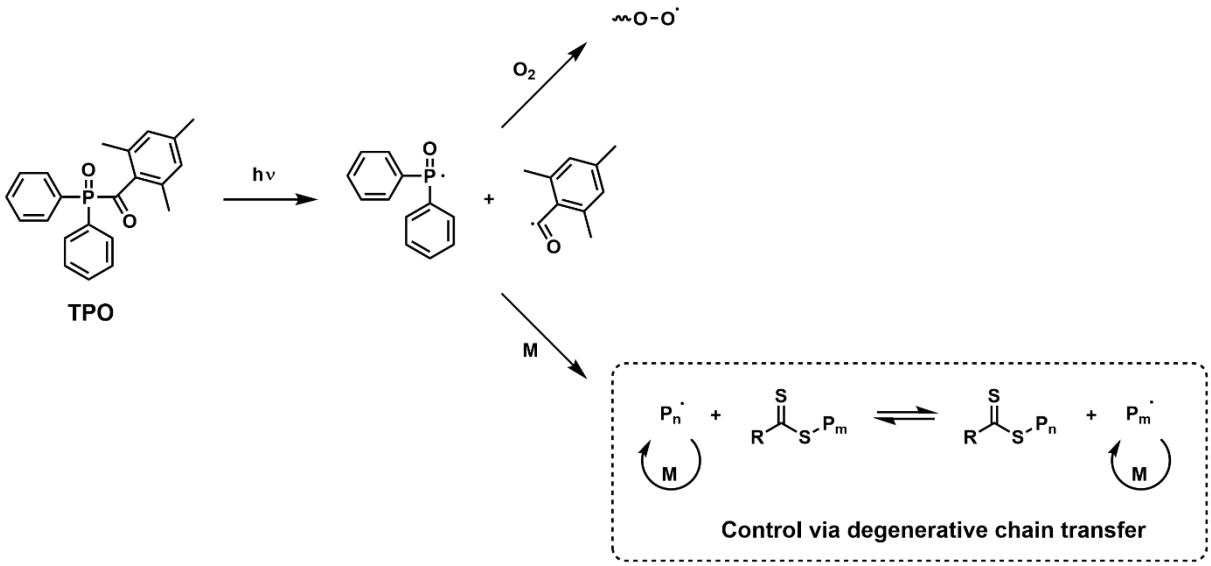

Scheme 2. 12: Proposed mechanism for NTI-RAFT. Mechanistic representation is based on mechanistic explanation and illustration in reference [302].

RPC-RAFT represents a radical-promoted cationic polymerization process including a monomer suitable for cationic polymerization, a radical photoinitator, an onium salt and a RAFT agent. Mechanistically starting with a homolytic decomposition of the photoinitator upon light irradiation, generated radicals are oxidized by the onium salt to cationic moieties. These induce die chain propagation process that is controlled in its network growth by degenerative chain transfer mechanism by the RAFT agent. Zhu *et al.* employed RPC-RAFT for SLA based 3D printing generating a ink fabricable with infrared light under ambient conditions.[308,309]

Aside from RAFT based systems, photoinduced ATRP was employed for 3D fabrication via DLP too. Qiao *et al.* designed as suitable ink system employing carbon quantum dots as photocatalyst for aqueous based ATRP under visible light conditions.[310] Summarizing proposed mechanism, carbon quantum dots are excited by photoirradiation in a first step. Subsequently the excited species reduces a copper (II) bromide species to copper (I) complexes, that is able to activate an alkyl bromide generating carbon centered radicals and a cooper (II) bromide species. Control of the process is provided by reversible deactivation via bromination forming the dormant state of the propagating chains and a cooper (I) complex. Employing this reaction type build speeds up to 30 mm h^{-1} were achieved. Furthermore, fluorescence due to incorporated quantum dots was observed for 3D printed architectures.[309]

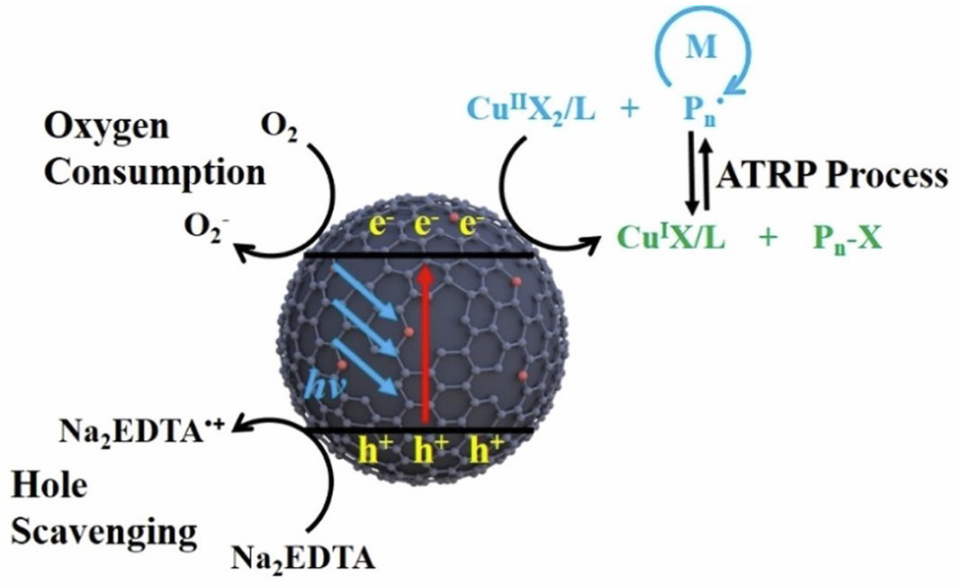

Figure 2.5: Illustration of chemical processes during the photoinduced ATRP process employed for DLP printing. Adapted with permission from [310]. Copyright 2022 American Chemical Society.

2.4.4.2. Living Additive Manufacturing at the Microscale:

Based on additional requirements for ink systems to be printable via 2PLP, the amount of reported systems is rather limited. Thus, in the following only two systems based on RAFT and NMP will be treated both provided by the group of Spangenberg.[311,312]

In the first work the authors reported a two-step system including fabrication of microobjects via 2PLP implementing macro-photoiniferter RAFT groups into a pentaerythiritol triacrylate PETA resin as first step and surface postmodification with N-isopropylacrylamide in the seconds step.[311] Both fabrication steps were performed with a wavelength of 532 µm at scan speeds below 50 µm s^{-1}. Postfunctionalization was in this case possible by photoinduced reactivation via the photoiniferter mechanism.

In a very recent example Spangenberg *et al.* designed a 2PLP fabricable ink system based on nitroxide-mediated photopolymerization (NMP2).[312] PETA based structures printed in a first step by photoinitiatable alkoxyamine species were surface functionalized with either trimethylolpropane triacrylate (TMPTA) or poly(ethyleneglycol)diacrylate (PEGDA) without usage of photoinitators in both cases but by reactivation of alkoxyamine bonds (see Scheme 2.13). Depending on the employed monomer change of surface in mechanical properties in the range of 2 orders was accessible. Although remarkable due to its oxygen tolerant application of a living NMP based microprintable reaction, 3D printing showed very low performance in regard of scan speed reaching only 14.3 µm s^{-1}.

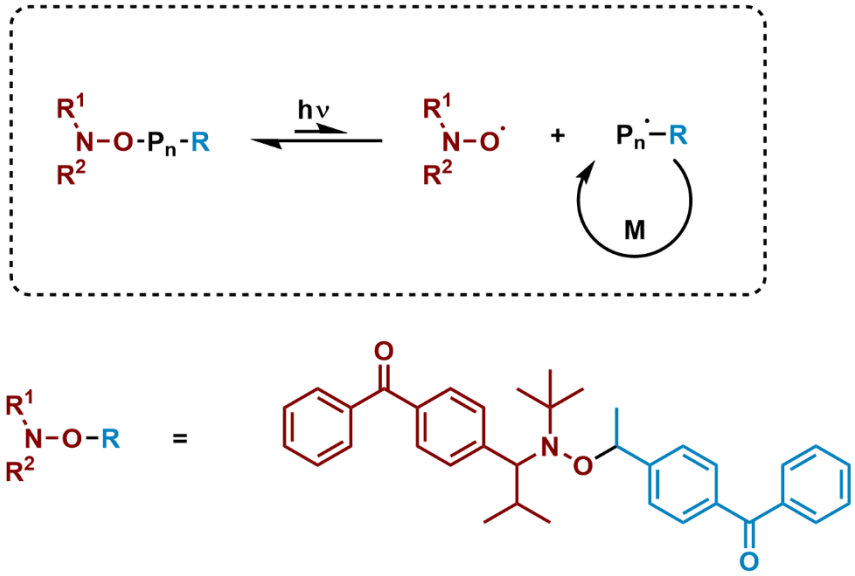

Scheme 2.13: Proposed mechanistic pathway for photoinduced NMP reaction and representation of the alkoxyamine initiating unit. Illustration is produced based on illustrations and descriptions in reference [312].

Chapter 3

4D Printing of Shape Memory Polymers: From Macro to Micro

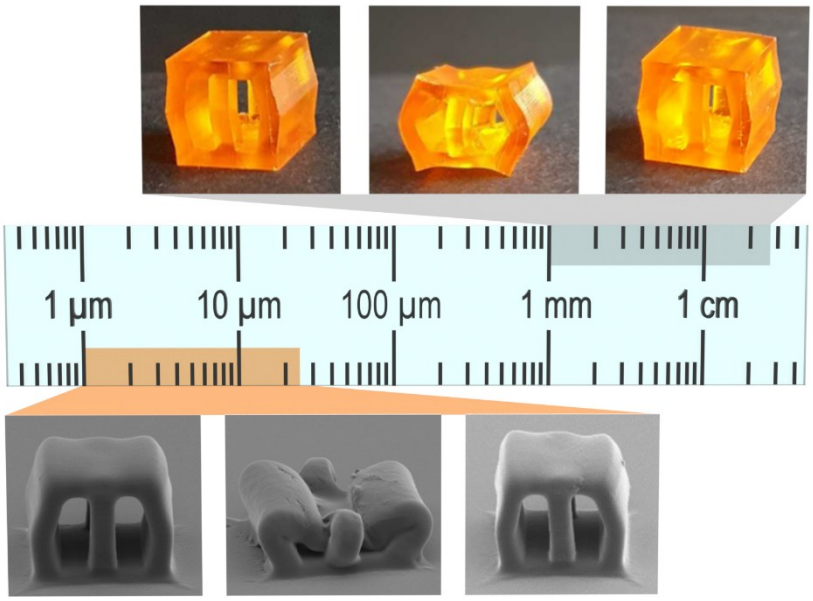

Printing 4D SMPs at the macro and microscale.

3.1. Motivation and Aims:

Since the time of conceptualization of 4D printing in 2013 and the identification of SMPs as one of its core material classes, 4D fabrication of SMPs has made remarkable progress to the present day – especially at the macroscale using light-based printing techniques respectively extrusion-based methods. However, microscale 4D printing of this impressive materials was at the time I started to work on this topic – in 2019 – only scarcely investigated, visible by the absence of any publication at that time.

As discussed in chapter 2, there is a range of remarkable SMP systems present for macroscale printing, however the very few existing 2PLP systems at the microscale suffer from several disadvantages including: i) non-accessibility towards 3D structures, ii) necessary synthetic efforts to generate ink components and necessary synthetic effort to render an ink printable – two points resulting in the exclusion of parts of the community without synthetic background, iii) high necessary curing laser powers, iv) low 3D microstructure fabrication quality as well as v) limitation in terms of SME activation to solely liquid conditions. Furthermore, despite of the fact that systems were reported at the macro- and microscale, no system was reported connecting both scales allowing 4D macro- as well as microfabrication using the same functional ink system. However, bridging both scales with one basic ink system later improved for each of the methods separately would increase its general applicability in the scientific and industrial community permitting prosperous developments at macro and microscale 4D fabrication in promising fields such as soft robotics, sensors, electronics and biomedical approaches.

Tackling this challenge, the first goal of my thesis was the design of a SMP ink system making a first step towards connection of macroscale fabrication via DLP and microscale fabrication via 2PLP. Moreover, I planned to overcome the limitations of present systems – especially at the microscale – by rendering the SMP ink system simple in its preparation, and accessible to the community. Besides major care will be taken that printability as well as shape memory response would be at good quality level for both dimensions.

3.2. Results and Discussion:

3.2.1. Identification of a Functional Ink System suitable for Macro- and Microprinting

To design SMP inks permitting 3D macro- and microfabrication via DLP and 2PLP, first step included the identification of suitable functional ink components. In view of its later application at different size

regimes four criteria were defined that must be fulfilled by this core components of the SMP ink: I) good printability employing the two selected 3D printing methods (DLP and 2PLP), ii) ink components must offer the potential for excellent shape memory response in terms of programmability, shape fixation and shape recovery in the final ink, iii) easy access towards all utilized ink components, iv) simple ink preparation without the need of additional synthetic effort.

First, it was necessary to consider the different requirements for an ink system to be suitable for DLP as well as for 2PLP technology. The functional monomers employed in the system must be compatible with each of the techniques, that, although based both on photopolymerization, dramatically differ in their 3D fabrication mechanism in regard of their curing source, their initiation process, the way how objects are constructed as well as their curing (print) speed and the dimensions of finally manufactured 3D geometries. As explained in chapter 2 DLP uses an UV-LED light source giving access to linear one-photon absorption-based initiation. Structure fabrication is performed in layer-by-layer manner allowing fabrication of macroobjects in the size regime of mm to cm. 2PLP contrarily uses a tightly focused femtosecond pulsed laser in the near infrared regime, permitting nonlinear two-photon absorption-based initiation of polymerization. Due to the low probability of this process to occur all parameters that allow faster polymerization respectively faster approach towards the polymer's gel point and above must be optimized. Thus, especially a high photoreactive group density as well as high viscosities are favorable in view of the 3D structure building process and must be considered during ink design. Besides printability the second key element the SME and its inclusion into the 4D fabricated objects at both scales in a high quality is the second essential criteria designing a functional SMP ink. This implicates that the resulting SMP structures at both scales need to feature a thermal transition permitting easy deformability for programming the temporary shape above transition temperature and good fixation property enabling structural maintenance of this programmed temporary shape below transition temperature. Fulfilling the third conditions, all ink components employed for ink preparation must be commercially available as standard chemicals, guaranteeing accessibility of the designed ink system to the whole 4D printing community in this way. Satisfying requirement four, the preparation of the ink must be kept as easy as possible. The simpler the ink preparation the more appealing is the potential usage of the system for other applicants without synthetic chemistry background increasing the impact of our system for the community in this way. To ensure the ink preparation will be adjusted in a way that simple weighting in and stirring of all the components is sufficient without any heating or cooling protocols respectively precuring procedures under potentially dangerous UV light.

To fulfill these four criteria, development of a functional ink system was designed allowing for the printing of amorphous SMPs with both printing techniques, whose SME is based on a glass transition

temperature (see Figure 3.1). In terms of ink components, isobornyl acrylate (IsobA) was selected as monofunctional monomer, featuring the role as main component and linear chain builder, mainly responsive to set the glass transition and SME property. Furthermore, IsobA is known monomer in the 3D printing community, highly appreciated for its printing performance and the excellent mechanical properties of its polymer.[313,314] In regard of crosslinker, selection was concentrated on diacrylates, using one functional group type and not including methacrylate crosslinkers avoiding in this way distinct reactivities within the inks caused by different reaction kinetics as well as reduced reactivity due to the structure caused kinetic inhibition in case of methacrylates. After initial screening final decision was made in the end for a dual crosslinker system composed of a soft elastomer poly(ethylene glycol) diacrylate (average M_n = 575 g mol^{-1}, PEGDA 575) integrating chain flexibility into the final polymeric network and tricyclo[5.2.1.0^{2,6}]decanedimethanol diacrylate (TcddA), as stiffer diacrylate. Here evaluating the right balance was especially important for successful incorporation of the shape memory properties into macro- as well as microstructures. To high content of the soft component will prevent your structures from efficient fixation of the temporary shape, contrastingly higher content of TccdA will render the polymer network rather undeformable due to incorporated stiffness making efficient SMP actuation impossible. Further consideration must be involved in setting the total amount of crosslinker ratio for each printing method to achieve the right level of printability without losing the SME. This point will be more exhaustively discussed in the next sections.

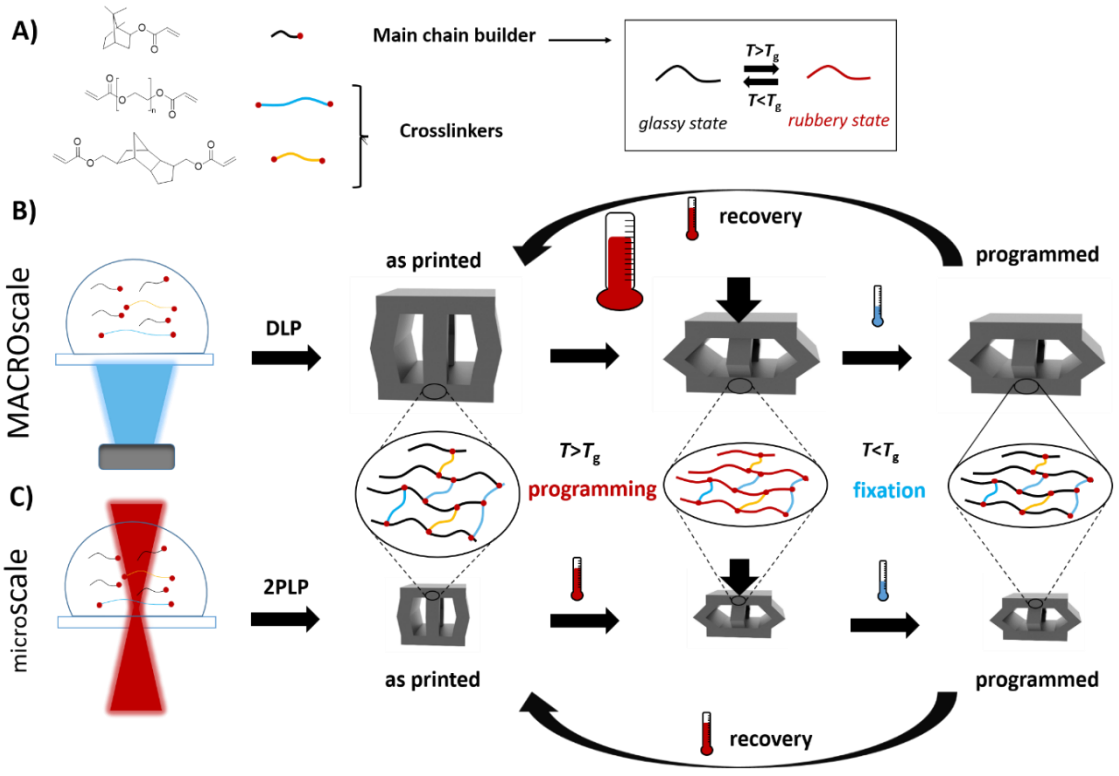

Figure 3.1: Designed SMP ink system for 4D macro- and microscale printing. A) The functional core system was composed of IsobA as functional monomer and a dual crosslinker system including PEGDA 575 and TcddA. Fabricated 3D geometries at both size regimes are amorphous networks exhibiting a T_g-based SME. Scheme of the employed 4D printing process B) DLP

at the macroscale and C) 2PLP at the microscale. Shape memory cycles can be performed utilizing an adequate temperature (T > Tg), the initial shape is programmable to an arbitrary temporary shape and recoverable on demand to its initial shape. Adapted from reference [210].

A further key element for the success of an ink applied in photopolymerization-based techniques is the right choice of photoinitiator. Its performance and efficiency are critical for defining the printability – including range of employed light energy doses and achievable curing speeds – of an ink system and the quality of finally fabricated structures. In case of this work the selection of a suitable PI is even more intricate because the final ink system must be applicable in DLP and 2PLP fabrication, working via initiation mechanisms based on two distinct absorption mechanism – linear one-photon and nonlinear two-photon absorption. Fortunately, phenylbis(2,4,6-trimethylbenzoyl)phosphine oxide (BAPO) was identified as a promising candidate that is commonly used in both printing methods, DLP and 2PLP as discussed in chapter 2. Featuring suitable absorption in the range of 360 to 400 nm, qualifies its usage as PI for light-based curing at 385 nm employing our DLP system. Furthermore, it features also sufficiently two-photon absorption activity at the laser wavelength of 780 nm offered by the commercial 2PLP system employed.

Establishing the core ink components with the selection above, the focus of the subsequent work was shifted towards the optimization of the inks for DLP and 2PLP technology as well as the successive characterization of the shape memory properties of fabricated 4D structures. In the next sections first the work done establishing an efficient SMP formulation at the macroscale is treated and subsequently efforts establishing the microscale formulation fulfilling prior defined criteria.

3.2.2. 4D Printing of Shape Memory Polymers at the Macroscale

3.2.2.1. Optimization of the Formulation for 4D Structure Fabrication via DLP

Making use of the functional system introduced in the section before, the ink formulation was adapted and optimized for macroscopic printing via DLP (see Scheme 3.1). By considering the more efficient linear initiation process, and thus a preference for faster curing and simultaneously higher crosslinking density, the ratios of the core monomer and crosslinker content were adapted. In particular, the amount of crosslinker was lowered drastically compared to the monofunctional component, ensuring in this way an operative SME effect in later printed 4D structures without possible inhibition caused by too high crosslinking density. However, careful adjustment was necessary, because too low crosslinking content would destabilize beside the printing process the permanent shape too, resulting in an insufficient recovery process. After successful optimization the final ink system for macroscale SMP printing was composed of a mixture of main chain builder IsobA, flexible crosslinker PEGDA 575

and stiff crosslinker TccdA. As further monomer component small portions of hexyl acrylate were incorporated into the formulation, improving the printability and the deformability during programming, as visible in the later sections. 3D fabricability of the macroscale formulation was ensured by incorporation of BAPO as photoinitiator and further improved by addition of small amounts of Sudan I, acting as photoabsorber, permitting reduction of the achievable minimal layer thickness. Importantly, HexA and Sudan I can be seen as additional additives supporting the printing process and enhancing the quality of the SME in general. However, 3D fabrication and 4D actuation by omitting them was possible as well.

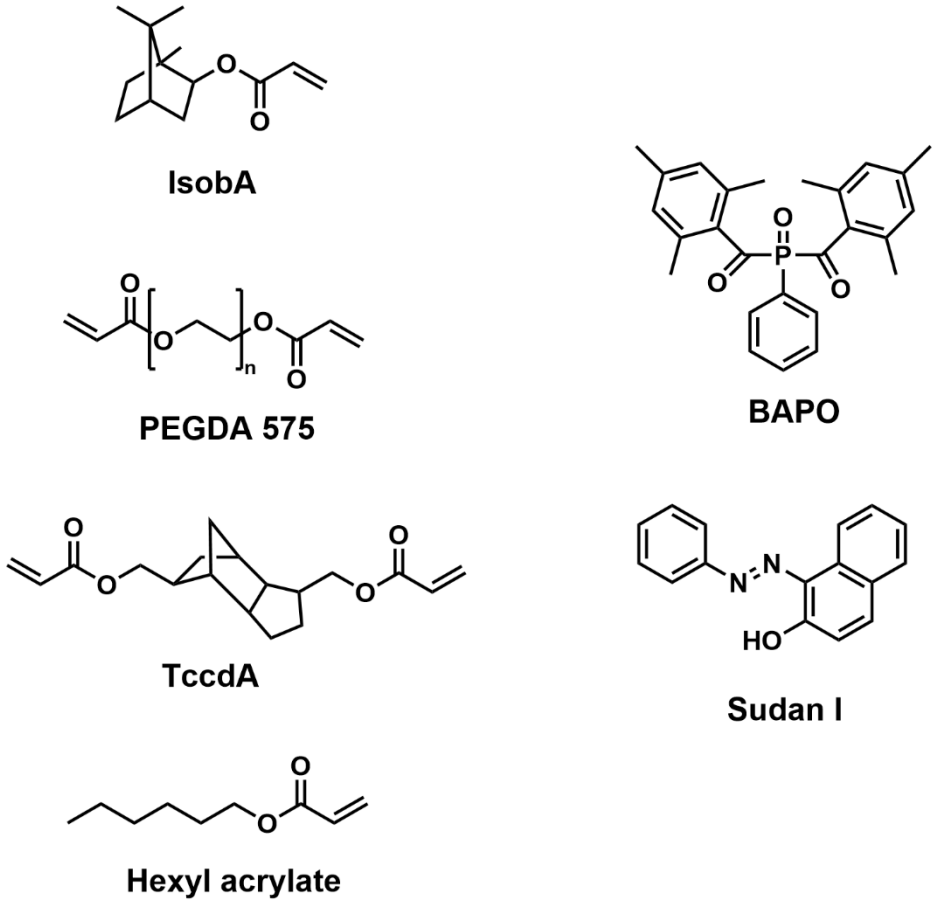

Scheme 3.1: Ink components of SMP formulation optimized for macroscale 3D printing via DLP. In particular, the ink was composed of IsobA (80 mol%), flexible crosslinker PEGDA 575 (3 mol%) and stiff crosslinker TccdA (14 mol%) and small amounts of hexyl acrylate (3 mol%). Additionally, BAPO was employed as photoinitiator (2 wt.% of formulation) and Sudan I (0.05 wt% of formulation) as photoabsorber.

3.2.2.2. 3D Printing via DLP

After successful establishment of a potential macroscale formulation, printing parameter screening was performed and successive 3D printing was conducted on a commercial DLP printer utilizing a 385 nm high power UV-LED. Further modification by utilization of a home-built aluminum tray print head featuring a build area of 2.5 x 2.5 cm^2 as well as a downscaled ink tray enabled printing with 2 to 5 g of

ink, permitting parameter screening as well as testing in a scale appropriate for research and development (Precise description of all modification is provided in the Experimental section of this thesis).

Searching for suitable curing conditions irradiation intensities of 8.0 and 13.0 mW cm^{-2} were identified and further investigated by evaluation of resulting cure depths at different irradiation times. Jacobs working curves were generated by semilogarithmic depiction of exposure dose energy versus cure depth for the two curing conditions applied (see Figure 3.2 A and B). For both investigated intensities a linear relationship between both measured quantities was observed, giving access to the critical exposure dose (E_c) and the penetration depth (D_p). For polymerization with 8 mW cm^{-2} a E_c of 4.3 ± 1.1 mJ cm^{-2} and a D_p 0.09 mm was calculated. Curing with 13 mW cm^{-2} gave values of 4.9 ± 1.2 mJ cm^{-2} for E_c and 0.08 mm for D_p. As expected, values for both quantities appear within the same size regime, as expected from similar formulations at different curing intensities.

On the basis of obtained values for E_c, D_p and the working curve, we continued to investigate the 3D fabricability of previously described SMP macroformulation. Excellent printability was achieved using minimal z layer thicknesses of 50 and 100 µm for each of the two employed curing conditions (8.0 mW cm^{-2} and 13 mW cm^{-2}). The possibility of fast 3D fabrication at high resolution was further demonstrated by excellent layer curing times of 1.6 s for 8.0 mW cm^{-2} and 1.5 s for 13 mW cm^{-2} aiming at a minimal z-layer of 50 µm.

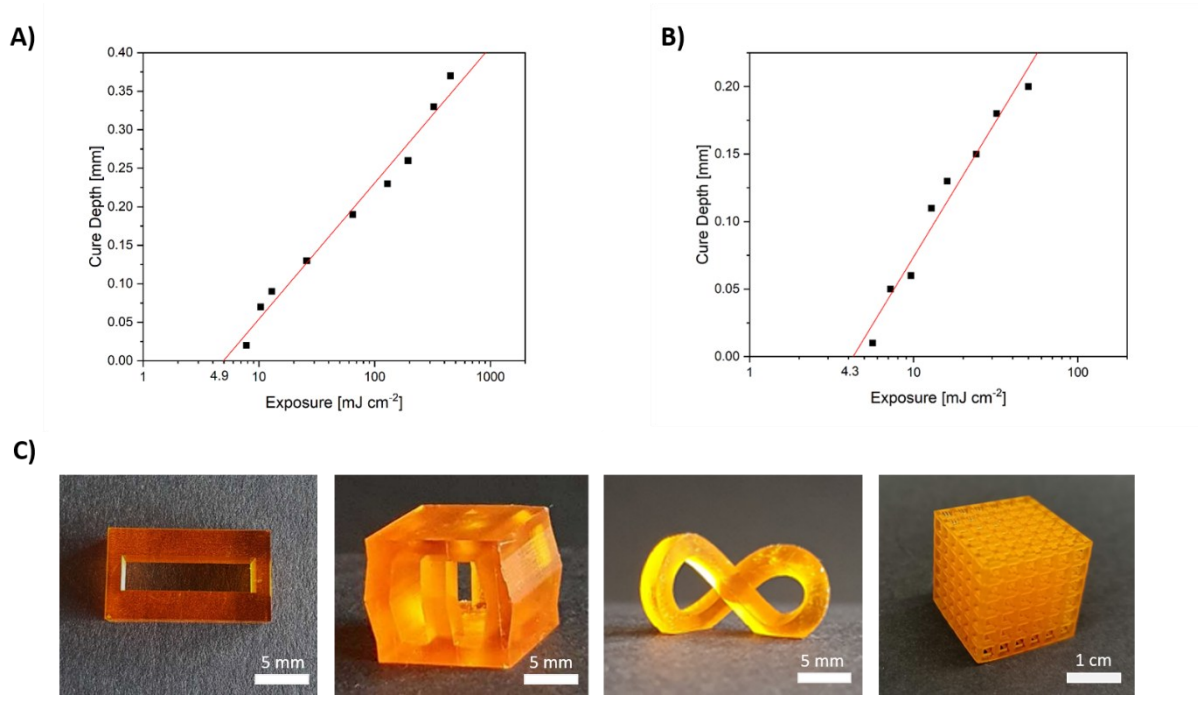

Figure 3.2: 3D Printing of the SMP macroformulation via DLP. A) Jacobs working curve for 13.0 mW cm^{-2} curing condition. Data points correspond to the measured curing thickness at different energy exposure doses. The x-intercept corresponds to the critical exposure. B) Jacobs working curve generated at 8 mW cm^{-2}. C) Images of exemplary 3D printed structures

employing the SMP macroformulation including: frame, double platform geometry, infinity ring and cubic grid structure (from left to right). Adapted from reference [210].

To evaluate the versatility of our macroink system in terms of 3D structure fabrication, we designed and successfully printed a large variety of 3D geometries offering different levels of structural complexity (see Figure 3.2 C). 3D fabrication of less complex structures such as simple cylinders and frames was possible as well as printing of more challenging geometries such as the double platform structures or infinity rings featuring large overhanging parts up to the rather sophisticated cubic grid geometry predominantly consisting of thin overhanging bars as structural elements. All structures were printed in superior quality exhibiting low surface roughness and hardly visible transitions between cured layers, both factors indicating excellent fabrication performance of the developed macroink. This is particularly evident in case of the obtained structural quality for the complex 3D cubic grid. Even finest structural elements were printed without any visible damage respectively defect, showing dimensional homogeneity within the whole structure. After successfully proving large compatibility of our macroink formulation with a large variety of different designs, next steps included evaluation of the minimal possible feature size printable while still permitting generation of stable structures. For this purpose, a base model containing of single quadratic pillars of 7.4 mm height and different side lengths of 0.5 mm 1 mm, 1.5 mm and 2 mm was designed (see Figure 3.3). Successful printing of this test structure evinced the feasibility of printing structures featuring dimensions far below 1 mm as well as excellent mechanical stability of them.

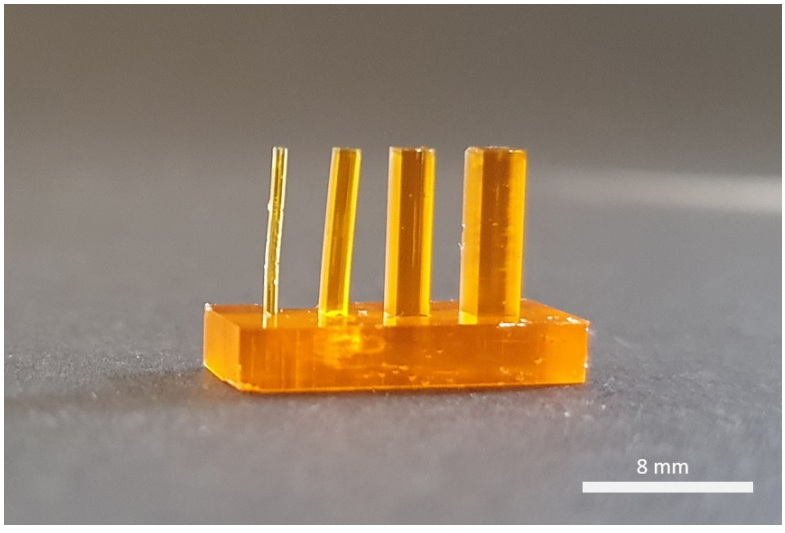

Figure 3.3: 3D printed test structure for evaluation of minimal structure size. Structure consists of a stable rectangular base plate with four quadratic pillars of 7.4 mm height and different side lengths of 0.5 mm 1 mm, 1.5 mm and 2 mm. Adapted from reference [210].

3.2.2.3. Shape Memory Effect at the Macroscale

Having established the ink formulation as well as the printing parameters, evaluation of the shape memory effect (SME) was the next logical step. In this process the first step was the determination of the shape memory transition temperature – the glass transition temperature (T_g) in case of this system – of macroscopic 3D printed structures. The transition temperature is especially important for the design of subsequent shape memory tests, since it is the main key element defining what temperatures are employed during programming and recovery (above T_g) and fixation (below T_g) temperatures of the SME cycle.

For characterization we searched for a method allowing evaluation of T_g at both size regimes: macro- and microscale. In the end we decided for dynamic nanomechanical analysis (DnMA) utilizing a nanoindentation system as suitable method for this purpose. Employing this characterization method, viscoelastic properties of the macrosamples were characterized, using a model described in literature. In essence, the indenter sample system was considered as a mechanical circuit composed of three elements arranged in parallel: i) a black box element corresponding to the sample-indenter load frame, ii) a spring element describing the load supporting spring of the nanoindenter, and iii) a dashpot element being equivalent to the damping between the capacitive plates of the nanoindenter. The specimen itself was treated as a Voigt solid[315-317], allowing execution of the measurement without utilization of a specific material model. At the macroscale 3D DLP fabricated cylindrical samples having a height of 1 mm and a diameter of 3 mm were employed as test specimens. Viscoelastic properties, in particular storage modulus, loss modulus and tangent delta were evaluated in the temperature range between 20 and 150 °C in steps of 10 °C, except for the range between 60 °C and 80 °C where smaller steps of 5 °C were used (see Figure 3.4). The viscoelastic characterization was conducted for 3D printed samples prepared by both prior selected curing intensities, 8.0 mW cm^{-2} (see Figure 3.4 A) and 13 mW cm^{-2} (see Figure 3.4 B). For both printing conditions increase of temperature resulted in a sharp decrease of the storage modulus. Associated with this behavior was a strong growth in tangent delta starting at about 50 °C, showing a peak maximum at 100 °C. Moreover, loss modulus exhibited a peak in the range of 70 °C, being equivalent to the glass transition region. Notably, T_g regions of both curing conditions appeared within the same temperature range, although fabrication intensity was different, usually implying distinct crosslinking densities and thus slight changes in the T_g. This behavior is a result of two aspects, in particular consequences of 3D fabrication and the DnMA measurements: i) during 3D fabrication UV-light curing was applied for all samples after printing giving access to more homogeneous 3D structures as well as nonreactive surfaces due to the removal of nonreacted acrylate bonds; ii) during the DnMA measurements measurement steps of 5 °C and 10 °C were applied, resulting in a rather rough depiction of the viscoelastic properties in view of the only slight differences of T_g due

to network density. However, to gain access towards a transition temperature employable for designing a SME cycle, the obtained level of measurement precision was of sufficient precision.

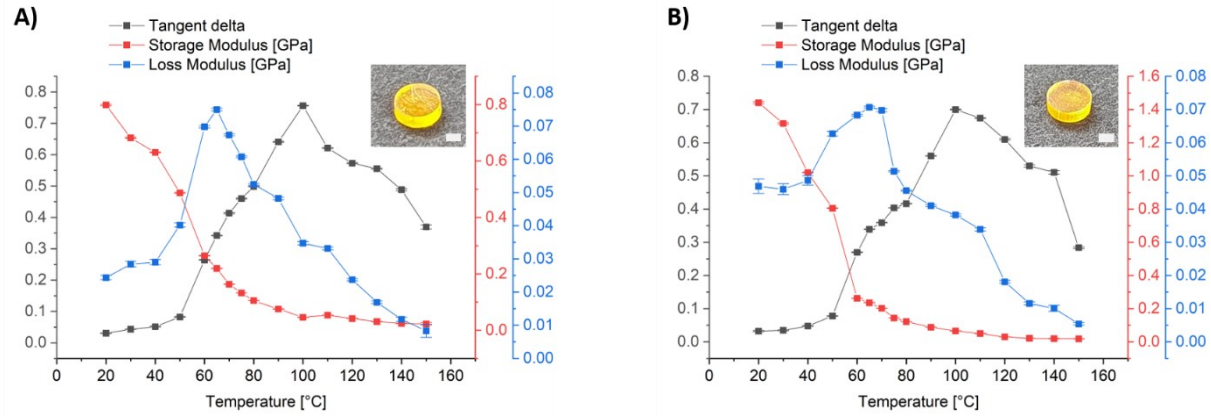

Figure 3.4: Analysis of viscoelastic properties at the macroscale by DnMA measurements of cylindrical samples printed with A) 8.0 mW cm^{-2}, and with B) 13.0 mW cm^{-2} after postcuring (30 s UV light). Data points for tangent delta, storage modulus, and loss modulus are plotted in a temperature range between 20 °C and 150 °C. Error bars represent standard deviation n = 360. For each temperature, a different position of the test sample was measured 360 times within one measurement series. An image of the test samples is included as inset within each plot. The scale bar corresponds to 1 mm. Adapted from reference [210].

After characterization of the T_g for the microprinted materials in the range of 70 °C, shape memory cycles based on these experimental values were designed for and performed on 4D printed structures. A temperature of 80°C – above T_g – was chosen as programming and recovery temperature assuring that the polymeric network is in its rubbery state. Fixation of the temporary shape was performed by cooling down to rt – below T_g. Reaching this lower temperature, the 3D fabricated structures transform from a rubber state to a glassy state allowing to "freeze" the new temporary shape obtained by mechanical deformation. Application of this shape memory procedure permits quantitative description of the shape memory quality. In particular shape memory parameters describing the efficiency of the SME – the shape fixity ratio (R_f) and the shape recovery ratio (R_r) – were determined by a shape memory bending test. The tests were performed on a simple rectangular strip geometry featuring a length of 30.0 mm, a width of 8.0 mm and a thickness of 0.8 mm. Describing the test procedure, initial heating of the test samples in a water bath to 80 °C, was followed by deforming them to an angle of 180°. Subsequent fixation of these bent geometries was performed by cooling them inside a water bath temperate towards rt. Images of initial, programmed and recovered shapes are depicted in Figure 3.5. From experimental results a R_f of 98% and a R_r of 97% were calculated, proving excellent shape memory properties in regards to temporary shape fixation and initial shape recovery for fabricated 3D SMP macrostructures, being competitive with towards best one-way SMP materials reported nowadays.

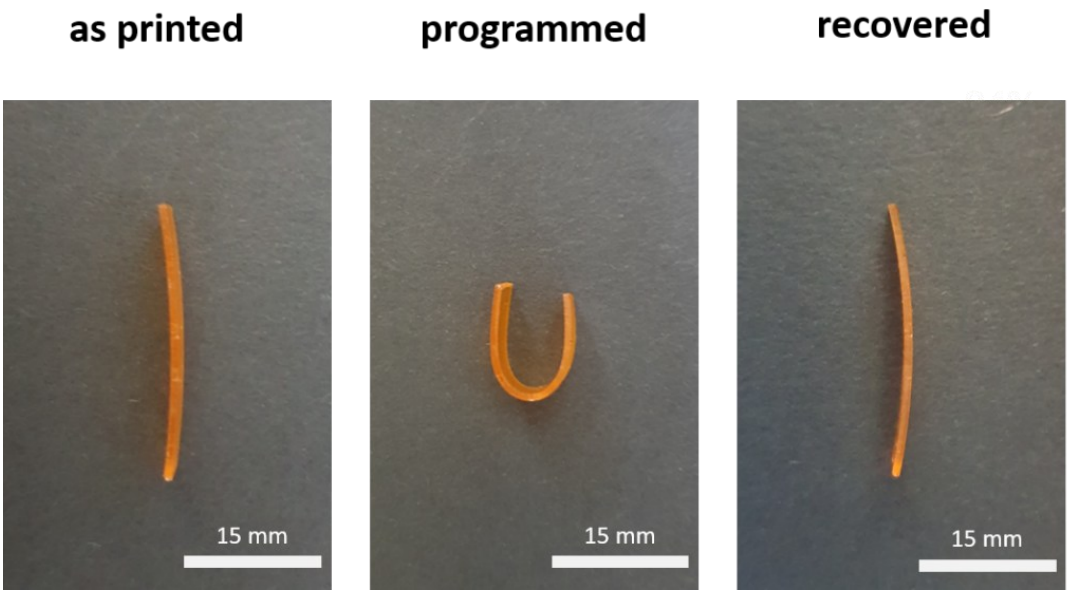

Figure 3. 5: Quantitative evaluation of shape memory performance by bending test employing a strip geometry. Adapted from reference [210].

In the next step, SME was tested qualitatively on 4D printed geometries featuring higher levels of complexity. Tested 4D structures included the double platform structure, the infinity ring, and the frame structure. Shape memory test cycles were performed employing the procedure described in the previous paragraph and in the experimental section. In particular, programming and recovery were conducted at 80 °C and fixation of the temporary shape at rt. Images were taken from the different 4D geometries at the different SME states of the initial shape, the temporary shape and the recovered shape are represented in Figure 3.6. As visible from these pictures the qualitative results obtained from complex structures match perfectly with previously obtained quantitative SME measures. Programming and fixation of the temporary shape worked almost without any loss in temporary shape after stress release. Recovery produces shapes structurally identical to the initial shape. Importantly no structural damage, such as cracks or delamination of the individually cured layer – an often met problem in DLP printed structures – during programming, fixation and recovery was observed.

To provide an even better visualization of the SMP cycle a movie of the whole process including programming, fixation and recovery was recorded and is depicted in Figure 3.7 as sequence of images. Referring to the well-known ship in the bottle problem, an infinity ring having dimensions too large to fit through the neck of a glass bottle was designed and printed for this purpose. The structure was first heated and then deformed in 80 °C hot water, visible at the temperature display of the magnetic stirring plate. Subsequently, the deformed temporary shape was fixed in water at rt. As visible the temporary shape maintained its geometry without of any back-bending observable. Now suiting the geometrical requirements, the infinity ring in its temporary shape was insertable through the neck of the glass bottle. After addition into the glass bottle, the preheated water at 80 °C, induces immediate

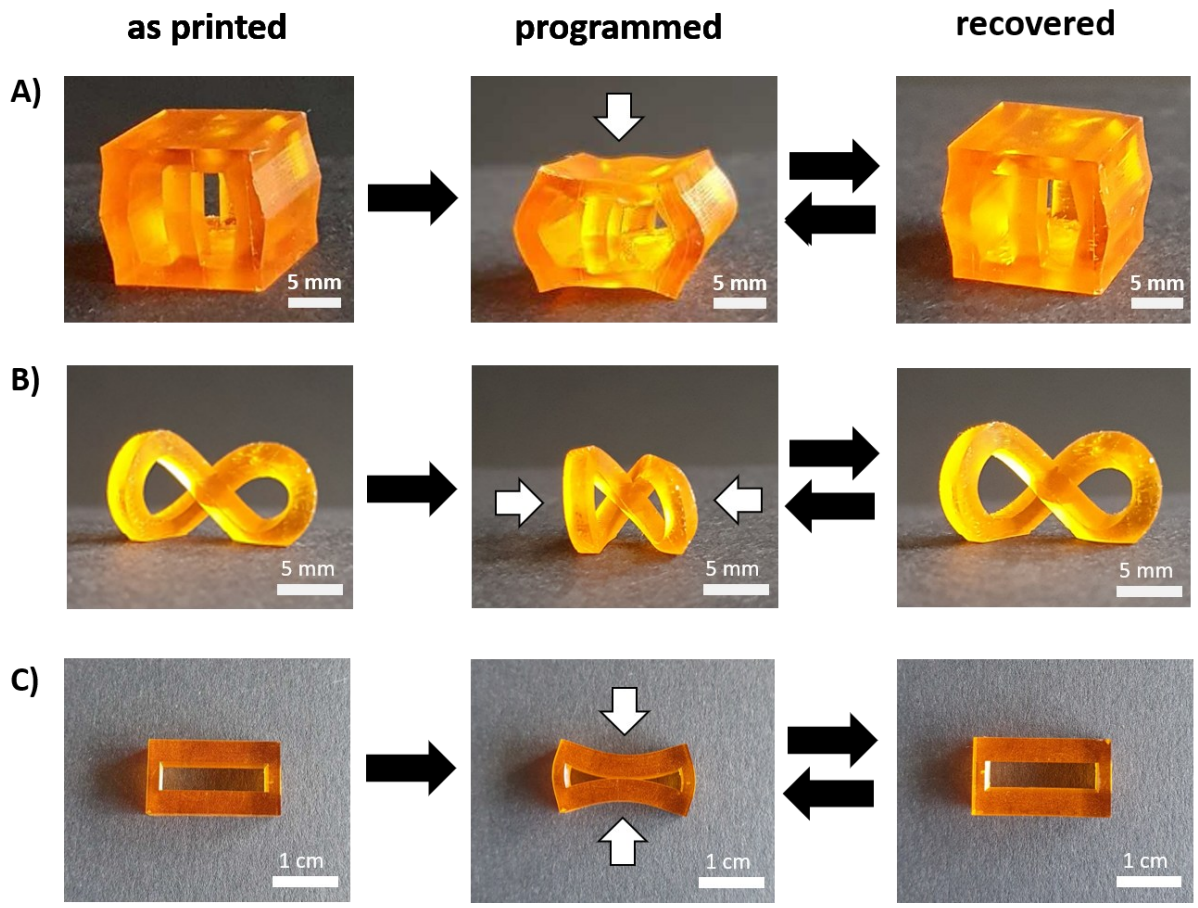

Figure 3.6 Qualitative shape memory tests at the macroscale. Images of the 4D printed geometries including A) a double platform, B) a infinity ring and C) a frame in their initial shape, temporary shape and recovered shape. All structures were programmed and recovered in preheated water at 80 °C and fixed in water at rt. Adapted from reference [210].

shape recovery permitting to have the infinity ring in its recovered, initial shape inside the glass bottle. As visualized in Figure 3.7 the recovered infinity ring is trapped inside the vessel, similarly to a decorative ship in a bottle. The SME process including successive programming, fixation and recovery steps was repeated seven times applying the same printed structure without any loss in its initial dynamic properties and structural damage observable, proving the repeatability of the SME without performance drop. Based on these results the feasibility of an even higher number of SME cycles can be expected.

Up to this point shape recovery was conducted for all experiments in hot water above T_g. To demonstrate the possibility of SME under dry conditions, showing the application flexibility in terms of environment, recovery of the 3D printed frame structure was conducted by heating the geometry above T_g applying hot air. Repeating the programming and fixation procedure described before the frame was deformed in a water bath at 80 °C and fixed in water at rt. Recovery was conducted this time by heating the structure above T_g inducing in this way complete and fast recovery. The process of recovery initially monitored as movie is depicted in form of a sequence of images at different points in time in Figure 3.8.

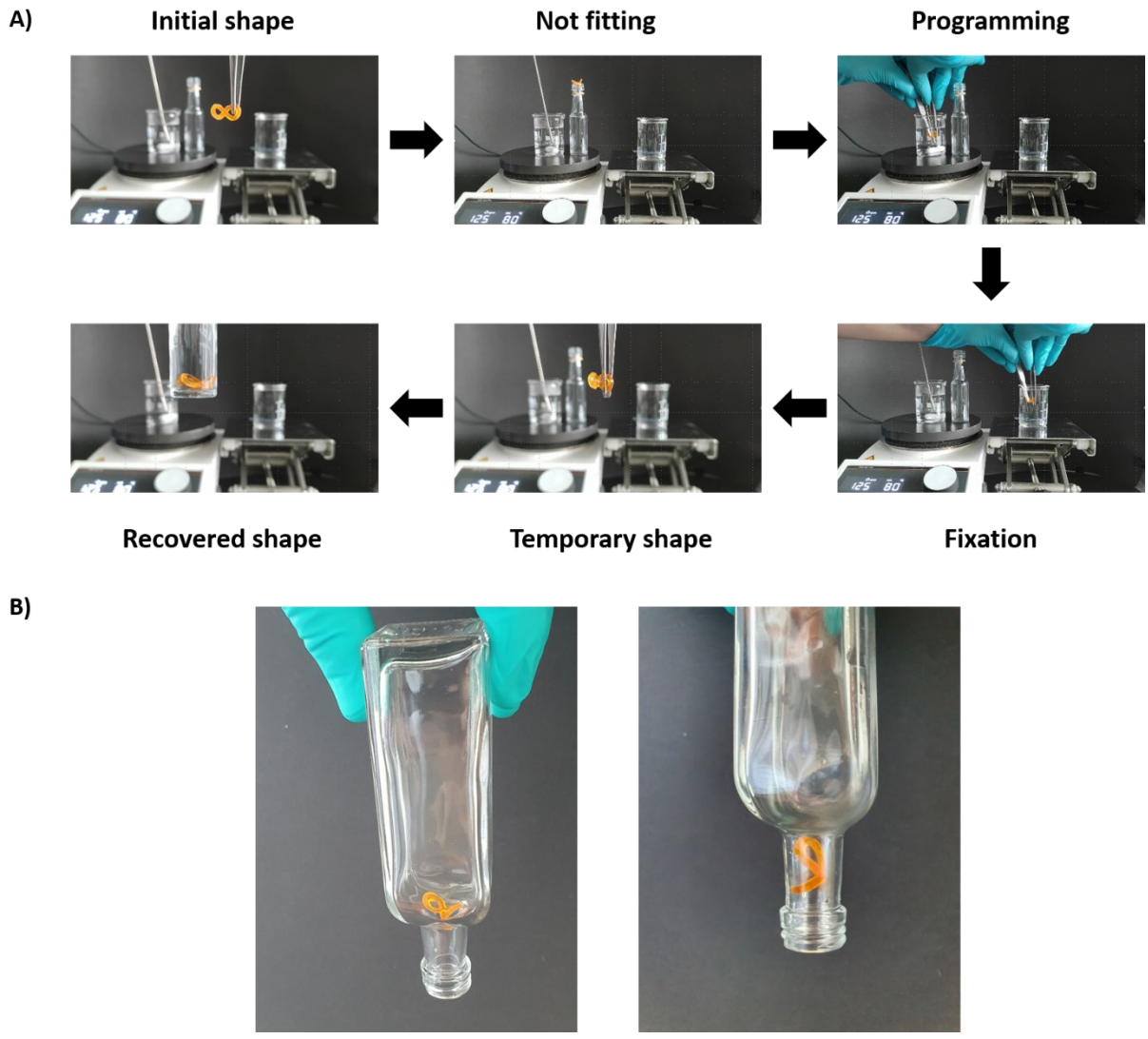

Figure 3.7: Depiction of the ship in the bottle problem and its solution via application of the thermally induced SME. A) Shape memory procedure to place the infinity ring structure inside the bottle. B) Permanent shape of infinity ring is trapped inside the bottle.

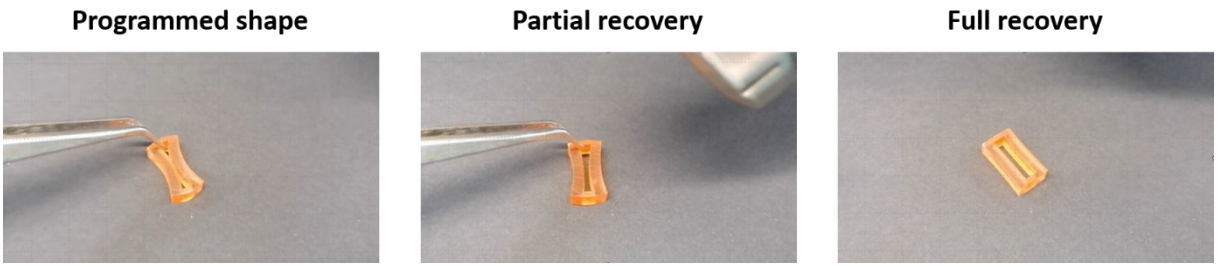

Figure 3.8: Recovery process of the frame structure in air – outside water – employing a heat gun to heat above transition temperature activating in this way full recovery of the initial shape.

3.2.3. 4D printing of Shape Memory Polymers at the Microscale

3.2.3.1. Adaption of the Formulation towards 2PLP microprinting

After successful design and development of an SMP ink formulation that shows excellent printability by DLP at the macroscale as well as remarkable SME properties, the focus was turned towards the microscale, more precisely the microfabrication of dynamic SMP geometries via 2PLP. Importantly the formulation needs to be slightly adapted to fulfill the requirements allowing optimal 3D structure fabrication via 2PLP at the microscale. These specific requirements are based on the differences between DLP and 2PLP in regard of technology and the physical absorption process employed for microprinting. In contrast to the macroscale, 2PLP uses a femtosecond pulsed near-infrared laser featuring a wavelength of 780 nm that scans rapidly – in a range of thousands of micrometers per second – through the resin solidifying the liquid ink within this short timeframe of interaction for 3D microstructure generation. The whole process is based on the quite improbable process of initiation via two-photon absorption. Besides usage of a photoinitiator suitable for TPA, a sufficient high density of photopolymerizable groups per volume must be present within the ink to enable fast and successful microfabrication. The simplest way to achieve this is the direct increase of the mol% of crosslinker within the ink. However, the ratio of crosslinker portion to monofunctional monomer portion must be carefully adjusted and tested. To high amount of crosslinker within the ink would improve printability drastically but remove the SME from fabricated 3D microstructures, rendering them static. Too low crosslinker content lowers 3D microprinting performance drastically up to nonprintability of the ink. Similar considerations must be taken in account for the ratio of flexible and stiff crosslinker within the total crosslinker amount. To high content of flexible crosslinker PEGDA 575 removes any shape fixation property from the 3D microstructures, generating material in the rubber state. In contrast higher contents of stiff crosslinker TccdA result in nondynamic structures, featuring no or insufficient recovery property during the SME cycle, due to majorly non-entropic plastic deformation during programming. Considering all these points the mol% of crosslinker was increased in a first step and the ratio between flexible and stiff crosslinker optimized in the second step. In particular, a crosslinker and monomer mixture consisting of IsobA (50 mol%), PEGDA 575 (20 mol%), and TccdA (30 mol%) was employed (see Figure 3.9). The ability of two-photon based photoinitiation was incorporated by addition of BAPO (2.2 wt%), a photoinitiator suitable for linear one-photon absorption and nonlinear two-photon absorption as explained in the prior section. Notably, in comparison to the macroscale formulation, the microscale ink misses any additional monofunctional monomer such as HexA or additives such as Sudan I. HexA was excluded from the microformulation based on two reasons. First further inclusion of monofunctional monomer into the mixture at the cost of crosslinker content reduces the density of

photoreactive groups and thus the printability via 2PLP. Furthermore, HexA lowers the viscosity of the ink. As this consequence is favorable for macroscopic 3D DLP printing, as shown by many examples where application of a reactive monofunctional diluent was applied, successfully visible in the prior chapter, higher viscosities are in general favorable for 2PLP microfabrication. Exclusion of photoabsorbing additives such as Sudan I can be reasoned by the inherently present high resolution offered by 2PLP, making employment of photoabsorbers in general unnecessary.

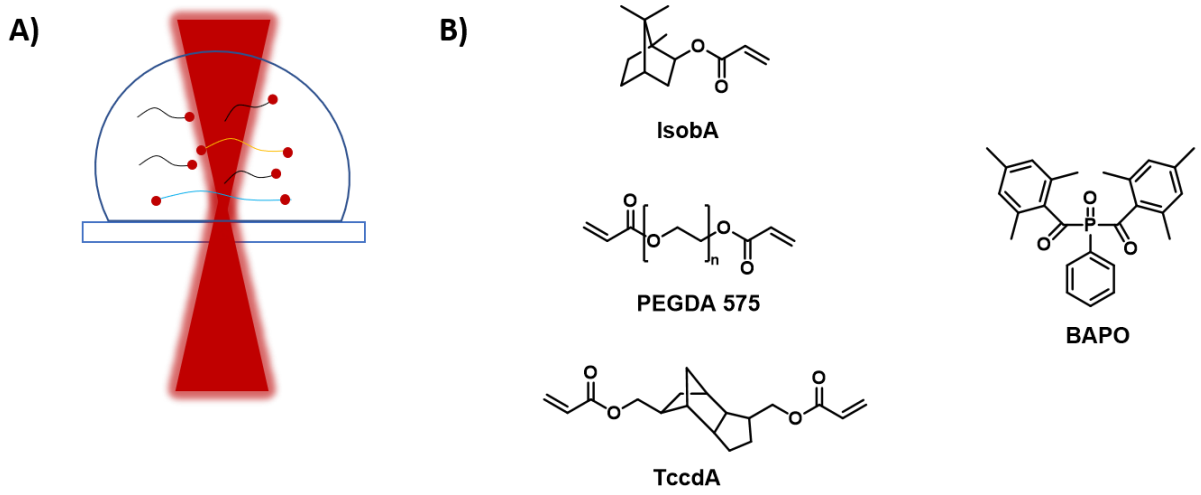

Figure 3.9: Designed SMP formulation applicable for 2PLP at the microscale. A) Scheme of a 2PLP laser focus curing process: A femtosecond pulsed laser is tightly focused within a droplet of SMP ink. Curing occurs within the focus allowing high-resolution 3D printing. B) Components of the formulation for 3D structure fabrication at the microscale: IsobA, PEGDA 575, TcddA, Irg819. Adapted from reference [210].

3.2.3.2. 3D Fabrication via 2PLP

In the next step the prior presented and discussed ink formulation for SMP microstructure fabrication was applied for 2PLP-based 3D microprinting utilizing a commercial two-photon laser printing device with a central wavelength of 780 nm. After careful parameter screening and subsequent optimization, adequate 3D microprintability was obtained for average laserpowers in the range of 19.5 to 22.5 mW and a scanspeed of 1000 µm s^{-1}. In the next step quality of printing parameters and microink formulation was tested by 3D fabrication of a range of distinct microstructures. Mirroring the wide range of macrostructures printable using DLP, a variety of microstructures featuring distinct levels of complexity was successfully printed (see Figure 3.10). Ranging from the micrometric version of the double platform structure, designed with STL model dimensions of 20 x 20 x 18 $µm^3$, over to a box like structure, resulting from a self-made STL model with area dimensions of 20 x 20 $µm^2$, a box wall height of 8 µm and a lid height of additional 15 µm, to the microscopic version of the infinity ring featuring in its STL design a length of 20 µm and a height of 15 µm, several structure types were fabricated applying prior presented parameter values for laser power and scanspeed. Remarkably 3D structure manufacturing of complex parts such as the large freestanding parts of the double platform structures

or the overhanging rather delicate structural moieties of the infinity ring were manufacturable without appearance of visible structural collapse after development. Furthermore, all structures exhibited smooth and defect-free surfaces of exceptional quality, which is an obvious sign for the absence of microexplosions respectively microbubbles during the microfabrication process within the range of employed optimized fabrication conditions. Especially this point gives evidence for the high stability and compatibility of the microink formulation towards 2PLP-based microprinting.

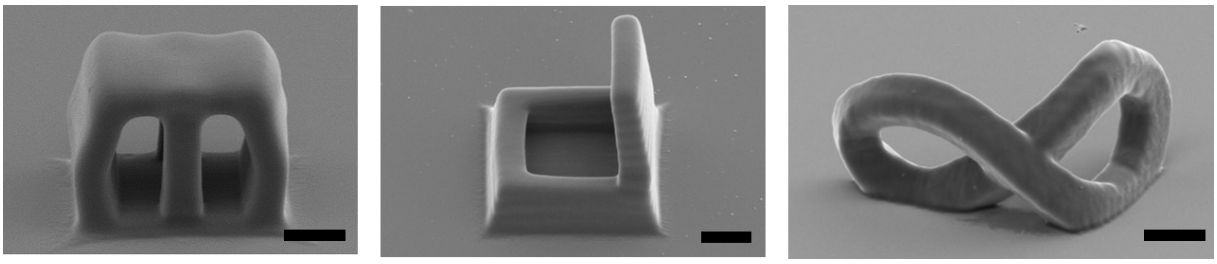

Figure 3.10: Scanning electron microscope (SEM) images of fabricated microstructures via 2PLP including a double platform structure, a box-like geometry, and an infinity ring (left to right). Scale bar corresponds to 5 µm. Adapted from reference [210].

3.2.3.3. Evaluation of Network Transition Temperature

After successful design and adaption of the microscale ink formulation for 3D manufacturing via 2PLP the next step involved the evaluation of the T_g of printed microstructures, equivalent to the transition temperature of the amorphous network. As explained in the prior section, DnMA was identified as suitable characterization method for both macro- and microscale, bridging both worlds not only in terms of core ink components but in terms of analytics too. Especially at the microscale this analytical method is an often-made choice for viscoelastic characterization of thin polymeric films, however, usage in case of microstructures was already reported too, as discussed in the theoretical and background part of this thesis. Another additional advantage of this approach is that T_g data can be obtained directly from printed structures at the microscale, a regime for which other methods are rather limited in their applicability. Usually deployed methods such as differential scanning calorimetry (DSC) or standard dynamic mechanical analysis are apparently not suitable owing to the low amount of effectively polymerized material offered by 2PLP microfabrication and the micrometric dimensions in the targeted size regime. Performing viscoelastic characterization via the DnMA-based measuring approach at the microscale, a similar model was used as for the macroscale and the viscoelastic properties of the microstructures were directly obtained. Specimens used for the microanalysis were cylindrical shaped pillars with dimension of 10 µm for the diameter and 20 µm for the height. This structural design allows to exclude structural effects that possibly distort measured values and thus inhibit inclusion of systematic errors based on the geometry itself. As result of the viscoelastic characterization values of storage modulus, loss modulus and tangent delta were obtained in a

temperature range between 20 and 50 °C in steps of 5 °C for 3D pillars printed at three different average laserpowers – 21.5 mW, 22.0 mW and 22.5 mW (see Figure 3.11).

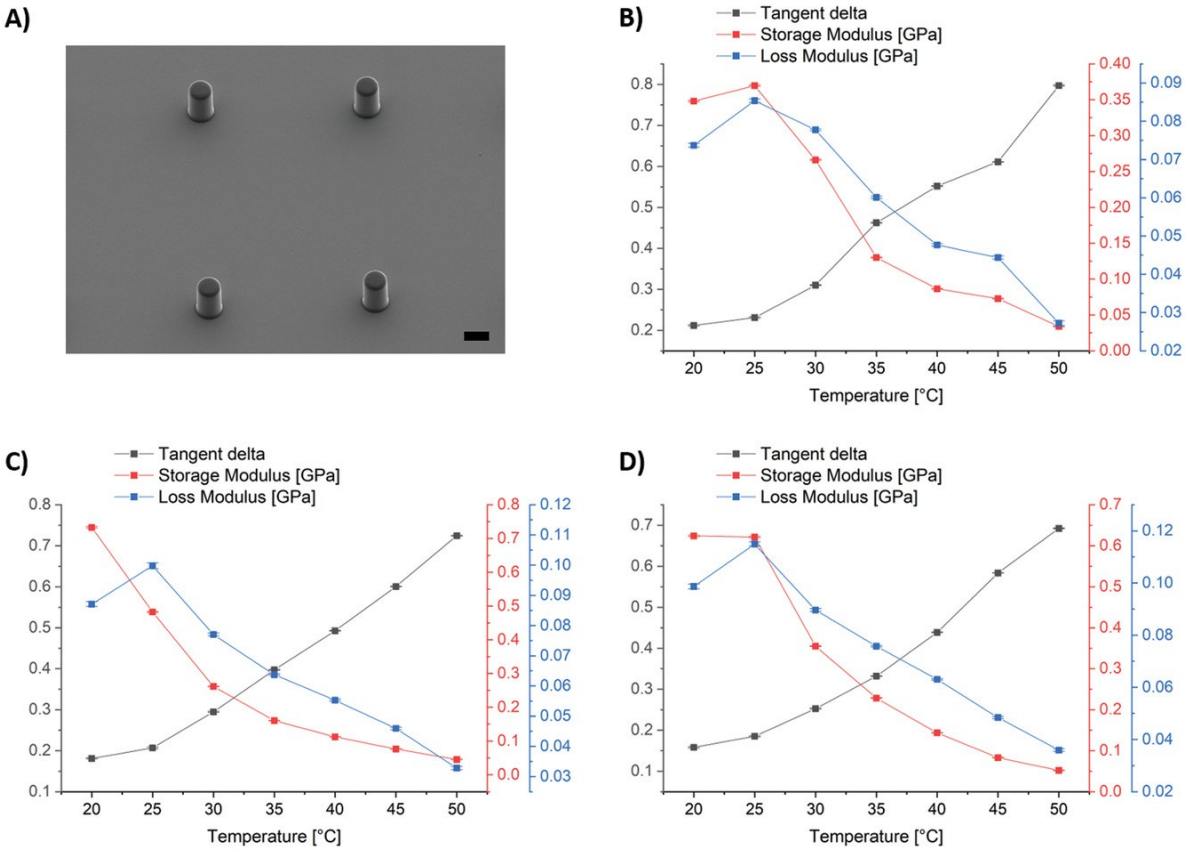

Figure 3. 11: Viscoelastic characterization of the 3D printed microstructures by DnMA via nanoindentation. A) SEM image of a cylindrical test structure (diameter: 10 µm, height: 20 µm). Scale bar corresponds to 10 µm. Measurements were performed on samples fabricated at different laser powers including B) 21.5 mW, C) 22.0 mW, and D) 22.5 mW. Values of tangent delta, storage modulus, and loss modulus are depicted within a temperature range from 20 °C to 50 °C for each measured sample. Error bars represent standard deviation n = 360. Adapted from reference [210].

Samples prepared with all three power conditions exhibited a strong decrease in storage modulus associated by a growth of tangent delta with increase in temperature. Maxima of the loss moduli, conforming to the glass transition region of the microstructures were found around 25 °C for analyzed 3D structures of all employed laserpowers. Notably, the T_g values obtained for the microstructures were distinctly lower than those evaluated for the macrostructures. The higher amount of soft PEGDA 575 crosslinker in the microformulation might be one of the reasons, because it is well-known to have an effect on the mechanical properties of the materials, in particular reduction of T_g. Furthermore, the lower portion of IsobA, known for its formation of high T_g homopolymers, in the microink might be seen as another reason for the lowering in the resulting T_g of the whole amorphous network.

During viscoelastic characterization material behavior directly correlated to the measured values for T_g was found by observation of the measurement process via the internal optics of the nanoindentation device. By performing indentations below T_g a pyramidal imprint was visible after measurement,

caused by a plastic material deformation in the glassy state. In contrast, for indentations conducted above evaluated T_g no imprint or deformation was identifiable on the surface of the pillars after indenter tip removal and associated stress release, proving the material's presence in an elastic rubbery state permitting immediate structural recovery.

3.2.3.4. Shape Memory Effect at the Microscale

Based on the obtained knowledge about the T_g of the micromaterial successive investigation of the shape memory effect at the microscale was possible by application of the already described three-step shape memory cycle procedure composed of programming, fixation, and recovery. However, changing from macroscale to microscale renders proof of the shape memory effect rather challenging, making direct application of the methodology employed at the macroscale unsuitable. Considering the microdimensional structure two challenges necessary to be solved arose during development of an appropriate micro shape memory test methodology. Programming by shape manipulation must be performed in a facile but precise enough way, without damaging microstructures or entirely destroying them. Another point is the monitoring of the transformation from the temporary shape back to the initial shape during the recovery step. Apparently, structural changes within the small dimensions offered by 2PLP fabricated microstructures cannot be followed by naked eye making observation by microscopy – optical microscopy or scanning electron microscopy (SEM) – obligatory. Furthermore, a suitable device allowing precise temperature control is necessary, to gain more insight into the temperature-induced recovery response.

In the end an appropriate methodology captivating due to its simplicity was developed to perform shape memory tests at the microscale. For programming a simple metal block was employed to produce the necessary stress to deform the microscopic structures in their rubber state. Here special attention was paid to polish the sides of the metal block used for programming – meaning the sides in direct contact with the microstructures during the SME tests – as homogeneous as possible. In particular, the substrate containing the microstructures in their initial shape were heated above transition temperature inside a heating oven together with the metal block. Programming was performed by carefully placing the hot block at temperatures above T_g onto the microstructures, compressing – programming – them through stress induced by the blocks own weight. Subsequent fixation was performed by cooling down to rt – below T_g and successive cautious removal of the block. Inspection of the temporary shape was performed by observation of the deformed microstructures under the optical microscope. Importantly, shape memory recovery was induced in a controlled way by heating the microstructures inside a heating stage above T_g while monitoring the recovery process in situ utilizing an optical microscope.

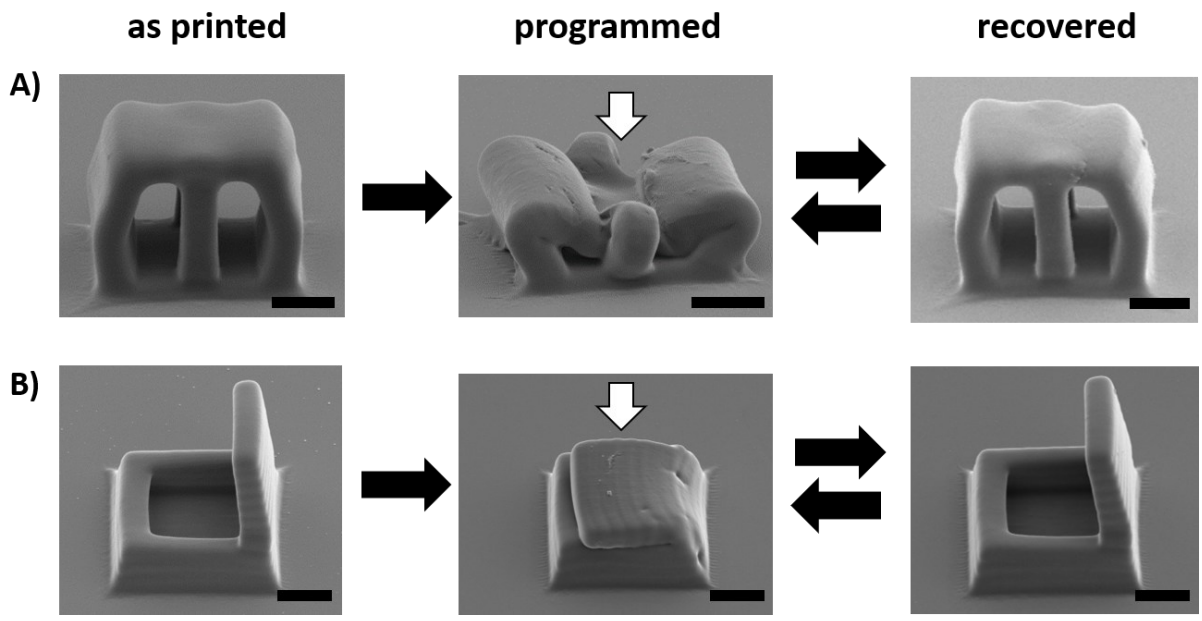

Figure 3.12: Shape memory effect of 2PLP fabricated geometries at the microscale. SEM pictures of A) the double platform structure and B) the box-like structure as depicted in their as printed (initial) shape, programmed shape and recovered shape. The scale bar corresponds to 5 µm. Adapted from reference [210].

Above presented procedure was applied on the double platform structure and the box like structure, considering their advantageous laterally visible deformation in response to axially applied stress. Structural changes between initial, programmed and recovered shapes were in this way perfectly observable via optical microscope. Additionally, initial, programmed, as well as recovered shapes of both geometries were inspected by SEM gaining a better 3D visualization of the structural quality after each of the processes (see Figure 3.12 A and B). Inspecting the temporary shape, it is evident that the micromaterial shows excellent deformability at the rubber state, apparent for instance by the possible bending of the microlegs of the double platform, without any visible structural damage in the temporary and the later recovered shape. Notably, despite the low transition of the polymeric network, programmed microstructures showed no sign of undesired recovery after block and thus stress removal at rt resembling the excellent temporary shape fixing performance at the macroscale. Remarkably, direct comparison between initial and recovered shape exhibited hardly any differences, better said both states are almost perfect copies of each other, being indicative of an excellent SME, mirroring qualitatively the quantitative and qualitative results obtained at the macroscale.

The recovery process was further investigated in detail by prior mentioned setup combining a heating stage for precise temperature control and an optical microscope for shape recovery monitoring. Figure 3.13 illustrates image sequences of recorded movies showing the recovery of the double platform geometry (Figure 3.13 A) and recovery of the box-like structure (Figure 3.13 B). The temperature shown on the individual images of a sequence conforms to the temperature readout of the heating stage. Starting with the compressed temporary shape, the double platform geometry feature

previously mentioned excellent deformability of the rubber state by outside bending of the four "microlegs". During the recovery process all four legs bend perfectly back to their initial position, indicating the raising of the upper platform towards the shape of the initial state. In case of the other structure employed in shape memory tests, the box-like microstructure, programming, and fixation resulted in a closed box as temporary shape. However, by comparing its recovery process to the recovery of the double platform structure it was evident that geometry plays a role in the nature of the recovery in terms of speed and necessary applied temperatures. In case of the first geometry (double platform), the recovery appears to be very abrupt as soon as it starts. Contrastingly, opening of the smart box's lid was induced at lower temperature and the recovery seems to be slower. Such a geometry dependency was less apparent for the fabricated structure at the macroscale.

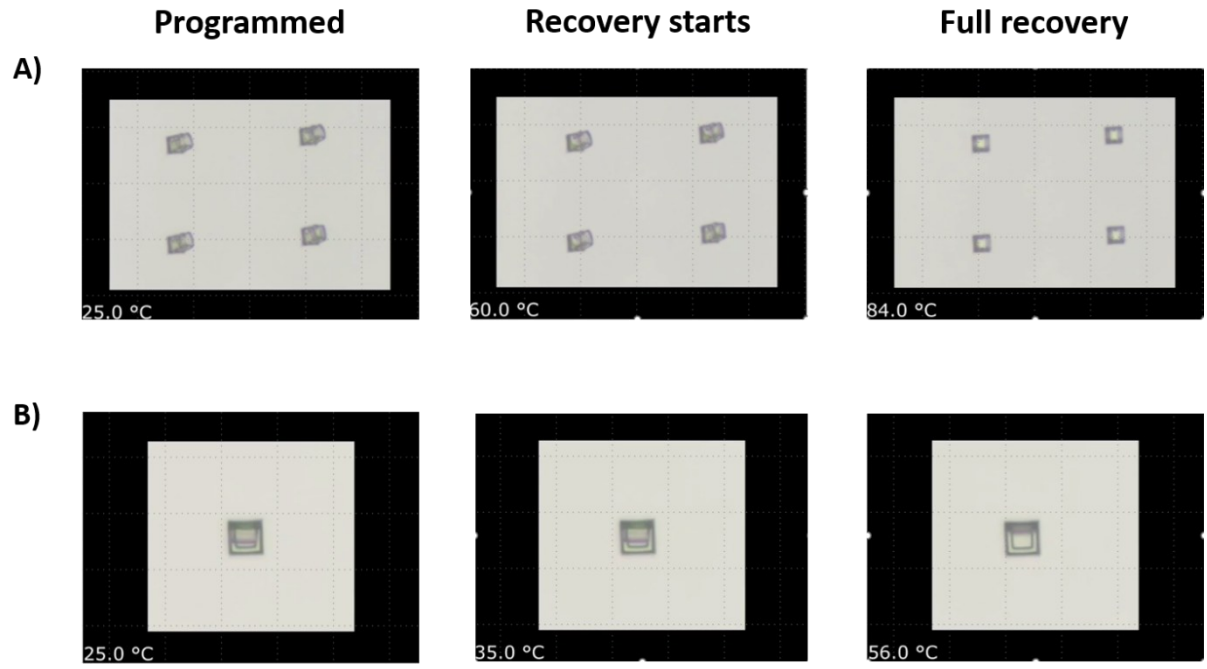

Figure 3.13: Optical microscope images of A) double platform structure and B) smart box in the programmed state, at the point when recovery starts and at the point when full recovery was reached. Experiments were performed inside a heating stage and monitored during microscopic observation.

To illustrate the stability of presented shape memory process at the microscale, a substrate was prepared containing a larger entity of double platform structures printed close to each other. Images of their initial, temporary, and recovered state were recorded by optical microscopy and presented in Figure 3.14. Recognizably all structures show superior programmability and fixability of the temporary shape, indicative for excellent deformation properties at the rubber state. All structures bent back to their initial state during recovery, underlining the extreme stability of the designed SMP micromaterial in terms of SME. Importantly this process was repeatable for several times. The only limitation concerning repeatability was the metal block addition and removal by hand during programming and fixation. Here small motions caused by shivering of the hand might lead to structural damage.

However, future experiments using a more precise method for programming, for example a micromanipulator in combination with a SEM and a heating stage, will allow to circumvent this issue.

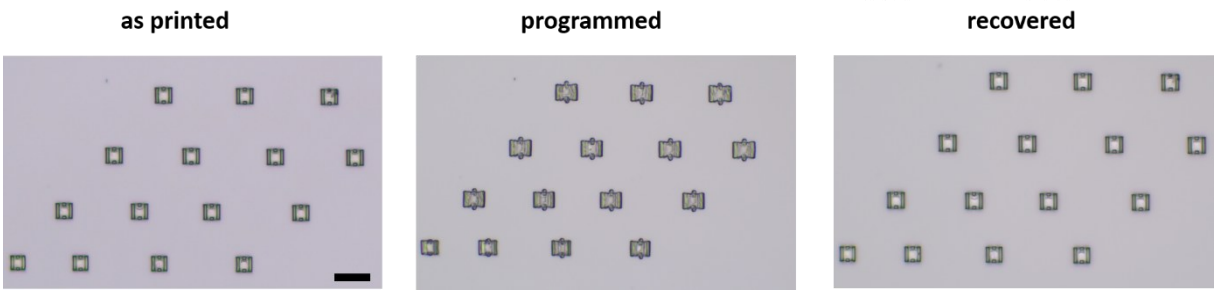

Figure 3.14: Optical microscope images of a larger entity of double platform structures in their printed initial shape, their temporary shape after programming and their recovered shape after successful performance of a shape memory cycle. As visible all structures recovered, pointing out the process stability of the SMP material.

To demonstrate the functionality and versatility of the presented microsystem, we employed the thermal actuation to generate a smart box permitting size-selective entrapping of microparticles (see Figure 3.15). To be more precise we applied the box-like microstructure for trapping of poly(styrene-co-divinylbenzene) microspheres (6.0 – 10.0 µm). Trapping of microparticles was done in this process by simple deposition of a microsphere-loaded suspension onto the structures. After solvent evaporation, the filled smart box was closed by programming the lid to a closed state using the mentioned programming procedure, resulting in spatially trapped microspheres inside. Utilizing a suitable temperature stimulus, the lid was openable on demand allowing controlled release of the microspheres.

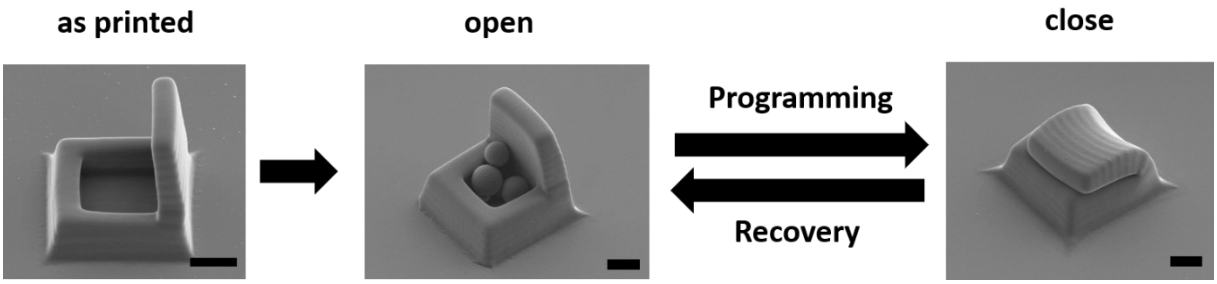

Figure 3.15: Functional smart box suitable for size selective trapping of microspheres. The printed structure was first filled with microspheres of suitable dimensions. By programing and recovery, the box can be closed and opened on demand. Adapted from reference [210].

3.3. Summary

A novel and versatile shape memory ink system appropriate for 4D printing at the macro- and microscale employing DLP and 2PLP 3D printing methods was developed. In a first step a functional system based on a monomer component, a dual system of soft and stiff crosslinker and a suitable phoinitator was designed, meeting all the requirements for printing and SME actuation at the macro- and microscale. In particular the system was composed of isobornyl acrylate as chain builder, poly(ethylene glycol) diacrylate (M_n = 575 g mol^{-1}) as soft crosslinking component, tricyclo[5.2.1.0^{2,6}]decanedimethanol diacrylate as stiff crosslinker and phenylbis(2,4,6-trimethylbenzoyl)phosphine oxide a photoinitiator suitable for linear one-photon absorption and nonlinear two-photon absorption, fulfilling the requirements for successful initiation in terms of absorptive properties at the macro- and microscale simultaneously. In the next step this functional system was adapted and optimized for both printing methods in terms of component ratios and additional additives, finally resulting in a macroink formulation applicable for DLP and a microink formulation for 2PLP. Subsequent parameter screening and optimization of these formulations utilizing the associated printing method allowed 4D printing in excellent quality, obvious by the range of structural types printable at both regimes. Employing DLP, a variety of 3D geometries spanning a range from simple strips and frames, to more demanding double platform structures or infinity rings as well as highly complex cubic grid structures, was fabricabe in the centimeter regime. Efficient high-resolution 3D macroprinting was realized, apparent from achieved layer heights of 50 and 100 µm at fast building speeds. In case of 2PLP microscopic versions of the double platform structure and the infinity ring were fabricable with high scanning speeds of 1000 µm s^{-1} offering high structural quality. After adjustment and optimization of formulation and printing parameters at both size regimes viscoelastic characterization was performed on specimens at both scales by DnMA, permitting access to glass transition temperatures (T_g), the transition temperature of the shape memory effect for these materials. In particular, a T_g around 70 °C was evaluated for macroscopic specimens, whereas the test samples at the microscale featured a T_g in the range of 25 °C. Especially the lower T_g might be attractive towards potential applications, that need rather low actuation temperatures. Notably excellent shape memory effect properties were proved for all printed 3D structures at both size regimes.

Comparing the present system to other reported systems at the macroscale, the above presented formulation is comparable with recently reported SMP systems in terms of printing behavior and shape memory effect quality. However, at the microscale the designed formulation is superior in terms of applicability and accessibility compared to other reported 2PLP SMP formulations that are limited by previously described issues: i) it is possible to print real 3D structures featuring complex overhanging features; ii) no synthetic efforts are necessary to generate the ink component or to render the ink

components printable – excluding no part of the 4D community from application of the presented system. All applied components are commercially available and in the lower price segment in case of both size regimes. Additionally, preparation of both inks solely includes simple mixing of their components by stirring them at rt. Both factors facile accessibility drastically; iii) in terms of curing conditions structures were fabricable within an acceptable range of laser powers; iv) 3D microstructures were fabricated in high quality obvious by smooth surfaces lacking any sign of defect or damage from the uncontrolled curing processes; v) the shape memory process can be activated under ambient conditions in air in response to a suitable temperature stimulus too.

Concluding this part all prior presented criteria were fulfilled by above presented system. In addition, the designed basic ink system allows for the first time printing in both size regimes – the macro and microscale – attempting in this way an interdimensional “bridging” in regard to the material.

Chapter 4

4D Printing of Light Activated Shape Memory Polymers with Organic Dyes

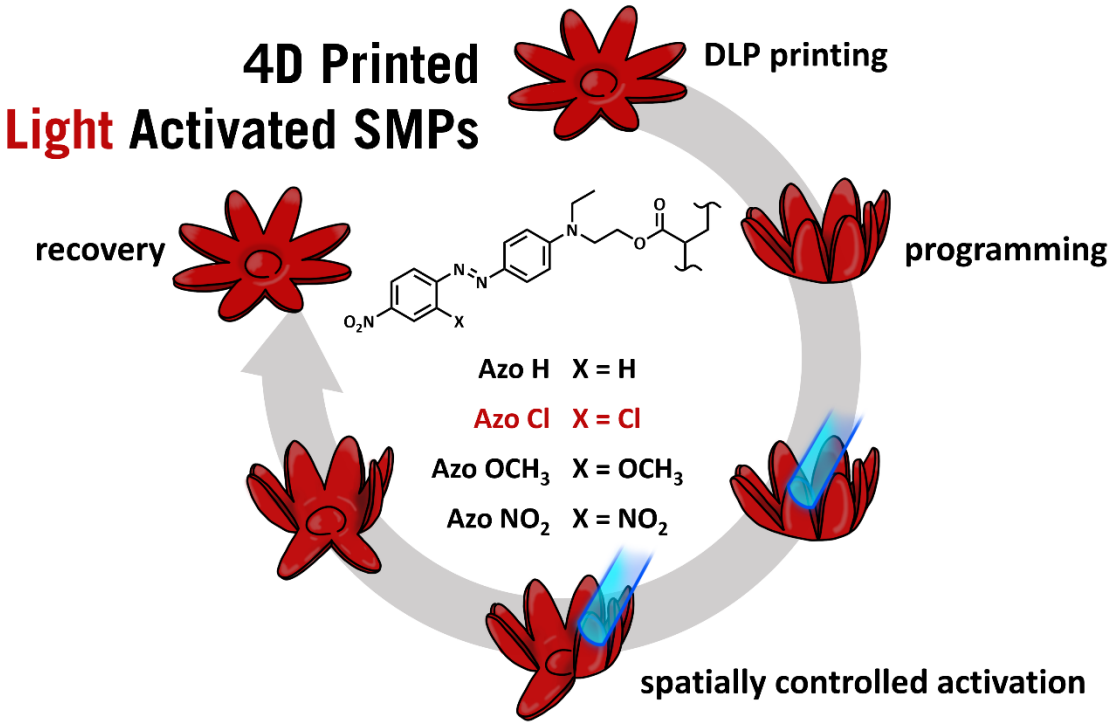

Figure 4: Adapted from reference [212]. Permission by Royal Society of Chemistry.

Towards spatial control

4.1. Motivation and Aims:

In the previous chapter I introduced a novel shape memory printable system showing a thermally induced shape memory effect. However, one major disadvantage of the stimulus temperature is the lack of precise control during actuation – recovery – limiting the wider application of one-way shape memory polymers drastically. As explained in the theoretical part of this thesis, one approach to overcome this issue is the introduction of light as stimulus to induce responsive behavior, giving permission to a high level of spatial control during actuation. In case of materials featuring a thermally induced shape memory effect, it is better to describe it as translation of the responsive stimulus temperature to light, because the effective stimulus remains in this case temperature. The only difference is that through addition of suitable functionalities towards a printable formulation energy provided by light irradiation is translated within the material to heat, overcoming in this way the transition temperature, either a melting point or a glass transition temperature. Such a "translation" approach has been already applied as pictured in the chapter 2, however, in most cases it was achieved by incorporation of inorganic fillers and additives. Application of such chemical moieties in functional materials rises questions of biocompatibility and long-term material performance due to non-covalent incorporation into the network and thus the possibility of continuous removal of functional units during washing processes or applications in liquid environments. One promising alternative to inorganic fillers and other additives is the usage of organic dye compounds such as azo-dyes, able to convert absorbed light-based energy by thermal relaxation after prior excitation. Importantly azo-dyes have shown further advantages through their facile and straightforward preparation and chemical functionalization, allowing in principle synthetic attachment of photopolymerizable functionalities. Enabling in this way incorporation of such functionalized azo-dyes into the polymeric network during the light-based printing process would circumvent prior described disbenefits of non-functionalized inorganic fillers and additives. Furthermore, azodyes are often applied in macroscale vat photopolymerization, especially in SLA and DLP 3D fabrication, as photoabsorbers in inks, permitting access to highly resolved 3D macrogeometries and controlled curing processes.

Thus, my aim here was the incorporation of such functionalized organic dyes into smart 3D printable materials such as shape memory polymers to allow: i) incorporation of a light-based SME into the network associated with the feature of spatial control and all its advantages concerning applicability for instance more accessible temporary states during the recovery process as well as ii) the inherent ability of the ink formulation to produce high precision structures during macrofabrication due to mentioned photoabsorbing effect of the functionalized dye molecules (see Figure 4.1). Based on its simplicity, flexibility, and reliability such a SMP macroink system featuring above mentioned properties

would open new opportunities in a wide range of promising fields such as soft robotics, actuators, or smart sensing applications.

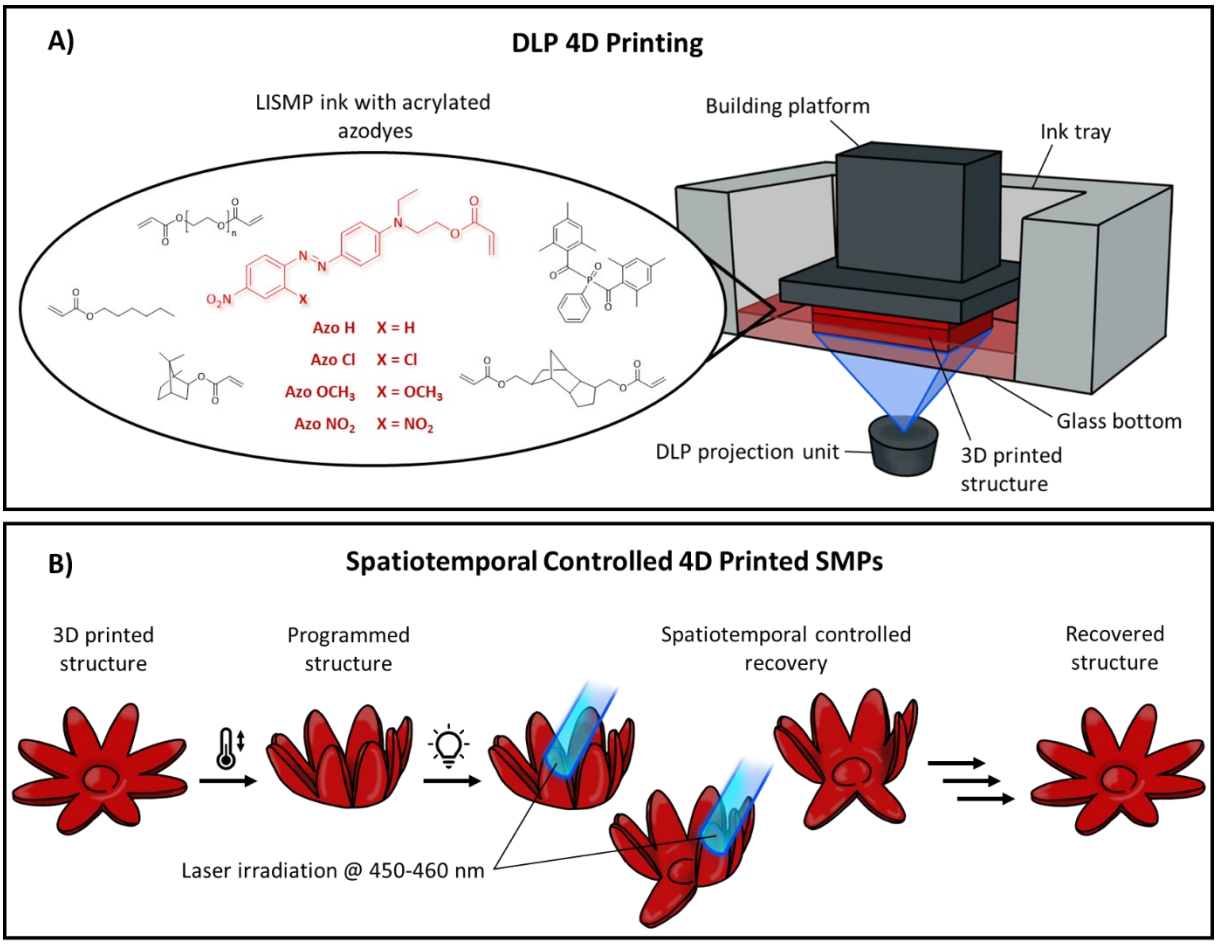

Figure 4.1: General concept of 4D printing of light activated shape memory polymers including: a) DLP printing of a ink formulation based on an acrylate-based SMP ink including photopolymerizable azo dyes, and b) the light induced shape memory cycle of DLP fabricated geometries including a temperature-initiated programming step followed by spatiotemporal controlled light induced recovery. Adapted from reference [212]. Permission by Royal Society of Chemistry.

4.2. Results and Discussion:

4.2.1. Identification of a suitable Light-Responsive Functionality

In a first step suitable photoresponsive moieties are identified permitting suitable photothermal properties as well as the possibility of easy synthetic incorporation of photopolymerizable units, in particular acrylate functionalities, accessing in this way 3D fabricability via light-based methods such as DLP. For this purpose, push-pull azo-dyes were identified and selected as ideal photoresponsive units. As explained before, their functional role in the SMP ink is two-fold: I) enhancing the resolution during the process of 3D fabricability permitting high-quality printing in terms of resolution and minimal feature size and II) incorporation of the ability to perform light activated shape changes during

the recovery process of the shape memory cycle, translating in this way the stimulus temperature to the stimulus light. After final decision for this class of compounds a selection of acrylate functionalized push-pull azo-dyes, containing different functional groups was first synthesized (synthetic procedures described in the Experimental part of this work). In particular different functional groups including a hydrogen, a chlorine, a methyl ether and nitroxide functionality were introduced in ortho position with respect to the diazo functionality. Incorporation of these additional functionalities allows to control and tune the photochemical properties through steric or electronic effects, offering a selection of different compounds to reach the optimum in the later 3D printing and light induced shape memory processes by choice of the best performing molecule. Further, acrylate functionalization of each compound allows direct incorporation of the functional unit into the polymeric network and thus fixation of the amount of photoresponsive moieties within the network by covalent carbon-carbon bonds. Thus, quality of light response performance should not be reduced during washing steps or by programming, fixation, or recovery steps in liquid environments, because possible leaking of photoresponsive units is inhibited. Furthermore, necessary absorbance in the visible range of 400 nm to 600 nm was approved by absorbance spectra (see Figure 4.2), enabling easy access to a light stimulus suitable to induce photothermal conversion of energy – and thus shape memory recovery actuation – as well as harmless irradiation condition. Importantly no interference with the 3D curing wavelength at 385 nm in terms of absorption was determined from the absorbance data obtained.

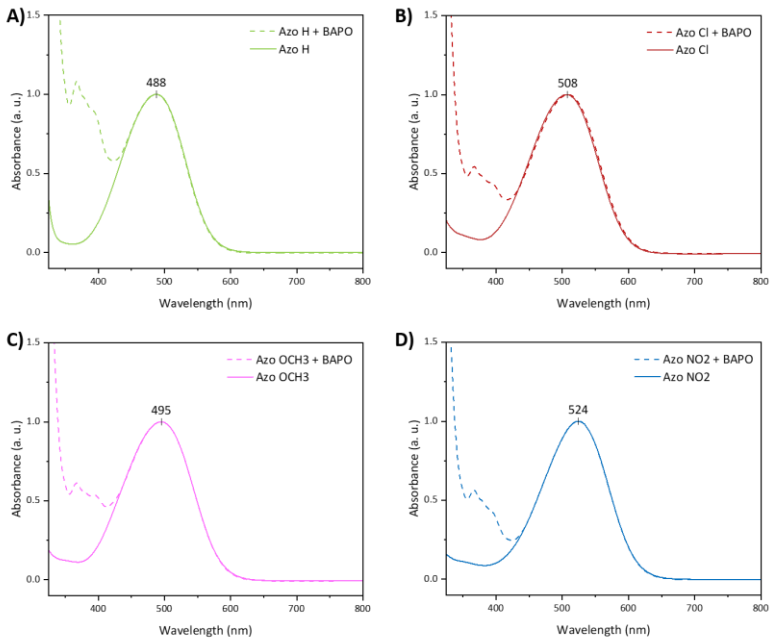

Figure 4.2: Normalized UV-Vis spectra of the four synthesized acrylate-functionalized azo-dyes. The absorption spectra were measured in ethanol, alone (0.1 wt.%) as well as in mixture with photoinitiator BAPO in a concentration of 2 wt.% conforming to later concentrations employed in the ink. Strong absorption behaviour is observable within the Vis range of 400 nm to 600 nm, whereas no significant absorption was visible in the curing wavelength range about 385 nm. Adapted from reference [212]. Permission by Royal Society of Chemistry.

4.2.2. Ink Design, DLP parameter screening and Evaluation of Accessible Lateral Resolution

4.2.2.1. Design of Functional Ink for Digital Light Processing

After successful synthetic preparation of above described acrylated azo-dye compounds (for information about synthetic preparation see Appendix) their applicability in SMP inks was tested for 3D fabrication via digital light processing (DLP). For this purpose, the simplest strategy was reverting to the macroprintable SMP formulation – offering high-quality 4D structure fabricability as well as excellent shape memory properties – introduced in the previous chapter. In particular, this SMP-based system was composed of isobornyl acrylate (IsobA) as main component setting the transition temperature in form of the glass transition temperature (T_g) of the amorphous network, and a dual system of a soft and a stiff crosslinker. As soft crosslinker poly(ethylene glycol) diacrylate (M_n = 575 g mol^{-1}, PEGDA 575) was employed, for the hard crosslinking component tricyclo[5.2.1.$0^{2,6}$] decanedimethanol diacrylate (TcddA) was chosen. Additional small quantities of hexyl acrylate (HexA) were added, having mainly the purpose to improve deformability in the rubber state above transition temperature. Phenylbis(2,4,6-trimethylbenzoyl)phosphine oxide (BAPO) was added as photoinitiator suitable for the employed DLP curing wavelength at 385 nm. Departing from the original formulation the usage of Sudan I as photoabsorber was avoided as the now included azo-dyes are planned to acquire this position and function. Thus, the optimal concentration of azo-dye component in the light activated shape memory polymer (LSMP) ink was determined in the next step. To achieve this several ink formulations increasing in their content of azo-dye compound AzoCl from 0.1 to 2.0 wt% were prepared and the curing time for each sample was determined by polymerizing it under UV-LED irradiation in the wavelength range from 380 nm to 390 nm, mirroring the wavelength region of the DLP curing wavelength. The resulting curing times are summarized in Table 4.1. From obtained result it was obvious that higher azo-dye content result in longer curing times, since it acts as photoabsorber being in direct competition with the photoinitiator, reducing the number of available photons per unit volume usable for initiation. Finally, an azo-dye concentration of 0.1 wt% was selected as appropriate amount within the LSMP ink, not expected to affect the printing process in its efficiency drastically as visible by the fast-curing speed of 1.5 s, acceptable for fast and efficient 3D fabrication.

Table 4.1: Determination of the optimal concentration of the chlorine azo-dye compound in the LSMP ink. The LED irradiation time represented in the right column was determined for each azo-dye concentration individually. The LED irradiation time corresponds to the curing time necessary to complete photopolymerization under UV-light conditions (380-390 nm).

Cl-Azo-dye Concentration (wt%)	Irradiation time (s)
0.0	1.5
0.1	3.5
0.2	4.5
0.3	6.0
0.4	8.5
0.5	9.5
1.0	>15
2.0	>15

4.2.2.2. Parameter Screening and 3D Printing Performance

In the next step parameters for printing were carefully optimized for each of the inks including AzoH, AzoCl, $AzoOCH_3$ and $AzoNO_2$ with regard to layer thickness and curing time, targeting a precise and efficient 3D printing process. Performing material tests, values of critical exposure doses (E_c) and penetration depth (D_p) were determined from obtained Jacobs working curves evaluated at 10 mW m^{-2} (see Figure 4.3).

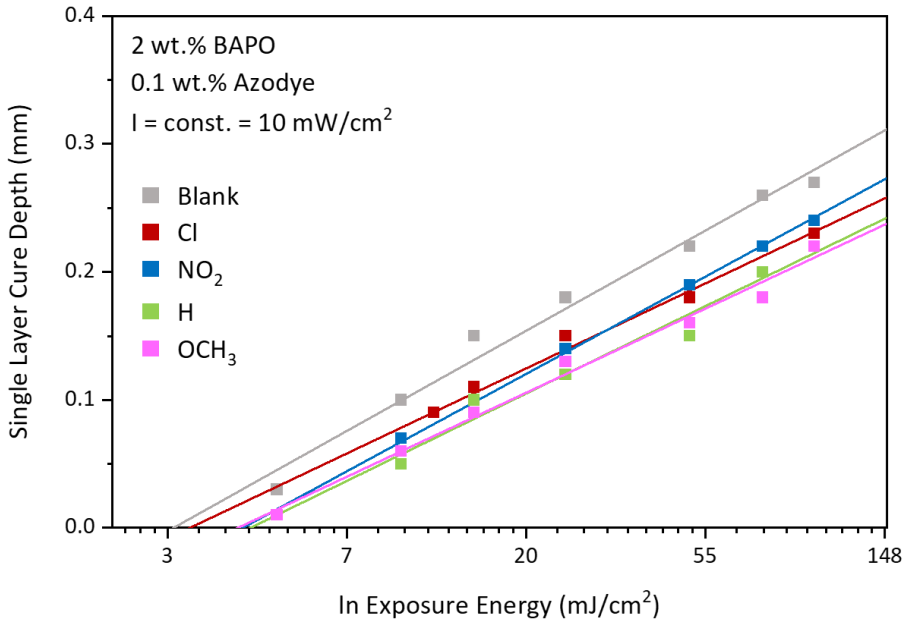

Figure 4.3: Jacobs working curve obtained from materials tests of inks including 2 wt % BAPO and 0.1 wt.% of the azo-dye compounds. A "blank" formulation containing no azo-dye was investigated for comparison. Adapted from reference [212]. Permission by Royal Society of Chemistry.

E_cs ranging from 3.08 mJ cm^{-2} for AzoCl-ink to 4.31 mJ cm^{-2} in case of AzoH-ink were determined as well as D_ps at about 0.07 mm for all azo-dye ink formulation. In contrast, the blank formulation exhibited an E_c of 2.81 mJ cm^{-2} and a D_p of 0.08 mm. These differences result from the absence of any photoabsorbing unit and the lack of competition with the photoinitator, allowing to reach the gel point of the ink at lower exposure dose values. Lower amount of photoabsorbing units consequently results in higher depths of penetration into the ink, explaining the slight difference. The excellent agreement of obtained experimental data is underlined by the high coefficient of determination (R^2) featuring values above 0.98.

From evaluated parameters including data of E_c, D_p and working curve lines establishment of optimized printing parameters such as printing layer thickness and necessary curing times to achieve them were determined (see Table 4.2). In particular optimal irradiation times were identified in the range of 1.5 s for inks containing AzoCl to 2.0 s for formulations including $AzoOCH_3$ dye for curing a layer thickness of 50 µm at a LED intensity of 10 mW cm^{-2}.

Table 4.2: Optimized parameters for 3D fabrication via DLP as well as the obtained values of E_c, D_p and coefficient of agreement (R^2) for all azo-dye inks studied and the blank formulation lacking azo-dye component. In particular, each azo-dye ink comprises 2 wt % BAPO and 0.1 wt.% of azo-dye component.

Ink	Irradiation time (s)	Exposure Intensity (mW cm^{-2})	E_c (mJ cm^{-2})	D_p (mm)	R^2
Blank	1.10	10.00	2.81	0.08	0.98
H-Azo-dye	2.00		4.31	0.07	0.98
Cl-Azo-dye	1.50		3.08	0.07	0.99
OCH_3-Azo-dye	2.00		4.02	0.07	0.99
NO_2-Azo-dye	1.75		4.13	0.08	0.99

To gain more insight about the accessible lateral resolution applying these ink systems, a custom-designed resolution test was employed. Allowing quantitative evaluation of the lateral resolution, special test structures were developed consisting of a rectangular block engraved with line gratings of different line width and period exhibiting values ranging from 1000 µm down to 30 µm. Applying previously optimized parameters, these test models were printed by DLP in case of all azo-dye based inks and for the blank ink lacking any azo-dye for comparison (see Figure 4.4). Detailed microscopic analysis showed for all azo-dye inks good results down to 40 µm lateral resolution, located quite close to the optimal value of 27 µm offered by the pixel size of the printing device. Direct comparison between azo-dye based inks and blank ink proves the printing resolution enhancing effect of the azo-dye acting in his role as photoabsorber. Additionally, application of azo-dye based inks gave access to a far more accurate reproduction of the provided digital test structure model by enhancement of printing precision.

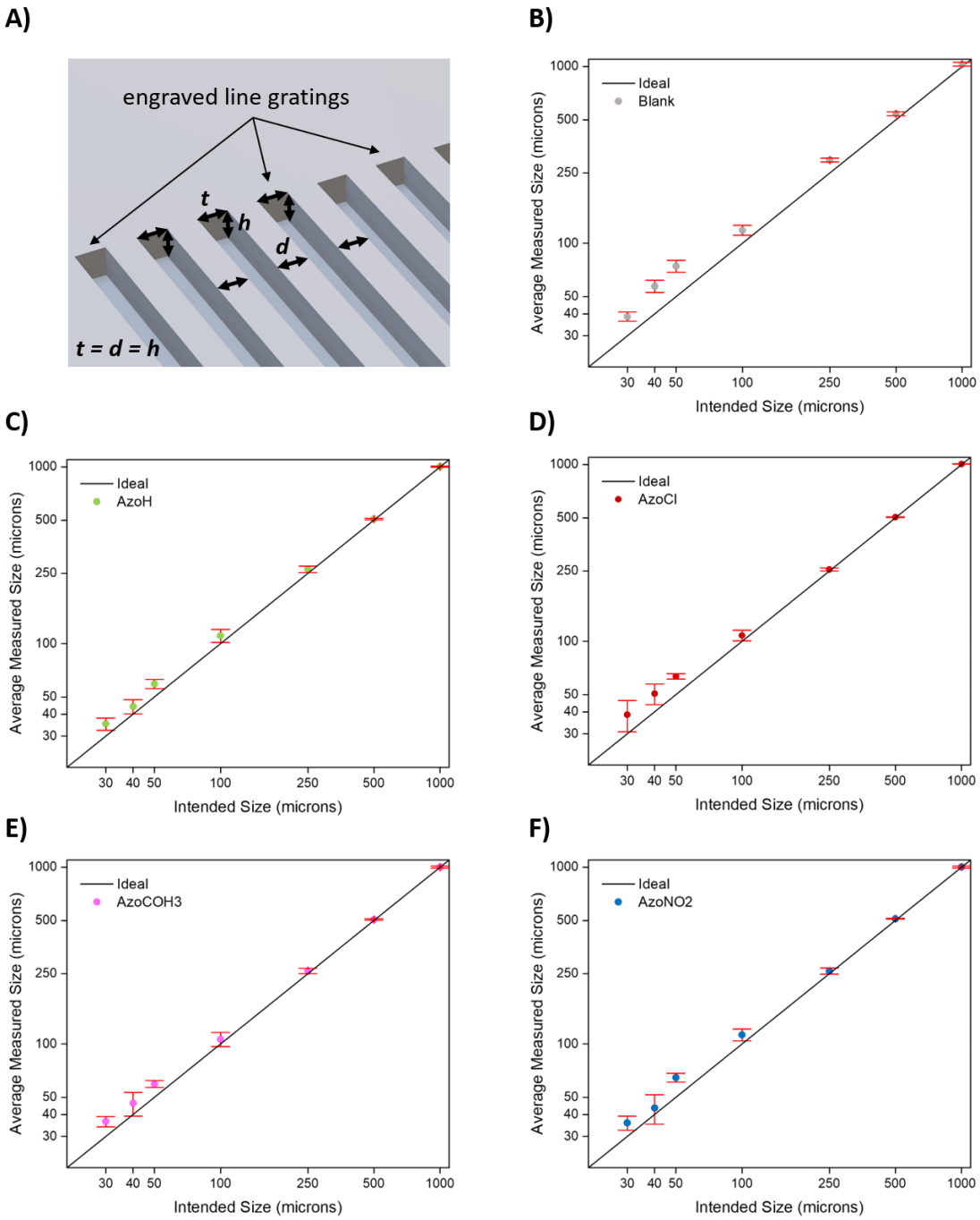

Figure 4.4: Analysis of the lateral resolution achievable with designed LSMP ink formulation containing azo-dyes and blank SMP formulation lacking any azo-dye. A) Schematic representation of the custom-designed test specimen geometries composed of a rectangular block engraved with line gratings with varying period and width. Here t conforms to the thickness, h to the depth and d corresponds to the distance between the printed lines. Measured values for lateral resolution for blank ink (B) and the LSMP inks including azo-dyes (C to F) are depicted for comparison. Measurements were performed by microscopic analysis of printed test samples. Adapted from reference [212]. Permission by Royal Society of Chemistry.

4.2.3. Study of Opto-Thermo-Mechanical Properties

After characterization of optimal printing parameters and evaluation of achievable layer height and lateral resolution for each of the azo-dye based inks, further investigation was performed to get more insight into the opto-thermo-mechanical properties of fabricated LSMP structures. Having knowledge of these properties helps further to select most effective dye candidate for later 4D fabrication of more complex structures. In particular, the main interest was located in the determination of the transition temperature, in this case the glass transition temperature (T_g) of the amorphous LSMP network. Furthermore, investigation included the question if light as stimulus is appropriate respectively strong enough to overcome the T_g inducing the recovery process in the process of the shape memory cycle. For T_g determination viscoelastic characterization by dynamic mechanical analysis (DMA) was applied on simple flat specimens of dimension 30 x 10 x 1 mm^3 fabricated with each of the presented azo-dye based inks and the blank ink as reference (see Figure 4.5).

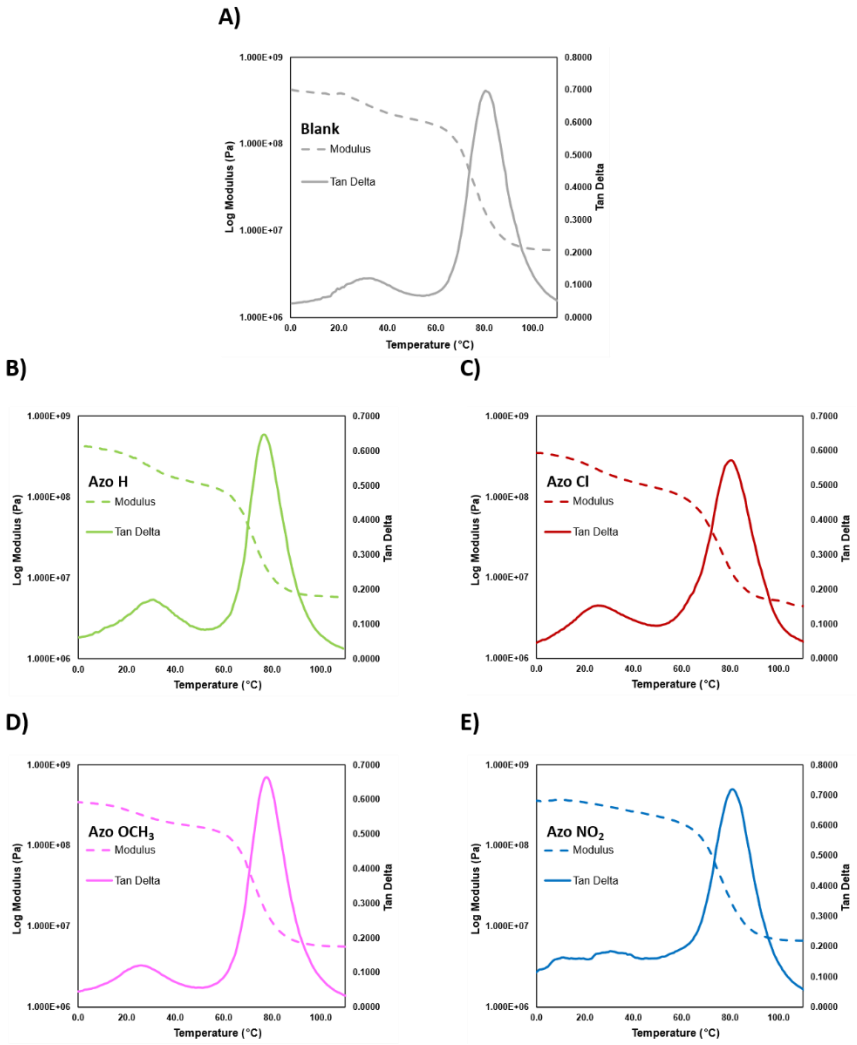

Figure 4.5: Viscoelastic characterization of 3D samples fabricated employing designed ink systems. Thermograms of blank (A) and azo-dye containing inks (B-E) are depicted, featuring all two T_gs, evaluated from the peak maxima of the tangent delta curves (Tan Delta). Adapted from reference [212]. Permission by Royal Society of Chemistry.

For all samples two transition temperatures were detectable from peak maxima of tangent delta curve emerging in the DMA thermograms. The major peak featuring high intensity was located at about 80 °C conforming to the T_g of the main component of the light-cured polymeric network – the IsobA monomeric unit. The second weaker transition temperature appeared in the range of 30 °C, corresponding most likely to the aliphatic component of the network. By comparison of the azo-dye functionalized networks with the reference blank network no significant difference in viscoelastic properties was observed. Being expectable, as the azo component is only present in 0.1 wt% in the ink formulation, meaning that the main adjuster of viscolelastic properties is the SMP monomer matrix. To prove thermal stability of the LSMP networks in the temperature range above transition temperature – above 80 °C – thermal stability was investigated by thermogravimetric analysis (TGA) (see Figure 4.6 and Figure S6, Appendix). Although the incorporation of azo-dyes results in a reduction of decomposition temperature, all samples show sufficient stability until 130 °C. Giving access to a wide enough temperature region between transition temperature (~80 °C) and degradation temperature (~130 °C), shape memory programming as well as recovery can be performed by overcoming the transition temperature without occurrence of material degradation.

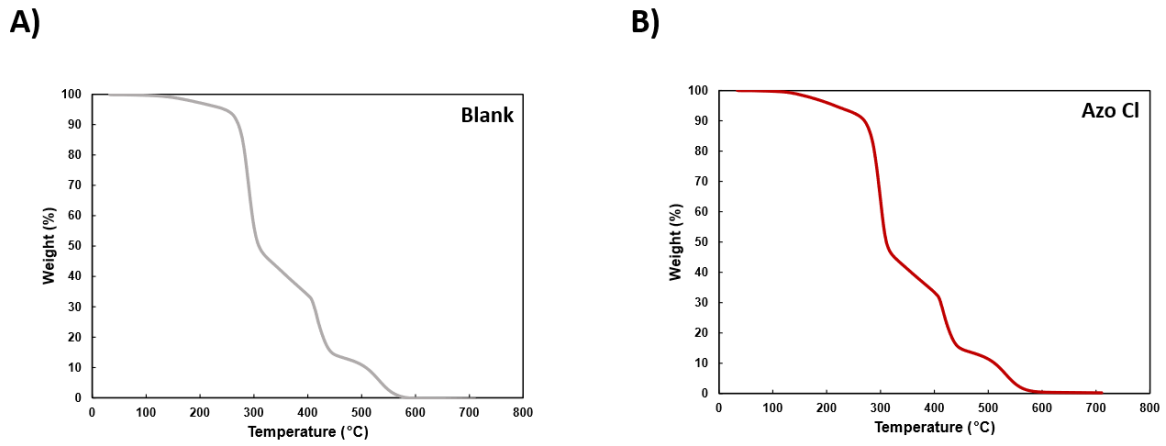

Figure 4.6: Thermal characterization via TGA. Measured thermograms of A) Blank, B) Cl samples are depicted. Adapted from reference [212]. Permission by Royal Society of Chemistry.

In the next step the focus of investigation was changed towards evaluation of opto-mechanical properties of the azo-dye-containing printing materials. For that purpose, characterization of azo-dye containing specimens was conducted by DMA measurement under LED irradiation of 459 nm wavelength (see Figure 4.7 and Figure S7, Appendix). While switching on and off the irradiation of the LED light, a change in storage modulus was monitored for the azo-dye containing samples, whereas the blank sample showed no significant response towards the stimulus light. During irradiation heating of the samples above transition temperature caused by the incorporated photothermal effect

transformed the samples' initial stiff properties associated with the glassy state to softer ones exemplary for the elastic rubber state. This process of glass-to-rubber transformation is pictured by the reduction of storage modulus (E') associated with the activation of light irradiation. Importantly this behavior is reversible visible by the increase of storage modulus by irradiation cut-out, representing the transformation of the glassy state back to the rubbery. A rise in the LED intensity by increasing the current of the power supply led to faster response and more reduced values of storage modulus.

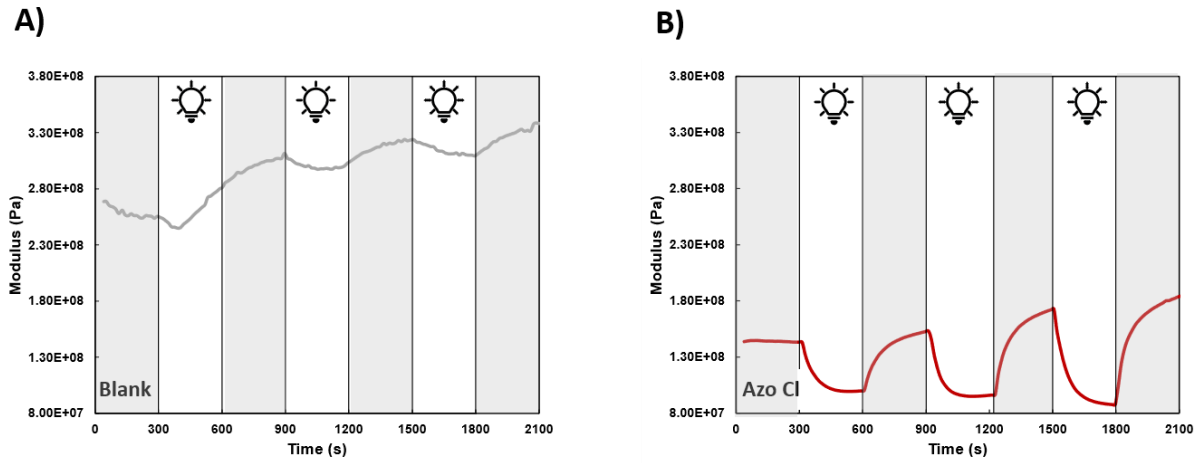

Figure 4.7: DMA analyses of 3D polymeric specimen under LED irradiation while successively increasing LED output intensity at every cycle. The change in storage modulus was monitored for samples fabricated from a) the blank ink and from the LSMP ink containing azo-dye compound B) Cl. Adapted from reference [212]. Permission by Royal Society of Chemistry.

4.2.4. Evaluation of Shape Memory Performance and Light induced Recovery

Finalizing the decision for the ink candidate for fabrication of more complex 4D LSMP geometries, investigations concerning the shape memory performance of structures fabricated by the individual azo-dye based inks were performed. In this process, simple printed flat strips were heated inside a water bath at 80 °C towards their deformable state allowing bending of the strips towards an angle of 180°. Fixation done in cold water of 15 °C enabled geometrical locking of the temporary shape. Subsequent activation of light induced recovery was performed by irradiation of the samples using a LED featuring a wavelength output of 459 nm, allowing heating of the sample photothermally.

To monitor the light activated recovery process, the recovery parameter, equivalent to the recovered bending angle, was measured throughout the process (see Figure 4.8).

Remarkably, all samples investigated, were able to reach a recovery level of 100% meaning complete transformation back to the initial flat shape of the stripe, indicating a highly efficient shape memory feature. However, specimens based on different azo-dye components show different performance regarding the time to finish the recovery process. Specimens based on AzoOCH$_3$ and AzoH completed

the recovery process in 6 and 7 minutes. Much faster recovery was observed for samples printed from AzoCl and $AzoNO_2$, showing transformation back towards the initial state within only 4 minutes. Thus, considering their light activated recovery feature, AzoCl and AzoH based printed samples stood out of the spectrum of designed LSMP inks.

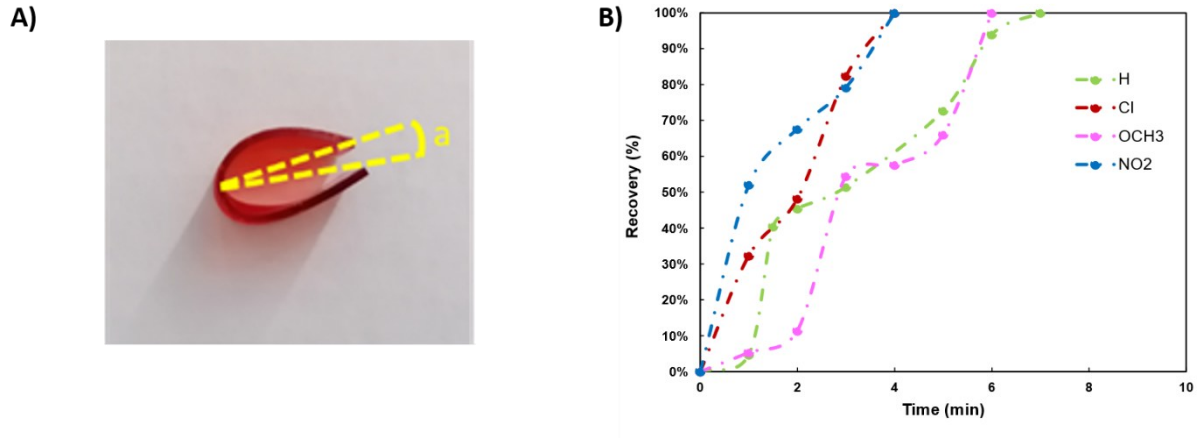

Figure 4.8: Analysis of light induced shape memory recovery of printed all printed azo-dye samples utilizing a flat strip as test structure. a) Determination of the recovery parameter a – equivalent to the recovery bending angle – during the light activated recovery process. b) Monitoring of the recovery process against time for all strip samples of all applied azo-dyes inks. Adapted from reference [212]. Permission by Royal Society of Chemistry.

4.2.5. 4D printing of Complex Structures

The next step treated the 4D fabrication of LSMP geometries of higher complexity that will later be employed in shape memory cycles. Undertaking this, the amount of employed azo-dye LSMP inks was limited to the best performing azo-dye ink candidate with regard to prior results and data collected for printing parameters, thermo-mechanical and opto-mechanical properties and light induced shape memory recovery performance. Considering all these points the final decision was made for the AzoCl ink. Summarizing the reasoning, AzoCl acted as the best dye to obtain 4D geometries based on i) its good light activated shape memory recovery properties, ii) its excellent printing behavior while incorporated in the SMP ink formulation visible in the fast-curing speed at low layer thicknesses, and iii) its facile synthetic preparation. Thus, the LSMP ink formulation including AzoCl was chosen for all following work including printing of more complex 4D geometries as well as their light-based shape memory actuation.

Employing evaluated optimized printing parameters the next step includes the 3D fabrication of a range of different structure types, featuring different levels of complexity (see Figure 4.9). In particular 3D geometries ranging from simple stripes, butterflies, flowers, and chain segments to more complex architectures like the 3D box exhibiting overhanging structural features as well as geometrically highly complex structures such as the Pisa tower, proving the ability of printing even finest features. More precise inspection of all fabricated structures exhibited no signs of bubbles within the geometry – an often-faced defect in DLP printing – as well as excellent structure fabrication allowing errorless

manufacturing of rather delicate features and very smooth surfaces due to the absence of interlayer discontinuities. All these points were evidence for excellent printability comparable with commercial DLP inks.

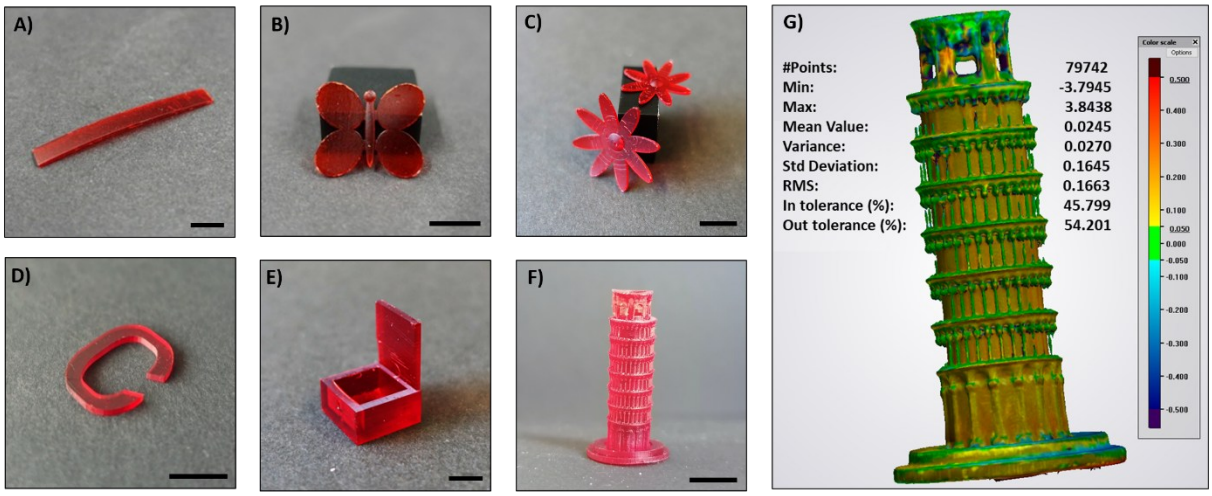

Figure 4.9: 4D printing of complex geometries via DLP and evaluation of structural fidelity. Range of 3D geometries printed via DLP employing the AzoCl containing ink: A) stripe, B) butterfly, C) flower, D) chain segment E) box, F) Pisa tower. G) Generated heat map illustrating deviations between the 3D scanned image of the printed Pisa tower structure with its STL file, indicating a high level of structural fidelity. Scale bar corresponds to 10 mm. Adapted from reference [212]. Permission by Royal Society of Chemistry.

Considering the level of structural fidelity achievable the printed structure of the Pisa tower was further investigated utilizing a 3D scanner. By comparison respectively overlap of the obtained digital structural data with the initial STL file a heat map depicted in Figure 9g was produced, indicating a high level of structural fidelity.

After successfully fabricating a range of structures, a question upcoming was the amount of double bond conversion during the printing and postcuring process. Furthermore, comparison of changes in signals relevant for double bond before and after light induced recovery would also point out possible issues in terms of undesired postcuring during shape memory cycles lowering the efficiency of the SME due to successive increase of crosslinking density by application. Besides, having high levels of double bond conversion is especially relevant in terms of biocompatibility extending the range of future applications of this system. To obtain a valid response to these questions the AzoCl-based ink as well as a printed geometrically simple specimen in form of a stripe were analyzed by Fourier-transform infrared (FTIR) spectroscopy (see Figure 4.10). For analysis the printed sample was measured directly after the printing and subsequent postcuring process and after a shape memory cycle performing one light induced recovery step. Comparison FTIR spectra revealed that bands associated with double bonds of acrylate groups located at 1635 cm^{-1}, 1619 cm^{-1} as well as 809 cm^{-1} were dramatically reduced during the 3D curing process, an obvious indication for their consumption during printing. Comparing the signal area ratio of the signals at 809 cm^{-1} associated with the acrylate double bond and at 1720 cm^{-1} corresponding to the stretching signal of the carbonyl groups between the ink and the printed

state enabled the identification of a double bond conversion in the range of 85%. From comparison of the FTIR spectra before and after a shape memory cycle no significant difference was obvious, proving absence of postcuring based on temperature-induced programming respectively light induced recovery and more importantly no photodegradation during actuation.

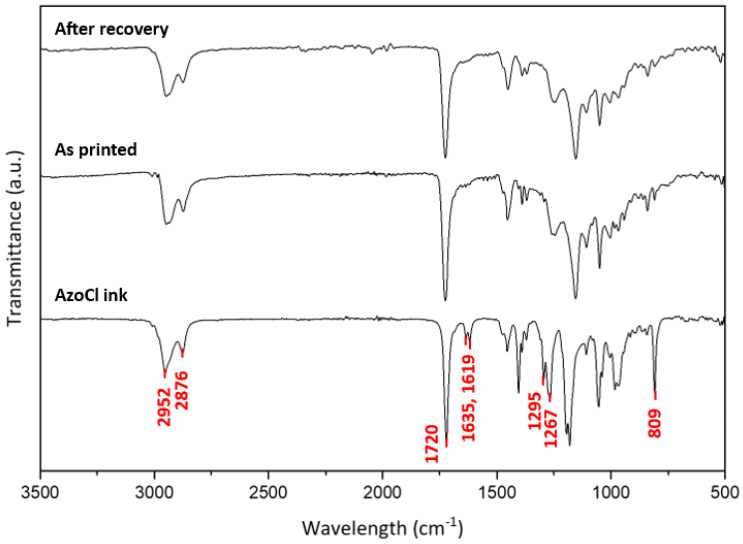

Figure 4.10: FTIR spectra of the AzoCl-based ink and a printed structure before and after recovery. By comparing the signal intensity of double bond signals from acrylate groups (1635 cm^{-1}, 1619 $cm^{-1}$and 809 cm^{-1}) between ink state and printed state a high double bond conversion due to light-based printing was obvious. Comparison of the same signals before and after shape memory cycle indicated the absence of any postcuring during the process. Adapted from reference [212]. Permission from Royal Society of Chemistry.

4.2.6. Light Activated Shape Memory Effect

Having prepared a spectrum of different 4D geometries, these demonstrators were used in the following for qualitative evaluation of the light actived shape memory effect. In contrast to prior shape memory experiments treated in this chapter, where a LED light source was employed, all shape memory cycles described in this part included a blue laser (450–460 nm) for execution of the light induced recovery step. For evaluation if suitable conditions to induce shape memory recovery were achievable by laser irradiation the temperature increase observable on printed 4D structures in response to irradiation was investigated via a thermal camera. In particular temperatures between the shape memory transition temperature, in case of this amorphous network the T_g appeared at 80 °C, and the degradation temperature, measured at 130 °C via TGA before, must be reached to permit efficient light-based recovery. Analysis of the results showed that temperatures up to 125 °C were reached in a facile and fast – within seconds – way by irradiation (see Figure 4.11) – particularly remarkable since this drastic temperature increase was induced by incorporation of solely 0.1 wt% of photresponsive azo-dye component. In contrast blank samples excluding any photoresponsive azo-dye functionality exhibited no respectively nonsignificant temperature increase – unsuitable to induce the shape recovery process.

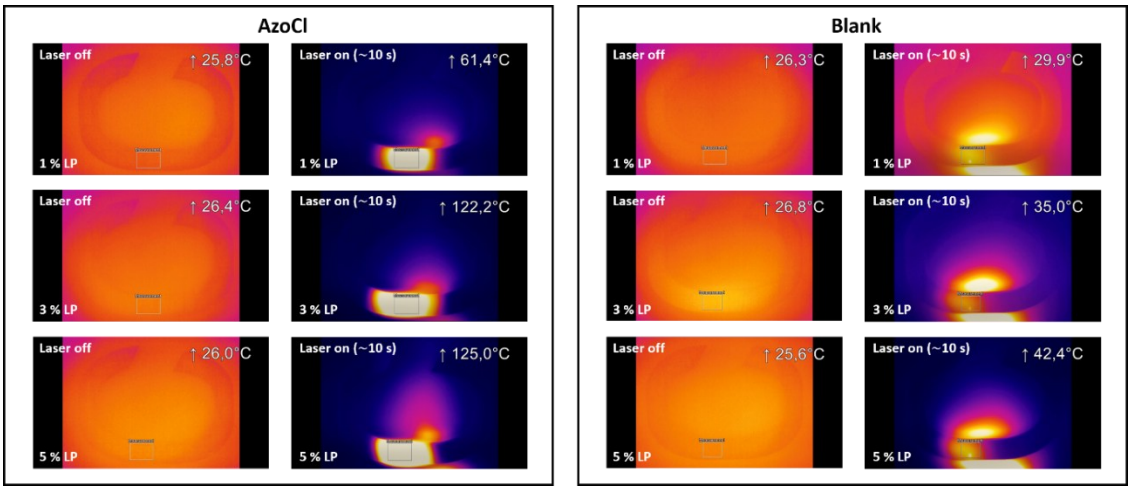

Figure 4.11: Analysis of photothermal response of 3D printed LSMP samples upon of laser irradiation (450 to 460 nm) at different intensities. Measured surface temperatures of an AzoCl containing sample (left block) and a blank sample (right block) before irradiation (left column in each block) and after irradiation for 10 seconds (right column in each block). Analysis was performed at three different laser intensities including 1% (approx. 99 mW cm^{-2}, first row), 3% (approx. 344 mW cm^{-2}, second row), and 5% (567 mW cm^{-2}, third row). Adapted from reference [212]. Permission by Royal Society of Chemistry.

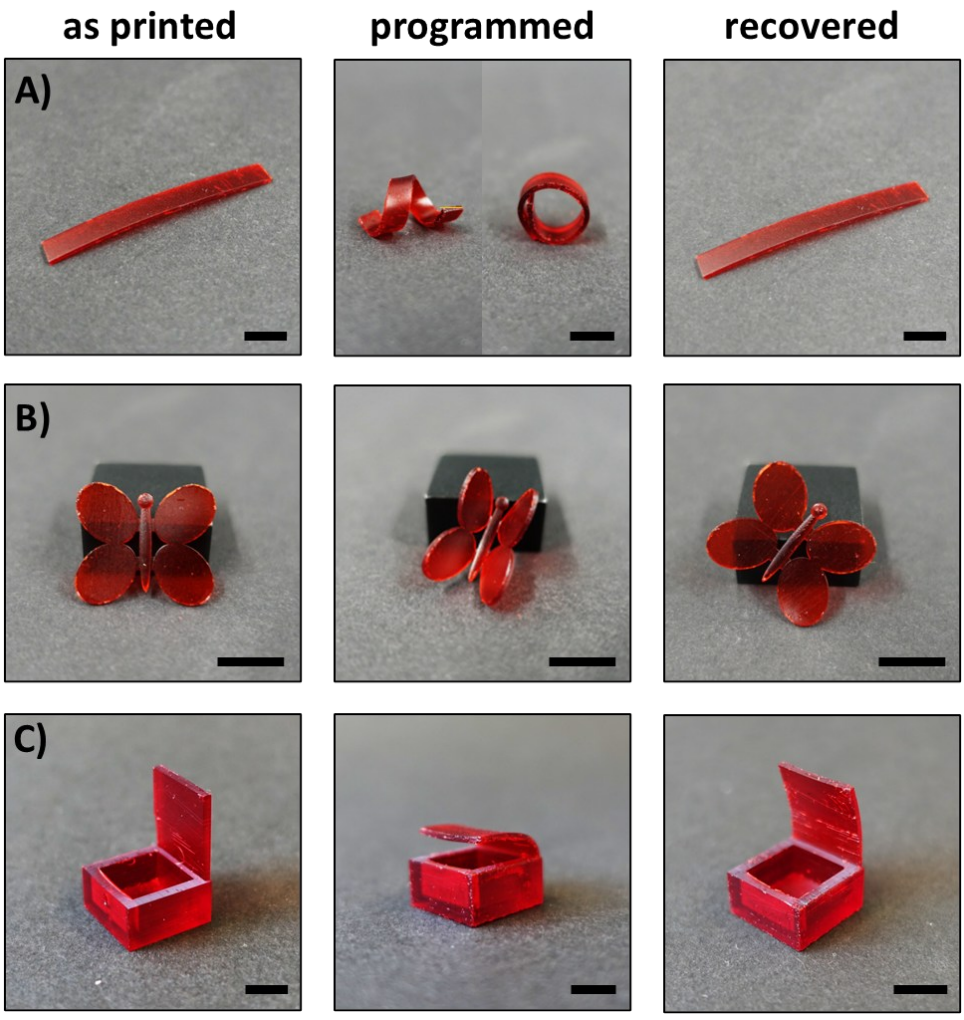

Figure 4. 12: Shape memory test of DLP-printed complex LSMP structures. Distinct states accessible in the process of the shape memory cycle including initial (as printed), temporary and recovered shapes of a) a strip, b) a butterfly, c) as "smart" box are

depicted. Temporary shapes were accessible by programming the initial shapes in preheated water at 95 °C and subsequent fixation in cold water at 15 °C. Subsequent light-based shape memory recovery was induced by application of a laser irradiating at the blue wavelength regime (450–460 nm) at a laserpower of 567 mW cm^{-2}. Scale bars correspond to 10 mm. Adapted from reference [212]. Permission by Royal Society of Chemistry.

After ensuring suitable conditions for the light stimulus, the next step involved the performance of shape memory cycles on prior fabricated complex LSMP geometries (see Figure 4.12).

In particular, the initial printed shape was heated to 95 °C and programmed to a temporary shape that was fixed at 15°C. Light induced recovery of the initial shape was enabled subsequently applying priorly described laser system. Starting with a simple geometry, the flat stripe, several temporary shapes such as circular and helical ones were programmed and fixed and simply recovered back to the initial state employing the mentioned light stimulus. Further successful evidence for programming and light induced recovery was provided by executing the described shape memory cycle on more complex geometries such as the butterfly. Further potential functionalities like a “smart” box – able to open its lid on demand by programming in the closed state – were demonstrated too.

Importantly the presented system featured excellent stability of the programmed temporary shape at room temperature within timeframes relevant for technical and industrial application, expanding in this way the material applicability – illustrated in case of strip geometry in a programmed helical shape (see Figure 4.13).

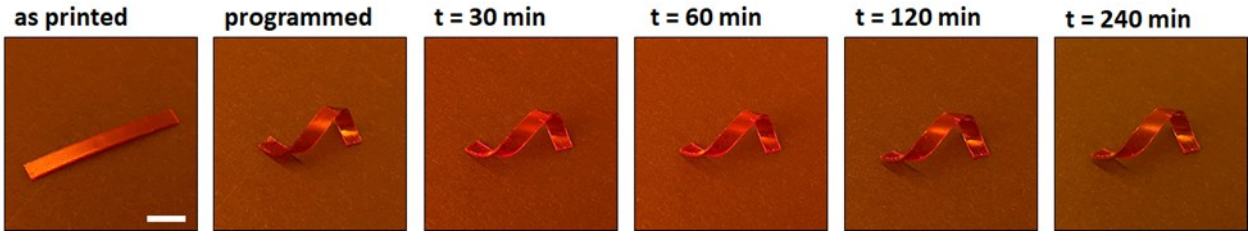

Figure 4.13: Depiction of the fixation stability of the programmed temporary shape at rt within technical relevant timeframes. Scale bar corresponds to 10 mm. Adapted from reference [212]. Permission by Royal Society of Chemistry.

Above illustrated light induced shape memory cycle proved the successful incorporation of light as possible stimulus for responsive behavior in multiple different 4D printed structures. However, full exploitation of the stimulus light meaning the possibility of spatial control in regard to recovery associated with finer manipulation of shape morphing has not been shown yet in this work. Illustrating the opportunity for spatial control of recovery activation, demonstrators appropriate for its visualization – the chain links and the flower geometry – were printed in an “open” state and successively programmed and fixed in a “closed” temporary state. In particular, three chain segments were linked with each other to a chain and the petals of the flower were bent upwards covering the inner part. Employing the described blue laser, it was possible to locally heat the structures based on the photothermal effect above T_g of the amorphous printed geometries. This heating effect appeared

to be restricted to a small irradiated area thanks to the poor thermal conductivity exhibited by polymer-based materials, resulting in no temperature increase for the residual part of the structure. Consequently, shape recovery takes only place at irradiated areas, permitting partial recovery of the geometry – rendering the recovery process spatially resolved – and thus enabling access to a multiplicity of intermediate programmed states during the recovery process (see Figure 4.14). Considering the chain geometry consisting of three connected links by previous programming and fixation, selective opening of the central element without any sign of recovery for the other two was possible. In a later recovery step these can be opened too if desired. To focus more on the possibility of this system to access intermediate states, a similar recovery experiment was performed on the programmed flower structure. Here selective opening of the petals individually in the desired sequence was possible by focusing the laser on the corresponding intersection.

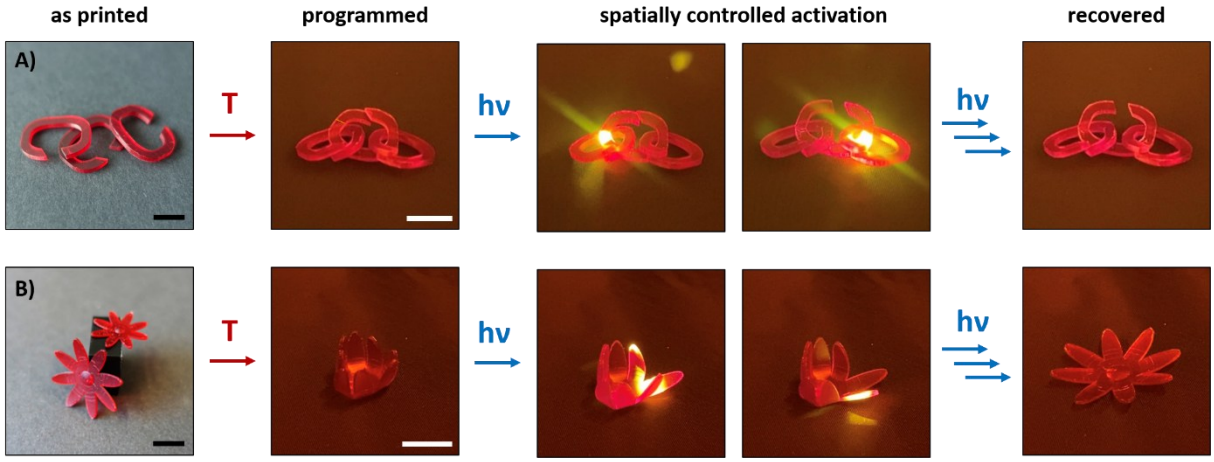

Figure 4.14: Demonstration of a spatially controlled recovery process of a) a chain geometry and b) a flower geometry. Programming was performed in water of 95 °C, fixation in cold water at 15 °C and spatially controlled recovery via laser irradiation at the blue light regime (450–460 nm) applying a laserpower of 567 mW cm^{-2}. Scale bars correspond to 10 mm. Adapted from reference [212]. Permission by Royal Society of Chemistry.

4.3. Summary:

In this study functional LSMP inks based on push-pull azo-dyes were designed offering high resolution 4D macrostructure fabrication via DLP technology. Push-pull azo-dye components in the LSMP inks offer an inherent photoabsorbing effect during 3D structure fabrication, the inclusion of light as a responsive stimulus based on the photothermal effect as well as the feature of spatial shape memory actuation with a high degree of control and actuation precision. To achieve this, we identified in a first step push-pull azo-dyes as suitable components in terms of facile synthetic preparation, simple chemical functionalization, and most importantly photothermal functionality for translation of the responsive stimulus from temperature towards light. In a next step a library of push-pull azo-dyes bearing distinct functional groups, located on the phenyl ring ortho to the diazo group was prepared synthetically. Polymerizable functionality was introduced by integration of an acrylate moiety

permitting direct incorporation of the photoresponsive moiety into the polymeric network during light-based 4D printing. For ink design prepared functional azo-dyes were combined with the shape memory macroink, developed in chapter three featuring efficient DLP printability and excellent shape memory performance at the macroscale. In total four ink formulations were prepared containing each one of the synthesized azo-dyes in an optimized concentration of 0.1 wt%. Employing these light activated shape memory polymer (LSMP) inks, first, printing parameters such as the critical exposure dose (E_c) and the penetration depths (D_p) were calculated from experimental determined Jacobs working curves. Using these parameters ideal curing times for each of the inks for curing layer thicknesses of 50 and 100 µm were determined and applied for DLP fabrication of custom-designed test structures to evaluate the optimum of achievable lateral resolution. Here, all investigated azo-dye based inks offer excellent performance down to lateral resolutions in the range of 40 µm. Subsequently, 3D printed strip structures were generated for viscoelastic characterization via dynamic mechanical analysis (DMA) involving determination of transition temperatures – to be more precise glass transition temperatures (T_g) of the amorphous polymeric network – as well as demonstration of transformation from glassy to rubbery network states and its reversibility in case of presence or absence of a light stimulus. In particular, two transition temperatures were found during characterization, one with significant intensity in the range of 80 °C and one of weaker appearance in the region of 30 °C. Here only the former one corresponding to the T_g of the major ink component isobornyl acrylate (IsobA) was considered for later shape memory procedures. Furthermore, thermogravimetric analysis (TGA) was performed on printed strip samples prepared from all azo-dyes giving insight into thermal properties such as a degradation temperature being present at about 130 °C. Subsequently, shape memory recovery performance was determined showing that azo-dye based inks containing dye molecules bearing a chlorine (AzoCl) as well as a nitro ($AzoNO_2$) functionality have faster recovery than the residual ones. Having at this point collected enough data for a reasonable decision of the best azodye candidate with regard to printing parameters, achievable resolution, thermo-mechanical and opto-mechanical properties and light induced shape memory performance, the ink containing AzoCl was selected. Employing its previously optimized printing parameters including a curing speed of 1.5 s for a layer thickness of 50 µm a spectrum of 4D geometries of different structural complexity was fabricated via DLP including again simple strips, butterflies, flowers, “smart” boxes, chain segments and even a highly complex geometry representing a centimeter model of the Pisa tower. Excellent 3D printability was found, comparable to commercial inks. Determination of the structural fidelity of this fabricated 3D Pisa tower by comparing the printed model with its digital version employing a 3D scanner exhibited excellent geometrical agreement. Furthermore, for printed structures based on AzoCl inks a double bond conversion of 85 % was calculated from FTIR characterization of the initial ink compared to printed 4D objects. Comparison of FTIR spectra of a printed 3D structure and a 3D

structure after experiencing one light-based actuation cycle features no significant difference, but mirroring of each other in terms of signals and associated intensities, indicating absence of photodegradation and post-curing caused by light-based actuation. By laser irradiation in the regime of blue wavelengths – 450 to 460 nm – as light source, light induced shape memory cycles composed of a thermal programming and fixation step and a light induced recovery step were performed on a variety of 4D LSMP geometries. Excellent light induced shape recovery properties were observed for all tested structures including the strip, butterfly, and “smart” box geometries. Making use of the poor thermal heat conductivity of polymeric materials as well as the confined area irradiated by the laser beam within a structure light induced recovery of a chain and a flower geometry was presented exhibiting a high degree of spatial control – allowing in case of the flower access to a multiplicity of intermediate shapes during the recovery process rendering the system more versatile in terms of applicability.

Chapter 5

Combining Two-Photon Laser Printing and Alkoxyamine Chemistry: Toward Living 3D Microstructures

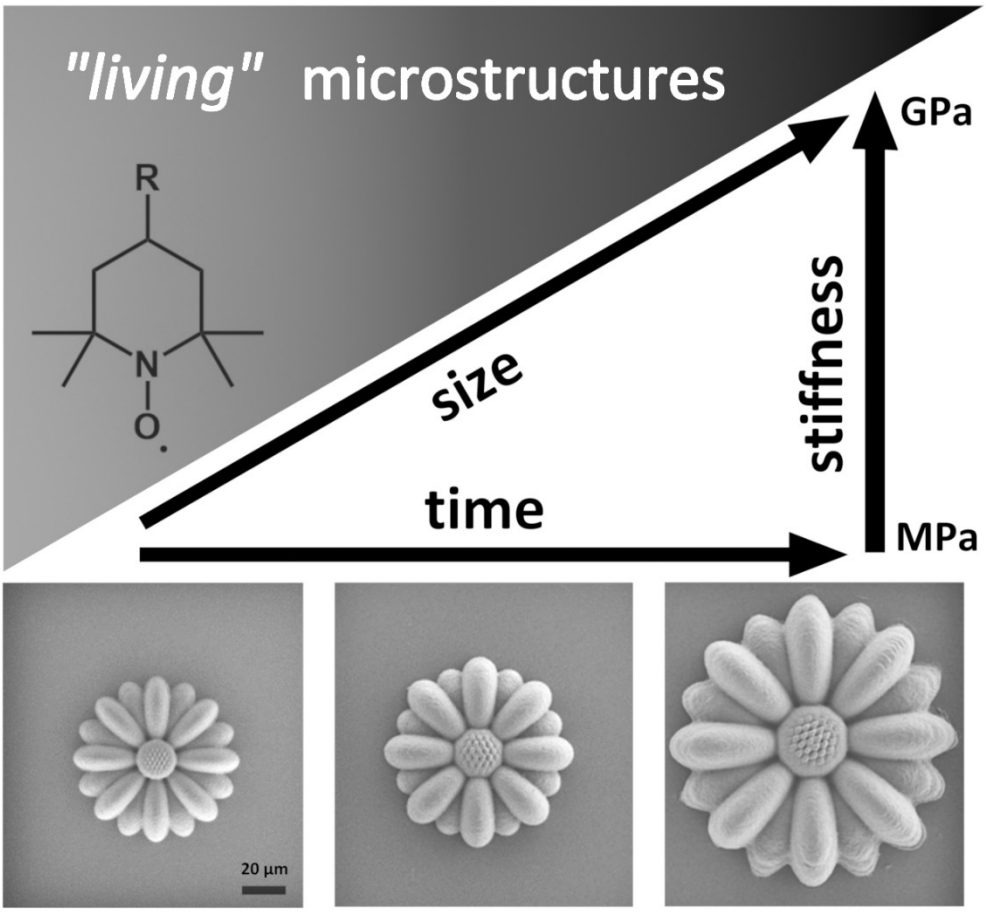

Towards "living" microstructures

5.1. Motivation and Aims

The generation of geometries featuring custom geometry and precisely adjusted mechanical properties, becomes more and more important for applications in fields such as engineering, soft robotics, biomedical therapies or soft electrics or sensors. At the macroscale approaches were already designed especially for fabrication via digital light processing (DLP). In particular methodologies combining controlled RAFT polymerization with DLP allow 3D fabrication of structures able to be postmodified due to the living character of the incorporated RAFT species. At the microscale a methodology for this purpose was at the time this work was performed and published not existent. This is especially interesting, because going from macroscale towards microscale the need for customizable properties maintains of high relevance. High potential for such microprinted dynamic systems can be envisioned for instance in areas of microrobotics, microelectronics, or smart sensors. Here, precisely fabricated microparts as well as suitable mechanical properties are of particularly high necessity. Employing 3D microfabrication with such dynamic materials will offer highly desired adjustability on customer's demand allowing matching of fabricated microparts perfectly with final applications. As discussed in the introductory part, 2PLP offers the ability to fabricate microgeometries with a superior feature size in the regime of hundreds of nanometers to micrometers. Furthermore, in principle structural design by digital modeling is limitless in terms of accessible geometries, allowing first design of arbitrary architectures by preparation of a digital model as well as printability of it via 3D printing methods. Considering this 2PLP is the perfect fabrication method to generate custom-built structures. However, fulfilling the second point, the customized adjustment of those generated 3D microstructures in terms of for example mechanical properties, appears to be a more sophisticated issue. Transferring this ability towards a microstructure implies the presence of some kind of dynamic functionality allowing the incorporation of other materials on demand under special conditions, while being stable at ambient conditions for optimal performance in the desired application. Mirroring approaches successfully applied at the macroscale one way to incorporate such features is the combination of "living" polymerization methods together with 3D printing leading to living additive manufacturing as explained in the theoretical part of this work. Searching for a suitable functionality incorporable in microscale geometries alkoxyamine bonds appear to be excellent candidates. These dynamic bonds offer on the one hand the potential to incorporate extrinsic monomers and thus functionalities or changes in mechanical properties by nitroxide-mediated polymerization (NMP), on the other hand, mechanical properties can be directly adjusted by nitroxide exchange reaction, for example by crosslinking reduction using an excess of TEMPO moiety. Thus, incorporating such a covalent adaptable system including the feature of chain extension by NMP into a 2PLP ink would give rise to microstructures, resembling alkoxyamine-based CANs, able to be fully customizable in terms of

mechanical properties, while maintaining structure fabrication at highest precision offering in this way large advantages for application in industry and science.

Thus, the goal of this project was to design such a functional ink system transferring covalent adaptable character and “living” features towards 2PLP microstructures. Thus, first, suitable components must be identified. After identification of an appropriate nitroxide source, photopolymerizable crosslinking units, a photoinitiator, and if necessary, additives such as solvents, microstructures will be designed and characterized, proofing in this way presence of dynamic nitroxide bonds. Subsequently, suitable 3D microstructure geometries will be fabricated and postprinting modified by designed NER and NMP procedures investigating their potential for change and adjustment in mechanical properties (see Figure 5.1). If successful, more complex microstructures will be fabricated and optimized postprinting NER and NMP approaches will be performed on them evaluating the effect on geometries containing features of high complexity.

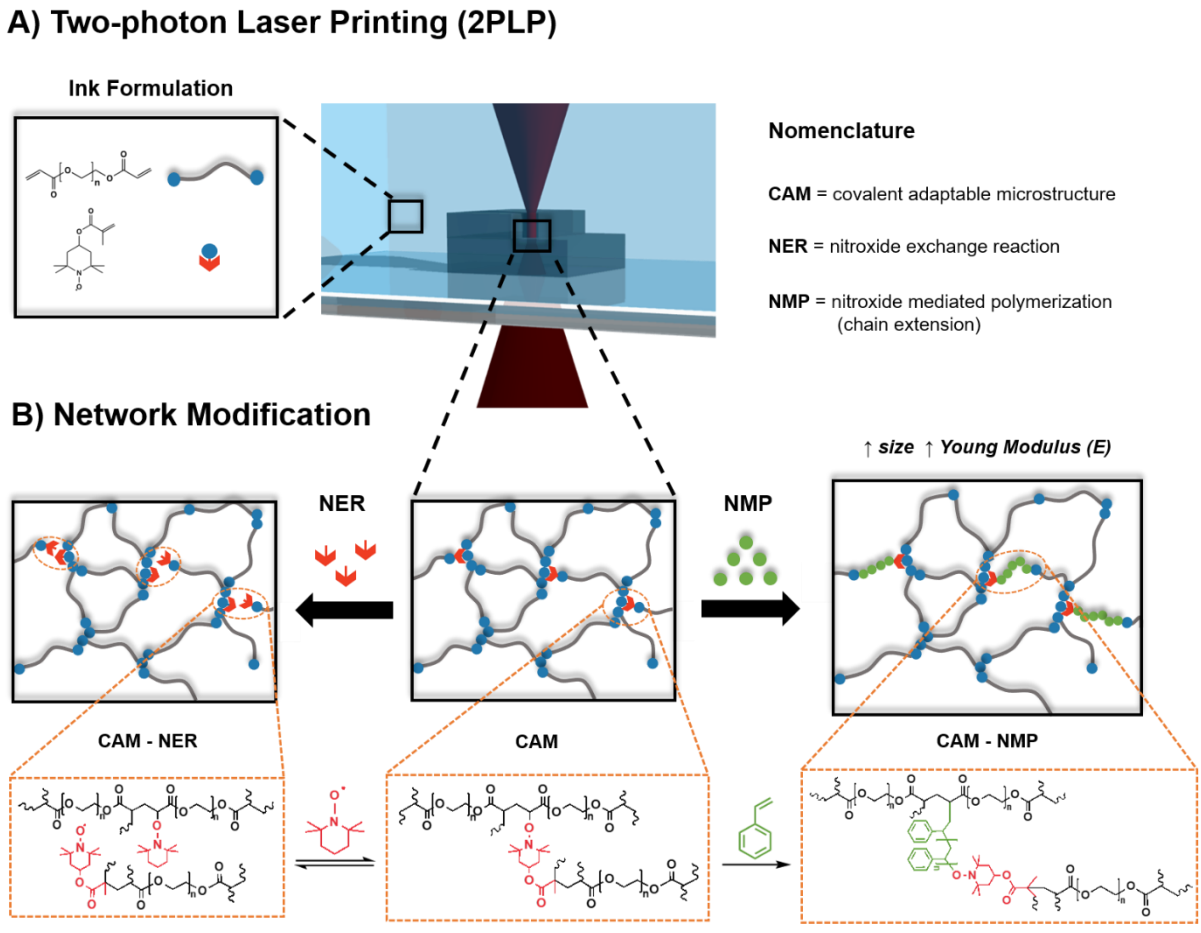

Figure 5.1: General concept of this work. A) An ink formulation including a nitroxide source is employed for 2PLP, allowing generation of covalent adaptable microstructures (CAMs) featuring dynamic alkoxyamine bonds. B) Alkoxyamine bonds reactivity implemented in CAMs will be utilized for postprinting modification via nitroxide exchange reaction (NER) meaning decrosslinking or nitroxide-mediated polymerization (NMP) allowing chain extension with an ink extrinsic monomer like styrene. Adapted from reference [62].

5.2. Results and Discussion:

5.2.1. Optimizing Ink Formulation for Two-Photon Laser Printing (2PLP) of Covalent Adaptable Microstructures (CAMs)

First step towards "living" covalent adaptable microstructures was the design of a suitable ink system offering the adaptivity feature. For this purpose, it is essential to include a type of dynamic covalent bond allowing for postprinting modification. In this case, the alkoxyamine bond was selected giving access to nitroxide exchange reaction (NER) as well as nitroxide-mediated polymerization (NMP) offering two synthetic pathways for property modification. To introduce this functionality a suitable– this means in this case photopolymerizable – nitroxide component, a promising precursor for the alkoxyamine bond, was searched for and identified in 4-methacryloyloxy-2,2,6,6-tetramethylpiperidin-1-oxyl (TEMPO-methacrylate). TEMPO-methacrylate fulfills both requirements for application in the envisioned "living" ink system: i) it contains the desired nitroxide functionality for later inclusion of the alkoxyamine bond during 3D photocuring and, ii) the incorporated methacrylate moiety provides a photopolymerizable group allowing efficient integration of theses functionalities into the polymeric network of CAMs. Based on the knowledge that 2PLP structure generation requires a rather high photocrosslinkable group density to ensure a stable 3D microfabrication process – not provided by solely TEMPO-methacrylate – a difunctional monomer component a crosslinker was included in the ink, too. Poly(ethylene glycol) diacrylate (PEGDA, average M_n = 700 g mol^{-1}) was selected for this purpose, appearing as main component in the ink formulation. PEGDA, a known monomer for 2PLP fabrication offers advantageous fabricability of rather soft 4D microstructures of elastomeric character. Thus, later postprinting modification towards the stiffer material regime could be exploited as possible strategy. Having set the photocrosslinkable components a suitable photoinitator allowing efficient radical generation, thus crosslinking during 2PLP structure generation was required. Here the choice of an efficient photoinitiator was of highest necessity due to the well-known quenching effect of nitroxides featuring a stable radical. Employing 7-diethylamino-3-thenoylcoumarin (DETC), a photoinitiator well known for its excellent multiphoton initiation efficiency was selected. To ensure complete dissolution of the present ink composed of TEMPO-methacrylate, PEGDA and DETC, a suitable solvent must be applied, considering two prerequisites for it. First, it must enable high solubility for all the components, so that minimal amounts of it are necessary as final ink component, thus, not decreasing the photopolymerizable group density by too high levels of dilution. Second, the solvent must exhibit high boiling points inhibiting in this way evaporation during the 3D fabrication process. Considering both demands for an efficient 2PLP solvent, solubility screening of the ink components was performed on dimethyl sulfoxide (DMSO), dimethyl formamide (DMF), diethyl

formamide (DEF) and dimethylacetamide (DMAc) (see Table 5.1). Crosslinker component, nitroxide source and photoinitiator were readily dissolvable in all of the mentioned solvents except for DMSO. However, optimizing the amount of solvent, to ensure minimal usage of it in the final ink system for better printing performance, DMAc was chosen as candidate, considering its best solubility performance for all ink components.

Table 5. 1: Solubility screening of TEMPO-methacrylate and DETC.

Solvent/Solvend	DMF [wt%][a)]	DMAc [wt%]	DMSO [wt%]	DEF [wt%]	PEG-DA M_n 700 [wt%]
TEMPO-methacrylate	65	80	30	65	60
DETC	20	30	5	20	0.5

a) Weight percent wt%: $w_i = m_{solvend}/(m_{solvend} + m_{solvent})$

After suitable ink components were identified, the next crucial step involves fine-tuning of the ratio between photoinitiator DETC and the nitroxide source TEMPO-methacrylate. The nitroxide source is necessary to be present in the ink to provide enough source for generation of alkoxyamine bonds during the photopolymerization process, mandatory to incorporate the dynamic adaptive feature within the fabricated 4D structure to achieve the desired "living" characteristic. However, as already mentioned, based on their nature as stabilized radicals nitroxides are commonly used as radical quenchers in polymerization processes, visible in their application as resolution-enhancing reagents in 2PLP. Consequently, higher concentrations of TEMPO-methacrylate in the ink can interfere with the initiation and propagation process by undesired radical recombination increasing the energy level of the fabrication threshold in 2PLP. Result of this effect is the necessity of high laser powers and low scanning speeds producing enough initiating radicals to create polymers overcoming the gel point enabling stable network formation and 3D structure fabrication. Thus, the amount of nitroxides within the ink is crucial for successful printing. Balancing this effect, the ink formulation was carefully optimized by stepwise adjustment of the concentration of TEMPO-methacrylate and photoinitiator DETC (see Table 5.2). To assess 3D printability of each formulation 3D laser printing of simple cubic test structures, featuring dimensions ranging from 10 × 10 × 3 to 42 × 42 × 30 µm^3, was performed using different laser powers and scan speeds. For each ink formulation optimized conditions and details of the printed structures and the 3D fabrication process in terms of accessible dimensions and quality were summarized in Table 5.2.

Table 5.2: Ink composition screening process with achievable laser printing parameters.

Ink	DETC [a] [wt%]	PEG-DA 700 [wt%]	TEMPO-methacrylate [wt%]	DMAc [wt%]	Laser Power [mW]	Scan Speed [µm s^{-1}]	Crosslinker: PI:NO (molar ratio) [b]	Block Size (length, width, height) [µm]	Py [c]
C1	2.1	70.1	4.6	23.2	-	-	15:1:3	-	-
C2	2.2	72.4	1.6	23.8	24	20	15:1:1	10, 10, 3	○
C3	5.5	59.2	2.0	33.3	22	400	10:2:1	32, 32, 6	◑
C4	3.7	61.0	1.2	34.1	23	600	15:2:1	42, 42, 10	◑
C5	0.9	92.4	1.5	5.2	48	2500	47:1:2	42, 42, 30	●
C6	0.9	91.4	2.7	5.0	-	-	47:1:4	-	-
C7	0.9	88.5	3.9	6.7	-	-	47:1:6	-	-

a) photoinitiator; b) molar ratio of PEG-DA (crosslinker), photoinitiator DETC (PI) and TEMPO-methacrylate (NO); c) ● printable, high scan speed; ◑ Printable, instabilities during writing, good scan speed; ○ printable with high risk of instabilities, low scan speed; - not printable.

As visible in Table 5.2 initial tests were performed using a 1:3 molar ratio between photoinitiator DETC and TEMPO-methacrylate (Ink C1) preventing stable printability. In particular, non-printability was caused by two effects: I) radical inhibition by the presence of TEMPO radicals and II) the high content of solvent leading to dilution of the photopolymerizable group density and thus inefficient microprintability. Such high content of solvent was necessary for complete dissolution of nitroxide and photoinitiating components. Consequently, the TEMPO-methacrylate content was decreased in the next step. Reducing its amount towards a 1:1 ratio permits 3D structure fabrication at inefficient printing conditions – high laser powers at low scan speeds. In fact, 3D structure formation was possible, however, the risk of occurrence of instabilities such as microexplosions and thus structural damage, was very high due to inefficient manufacturing conditions. Further increasing the photoinitiator component with regard to the nitroxide component, a ratio of 2:1 (ink C3 and C4) improved printability. 3D laser fabrication was possible with mediocre conditions in terms of scan speed, enabling production of 3D structures of larger dimensions at acceptable manufacturing times. Although an improvement in fabricability was observed, the formation of microbubbles during printing – likely a result of local heat accumulation caused by the laser- stable structure formation was not guaranteed and reproducibility of the printing process thus hindered. Interestingly drastic reduction of the photoinitiator content below 1 wt.% as well as fine-tuning the photoinitiator to nitroxide ratio toward a 1:2 ratio led to appropriate 3D printing performance (Ink C5). In particular efficient 3D structure fabrication was possible at high scanning speeds of 2500 µm s^{-1} enabling formation of larger 3D geometries at lower build times. In addition, microbubble formation was absent giving access to defect-free fabrication

rendering this formulation excellent for printing of more advanced structures containing more complex features. Main reason for this dramatic improvement in performance might be the associated reduction of necessary solvent due to a lower amount of photoinitator and TEMPO-methacrylate in the ink formulation. Further attempts to increase the nitroxide radical source content while maintaining similar levels of photoinitiator, aiming at effectively higher amounts of incorporated dynamic alkoxyamine bonds in final 3D microstructures, were unsuccessful (Ink C6 and C7). Photoinitiator to nitroxide molar ratios of 1:4 and 1:6 were not printable due to strong radical quenching of the TEMPO-methacrylate component leading to inefficient initiation and chain propagation.

Based on its superior performance in 3D microstructure fabrication Ink C5 composed of a crosslinker/photoinitiator/TEMPO-methacrylate molar ratio of 47:1:2 was selected as appropriate ink formulation for subsequent studies described in the next sections.

5.2.2. Characterization of the Covalent Adaptable Microstructures (CAMs)

After setting a working formulation for laser-based fabricability of 3D "living" microstructures, the next step included generation of suitable test microstructures and subsequent analytical characterization by Fourier-transformed infrared (FTIR) microscopy and time-of-flight secondary mass spectrometry (ToF-SIMS), both techniques applicable for chemical analysis of microstructures and associated low amounts of polymerized material. In particular, important spatially resolved information on the microstructures' chemical composition was accessible in this way. For characterization purpose test structures, in particular solid cuboid 3D microstructures featuring dimensions of 42 x 42 x 30 μm^3, were fabricated using the optimized ink formulation Ink C5 – labelled here covalent adaptable microstructures CAMs – in the spirit of CANs. Additionally, reference structures featuring same dimension were fabricated using a blank formulation with similar composition like Ink C5, but lacking any nitroxide components – labelled as Ref in this work. FTIR analysis was performed on CAMs and Ref microstructures. Furthermore, the initial ink was characterized by the same method for comparison (see Figure 5.2A). Going from ink to CAM or Ref recorded spectra show typical changes in signals and corresponding intensities resulting from the acrylate-based photocuring process. For example, characteristic bands at 1635 cm^{-1} and 980 cm^{-1} corresponding to the CH_2=CH stretching vibration associated with acrylate moiety of unreacted monomers decreased during photopolymerization due to acrylate double bond consumption during printing. Furthermore, the absorption band at 1720 cm^{-1} corresponding to C=O stretching vibration featured by conjugated α,β-unsaturated esters, shifted to 1730 cm^{-1} associated with aliphatic esters, the resulting species from polyacrylate formation during

printing of CAM and Ref. In addition, the spectrum of printed CAM exhibited an absorption band at 1470 cm^{-1} related to the CH_3 asymmetrical bending, hinting towards incorporation of TEMPO-methacrylate into the laser-fabricated functional polymeric network of CAMs. In agreement with this consideration, Ref microstructures without TEMPO moieties lack detection of this signal. In the next step time-of-flight secondary mass spectrometry (ToF-SIMS) was performed on CAM and Ref microstructures. Employing this characterization method ion species associated with PEG ($C_2H_5O^+$) as well as with alkoxyamines ($C_3H_8NO^+$) were detectable and compared between CAM and Ref (see Figure 5.2C). Ref microstructures and CAM exhibited both similar secondary ion count intensities for the signal specific for PEG assigned to $C_2H_5O^+$. As both types of microstructures (CAM and Ref) are composed mainly of PEG, this result is coherent with before-made expectations. Contrastingly, the ion signal of $C_3H_8NO^+$ was solely detectable in case of CAMs, being another evidence for further covalent incorporation of TEMPO-methacrylate moieties into the polymeric network as well as the presence of alkoxyamine moieties in it. Images recorded by ToF-SIMS imaging based on $C_2H_5O^+$ and $C_3H_8NO^+$ signal intensities visualize the differences in chemical composition of CAM and Ref cuboid microstructures, supporting further the successful incorporation of alkoxyamine functionalities into printed CAMs (see Figure 5.2D).

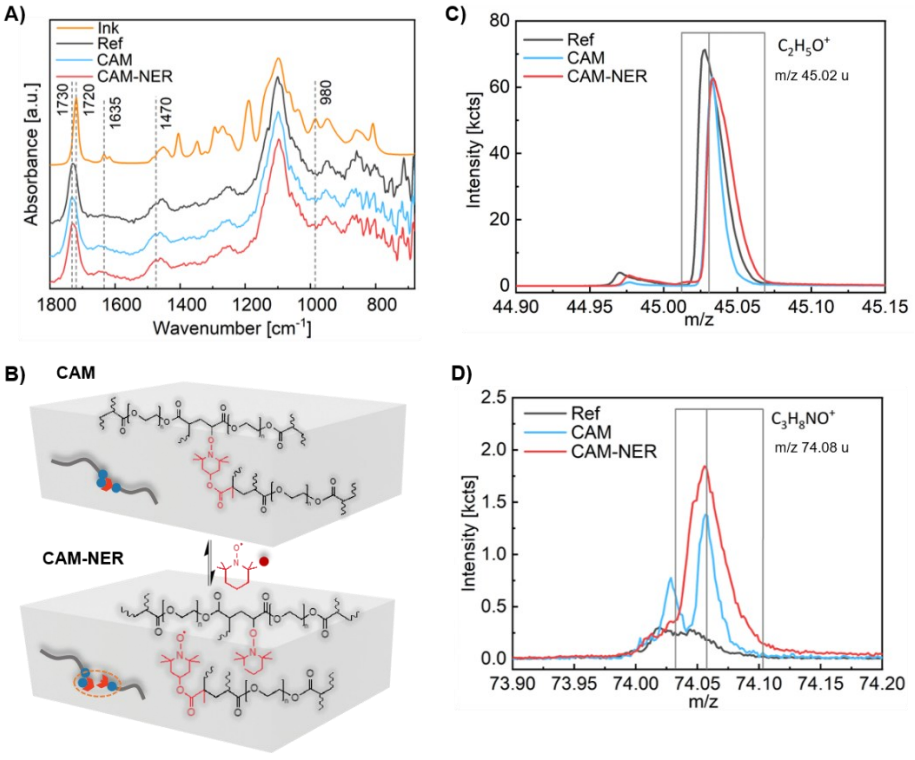

Figure 5.2: FTIR and ToF-SIMS characterization of CAM, CAM-NER, Ink and Ref. A) FTIR characterization of the ink (Ink), reference microstructure (Ref), CAM and CAM-NER. Absorption bands specific for acrylate moieties and alkoxyamine bonds are highlighted (gray dashed line). B) schematic illustration of postmodification of CAM to CAM-NER via nitroxide exchange reaction. C) ToF-SIMS characterization of reference microstructure (Ref), CAM and CAM-NER in the region of PEG specific

($C_2H_5O^+$) signals; D) ToF-SIMS characterization of Ref, CAM and CAM-NER in the region of alkoxyamine specific ($C_3H_8NO^+$) signals. Adapted from reference [62].

5.2.3. Postprinting modification of the Covalent Adaptable Microstructures (CAMs)

At this point a suitable ink formulation as well as parameters for fabrication of simple cuboid CAMs were found. Furthermore, incorporation of mandatory alkoxyamine functionalities for further postprinting modification was confirmed via FTIR and ToF-SIMS as illustrated in the previous section. The logic next step was the design and test of suitable synthetic procedures to postmodify fabricated "living" structures, demonstrating in this way the introduction of living aspect targeted in this work. In the following subsections design, test and characterization of two pathways possible to postmodify CAMs will be described: I) crosslinking reduction applying the nitroxide exchange reaction (NER) and II) chain extension via nitroxide-mediated polymerization (NMP) employing an ink-extrinsic monomer.

5.2.3.1. Nitroxide exchange reaction (NER)

Considering NER exchange reaction as dissociative covalent adaptable reaction type it can be expected that upon application of it on fabricated CAMs no alteration in crosslinking density thus no change in mechanical properties occur. However, performing the reaction in excess of unfunctionalized TEMPO moieties a higher overall TEMPO content compared to the original CAM, can be assumed for the product microstructure labeled with CAM-NER (Figure 5.2C). The reaction is supposed to lead to an overall reduction of crosslinking based on the exchange of alkoxyamine bonds, connected on one side via the piperidinyl moiety to another chain segment of the acrylate network, with newly formed alkoxyamine bonds by reaction with unfunctionalized TEMPO moieties. By using an excess of unfunctionalized TEMPO the NER reaction can be controlled to occur in favor of this "decrosslinking" pathway instead of typical covalent adaptable network reformation via bond exchange (see Figure 5.2C).

To test before made hypotheses, printed CAMs were reacted in the presence of an excess of free unfunctionalized TEMPO molecules, while heating, and characterized by FTIR microscopy and ToF-SIMS. In this context, FTIR microscopy allowed no observation of significant changes in obtained spectra for CAM-NER compared to initial CAM confirming overall preservation of the CAM network structure after NER postprinting modification. Reasoning about this, the main factor for this behavior is supposed to be the predominant character of PEGDA – being the main ink component and thus main network component in CAM and CAM-NER, whereas the amount of alkoxyamine bond is below 1 wt.% in the ink source, being likely lower in the final CAM structures. However, this fact makes it much more

remarkable that a significant change in ion count intensities for the signal associated with $C_3H_8NO^+$ species can be observed by comparing CAM and CAM-NER spectra via ToF-SIMS, being clear evidence for additional incorporation of alkoxyamine functionality during NER modification (see Figure 5.2D). As expected, the signal corresponding to the PEG characteristic ion species $C_2H_5O^+$ showed similar values in secondary ion count intensities for CAM and CAM-NER. Later observation can be rationalized as the PEG polymer chain segments are unaffected by further incorporation of TEMPO moieties by NER and the reduction in crosslinking density within the network during NER modification (see Figure 5.2C). Hinting further toward the decrease in crosslinking density and the consequential reduction in stiffness of the material visual observation of the CAM-NER state compared to initial CAMs exhibit a slight structural indentation.

However, as the main interest of this work lay in the development of "living" structures being adjustable on demand in their mechanical properties, further mechanical investigation was necessary to illustrate the effect of the reduction of crosslinking density towards mechanical properties such as the reduced Young's Modulus or the hardness. It is important to point out that mechanical characterization aimed at the reduced Young's modulus instead of the standard Young's modulus because material properties such as the Poisson ratio were unknown for the newly designed CAM material. Nevertheless, this value should provide suitability to give a general estimation of the material's mechanical properties, comparability to other material types as well as necessary precision to compare changes of mechanical properties between the different states of material including CAM and CAM-NER. Access to these mechanical quantities was provided by direct measurement of the microstructures via nanoindentation. For this purpose, previously 3D fabricated cuboid microstructures were applied in their CAM and their postmodified CAM-NER state. In agreement with prior made observations by ToF-SIMS a reduction in the reduced Young's Modulus to 7.2 ± 1.3 MPa for CAM-NER was determined from 14.3 ± 1.3 MPa exhibited by initial CAM (see Figure 5.3A and B). Similar trends were obtained for determined values for the hardness of the microstructures too. Whereas initial CAM features a value of 2.7 ± 0.3 MPa, evaluated values for CAM-NER were determined in the region of 1.4 ± 0.2 MPa. The reduction of approximately 50% in both quantities changing from CAM to CAM-NER is at the first glance not impressive, but if the low amount of alkoxyamine crosslinks is considered – ink component TEMPO-methacrylate was present in amounts below 1 wt.% - the 50% change can be seen as remarkable and rather drastic. Furthermore, despite of lowering the mechanical properties of prepared 3D structures, no significant changes in the 3D shape – meaning permanent damage of the microstructure or of parts of it were observable, in contrary the overall shape was perfectly retained after NER postprinting modification (see Figure 5.3C).

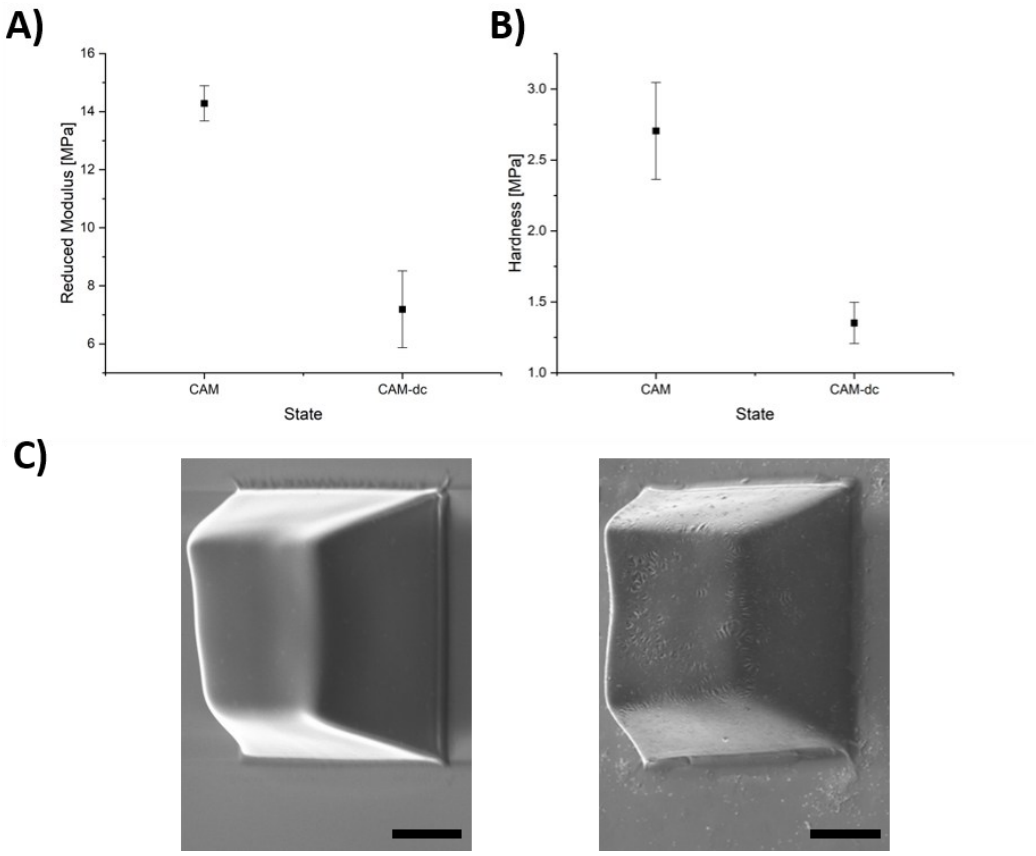

Figure 5.3: Mechanical characterization of CAM and CAM-NER employing nanoindentation. A) Results of measurements of reduced Young's modulus. B) Results of measurements of hardness. C) Tilted SEM image (tilt angle = 40°) of a CAM (left) and a CAM-NER (right) cuboid structure. SEM images were recorded using a magnification of 750x. Scale bars correspond to 10 µm. Adapted from reference [62].

5.2.3.2. Nitroxide-mediated polymerization (NMP)

Exploiting the living features offered by the alkoxyamine bond next step includes investigation of the other possible postprinting modification pathway, the incorporation of an ink extrinsic monomer into the CAM network via well-know controlled nitroxide-mediated polymerization (NMP). As the polymeric network of CAMs contains TEMPO-based alkoxyamine functionalities styrene was selected as a suitable monomer for chain extension within the CAM network, based on its well-known establishment for NMP – especially NMP based on TEMPO. Furthermore, styrene is a monomer that has not been reported as printable monomer for 2PLP yet, making it for the 3D microcommunity inaccessible. So, an operative methodology like the one tested here would incorporate styrene into the 2PLP material library, giving access to its advantageous mechanical properties at the microscale too. Another important point is that polystyrene mechanical properties differ strongly compared to PEG, the main component of the ink. PS exhibited its glass transition at much higher temperature, thus contrasting PEG with its rather low T_g. Thus, strongly deviating material properties were expected, permitting the "material" contrast for the measurement of mechanical properties successively. Thus,

by employing it for postprinting modification of CAM by NMP-based chain extension a distinct change in mechanical properties is expected for resulting CAM-NMP, that should be easily measurable by nanoindentation.

For design of the NMP-based chain extension protocol, a typical NMP procedure is employed including first immersion of the printed CAMs in degassed styrene, sealing the reaction under inert conditions, excluding inhibiting effects by atmospheric oxygen and conduction of NMP subsequently at higher temperatures, in particular 130 °C. To monitor the effect of the reaction time on structures and mechanical properties of initial CAM structures the reaction was conducted at several different reaction times. Obtained CAM-NMP microstructures were subsequently characterized by FTIR microscopy to investigate changes caused by performed modification. In particular measured spectra revealed the presence of characteristic bands for polystyrene, indicating incorporation of it into the CAM network. Comparing FTIR spectra of CAM-NMP with prior CAM, new bands were found for both alkyl stretching vibrations at 2920 cm^{-1} and aromatic C=C stretching vibrations at 1601 cm^{-1} and 1492 cm^{-1} as well as 1450 cm^{-1}. Further C-H out-of-plane bending vibrations were identified at 758 cm^{-1} and 699 cm^{-1}. The presence of all these bands indicates clear evidence for the successful incorporation of polystyrene into the CAM network by NMP chain extension (see Figure 5.4A and B).

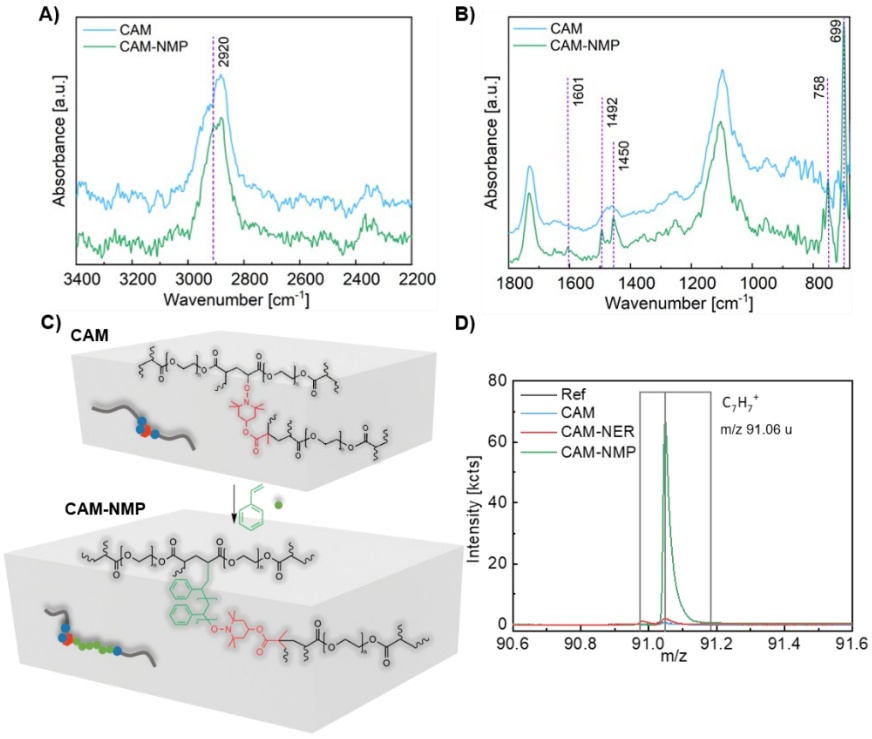

Figure 5.4: FTIR and ToF-SIMS characterization of CAM and CAM-NMP. A) FTIR characterization of CAM and CAM-NMP. Absorption peaks specific for polystyrene are highlighted in the corresponding spectra (purple dashed lines) in the region of 2200 cm^{-1} to 3400 cm^{-1}. B) FTIR spectra of CAM and CAM-NMP in the wavenumber range from ~700 cm^{-1} to 1800 cm^{-1}. Absorption peaks specific for polystyrene are highlighted (purple dashed lines). C) schematic depiction of the postprinting modification of CAM to CAM-NMP via nitroxide-mediated polymerization. D) ToF-SIMS characterization of CAM and CAM-

NMP showing spectra in the region of $C_7H_7^+$ ion species. This species, specific for styrene, is absent in the spectra of the reference microstructure (Ref), CAM and CAM-NER and solely present in the results for CAM-NMP as distinct strong peak. Adapted from reference [62].

Further confirmation of polystyrene integration was revealed by successive ToF-SIMS characterization. Specific for the presence of polystyrene, a strong signal associated with the tropylium cation $C_7H_7^+$ was observable by characterization of the CAM-NMP polymer network. From obtained spectra the strong signal for the tropylium cation is accompanied by a dramatic drop in intensity for the signal of $C_2H_5O^+$ specific for PEG, caused by the dilution effect due to additionally incorporated polystyrene chains. Thus, ToF-SIMS images based on the $C_2H_5O^+$ signal show hardly identifiable microstructures. Decrease of the secondary ion count signal intensities for the alkoxyamine-specific $C_3H_8NO^+$ signal in the CAM-NMP in comparison to CAM was affected by this effect too as visible in mass spectra and ToF-SIMS image (see Figure 5.4D). In addition to characterization results from FTIR and ToF-SIMS further proof for successful chain extension was provided by a dramatic structural increase of CAM-NMP compared to initial CAM geometry dimensions (see Figure 5.5).

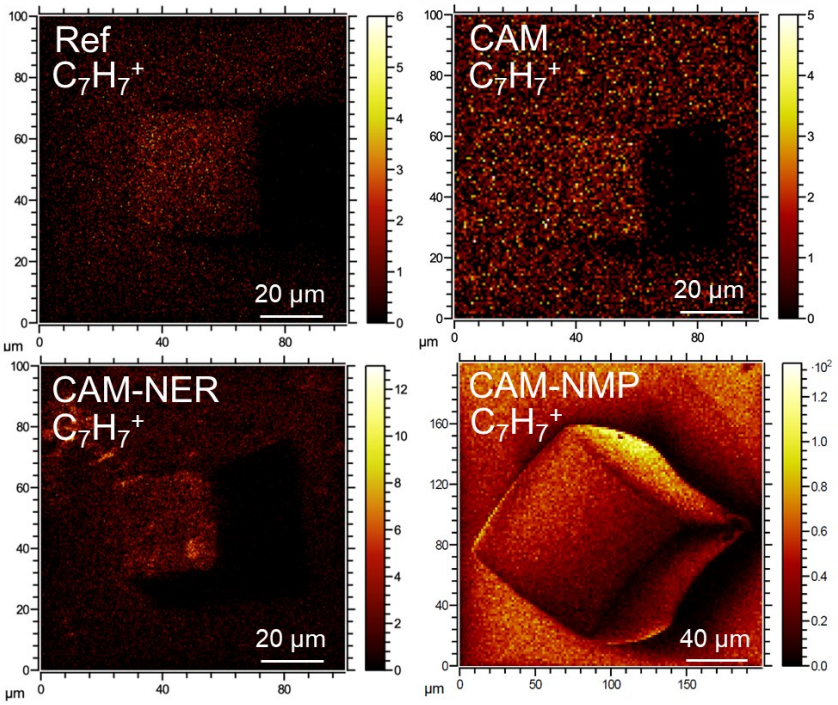

Figure 5.5: ToF-SIMS imaging results associated with the signal for $C_7H_7^+$ on cuboid microstructures of Ref, CAM, CAM-NER and CAM-NMP. Transition from CAM to CAM-NMP is associated with a dramatic increase in size. Adapted from reference [62].

Having confirmed the structural integration of polystyrene within the CAM network, a study of the effect of the polystyrene incorporation in CAM-NMP on the mechanical properties was determined by nanoindentation. For mechanical analysis CAM-NMP specimens were modified by NMP chain extension with styrene for two reaction times, 2 hours and 4 hours, to get additional insight into the temporal progress of property change. Subsequently, reduced Young's modulus as well as hardness

were measured for each sample. Remarkably CAM-NMP samples showed a dramatic increase in mentioned mechanical properties of two orders of magnitude for each of the two studied properties (see Figure 5.6). In particular, the initial value for reduced Young's modulus of 14.3 ± 0.6 MPa was measured for the CAM structures. CAM-NMP structures exhibited a value of 2660.6 ± 108.1 Mpa after 2 hours reaction time. Similarly, hardness increased from 2.7 ± 0.3 Mpa to 201.3 ± 26.4 Mpa. Revealed enormous change in properties is distinct evidence for the incorporation of polystyrene chains into CAM structures, transferring the stiffness originating from their glassy state to final CAM-NMP structures. Reacting the specimens for 4 hours led to no obvious change, but evaluated values for reduced Young's modulus and hardness in the same regime as before. The associated plateau-like behavior of the measured values resulted from the now dominating effect of incorporated polystyrene. Before mentioned structural growth after NMP chain extension was found for the 2 hours and 4 hours samples too (see Figure 5.6A and B). Here a growth in cuboid dimensions proportional to reaction time was evaluated (see SEM pictures in Figure 5.6C).

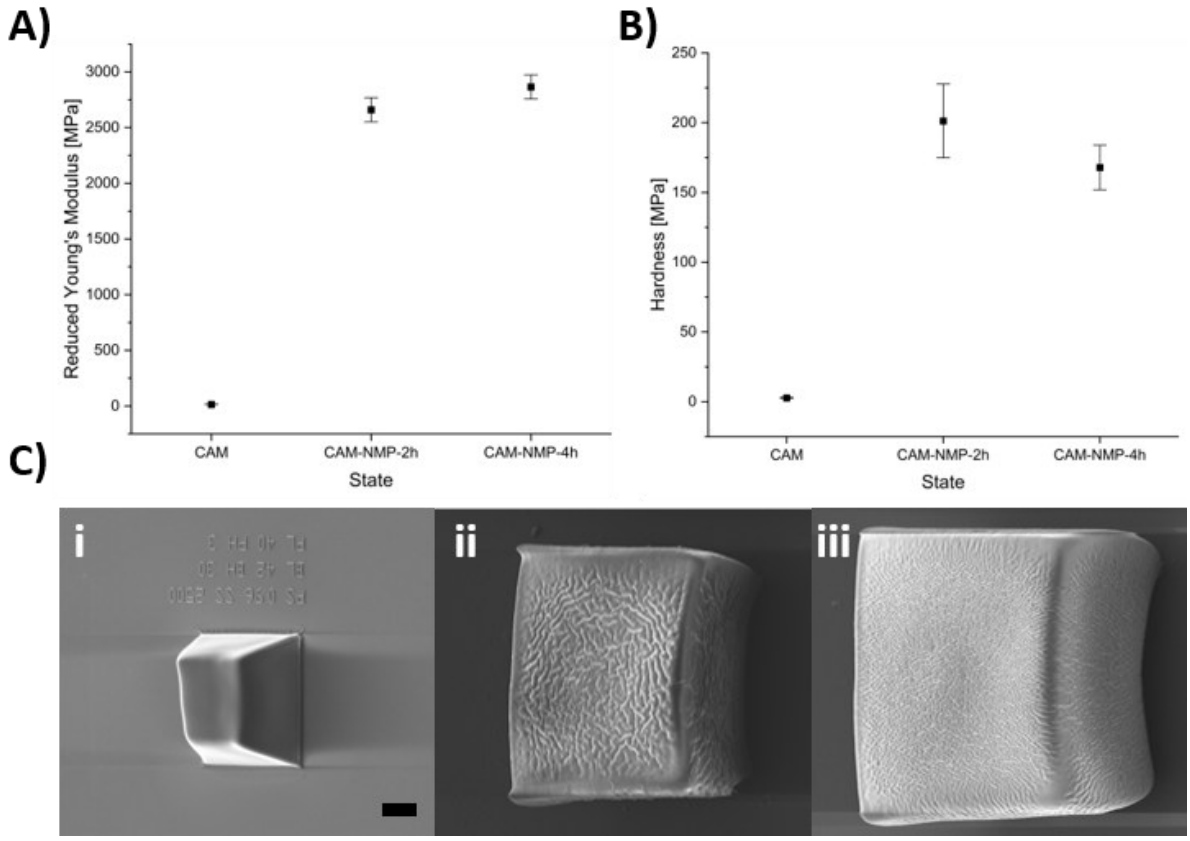

Figure 5 6: Mechanical characterization of CAM, CAM-NMP-2h (= 2 hours postmodification time) and CAM-NMP-4h (= 4 hours postmodification time). A) Measurement results for the reduced Young's modulus. B) Measurement results for the hardness. C) Tilted SEM images of exemplary samples of i) CAM, ii) CAM-NMP-2h and iii) CAM-NMP-4h. Remarkable is the dramatic size increase during postmodification. Adapted from reference [62].

5.2.4. Toward “living” 3D Complex Microstructures

Once the protocols for postprinting modification via NER and NMP were successfully established with simple cuboids, the next step included the generation of more complex 3D structures and investigation of the effect of both modifications on them. In particular main interests were located in the investigation of the quality of printed CAMs featuring higher geometrical complexity and the impact of the postprinting modification on their structural quality, features and size, showing in this way the versatility of the developed approach. In regard to the postprinting modification solely chain extension by NMP employing styrene as ink extrinsic monomer was employed. Initial studies on cuboid systems proved that the NMP modification has a larger impact on the microstructures in terms of property change as well as shape change. Thus, we expect in this case more feedback from the structures. NER was unfortunately quite limited from the rather low incorporation of alkoxyamine bonds during CAM fabrication due to a nitroxide content of less than 1 wt.% in the ink system.

For 3D microfabrication 3D models of a flower, an octopus, and a gecko were chosen, exhibiting the appropriate level of complexity to evaluate 3D printability of the designed ink system. After optimization of laserpower, CAMs featuring mentioned shapes were fabricated from the optimized ink containing TEMPO-methacrylate (see Figure 5.7, left column). Importantly all microstructures were printed on glass substrates pre-functionalized with methacrylate groups to ensure sufficient adhesion of the microgeometries, while performing the postprinting-modification reactions. Scanning electron microscopy (SEM) analysis revealed the high quality of fabricated 3D microstructures, recognizable at the delicate geometrical details such as the disk florets in the center of the flower architecture, or fine details such as the arms and eyes of the 3D octopus. Eminently high level of printability was visible in case of the gecko, where structurally demanding features such as the eyes or the legs were fabricable in a quality allowing to distinguish even between single toes.

After proving the excellent 3D microfabricability of the developed functional ink system, chain extension modification by NMP was performed using optimized reaction conditions. In particular, reactions were performed at different reaction times of 2 hours and 4 hours to see the progress in structure quality while successive styrene incorporation. SEM images of postmodified structures at each reaction time are provided in Figure 5.7 (middle and right column). In case of the microflower, the chain extended flowers after 2 hours and 4 hours display excellent quality in structure – even finest features such as before mentioned disc florets were still easily recognizable – despite enormous structural growth. Quantified, the diameter of the flower grew about 15% after 2 hours and approximately 75% after 4 hours of chain extension via NMP. Similar NMP procedure was performed on octopodes. Mirroring the behavior towards styrene incorporation of the flower geometry, octopodes feature remarkable extension in structural dimensions. After 2 hours of modification head

diameter increased by 69%, after 4 hours even more – 114% growth was observed compared to the initial CAM structure. From SEM pictures it is also obvious that the modified octopus lifted itself up, a consequence of the covalent connection to the methacrylated glass substrate. Importantly, in spite of this level of structural growth, features such as the arms or the eyes were not damaged and still maintained in good quality. Changing to the gecko structure similar observations as for the flower or the octopus geometry were obtained. By measuring the length from the tip of the tail to the tip of the head a length increase of 52% was calculated after 2 hours reaction time. NMP chain extension for 4 hours resulted in a structure length growth of 76%. Notably, the gecko exhibited the best quality of all three structure types – the CAM-NMP gecko, reacted for 4 hours, can be seen as an almost perfect copy of the initial CAM gecko, however much stiffer and larger. The high level of structural maintenance is especially visible by closer observation of the shape of the head, the eyes or the legs with each initial toes distinguishable. Precise inspection of the SEM images of the postmodified versions of the gecko even shows a foot print on the top half of the picture. This foot print shows in both pictures the position of the left back foot of the initial CAM structure, meaning that the structure was lifted partly during reaction, allowing in this way growth in size.

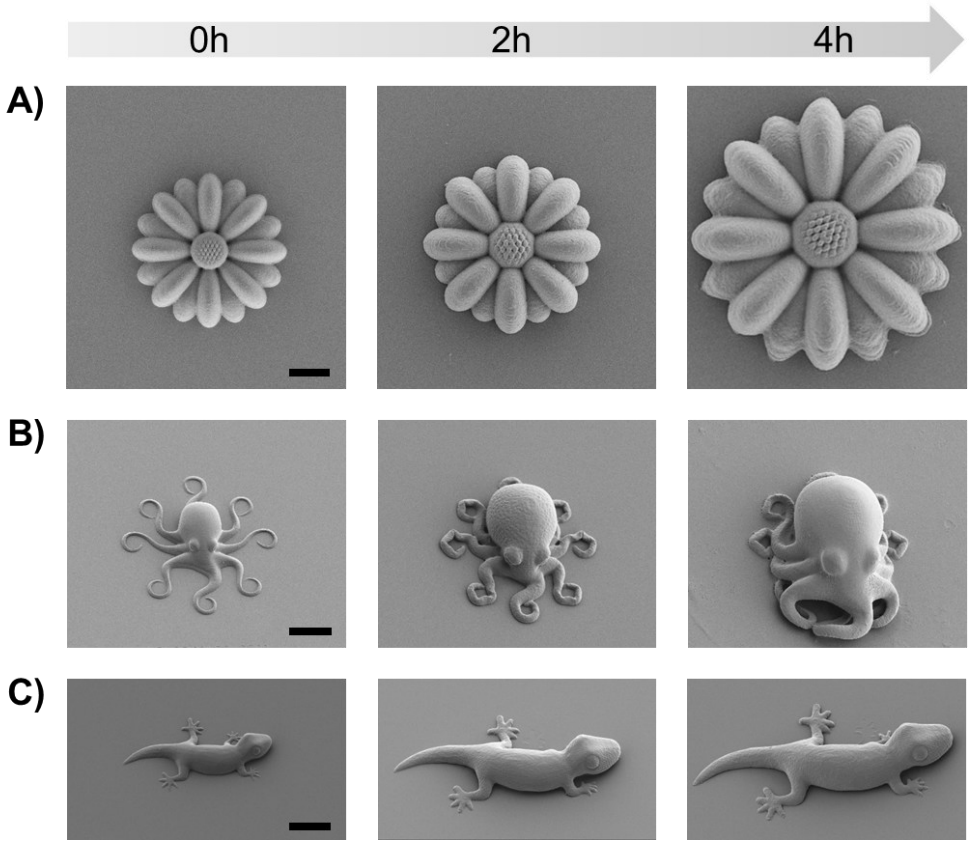

Figure 5.7: 2PLP fabrication of complex structures and their postmodification via NMP chain extension using styrene at different reaction times. Rows show SEM images of different complex structures incuding A) a sunflower (top view), B) an octopus (30° tilt angle for all images in row) and C) a gecko (30° tilt angle for all images in row). First column shows the initial CAM structures, middle column CAM-NMP after 2 hours reaction time and right column CAM-NMP after 4 hours chain extension time. All images of one geometry type were recorded with the same values for magnification allowing in this way size comparison. Scale = 20 µm for all images. Adapted from reference [62].

Comprising these remarkable qualitative results all three structure types show excellent shape and feature maintenance without exhibiting any damage after NMP-based chain extension with styrene. Furthermore, remarkable growth was observed for all geometries – especially notable here the homogeneity of the growing process, which is particularly important in view of practical application of this process for the design of customized parts.

5.3. Summary:

A functional ink formulation allowing 2PLP fabrication of 3D microstructures of highest precision was designed, whose mechanical properties and dimensions respectively size were adaptable by postprinting modification due to incorporation of alkoxyamine functionalities during microprinting. To this aim an ink system consisting of entirely commercially available components was designed. In particular, PEGDA as photocrosslinkable unit, DETC as efficient multiphoton photoinitiator and TEMPO-methacrylate as nitroxide functionality, were utilized allowing formation of alkoxyamine bonds during curing by the 2PLP process. To enable best printing performance optimization of ink composition was performed. Here special attention was given to the ratio of photoinitiator and TEMPO-methacrylate, the nitroxide component. Reason for this was the known inhibiting effect of nitroxides towards initiation and chain propagation, hindering the printing process in general. After optimizing the formulation and corresponding printing parameters, simple cuboid structures were fabricated for subsequent characterization. FTIR and ToF-SIMS characterization of these covalent adaptable microstructures (CAM) revealed the successful inclusion of alkoxyamine bonds into the polymeric network, the foundation for later postprinting modification protocols including nitroxide exchange reaction (NER) and nitroxide-mediated polymerization (NMP). Exactly these reactions were investigated and optimized in the subsequent step on former printed cuboid CAMs. NER reaction applying an excess of TEMPO resulted in the expected decrosslinking of initial CAM structures giving rise to an increased content of nitroxides within the new CAM-NER structures as confirmed by ToF-SIMS. Furthermore, mechanical properties such as the reduced Young's modulus or the hardness were decreased by a value of about 50% as revealed by nanoindentation, without visible observation of any kind of geometrical damage and full maintenance of shape and structural quality. In the next step chain extension by NMP-based postprinting modification was performed on cuboid CAMs employing styrene as ink extrinsic monomer. Styrene was chosen due to its drastically distinct properties compared to the main ink component PEG – being also the main component of the resulting cured polymer network of presented CAMs. In contrast to PEG being in its rubbery state and thus featuring high deformability due to high level of chain mobility within the polymeric network, styrene exhibiting its glassy state at ambient conditions will transform CAMs to much stiffer CAM-NMP structures as hypothesized. After design, optimization and application of a suitable NMP protocol, modified cuboid CAMs – now CAM-

NMP structures - were characterized by FTIR and ToF-SIMS as analytical tools. FTIR analysis displayed high intense bands specific for polystyrene within the modified polymeric network, indicative for polystyrene incorporation. Similar outcomes were obtained from characterization by ToF-SIMS – exhibiting polystyrene-specific signals for the tropylium cation with high intensity, reflecting further evidence for successful NMP chain extension with styrene. Mechanical properties measured by nanoindentation correspond perfectly to prior obtained results from chemical characterization of the CAM-NMP polymer network. A dramatic increase in mechanical properties in the range of two orders of magnitude was observed. Underlining this statement with quantities the reduced Young's modulus of initial CAM was about 14.3 ± 0.6 MPa and the hardness in the range of 2.7 ± 0.3 MPa – in comparison resulting CAM-NMP structures revealed a reduced Young's modulus of about 2660.6 ± 108.1 MPa and a hardness of 201.3 ± 26.4 MPa after 2 hours reaction time. This drastic increase in mechanical properties was accompanied by an enormous structural growth. Further incorporation of polystyrene by extension of the reaction time leads to no further increase in mechanical properties, reaching a plateau, meaning that polystyrene was at the point after 2 hours the material portion within the 3D structure dominating its mechanical properties. However, extension of reaction times resulted in continuous structural growth, enabling doubling of the size or explaining it from another perspective an increase of initial dimensions by the volumetric factor eight.

After design and development of a suitable functional ink system, optimization of its printing parameters and establishment of suitable protocols for postprinting modification reactions – decrosslinking via NER and chain extension via NMP – 3D printing and modification of 3D structures of more complexity was tackled. Here geometries inspired from nature were employed including a flower, an octopus, and a gecko model. The printability was evaluated by SEM image analysis of the microstructures. Exploiting their suitability for chain extension by NMP postprinting modification employing styrene, excellent structure maintenance was revealed for all geometry types, especially visible in the structural retention of finest features, despite enormous structural growth. Furthermore, no loss of the structural features was observed thanks to the homogeneity of the growth process, not limiting the applicability of the presented approach by loss of control.

Chapter 6

Experimental Section

Materials and experimental procedures

6.1. Materials

Isobornyl acrylate (technical grade, contains 200 ppm monomethyl ether hydroquinone as inhibitor, IsobA), poly(ethylene glycol) diacrylate (average M_n = 575 g mol^{-1}, PEGDA 575), poly(ethylene glycol) diacrylate (average M_n = 700 g mol^{-1}, PEGDA-700), tricyclo[5.2.1.0^{2,6}]decanedimethanol diacrylate (TcddA), hexyl acrylate (98%, contains 100 ppm hydroquinone as inhibitor, HexA), phenylbis(2,4,6-trimethylbenzoyl)phosphine oxide (97%, BAPO), Sudan I (Dye content ≥95%), 3-(trimethoxysilyl)propyl methacrylate (98%) and poly(styrene-co-divinylbenzene) microspheres (6.0–10.0 µm avg. part. size) were purchased from Sigma Aldrich. 4-methacryloyloxy-2,2,6,6-tetramethylpiperidine-1-oxyl (97%, TEMPO-methacrylate) was obtained from Alfa Chemistry. Styrene (99%) was obtained from Merck. Dimethylacetamide (99%, DMAc) was purchased from VWR. Styrene (99%) was obtained from Merck. Solvents for development including acetone and isopropanol or for postprinting modification were purchased from Sigma Aldrich or Fisher Scientific. All reagents employed for synthesis of azo dye compounds were purchased from Sigma Aldrich or Fluka. Sylgard 184 (Dow) was purchased from Farnell. All chemicals were used without further purification, unless otherwise noted.

6.2. Methods

Two-Photon Laser Microprinting (2PLP):

a) Shape Memory Polymers at the Microscale

Fabrication of shape memory polymers at the microscale was executed employing a Photonic Professional GT (Nanoscribe) direct laser writing system. Microfabrication of all structures was performed in oil immersion mode using a 63× oil immersion objective (NA = 1.4). Employing Describe software (Nanoscribe) GWL files were generated from STL files of desired geometries and executed by the printer for 3D structure fabrication. Slicing was set to 500 nm and hatching to 250 nm for all microgeometries. Printing was performed with a scan speed of 1000 µm s^{-1} and laser powers in the range of 19.5 to 22.5 mW depending on the structure type. To ensure stability of the samples a custom-built sample holder was used, where the ink was encapsulated. Fabricated structures on substrates were developed for 2 min in acetone and subsequently 1 min in isopropanol, followed by drying in air.

b) CAM sample preparation

Using a commercial 2PLP sample holder (Nanoscribe) for oil immersion mode methacrylate-functionalized glass slides were attached by tape. Immersion oil was added on the unfunctionalized glass slide surface and a hole containing PDMS frame was placed on the methacrylate-functionalized side of the glass slide. The functional ink was added into the hole of the frame, that was closed by placement of glass on top of it, ensuring in this way as far as possible air exclusion. The sample was

utilized directly for microprinting. The entire sample preparation was performed under yellow light conditions.

For preparation of covalent adaptable microstructures (CAM) 2PLP was performed utilizing a commercial Photonic Professional GT 2 (Nanoscribe GmbH) direct laser writing system. Fabrication of all microstructures was conducted in oil immersion mode employing a 63× oil immersion objective (NA = 1.4). GWL files for desired geometries were either coded directly or generated from STL files of 3D structures employing commercial Describe software (Nanoscribe). Slicing was adjusted for cuboid microstructures to 350 nm and hatching to 300 nm. For complex 3D microstructures optimized values of 200 nm for slicing and 300 nm for hatching were utilized. The laser power and scanning speeds were optimized for each geometry type individually. The printed microstructures were developed for 10 min in acetone and subsequently 1 min in isopropanol, followed by drying under ambient conditions. The printed samples were stored under ambient conditions. Microprinting and development were performed under yellow light conditions.

Digital light processing:

3D fabrication via Digital light processing (DLP) was performed utilizing a modified commercial Asiga MAX X27 (Asiga, Australia) DLP printer, offering a pixel resolution of 27 µm. The commercial build platform (Asiga) was exchanged with a home-made aluminum build platform offering a 25 × 25 mm^2 build area. For tray modification, an aluminum inlet was placed inside a commercial tray. Successively, the space between tray walls and aluminum inlet was filled with Sylgard 184 silicone elastomer and cured at rt for 24 h. For printing, STL files of all fabricated geometries were sliced with desired z-layer thickness (50 µm, 100 µm) using the Composer software (Asiga, Australia), and sent to the Asiga MAX X27. Printing was performed at rt under yellow light conditions. After printing the structures were developed for 5 min twice in isopropanol while sonicating them, successively dried, and finally postcured utilizing a Flash UV chamber (Asiga). Postcuring time was chosen individually depending on the geometry type.

Plasma treatment:

Plasma treatment for surface activation of substrates for microprinting was performed with piezobrush PZ2 handheld plasma cleaner (relyon plasma GmbH A TDK Group Company).

Optical Microscopy:

An optical microscope (Leica DM2700 M, Leica Microsystems) equipped with a 10× objective was employed for the inspection of the printed microstructures. Image acquisition and movie recording

were performed via analytical microscope software (LAS X, Leica Microsystems) utilizing a FLEXACAM C1 microscope camera (Leica Microsystems).

Heating stage:

A heating stage (LTS 420, Linkam Scientific Instruments) coupled to the optical microscope was employed to induce the recovery of previously programmed microstructures while heating. The temperature program consisted of a heating cycle from rt to 110 °C using a gradient of 10 °C min^{-1}.

Sputter coating:

Microscopic shape memory structures were sputter coated in initial, temporary and recoverd state with a 12 nm layer of gold. After DnMA measurement test samples were sputter coated with a 10 nm layer of graphite, providing ability for visualization via SEM.

In case of CAM, CAM-NER, CAM-NMP cuboid samples were sputter coated with a 10 nm layer of graphite. Complex 3D structures were sputter coated with 12 nm layer of Pd:Pt.

Scanning electron microscopy:

Scanning electron microscopy (SEM) was performed with Zeiss Supra 55VP (Carl Zeiss AG) at 5 kV. SEM of the micropillars was performed with Zeiss Ultra 55 (Carl Zeiss AG) at 3 kV.

Nanoindentation:

a) Evaluation of viscoelastic properties

For measuring viscoelastic behaviour of 4D macro- and microfabricated SMP nanoindentation experiments were performed using a Hysitron TI 980 Nanoindenter (Bruker) equipped with a nano-DMA low load head as measurement head. A Berkovich tip geometry was applied utilizing a loading rate of 100 µN s^{-1}, a peak force of 500 µN, and a target displacement amplitude of 40 µN at a measurement frequency of 55.75 Hz. Temperature was controlled during experiments by an xSol temperature stage (Bruker). It consists of two ceramic resistor heating modules, one under the sample, one circular around the sample. Both were controlled by a thermocouple and a PID temperature controller. The measurement was thermal drift compensated. Before measurement, the pillars were focused on utilizing the instrument's optics and an automatic drift correction was performed. The indentation head was calibrated against air as well as tip area function before measurement. At the macroscale, one position of the test sample was measured 360 times within one measurement series at each temperature. To assure reproducibility and exclude sample and/or thermal inhomogeneity, a different position within the sample was measured as a control. At the microscale, the measurement series was performed in the similar way as described for the macroscale. Thereby, the control

measurement series was performed for each temperature at a different microstructure printed using the same conditions.

b) Evaluation of reduced Young's modulus and hardness:

Nanoindentation of reference microstructure CAM, CAM-NER, and CAM-NMP was performed by application of a trapezoid loading function with a loading and unloading rate of 200 nm s^{-1} up to 1 µm and a plateau time of 2 s. The measurement was performed on dried samples with a diamond Berkovich tip and automatic drift control. For each sample type (CAM, CAM-NER, and CAM-NMP) n = 10 measurements were carried out and a mean value with standard deviation was calculated from the obtained results. Values for the reduced Young's Modulus and the hardness were calculated according to published work.[317]

Dynamic mechanical analysis (DMA):

DMA was employed to determine the thermomechanical properties of the printed materials. 3D printed strips were (29.40 mm length, 7.83 mm width and 0.90 mm thickness) characterized employing a Triton Technology TTDMA. The response of the samples was observed in the temperature range of 0 °C to 110 °C with a heating rate of 3 °C min^{-1} and a frequency of 1 Hz. For the opto-mechanical characterization, the DMA measurements were conducted under irradiation with a wavelength of 459 nm.

^{1}H NMR spectroscopy

^{1}HNMR spectra were recorded on a JEOL ECZR600 FT NMR spectrometer featuring a ^{1}H operating frequency of 600 MHz). ^{1}H chemical shifts were reported relative to TMS (δ = 0) and referenced against solvent residual peaks. Chloroform-d (Sigma-Aldrich, 99.8 atom%) or dimethyl sulfoxide-d6 (Sigma-Aldrich, 99.95 atom%) was employed as deuterated solvent (CDCl3: 7.26 ppm for ^{1}H NMR, DMSO-d6: 2.50 ppm for ^{1}H NMR).

UV/Vis Absorption spectroscopy:

UV/Vis Absorption spectra were recorded employing a Shimadzu UV-1900i UV-Vis Spectrophotometer, using a resolution of 0.5 nm.

Fourier transform infrared spectroscopy (FTIR):

FTIR analysis was conducted on a JASCO FT/IR-4600 FT-IR spectrometer.

Attenuated Total Reflection Fourier Transform Infrared (ATR-FTIR) spectroscopy

A Bruker Optics Tensor 27 spectrometer with room temperature deuterated triglycinesulfate (RT-DTGS) detector and a Bruker Optics Platinum ATR accessory (diamond crystal with one reflection) were used (Bruker Optics, Ettlingen, Germany). The ink, consisting of PEG-DA, DETC, TEMPO-methacrylate, and DMAc, was placed on the diamond crystal directly without any additional sample preparation. The spectrum was recorded at room temperature (≈22 °C) from 4000 to 400 cm^{-1} with a resolution of 4 cm^{-1} against an air background. The absorption band positions are given in wave numbers (cm^{-1}).

FTIR Microscopy

For FTIR Microscopy a Bruker Hyperion 3000 FTIR Microscope (Bruker Optics GmbH Ettlingen, Germany) equipped with a mid-band MCT-detector cooled by liquid nitrogen was used. The measurements of the structured micro samples were done by using a Bruker 20x ATR-objective with a Ge-crystal tip resulting in a field of view of ≈40 μm^2. The contact pressure on the sample was set to 0.5 N. Sixty-four scans were integrated for each spectrum, all spectra were measured against an air background with a bandwidth of 650–4000 cm^{-1} and all samples were examined in the dried state.

Time-of-Flight Secondary Ion Mass Spectrometry (ToF-SIMS)

ToF-SIMS of reference microstructure (Ref), CAM, CAM-NER and CAM-NMP was performed on a TOF.SIMS5 instrument (ION-TOF GmbH, Münster, Germany), all samples were measured in the dried state. The instrument features a Bi cluster primary ion source and a reflectron type time-of-flight analyzer. UHV base pressure was $<5 \times 10^{-8}$ mbar. For high mass resolution investigation, the Bi source was operated in the “high current bunched” mode, providing short Bi+ primary ion pulses at 25 keV energy, a lateral resolution of ≈4 µm, and a target current of 0.35 pA. The short pulse length of 1.0 ns enabled a high mass resolution. The primary ion beam was usually rastered across a 500 × 500 μm^2 field of view on the sample, and 256 pixels were recorded. Spectra were calibrated using the omnipresent C^-, C_2^-, C_3^-, or the C^+, CH^+, CH_2^+, and CH_3^+ peaks. Based on these datasets, the chemical assignments for characteristic fragments were determined. For high lateral resolution imaging, the primary ion source was operated in “delayed extraction” mode. In this mode, the lateral resolution of the instrument is in the range of 150 nm, and this mode provides a good mass resolution of >4000 m Δm−1. Here, in “delayed extraction” mode, a concentric field of 100 × 100 μm^2 on reference microstructure, CAM, CAM-NER, or a concentric field of 200 × 200 μm^2 on CAM-NMP were analyzed respectively, and 256 × 256 data points for all samples were recorded.

Thermogravimetric analysis (TGA):

TGA was performed applying a Q600 (TA Instrument) on polymeric samples heating them from 30 °C to 700 °C with a heating rate of 10 °C min^{-1}.

Digital microscopy:

Digital microscope images of the samples were recorded with a high-resolution digital microscope ZEISS Smartzoom 5 utilizing a ZEISS objective PlanApo D 1.6 x/0.1 FWD 36 mm.

3D scanning:

3D scans of the printed structures were recorded with a a E4 3D scanner (3Shape) featuring a scanning accuracy of 4 µm.

Infrared imaging:

Infrared imaging was conducted using a Optris PI 640i infrared thermal imaging camera.

6.3. Procedures

One-way-SMP-Ink Preparation (Macroscale formulation)

Sudan I (3.2 mg, 0.05 wt% in terms of monomer), BAPO (128 mg, 2.0 wt% in terms of monomer), TcddA (1227 mg, 4.03 mmol), PEGDA 575 (464 mg, 0.81 mmol), IsobA (4700 mg, 22.56 mmol), and HexA (126 mg, 0.81 mmol) were mixed for 24 h at rt protected by aluminum foil under yellow light conditions. After reaching a homogeneous solution the resin was directly used for DLP printing.

One-way-SMP-Ink Preparation (Microscale formulation)

BAPO (7.2 mg, 2.2 wt% in terms of monomer) was added to a mixture containing TcddA (96.4 mg, 317 µmol), PEGDA 575 (121.5 mg, 211 µmol) and IsobA (110.0 mg, 528 µmol) in a brown glass vial under yellow light conditions. The mixture was stirred for 1.5 h at rt to ensure homogeneity and stored protected from the light inside the fridge (at 6 °C) until usage.

LSMP-Ink Preparation (Macroscale)

Similar amounts and components as for the macroscale one-way SMP macroscale formulation. Additionally, Cl – Azo dye, H – Azo dye, NO_2 – Azo dye or OCH_3 – Azo dye for preparation of the corresponding LSMP ink (Azo Cl, Azo H, Azo NO_2 and Azo – OCH_3. After stirring for 24 hours protected by aluminum foil to ensure homogeneity at rt the ink was applicable for 4D fabrication. Preparation was performed under yellow light conditions.

CAM-Ink Preparation (2PLP)

TEMPO-methacrylate (8.24 mg, 0.0342 mmol) and DETC (5.00 mg, 0.0152 mmol) were added to a brown glass vial and suspended in PEGDA-700 (500 mg, 0.714 mmol, 446 µL) and DMAc (28.2 mg, 0.323 mmol, 30 µL). After sonication until complete dissolution of TEMPO-methacrylate and DETC, examination of the final ink under microscope was conducted to ensure absence of insoluble particles at the microscopic regime. The ink was stable and printable over several months of storage at rt in darkness or yellow light conditions.

Substrate Functionalization

To improve adhesion of 3D printed microstructures glass slides (Marienfeld, 170 ± 5 µm strength) were washed first with isopropanol, then with acetone, and dried using pressurized N2. Subsequently, the surface was cleaned and activated for 1 min by plasma treatment. Following this, the glass slides were immersed in a 4×10^{-3} M solution of 3-(trimethoxysilyl)propyl methacrylate in toluene for 1.5 h. After washing twice in toluene and once in acetone and successive drying by pressurized N_2, the methacrylate-functionalized glass slides were used as substrates for 2PLP microfabrication. The entire substrate functionalization and subsequent storage were performed under yellow light conditions.

Screening of Printing conditions at the Macroscale:

Applying the Material Test function of the Asiga MAX X27 (Asiga Australia), data points for generation of the material printing file were evaluated. Thereto after adjustment of the irradiation intensity (8.0 mW cm^{-2} and 13.0 mW cm^{-2}), a droplet of ink was placed on a glass slide (Marienfeld, 170 ± 5 µm) inside a commercial tray (Asiga) and irradiated. After irradiation for a selected time frame, the polymerized part of the droplet was washed with acetone. Afterward, the thickness of the solidified film was measured using a digital caliper. The film thicknesses were noted for several irradiation times and used for the generation of the material printing file and the Jacobs working curves.

Shape Memory Tests (Macroscale formulation):

3D printed macrostructures were heated to 80 °C utilizing a water bath, deformed and fixed in water at rt. Recovery was performed at 80 °C utilizing a preheated water bath. “Dry” recovery was performed by heating the 3D macrostructures above Tg employing a heating gun.

Shape Memory Tests (Microscale formulation):

The substrates containing the 3D printed microstructures were fixed via polyimide tape onto a microscope slide and heated inside a drying oven to 109 °C. After ensuring the sample to be above transition temperature, the programming of the sample was executed by positioning a polished metal

block (172.9 g) on top of the glass slide to induce deformation by compression and programming of the structure. By cooling to rt while maintaining the stress the temporary shape was fixed. The temporary shape was confirmed by observation via microscope. For recovery the sample was heated up to 110 °C applying a temperature gradient of 10 °C min^{-1} using a heating stage. Recovery was followed by microscopic observation and recorded via analytical microscope software.

Microsphere Trapping:

A poly(styrene-co-divinylbenzene) microsphere suspension (1 wt% in isopropanol) was prepared. A drop of the suspension was added to the microtraps in their initial shape. After evaporation of isopropanol and verification of successful loading by observation via microscope, previously described shape memory cycle was performed.

Analysis of double bond conversion (DOC) via FTIR

The recorded FTIR-spectra of the ink and the printed structure ("as printed") (see Figure 6.1) have been employed for estimation of the level of double bond conversion (DOC)[318] achieved during photocuring while 3D printing. To achieve this the signal area of the band at 809 cm^{-1} associated with the acrylate group's double bond was compared to the signal area of the band located at 1720 cm^{-1} corresponding to the stretching band of the carbonyl groups, and important for this purpose not affected during printing. Employing these ratios for the cured samples and the ink in equation 6.1 allows calculation of DOC.

$$DOC = 1 - \frac{A_{C=C}^{as\ printed} / A_{C=O}^{as\ printed}}{A_{C=C}^{ink} / A_{C=O}^{ink}}, \qquad \textbf{(Equation 6.1)}$$

To determine the DOC, regions of interests with the FTIR spectra were first normalized and baseline corrected. Subsequently, relevant peaks were fitted by Lorentz and Gaussian functions allowing to obtain the signal area of each peak. Employing these fitted peak areas in equation 6.1 enables calculation of the DOC.

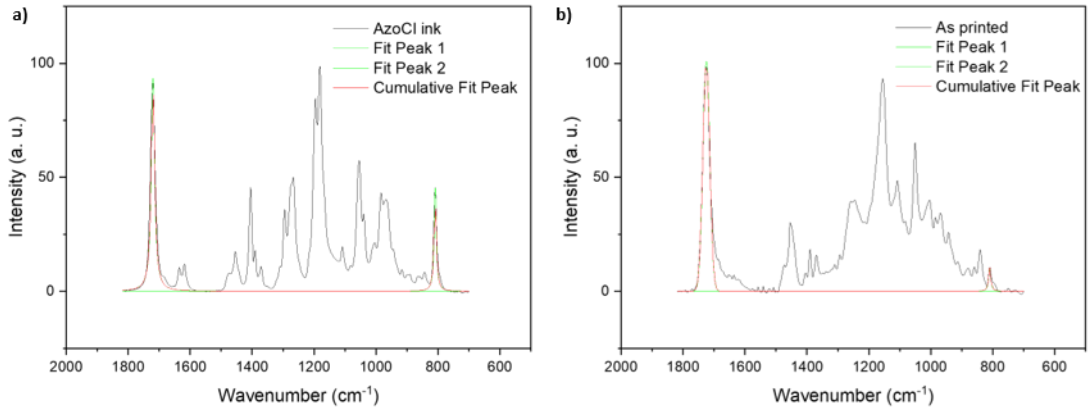

Figure 6.1: Regions of the FTIR spectra of a) the AzoCl based ink and b) the corresponding 3D printed polymer employed for the DOC calculation. The Signal at 809 cm^{-1} corresponds to the double bond of the acrylate functionality and the other signal at 1720 cm^{-1} is associated with the stretching band of the carbonyl group.

Analysis of the lateral resolution of the printed samples

A custom-designed test structure composed of a rectangular block with different engraved line gratings was employed for characterizing the optimal lateral resolutions. The line width and period of engraved line gratings had values of 1000, 500, 250, 100, 50, 40, 30 µm encompassing the relevant range of "fine" feature sizes within DLP printed structures. The models were 3D printed using each of the azo-dye based inks applying optimized printing parameters for each. Fabricated test structures were analyzed using a high-resolution digital microscope.

Postprinting Modifications: CAM-NER

The printed CAMs were placed in a sealed vessel with an excess of 2,2,6,6-tetramethylpiperidine-1-oxyl (TEMPO) (20.0 mg, 0.128 mmol), degassed toluene (1.80 mL, 1.56 g, 0.0170 mol), and methanol (0.200 mL, 0.158 g, 0.00493 mol) under N2 atmosphere and heated to 100 °C inside an oven. After 8 h reaction time, the samples were washed using THF and isopropanol to remove unreacted TEMPO. Afterwards CAM-NER samples were dried under vacuum and stored under ambient conditions.

Postprinting Modifications: CAM-NMP

Nitroxide-mediated polymerization (NMP) was performed by the addition of degassed styrene (2.00 mL, 1.82 g, 0.0175 mol) to a sealed reaction vessel containing the printed CAMs under N_2 atmosphere. After heating for 130 °C inside an oven for prior described reaction times, the samples were washed in THF and isopropanol to remove unreacted styrene, dried under vacuum, and stored under ambient conditions.

Chapter 7

Conclusions and Outlook

7.1. Conclusion

In the current thesis, several programable materials based on SMP and “living” systems have been designed and successfully integrated into light-based 3D/4D printing.

In a first work, (described in chapter 3 entitled “4D Printing of Shape Memory Polymers: From Macro to Micro”), a novel ink system was introduced allowing 4D fabrication of shape memory polymers at the macroscale as well as the microscale employing light-based 3D printing technologies. Macroscale 4D structure fabrication was performed using digital light processing (DLP) technology, whereas microscale 4D printing was conducted via 2PLP. Based on the specific requirements of each printing method, a general ink system was identified comprising ink core components suitable for both techniques. In particular, a system composed of monofunctional acrylate as main chain builder and a dual system of as soft and stiff crosslinker. Notably, the monofunctional component was responsible for setting the shape memory transition temperature, here a glass transition temperature, whereas crosslinkers accounted for appropriate printability. This core system was adapted and optimized for each printing technology in regard to component ratio and additional additives such as photoabsorbers to guarantee best performance in terms of printability as well as shape memory actuation at both size regimes. Finally, two formulations, one for each dimension, were developed and employed 4D structure fabrication. A spectrum of different structure types was fabricated at macro- and microscale – ranging in their level of complexity. In summary, excellent printing performance was evaluated both regimes, visible by defect-free fabrication processes and excellent structural quality. By measurement of viscoelastic properties via dynamic nanomechanical analysis (DnMA) a glass transition region in the range of 70 °C was evaluated for macroscale objects. Microscale structures exhibit rather low glass transition temperatures in the range of 25°C, one of the lowest yet measured for printed microscopic architectures. Having knowledge of the transition temperatures, shape memory test were designed for both scales. At the macroscale excellent qualitative actuation behavior was found, further supported by quantitative characterization revealing shape fixity values of 98% as well as shape recovery ratios of 97%. Similar actuation behavior was found at the microscale mirroring the quality achieved at the macroscale. Concluding the presented SMP macroformulation is in terms of printing and shape memory performance comparable with reported SMP systems in literature. However, the microformulation appears due to several features superior to all published systems yet. Importantly, it is possible to print complex structures featuring intricate structural units such as overhangs. Furthermore, there is no additional effort concerning synthetic preparation necessary to generate an ink component or to prepare the designed formulations. All substances necessary for the formulation are commercially available at a low price for developed systems at both size regimes. Ink preparation can be performed by simple mixing of the individual components at rt without the requisiteness of

special equipment or additional reaction steps. The structures can be fabricated directly from the ink and applied immediately after manufacturing. Thus, the whole 3D/4D printing community is capable of using described systems, because no special theoretical or practical knowledge in chemistry is needed. Additionally, the described microink formulation can be manufactured in an acceptable range of laser powers, rendering it less prone to structural defects during the 3D building process. This low propensity towards structural damage respectively defects is also reasoning the superior structural quality of fabricated SMP microgeometries, featuring altogether excellent surface smoothness and the absence of any irregularities. In contrast to reported examples described in the theoretical part, the designed SMP microsystem in this wok can be actuated in air or liquid. Moreover, the presented approach enables for the first time a functional SMP system that can be printed and actuated at both size regimes. I believe that the presented approach and materials have good prospects being employed in a variety of fields due to its versatility and facile accessibility opening opportunities for smart applications. Large application potential can be envisioned especially for the microformulation in soft microrobotics, in biomedicine or in smart microsensors due to its excellent printability and the opportunity for actuation at low temperatures.

In the next step (described in Chapter 4 entitled “4D Printing of Light activated SMP based on Organic Dyes”), a functional ink system allowing 4D fabrication of light activated shape memory polymer (LSMP) architectures was introduced. In particular, prior designed shape memory ink formulation for macroscale fabrication via DLP was modified by addition of a push-pull azo-dye species translating the prior stimulus temperature to light, by exploitation of their photothermal effect. At the same time azo dyes will also act as photoabsorbing units during 3D fabrication, enabling in this way high-quality 3D fabrication with excellently resolved features and low minimal structure sizes. To incorporate both effects a library of four push-pull azodyes was synthesized, each equipped with an acrylate functionality permitting direct covalent integration of the functional unit into the polymeric network, preventing in this way reduction in performance due to loss of functional structures during washing cycles. Following determination of suitable azo-dye concentrations in the ink, four LSMP inks containing each one of the azodyes were prepared. After evaluation of suitable printing parameters printing tests showed excellent printability visible by fast printing speeds at low layer thicknesses (50 µm) and excellent lateral resolutions down to 40 µm. Next test structures of each ink were analyzed in regard to their thermo-mechanical, opto-mechanical- and light induced shape recovery performance. Comparing all results, the ink system based on the azo-dye functionalized with a chlorine group was selected for fabrication of more complex LSMP structures for shape memory tests. Good printability was observed by manufacturing a range of structures featuring different complex structural moieties such as overhangs or fine features. Light activated recovery employing a blue laser at 459 nm revealed excellent spatially controlled shape memory behavior. Precise spatially confined recovery as well as a

multitude of intermediate shapes were accessible while performing recovery, superior to thermoresponsive actuation that offers solely one temporary and one permanent shape. Concluding this section, a simple strategy towards a LSMP system – based on a push-pull azo-dye – permitting the translation of the temperature stimulus towards a light stimulus with all its advantages was presented. Making use of the photoabsorbing and photothermal properties featured by azo-dyes allows 3D fabrication at high resolutions and incorporation of advanced light-responsive shape memory functionalities. Considering all these aspects the author believes that based on its simplicity, flexibility and reliability, the proposed system and approach will open new opportunities in a multiplicity of fields, such as soft robotics, actuators, or smart sensing applications to name some exemplary.

Accessing another aspect of 4D printing (described in chapter 5 entitled "Combining Two-Photon Laser Printing and Alkoxyamine Chemistry: Toward Living 3D Microstructures") a novel printable material comprising aspects of living additive manufacturing – by incorporation of dormant alkoxyamine bond enabling NMP-postfunctionalization – as well as features of covalent adaptable networks – the possibility for dissociative nitroxide exchange reaction – was designed. Offering in this way high potential for tunability of a variety of properties for the realization of custom design of precisely fabricated microparts, based on alkoxyamine chemistry. To achieve this, a simple ink system composed of entirely commercially available components was designed. Implementing the "living" feature, a methacrylated TEMPO moiety was selected as functional ink component, allowing fabrication of dormant alkoxyamine bonds during 2PLP fabrication. Optimization of the ink formulation and its printing parameters allowed precise fabrication of 3D microstructures. Subsequently, postprinting modifications including network decrosslinking via nitroxide exchange reaction (NER) as well as chain extension nitroxide-mediated polymerization (NMP) were designed and applied on cuboid CAM structures. By employing NER mechanical properties such as reduced Young's modulus and hardness were reduced by 50% while maintaining all structural features perfectly. This rather low decrease was explainable by the low amount of dynamic alkoxyamine bonds due to low source of TEMPO-methacrylate in the functional ink – below 1%. Having this in mind, the reduction was nevertheless quite remarkable. In addition, NMP using styrene as monomer had a more drastic effect on mechanical properties visible by the increase of two orders of magnitudes for both entities. Furthermore, a remarkable size increase towards eight times the original volume was observed, while maintaining the overall cuboid shape. Employing the functional ink complex microstructures including a flower, a octopus and a gecko geometry were printed in a remarkable quality featuring smooth surfaces as well as defect-free manufacturing. Performance of NMP postprinting modification based on styrene led to the expected increase in mechanical properties as well as growth in size, while perfectly maintaining the overall shape and corresponding fine features. Concluding this section, I am convinced that the presented approach to generate customized 3D microstructures will find broad application in a variety

of promising fields such as micro robotics, smart sensors, microfluidics or microengineering in general. The strength lies in the fact that designed methodology includes on the one hand simplicity in ink preparation – all components are commercially available –, excellent printability – scan speeds in the region of 2500 µm s^{-1} can be reached outperforming existing systems employing NMP mechanism for 2PLP, high precision in microstructure fabrication thanks to the features of the 2PLP method, facile post-printing-modifications – feasible with a minimum of synthetic effort –, as well as excellent control in adjustability of mechanical properties and size. Here the author just exploited postmodification by chain extension with styrene. Certainly, other monomers – unprintable via 2PLP – can be applied too, extending the library of accessible materials and properties for 2PLP fabricated architectures. Contrastingly to the presented approach tuning towards medium stiff or even softer materials is an offered feature, still to be performed. Paving the way towards fully adjustable structures in terms of mechanical and dimensional properties the developed approach will allow access to multiplicity of useful applications for science and industry as anticipated by the author.

7.2. Outlook

As visible in the chapter 3 and 4 one key point for the applicability of a 4D printed part is the amount of information – in case of shape memory polymers the number of shapes – that can be stored within one actuation respectively shape memory cycle. The presented systems exhibiting a one-way SME with one transition temperature only allow the accessibility towards one programmable temporary shape. Furthermore, the actuation is due to the inherent property of one-way SMPs irreversible, limiting in this way the extent of applicability. Tackling the first problem of limited number of accessible shapes, the transfer of the acting stimulus from temperature to light allows accessibility towards a multiplicity of temporary shapes due to the possibility of spatial resolved heating and thus spatial controlled recovery. This stimulus transfer of SMPs from temperature to light was at the time this thesis was written only possible at the macroscale and not investigated at the microscale. Direct transfer of the design concepts established in chapter 4 for light activated SMP structures is thus favorable for the microscale too, for example in case of light activated microrobots or microsensors. Another way to increase applicability of shape memory polymers is the incorporation of multi-stimuli responsive features, allowing on the one hand precise control as well as orthogonal applicability of each stimulus. In this way, complex systems such as microrobots whose functionalities are controlled by different stimuli decoupled from each other – for example motion via magnetic fields by inclusion of magnetic nanoparticles in the 2PLP ink, actuation such as “gripping” via temperature by incorporated temperature responsive moieties and drug release via light. Requirement for this is a printing technology permitting multimaterial fabrication, which is possible by 2PLP. Another strategy to increase versatility of 4D printed SMP is incorporation of multiple temporary shapes. This can either

be realized by incorporation of multiple transition temperatures or one broad glass transition temperature, taking advantage of the temperature memory effect. In theory, the first can be easily realized by incorporation of different immiscible polymer phases, for example two or more melting and crystallization transitions or several glass transitions by exploitation of the polymerization-based phase separation mechanism during the network curing process. The other option – the incorporation of one broad glass transition – might be possible by integration of large network crosslinking density. Major point for consideration must be taken for the level of crosslinking density. Dynamic actuation behavior will be inhibited by high crosslinking densities rendering the thermoplastic network to a stiff network with rather thermoset character. However, even if it is possible to integrate multiple transitions in a polymeric network, the shape memory actuation will be most likely irreversible meaning exhibiting one-way character. To overcome this, generation of reversible shape memory polymers – also termed two-way shape memory polymers – would be a possible solution. Temperature responsive reversible actuation would be particularly desirable for a multiplicity of applications starting from smart microactuators going to soft microrobots able to perform tasks multiple times or smart sensor being usable for several working steps without new programming. Especially the last-mentioned point would increase the applicability of such systems dramatically. Thinking further into future, combination of such micoreversible SMPs with multistimuli response features would allow to create the ideal “intelligent” device able to conduct a versatility of tasks imaginable in biomedical therapies or micro- and nanoengineering.

Changing from programmable materials towards “living” respectively “lifelike” 4D materials permitting adaptability and customized design in regard of geometrical and mechanical, physical or chemical properties large potential can be envisioned for industry, society and science. The present approach takes advantage of dynamic alkoxyamine chemistry exploiting NER and NMP as adjusters for mechanical properties. In case of NER decrosslinking a response of higher impact can be expected in case of higher dynamic alkoxyamine bond incorporation for example by utilization of crosslinking species containing two or more dormant units. In this way the inhibition effect caused by the stable nitroxide radical during the 2PLP initiation and propagation process could be reduced or completely avoided. In case of NMP chain extension other monomers apart from styrene can be employed. As discussed in the theoretical part of this thesis progress in nitroxide design extended the spectrum of applicable monomers drastically, opening lots of modification possibilities in regard of the here presented approach. Beside alkoxyamine chemistry other living chemistries can be in principle used to for fabrication of “living” structures. Here systems based on other “living” polymerization techniques such as RAFT would be in general favorable due to their oxygen tolerance and their rather fast curing kinetics as shown in several macroscale examples in the theoretical part.

Finally, one important consideration for future applications especially for biomedical applications is biocompatibility as well as biodegradability of functional 4D printed structures. Rendering above mentioned materials – programmable SMP structures and "living" adaptable microstructures – biocompatible would open new dimensions in applicability for biological research, biomedical therapy as well as customized medical approaches in general. Combined with full biodegradability would allow for example easy implementation of the printed systems for drug therapies etc. due to the absence of nondegradable plastics, that would accumulate. Biodegradability would also minimize the impact of these future materials on environmental pollution due to absence of waste accumulation by nondegradable printing products. So future efforts must be strained in this direction.

Worth mentioning too is that the recent decade has led to the appearance of a multitude of novel respectively advanced printing methods in light-based technologies including volumetric approaches or two-step absorption microfabrication. The library of applicable materials for these techniques is still limited and most available ones are static. Here lies an enormous potential for materials scientists and chemists to fill these voids with suitable functional and smart 4D materials.

Concluding I believe 4D materials – especially shape memory polymers and "living" materials – will have a great future and further progress in material development extending their programmability, their versatility and their biocompatibility as well as their biodegradability will confirm their status as advanced future key materials for society, industry and science.

Appendix

Synthetic procedures, spectra and additional data

a) Synthetic Preparation of Photopolymerizable Azo-dyes

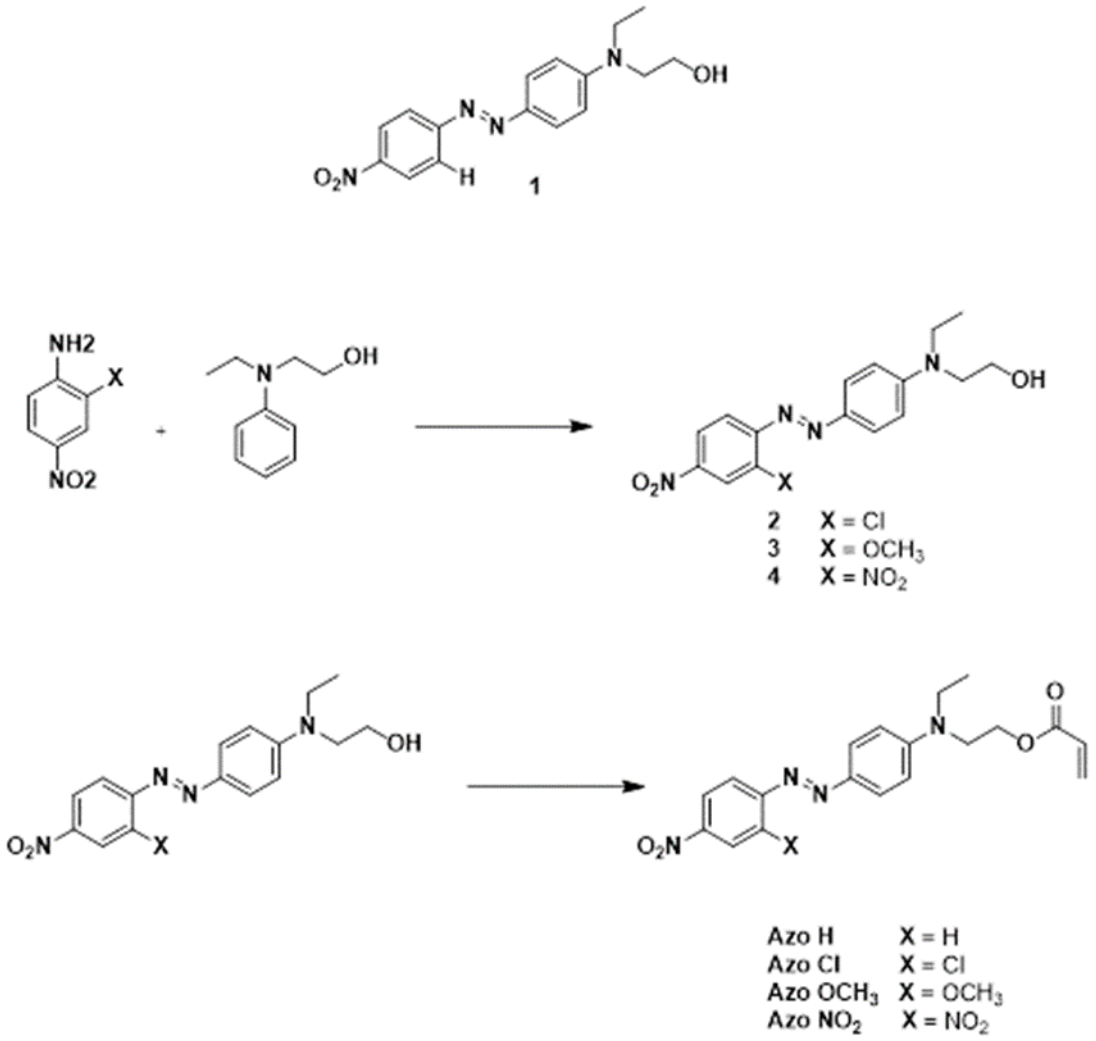

Scheme S1: Synthesis towards push-pull azo-dyes (top). Subsequent reaction step towards acrylate functionalized azo-dye compounds (bottom).

Compound 1 was obtained directly from Sigma-Aldrich and used without further purification.

Compound 2 was prepared according to a reported procedure.[319] Characterization data is in agreement with the reported data. A yield of 85% was obtained.

^{1}H NMR (600 MHz, Chloroform-d, Figure S1) δ 8.40 (d, J = 2.4 Hz, 1H), 8.16 (dd, J = 8.9, 2.4 Hz, 1H), 7.95 (d, J = 9.2 Hz, 2H), 7.78 (d, J = 8.9 Hz, 1H), 6.86 (d, J = 8.7 Hz, 2H), 3.91 (t, J = 5.8 Hz, 2H), 3.64 (t, J = 5.9 Hz, 2H), 3.59 (q, J = 7.1 Hz, 2H), 1.27 (t, J = 7.1 Hz, 3H).

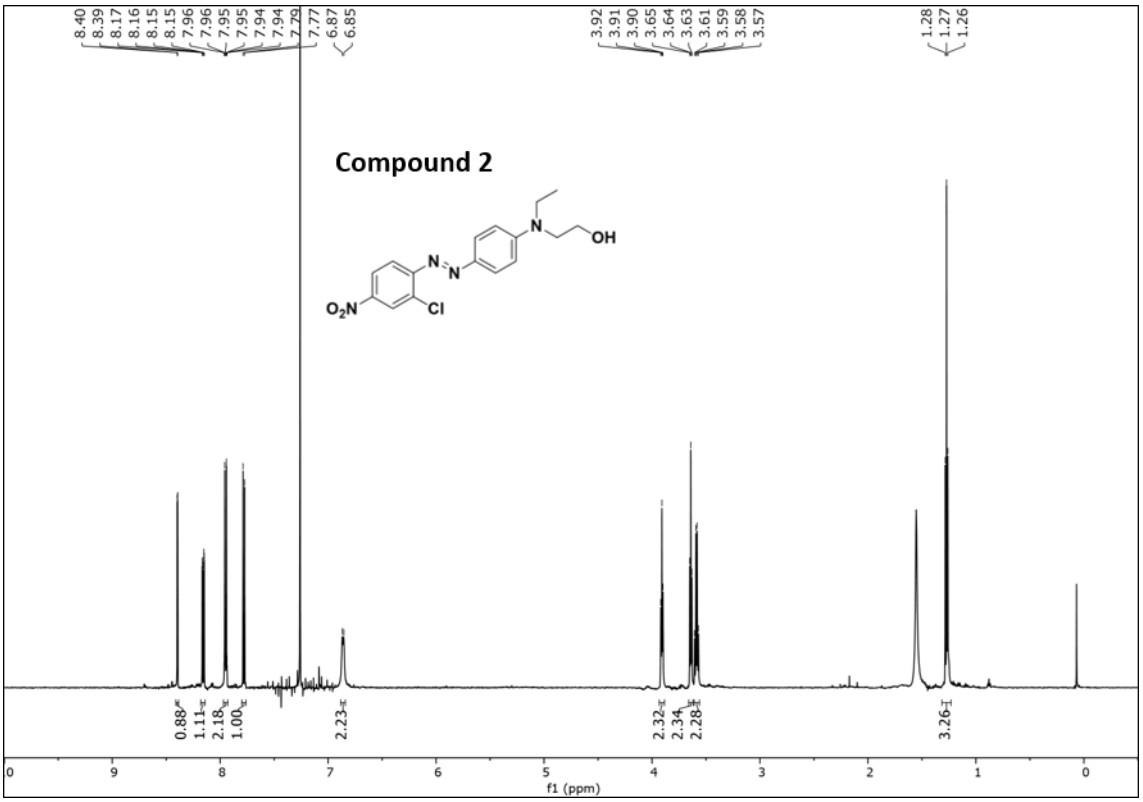

*Figure S1: [1]H-NMR spectrum of compound **2** (600 MHz, Chloroform-d).*

Compound 3 was synthesized according to the procedure depicted in Scheme X). Aniline (0.500 g, 2.97 mmol, 1 eq) was dissolved in 50 ml of a solution of H_2O/CH_3COOH (1:4) while being stirred in a round bottom flask. The mixture was put in an ice bath and the temperature was monitored to reach 0-5°C. $NaNO_2$ (0.225 g, 3.27 mmol, 1.1 eq) was dissolved in deionized H_2O (10 mL), cooled to 0-5°C and subsequently added to the aniline solution dropwise. After 30 minutes, 2-(N-ethylanilino)ethanol (0.577 mL, 3.564 mmol, 1.2 eq), was suspended in 5 mL of H_2O and 1 mL of methanol, enhancing the solubility. The resulting solution was added dropwise to the aniline solution under vigorous stirring. The reaction was left for 3 h and was then poured in crushed ice to obtain a red precipitate that was filtered, washed with cold water and dried. A yield of 93% was obtained (0.950 g, 2.76 mmol).

[1]H-NMR (600 MHz, Chloroform-d, Figure S2) δ 7.92 – 7.86 (m, 4H), 7.71 – 7.66 (m, 1H), 6.79 (d, J = 9.3 Hz, 2H), 4.08 (s, 3H), 3.89 (t, J = 5.9 Hz, 2H), 3.61 (t, J = 5.9 Hz, 2H), 3.56 (q, J = 7.1 Hz, 2H), 1.25 (t, J = 7.1 Hz, 3H).

λ_{max} (EtOH): 490 nm

ε (L mol^{-1} cm^{-1}): 30.5 x 103

HRMS: calculated 344.1485, found 345.1557 (M+1)

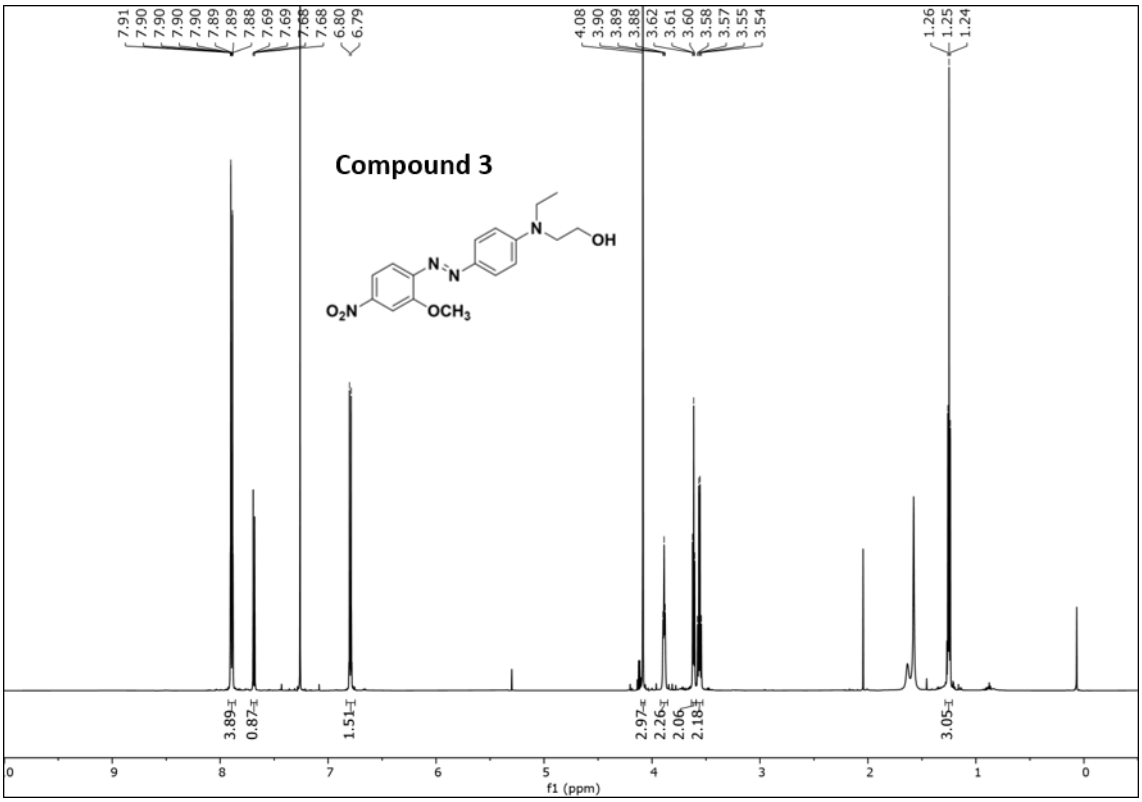

*Figure S2: ^{1}H-NMR spectrum of compound **3** (600 MHz, Chloroform-d).*

Compound 4 was synthesized according to the procedure described by Schab-Balcerzak *et al.* [320] Characterization was in agreement with the reported data (Yield: 38%).

^{1}H NMR (600 MHz, DMSO-d6, Figure S3) δ 8.86 (d, J = 2.5 Hz, 1H), 8.51 (dd, J = 9.0, 2.5 Hz, 1H), 7.92 (d, J = 9.0 Hz, 1H), 7.77 (d, J = 9.3 Hz, 2H), 6.93 (d, J = 9.4 Hz, 2H), 4.89 (t, J = 5.3 Hz, 1H), 3.67 – 3.52 (m, 6H), 1.17 (t, J = 7.1 Hz, 3H).

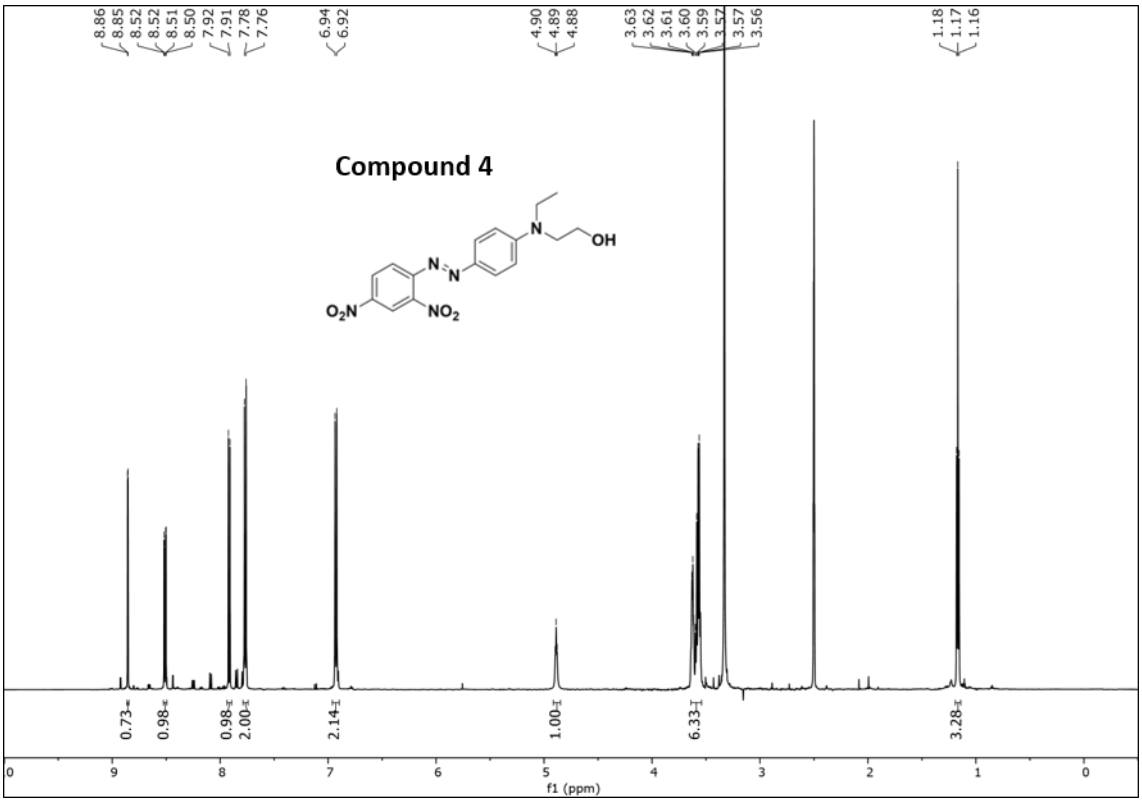

*Figure S3: [1]H-NMR spectrum of compound **4** (600 MHz, DMSO-d).*

Acrylate azo-dyes AzoH and AzoCl were synthesized following the reported procedure.[321,322] Characterization data is in agreement with reported data. For **AzoH** a yield of 92% and for **AzoCl** a yield of 90% were obtained.

AzoH: [1]H NMR (600 MHz, Chloroform-d, Figure S4a) δ 8.33 (d, J = 9.1 Hz, 2H), 7.96 (d, J = 9.0 Hz, 4H), 6.84 (d, J = 9.3 Hz, 2H), 6.42 (dd, J = 17.3, 1.3 Hz, 1H), 6.12 (dd, J = 17.3, 10.5 Hz, 1H), 5.87 (dd, J = 10.5, 1.3 Hz, 1H), 4.40 (t, J = 6.3 Hz, 2H), 3.75 (t, J = 6.3 Hz, 2H), 3.57 (q, J = 7.1 Hz, 2H), 1.28 (s, 3H).

AzoCl: [1]H NMR (600 MHz, Chloroform-d, Figure S4b) δ 8.39 (d, J = 2.4 Hz, 1H), 8.15 (dd, J = 8.9, 2.4 Hz, 1H), 7.95 (d, J = 9.2 Hz, 2H), 7.78 (d, J = 8.9 Hz, 1H), 6.83 (d, J = 9.2 Hz, 2H), 6.42 (dd, J = 17.3, 1.1 Hz, 1H), 6.13 (dd, J = 17.3, 10.5 Hz, 1H), 5.87 (dd, J = 10.5, 1.1 Hz, 1H), 4.39 (t, J = 6.3 Hz, 2H), 3.74 (t, J = 6.3 Hz, 2H), 3.56 (q, J = 7.1 Hz, 2H), 1.27 (t, J = 7.1 Hz, 3H).

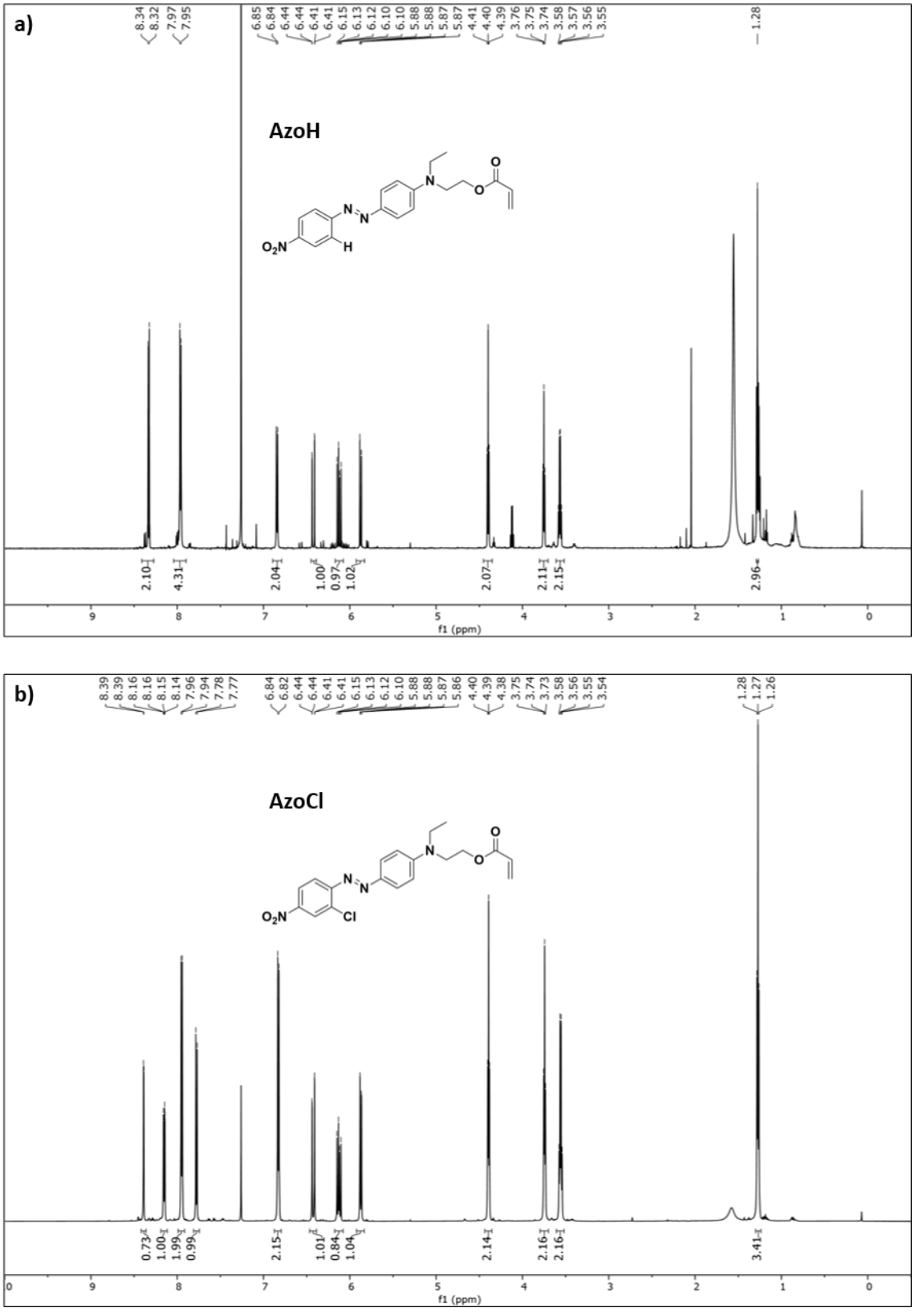

*Figure S4: [1]H-NMR spectra of a) **AzoH** and b) **AzoCl** (600 MHz, Chloroform-d).*

Acrylate azo-dyes AzoOCH$_3$ and AzoNO$_2$ were synthesized according to the following procedure. Compound **3** (0.500 g, 1.45 mmol, 1 eq) or **4** (0.500 g, 1.39 mmol, 1 eq) was added to a dried round bottom flask under inert Argon atmosphere and completely dissolved using anhydrous tetrahydrofuran while stirring. The flask was put in an ice bath and 1.1 eq (1.60 mmol, 0.223 mL for compound **3**; 1.53 mmol, 0.213 mL for compound **4**) of triethylamine was added. Then, 1.2 eq of freshly distilled acryloyl chloride (1.73 mmol, 0.141 mL for compound **3**; 1.67 mmol, 0.136 mL for compound **4**) was added dropwise over 15 minutes. After 30 minutes the ice bath was removed and the reaction was left for 24 h, while being monitored with TLC (Petroleum ether/Ethyl acetate 1:1). After reaction completion, the solution was filtered, the filter cake was washed with ethyl acetate to recover the desired product and the solvents were removed under vacuum at a temperature below 30°C.

Obtained solids were dissolved in ethyl acetate, washed 3 times with water and twice with brine. The aqueous fractions resulting from washing were combined and extracted 3 times with ethyl acetate until the aqueous solution became clear.

The organic fractions were combined, dried over sodium sulfate, filtered and the solvent was removed under vacuum at 30°C. The final product was obtained as a dark red solid. **AzoOCH$_3$** was obtained in a yield of 92% (0.5311 g, 1.334 mmol), **AzoNO$_2$** was obtained in a yield of 87% (0.500 g, 1.21 mmol).

AzoOCH$_3$: ^{1}H NMR (600 MHz, Chloroform-d, Figure S5a) δ 7.96 – 7.86 (m, 4H), 7.69 (d, J = 8.6 Hz, 1H), 6.83 – 6.79 (m, 2H), 6.41 (dd, J = 17.2, 1.4 Hz, 1H), 6.12 (dd, J = 17.3, 10.4 Hz, 1H), 5.86 (dd, J = 10.4, 1.3 Hz, 1H), 4.38 (t, J = 6.2 Hz, 2H), 4.08 (s, 3H), 3.72 (t, J = 6.2 Hz, 2H), 3.54 (q, J = 7.1 Hz, 2H), 1.26 (t, J = 7.1 Hz, 3H).

HR-ESI-MS: calculated 398.1590, found 399.1663 (M + 1)

AzoNO$_2$: ^{1}H NMR (600 MHz, Chloroform-d, Figure S5b) δ 8.39 (d, 1H), 8.15 (dd, J = 8.9, 2.4 Hz, 1H), 7.94 (d, J = 9.1 Hz, 2H), 7.77 (d, J = 8.9 Hz, 1H), 6.82 (d, J = 9.2 Hz, 2H), 6.42 (dd, J = 17.4, 1.3 Hz, 1H), 6.13 (dd, J = 17.3, 10.5 Hz, 1H), 5.87 (dd, J = 10.4, 1.3 Hz, 1H), 4.39 (t, J = 6.3 Hz, 2H), 3.74 (t, J = 6.3 Hz, 2H), 3.56 (q, J = 7.1 Hz, 2H), 1.27 (t, J = 7.1 Hz, 3H).

HR-ESI-MS: calculated 413.1335, found 436.1228 (M + Na+)

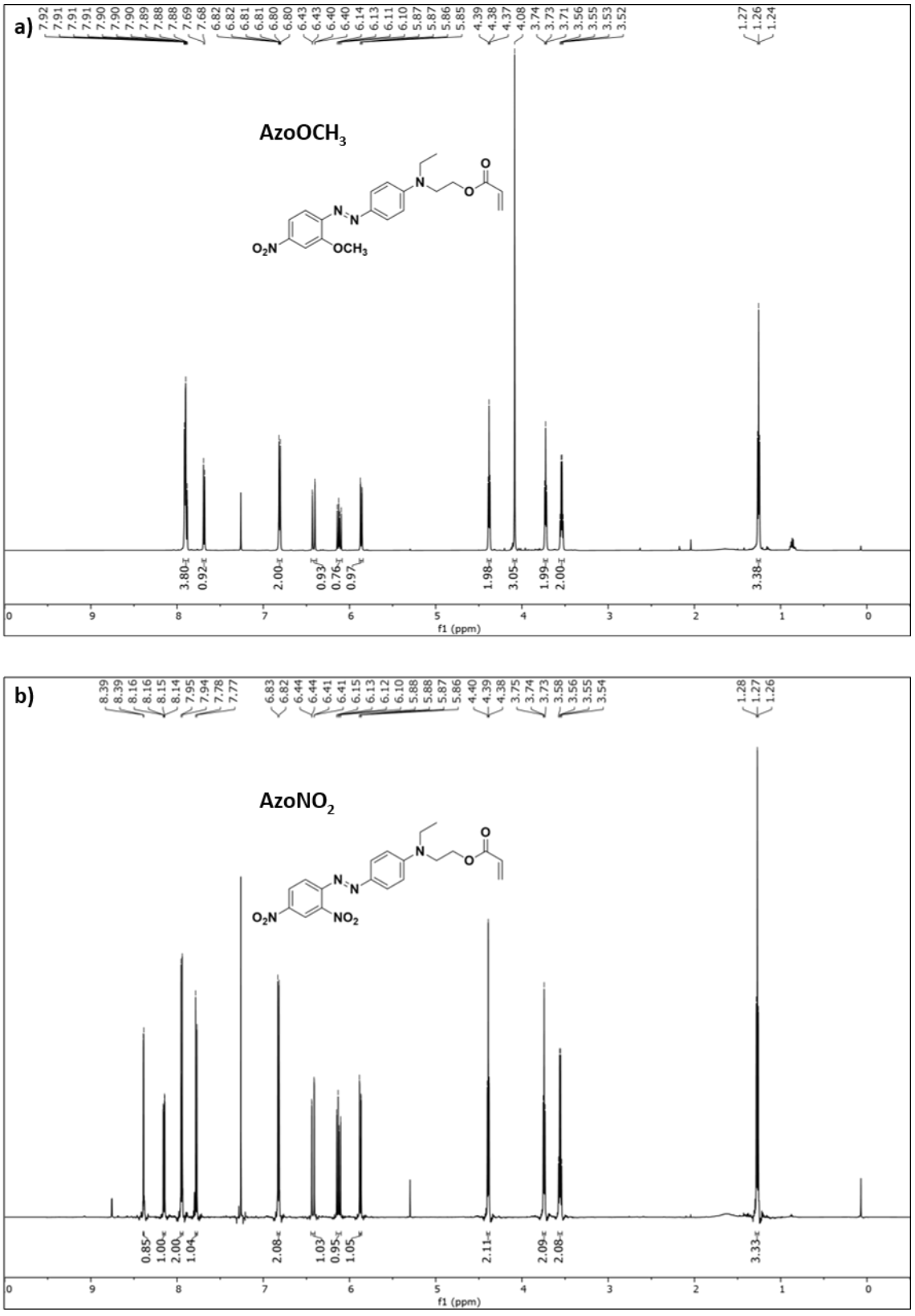

*Figure S5: ^{1}H-NMR spectra of **a) AzoOCH$_3$** and **b) AzoNO$_2$** (600 MHz, Chloroform-d).*

b) Additional characterization data of test samples for LSMP structures

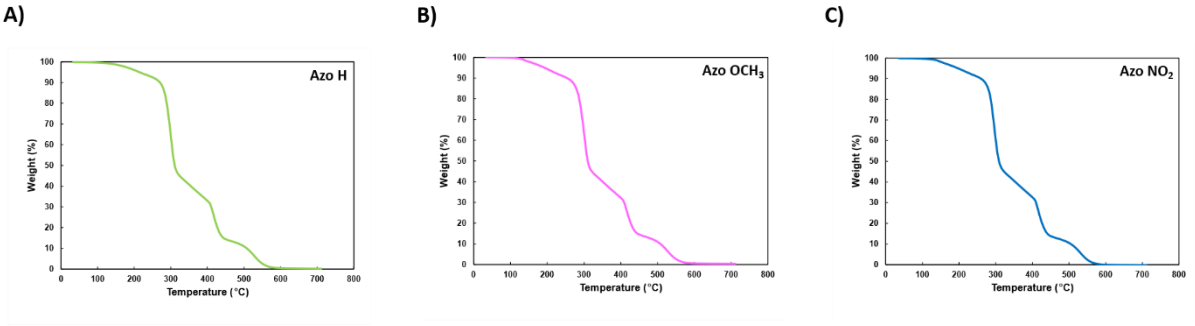

Figure S6: Results of TGA measurements of test samples fabricated from A) Azo H, B) Azo OCH_3 and C) Azo NO_3 -based inks.

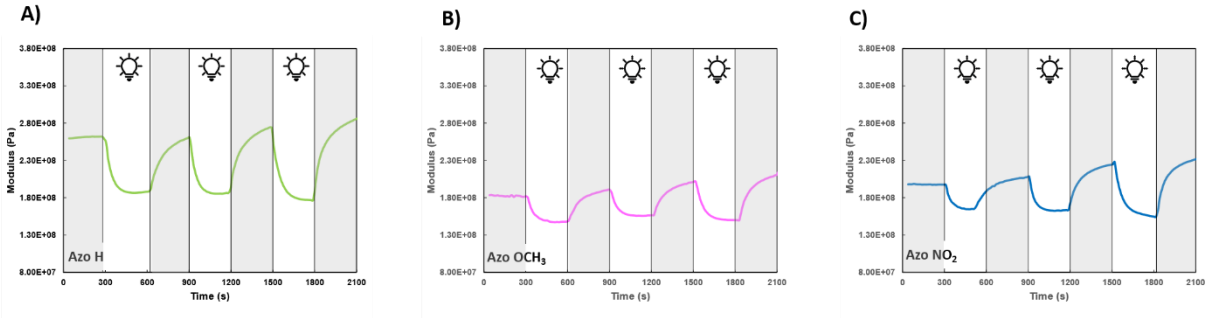

Figure S7: Opto-mechanical measurements of test samples fabricated from A) Azo H, B) Azo OCH_3 and C) Azo NO_3 -based inks.

Bibliography

[1] S. C. Ligon, R. Liska, J. Stampfl, M. Gurr, Rolf Mülhaupt, *Chem. Rev.* **2017**, *117*, 10212.

[2] E. A. Guzzi, M. W. Tibbitt, *Adv. Mater.* **2020**, *32*, 1901994.

[3] Y. Yang, X. Song, X. Li, Z. Chen, C. Zhou, Q. Zhou, Y. Chen, *Adv. Mater.* **2018**, *30*, 1706539.

[4] A. Velasco-Hogan, J. Xu, M. A. Meyers, *Adv. Mater.* **2018**, *30*, 1800940.

[5] A. Gebhardt, *Rapid Prototyping*, Hanser Verlag: Munich, DE, 2003.

[6] D.T. Pham, R.S. Gault, *Int. J. Mach. Tools Manuf.* **1998**, *38*, 1257.

[7] M. Layani, X. Wang, S. Magdassi, *Adv. Mater.* **2018**, *30*, 1706344.

[8] E. Peng, D. Zhang, J. Ding, *Adv. Mater.* **2018**, *30*, 1802404.

[9] Z. Zou, Y. Chen, S. Yuan, N. Luo, J. Li, Y. He, *Adv. Funct. Mater.* **2022**, 2213312.

[10] L. Hirt, A. Reiser, R. Spolenak, T. Zambelli, *Adv. Mater.* **2017**, *29*, 1604211.

[11] D. Shen, M. Zhang, A. S. Mujumdar, J. Li, *Trends Food Sci. Technol.* **2023**, *131*, 104.

[12] S. O'Halloran, A. Pandit, A. Heise, A. Kellet, *Adv. Sci.* **2022**, 2204072.

[13] G. Lazorenko, A. Kasprzhitskii, *Addit. Manuf.* **2022**, *55*, 102782.

[14] Y. Bao, N. Paunović, J.-C. Leroux, *Adv. Funct. Mater.* **2022**, *32*, 2109864.

[15] M. Qu, C. Wang, X. Zhou, A. Libanori, X. Jiang, W. Xu, S. Zhu, Q. Chen, W. Sun, A. Khademhosseini, *Adv. Healthc. Mater.* **2021**, *10*, 2001986.

[16] E. Sachyani Keneth, A. Kamyshny, M. Totaro, L. Beccai, S. Magdassi, *Adv. Mater.* **2021**, *33*, 2003387.

[17] S. R. Dabbagh, M. R. Sarabi, M. T. Birtek, S. Seyfi, M. Sitti, S. Tasoglu, *Nat. Commun*. **2022**, *13*, 5875.

[18] G. Ge, Q. Wang, Y.-Z. Zhang, H. N. Alshareef, X. Dong, *Adv. Funct. Mater.* **2021**, *31*, 2107437.

[19] Y.-G. Park, I. Yun, W. G. Chung, W. Park, D. H. Lee, J.-U. Park, *Adv. Sci.* **2022**, *9*, 2104623.

[20] Y. Peng, C. Unluer, *Compos. B. Eng.* **2023**, *252*, 110492.

[21] L. Sabantina, F. Kinzel, A. Ehrmann, K. Finsterbusch, *OP Conf. Ser.: Mater. Sci. Eng.* **2015**, *87*, 012005.

[22] ASTM F2792-12a. *Standard Terminology for Additive Manufacturing Technologies*; ASTM International: West Conshohocken, PA, **2012**.

[23] Z. Jiang, B. Diggle, M. L. Tan, J. Viktorova, C. W. Bennett, L. A. Connal, *Adv. Sci.* **2020**, *7*, 2001379.

[24] A. Cano-Vicent, M. M. Tambuwala, Sk. S. Hassan, D. Barh, A. A. A. Aljabali, M. Birkett, A. Arjunan, A. Serrano-Aroca, *Addit. Manuf.* **2021**, *47*, 102378.

[25] M. A. S. R. Saadi, A. Maguire, N. T. Pottackal, M. S. H. Thakur, M. M. Ikram, A. J. Hart, P. M. Ajayan, M. M. Rahman, *Adv. Mater.* **2022**, *34*, 2108855.

[26] T. Ahlfeld, V. Guduric, S. Duin, A. R. Akkineni, K. Schütz, D. Kilian, J. Emmermacher, N. Cubo-Mateo, S. Dani, M. v. Witzleben, J. Spangenberg, R. Abdelgaber, R. F. Richter, A. Lode, M. Gelinsky, *Biomater. Sci.* **2020**, *8,* 2102.

[27] A. Elkaseer, K. J. Chen, J. C. Janhsen, O. Refle, V. Hagenmeyer, S. G. Scholz, *Addit. Manuf.* **2022**, *60*, 103270.

[28] K. Zub, S. Hoeppener, U. S. Schubert, *Adv. Mater.* **2022**, *34*, 2105015.

[29] A. Mostafaei, A. M. Elliott, J. E. Barnes, F. Li, W. Tan, C. L. Cramer, P. Nandwana, M. Chmielus, *Prog. Mater. Sci.* **2021**, *119*, 100707.

[30] A. Bagheri, J. Jin, *ACS Appl. Polym. Mater.* **2019**, *1*, 593.

[31] V. Hahn, P. Rietz, F. Hermann, P. Müller, C. Barner-Kowollik, T. Schlöder, W. Wenzel, E. Blasco, M. Wegener, *Nat. Photon.* **2022**, *16*, 784.

[32] J. R. Tumbleston, D. Shirvanyants, N. Ermoshkin, R. Janusziewicz, A. R. Johnson, D. Kelly, K. Chen, R. Pinschmidt, J. P. Rolland, A. Ermoshkin, E. T. Samulski, J. M. DeSimone, *Science*, **2015**, *347*, 1349.

[33] D. Loterie, P. Delrot, C. Moser, *Nat. Commun.* **2020**, *11*, 852.

[34] P. Kulinowski, P. Malczewski, E. Pesta, M. Łaszcz, A. Mendyk, S. Polak, P. Dorożyński, *Addi. Manuf.* **2021**, *38*, 101761.

[35] L. E. Murr, *Addit. Manuf.* **2015**, *5*, 40.

[36] D.-G. Ahn, *Int. J. of Precis. Eng. and Manuf.-Green Tech.* **2021**, *8*, 703.

[37] M. Feygin, *Apparatus and Method for Forming an Integral Object from Laminations.* U.S. Patent 4752352, **1988**.

[38] Z. Dong, M. Vuckovac, W. Cui, Q. Zhou, R. H. A. Ras, P. A. Levkin, *Adv. Mater.* **2021**, *33*, 2106068.

[39] M. Wang, W. Li, L. S. Mille, T. Ching, Z. Luo, G. Tang, C. E. Garciamendez, A. Lesha, M. Hashimoto, Y. S. Zhang, *Adv. Mater.* **2022**, *34*, 2107038.

[40] T. Abele, T. Messer, K. Jahnke, M. Hippler, M. Bastmeyer, M. Wegener, K. Göpfrich, *Adv. Mater.* **2022**, *34*, 2106709.

[41] M. Monzón, Z. Ortega, A. Hernández, R. Paz, F. Ortega, *Materials*, **2017**, *10*, 64.

[42] N. Tsutsumi, A. Fukuda, R. Nakamura, K. Kinashi, W. Sakai, *Appl. Phys. A* **2017**, *123*, 553.

[43] M. Carlotti, O. Tricinci, V. Mattoli, *Adv. Mater. Technol.* **2022**, *7*, 2101590.

[44] P. Kiefer, V. Hahn, M. Nardi, L. Yang, E. Blasco, C. Barner-Kowollik, M. Wegener, *Adv. Optical Mater.* **2020**, *8*, 2000895.

[45] N. Ballard, J. M. Asua, Prog. Polym. Sci. **2018**, *79*, 40.

[46] T. Y. Lee, C. A. Guymonc, E. Sonny Jönsson, C. E. Hoyle, *Polymer* **2004**, *45*, 6155.

[47] F. Tudos, T. Foldes-Berezsnich, *Prog. Polym. Sci.* **1989**, *14*, 717.

[48] C. C. Cook, E. J. Fong, J. J. Schwartz, D. H. Porcincula, A. C. Kaczmarek, J. S. Oakdale, B. D. Moran, K. M. Champley, C. M. Rackson, A. Muralidharan, R. R. McLeod, M. Shusteff, *Adv. Mater.* **2020**, *32*, 2003376.

[49] Z.-C. Ma, Y.-L. Zhang, B. Han, X.-Y. Hu, C.-H. Li, Q.-D. C, H.-B. Sun, *Nat. Commun.* **2020**, *11*, 4536.

[50] T.-Y. Huang, M. S. Sakar, A. Mao, A. J. Petruska, F. Qiu, X.-B. Chen, S. Kennedy, D. Mooney, B. J. Nelson, *Adv. Mater.* **2015**, *27*, 6644.

[51] J. V. Crivello, *J. Polym. Sci., Part A: Polym. Chem.* **1999**, *37*, 4241.

[52] W. A. Green, *Industrial Photoinitiators: A Technical Guide*; CRC Press: Boca Raton, FL, **2010**.

[53] J. Zhang, P. Xiao, *Polym. Chem.* **2018**, *9*, 1530.

[54] X. Peng, L. Yue, S. Liang, S. Montgomery, C. Lu, C.-M. Cheng, R. Beyah, R. R. Zhao, H. J. Qi, *Adv. Funct. Mater.* **2022**, *32*, 2112329.

[55] Q. Ge, Z Chen, J. Cheng, B. Zhang, Y.-F. Zhang, H. Li, X. He, C. Yuan, J. Liu, S. Magdassi, S. Qu, *Sci. Adv.* **2021**, *7*, eaba4261.

[56] K. J. Schafer, J. M. Hales, M. Balu, K. D. Belfield, E. W. Van Stryland, D. J. Hagan, *J. Photochem. Photobiol. A: Chem*. **2004**, *162*, 497.

[57] T.-L. Huang, Y.-H. Li, Y.-C. Chen, J. Polym. Sci. **2020**, 58, 2914.

[58] T. Chi, P. Somers, D. A. Wilcox, A. J. Schuman, J. E. Johnson, Z. Liang, L. Pan, X. Xu, B. W. Boudouris, *ACS Appl. Polym. Mater.* **2021**, *3*, 1426.

[59] P. Jacobs, *Rapid Prototyping & Manufacturing: Fundamentals of Stereolithography*, Society of Manufacturing Engineering, Dearborn, **1992**.

[60] S. Deng, J. Wu, M. D. Dickey, Q. Zhao, T. Xie, *Adv. Mater.* **2019**, *31*, 1903970.

[61] D. Ahn, L. M. Stevens, K. Zhou, Z. A. Page, *ACS Cent. Sci.* **2020**, *6*, 1555.

[62] Y. Jia, C. A. Spiegel, A. Welle, S. Heißler, E. Sedghamiz, M. Liu, W. Wenzel, M. Hackner, J. P. Spatz, M. Tsotsalas, E. Blasco, *Adv. Funct. Mater.* **2022**, 2207826.

[63] Y. Bao, N. Paunović, J.-C. Leroux, *Adv. Funct. Mater.* **2022**, *32*, 2109864.

[64] H. Quan, T. Zhang, H. Xu, S. Luo, J. Nie, X. Zhu, Bioact. Mater. 2020, 5, 110.

[65] Z. Dong, H. Cui, H. Zhang, F. Wang, X. Zhan, F. Mayer, B. Nestler, M. Wegener, P. A. Levkin, *Nat. Commun.* **2021**, *12*, 247.

[66] Y. Sugihara, P. O'Connor, P. B. Zetterlund, F. Aldabbagh, *J. Polym. Sci. A Polym. Chem.* **2011**, *49*, 1856.

[67] Y. S. Zhang, A. Khademhosseini, *Science* **2017**, *356*, eaaf3627.

[68] M. Caprioli, I. Roppolo, A. Chiappone, L. Larush, C. F. Pirri, S. Magdassi, Nat. Commun. 2021, 12, 2462.

[69] M. Carlotti, V. Mattoli, *Small* **2019**, *15*, 1902687.

[70] Hull, C. (UVP, Inc.) *Apparatus for Production of Three-Dimensional Objects by Stereolithography.* U.S. Patent 4575330, **1986**.

[71] Z. Dong, J. Monti, H. Cui, A. Welle, S. A. Singaraju, E. Blasco, P. A. Levkin, *Adv. Mater. Technol.* **2022**, 2201268.

[72] C. Choi, Y. Okayama, P. T. Morris, L. L. Robinson, M. Gerst, J. C. Speros, C. J. Hawker, J. Read de Alaniz, C. M. Bates, *Adv. Funct. Mater.* **2022**, *32*, 2200883.

[73] C. Vazquez-Martel, L. Becker, W. V. Liebig, P. Elsner, E. Blasco*, *ACS Sustainable Chem. Eng.* **2021**, *9*, 16840.

[74] Formlabs, „What Does Resolution Mean in 3D Printing?", https://formlabs.com/blog/3d-printer-resolution-meaning/ ; formlabs (07.02.2023;20:54)

[75] B. Zhang, S. Li, H. Hingorani, A. Serjouei, L. Larush, A. A. Pawar, W. H. Goh, A. H. Sakhaei, M. Hashimoto, K. Kowsari, S. Magdassi, Q. Ge, *J. Mater. Chem. B*, **2018**,*6*, 3246.

[76] V. Tomeckova, J. W. Halloran, *J. Eur. Ceram. Soc.* **2010**, *30*, 3273.

[77] K. Wang, B. Li, K. Ni, B. Li, Z. Wang, *Polym. Test.* **2021**, *94*, 107039.

[78] U. Punia, A. Kaushik, R. K. Garg, D. Chhabra, A. Sharma, *Mater. Today: Proc.* **2022**, *63*, 566.

[79] M. Zarek, M. Layani, S. Eliazar, N. Mansour, I. Cooperstein, E. Shukrun, A. Szlar, D. Cohn, S. Magdassi, Virtual Phys. Prototyp. 2016, 11, 263.

[80] R. Janusziewicz, J. R. Tumbleston, A. L. Quintanilla, S. J. Mecham, J. M. DeSimone, *Proc. Natl. Acad. Sci. U. S. A.* **2016**, *113*, 11703.

[81] D. A. Walker, J. L. Hedrick, C. A. Mirkin, *Science* **2019**, *366*, 360.

[82] L. Wu, Z. Dong, H. Du, C. Li, N. X. Fang, Y. Song, *Research* **2018**, *2018*, 1.

[83] B. E. Kelly, I. Bhattacharya, H. Heidari, M. Shusteff, C. M. Spadaccini, H. K. Taylor, *Science* **2019**, *363*, 1075.

[84] M. Regehly, Y. Garmshausen, M. Reuter, N. F. König, E. Israel, D. P. Kelly, C. Y. Chou, K. Koch, B. Asfari, S. Hecht, *Nature* **2020**, *588*, 620.

[85] B. Wang, E. Engay, P. R. Stubbe, S. Z. Moghaddam, E. Thormann, K. Almdal, A. Islam, Y. Yang, *Nat. Commun.* **2022**, *13*, 367.

[86] D. Gonzalez-Hernandez, S. Varapnickas, A. Bertoncini, C. Liberale, M. Malinauskas, *Adv. Optical Mater.* **2023**, *11*, 2201701.

[87] I. Bernardeschi, M. Ilyas, L. Beccai, *Adv. Intell. Syst.* **2021**, *3*, 2100051.

[88] S. Maruo, O. Nakamura, S. Kawata, *Opt. Lett.* **1997**, *22*, 132.

[89] J. Serbin, A. Ovsianikov, B. Chichkov, *Opt. Express* **2004**, *12*, 5221.

[90] M. Göppert-Mayer, *Ann. Phys.* **2009**, *18*, 466.

[91] W. Kaiser, C. G. B. Garrett, *Phys. Rev. Lett.* **1961**, *7*, 229.

[92] K. Takada, H.-B. Sun, S. Kawata, *Appl. Phys. Lett.* **2005**, *86*, 071122.

[93] X.-Z. Dong, Z.-S. Zhao, X.-M. Duan, *Appl. Phys. Lett.* **2008**, *92*, 091113.

[94] M. Malinauskas, M. Farsari, A. Piskarskas, S. Juodkazis, *Phys. Rep.*, **2013**, *533*, 1.

[95] H.-B. Sun, K. Takada, M.-S. Kim, K.S. Lee, S. Kawata, *Appl. Phys. Lett.* **2003**, *83*, 1104.

[96] T. Zandrini, N. Liaros, L. J. Jiang, Y. F. Lu, J. T. Fourkas, R. Osellame, and T. Baldacchini, *Opt. Mater. Express* **2019**, *9*, 2601.

[97] J. B. Mueller, J. Fischer, F. Mayer, M. Kadic, M. Wegener, *Adv. Mater.* **2014**, *26*, 6566.

[98] A. Pikulin, N. Bityurin, *Multiphoton Lithography*, Wiley-VCH, Weinheim **2016**, pp. 65–93.

[99] L. Yang, A. Münchinger, M. Kadic, V. Hahn, F. Mayer, E. Blasco, C. Barner-Kowollik, M. Wegener, *Adv. Opt. Mater.* **2019**, *7*, 1901040.

[100] J. Fischer, M. Wegener, *Laser Photonics Rev.* **2013**, *7*, 22.

[101] T. Baldacchini, *Three-Dimensional Microfabrication Using Two-Photon Polymerization*, William Andrew Publishing, Oxford, UK, **2016**.

[102] C. Peters, M. Hoop, S. Pané, B. J. Nelson, C. Hierold, *Adv. Mater.* **2016**, *28*, 533.

[103] H. Ceylan, I. C. Yasa, O. Yasa, A. F. Tabak, J. Giltinan, M. Sitti, *ACS Nano* **2019**, *13*, 3353.

[104] U. Bozuyuk, O. Yasa, I. C. Yasa, H. Ceylan, S. Kizilel, M. Sitti, *ACS Nano* **2018**, *12*, 9617.

[105] T. Wloka, M. Gottschaldt, U. S. Schubert, *Chem. Eur. J.* **2022**, *28*, e202104191.

[106] M. Pawlicki, H. Collins, R. Denning, H. Anderson, *Angew. Chem. Int. Ed.* **2009**, *48*, 3244.

[107] E. Scarpa, E. D. Lemma, R. Fiammengo, M. P. Cipolla, F. Pisanello, F. Rizzi, M. De Vittorio, *Sens. Actuators B Chem.* **2019**, *279*, 418.

[108] J. Song, C. Michas, C. S. Chen, A. E. White, M. W. Grinstaff, *Adv. Healthcare Mater.* **2020**, *9*, 1901217.

[109] Z. Li, M. Siklos, N. Pucher, K. Cicha, A. Ajami, W. Husinsky, A. Rosspeintner, E. Vauthey, G. Gescheidt, J. Stampfl, R. Liska*, J. Polym. Sci. Part A* **2011**, *49*, 3688.

[110] S. Zhang, S. Li, X. Wan, J. Ma, N. Li, J. Li, Q. Yin, *Addit. Manuf.* **2021**, *47*, 102358.

[111] G. Lemercier, C. Martineau, J.-C. Mulatier, I. Wang, O. Stéphan, P. Baldeck, C. Andraud*, New J. Chem.* **2006**, *30*, 1606.

[112] P. Hu, J. Zhu, R. Liu, Z. Li, *J. Photopolym. Sci. Technol.* **2019**, *32*, 257.

[113] H. Y. Woo, B. Liu, B. Kohler, D. Korystov, A. Mikhailovsky, G. C. Bazan, *J. Am. Chem. Soc.* **2005**, *127*, 14721.

[114] M. Hippler, E. Blasco, J. Qu, M. Tanaka, C. Barner-Kowollik, M. Wegener, M. Bastmeyer, *Nat. Commun.* **2019**, *10*, 232.

[115] M. Suter, L. Zhang, E. C. Siringil, C. Peters, T. Luehmann, O. Ergeneman, K. E. Peyer, B. J. Nelson, C. Hierold, *Biomed. Microdevices* **2013**, *15*, 997.

[116] S. Tottori, L. Zhang, F. Qiu, K. K. Krawczyk, A. Franco-Obregón, B. J. Nelson, *Adv. Mater.* **2012**, *24*, 811.

[117] P. Prabhakaran, Y. Son, C.-W. Ha, J.-J. Park, S. Jeon, K.-S. Lee, *Adv. Eng. Mater.* **2018**, *20*, 1800320.

[118] J. Kustra, E. Martin, D. Chateau, F. Lerouge, C. Monnereau, C. Andraud, M. Sitarz, P. L. Baldeck, S. Parola, *RSC Adv.* **2017**, *7*, 46615.

[119] C. Barner-Kowollik, M. Bastmeyer, E. Blasco, G. Delaittre, P. Müller, B. Richter, M. Wegener, *Angew. Chem. Int. Ed.* **2017**, *56*, 15828.

[120] V. Hahn, P. Kiefer, T. Frenzel, J. Qu, E. Blasco, C. Barner-Kowollik, and M. Wegener, *Adv. Funct. Mater.* **2020**, *30*, 1907795.

[121] S. W. Hell, J. Wichmann, *Opt. Lett.* **1994**, *19*, 780.

[122] E. Rittweger, K. Y. Han, S. E. Irvine, C. Eggeling, S. W. Hell, *Nat. Photon.* **2009**, *3*, 144–147.

[123] J. Fischer, J. B. Mueller, A. S. Quick, J. Kaschke, C. Barner-Kowollik, M. Wegener, *Adv. Opt. Mater.* **2015**, *3*, 221.

[124] L. Li, R. R. Gattass, E. Gershgoren, H. Hwang, J. T. Fourkas, *Science* **2009**, *324*, 910.

[125] J. Fischer, G. von Freymann, M. Wegener, *Adv. Mater.* **2010**, *22*, 3578.

[126] T. F. Scott, B. A. Kowalski, A. C. Sullivan, C. N. Bowman, R. R. McLeod, *Science* **2009**, *324*, 913.

[127] Y. Cao, Z. Gan, B. Jia, R. A. Evans, M. Gu, *Opt. Express* **2011**, *19*, 19486.

[128] V. Hahn, T. Messer, N.M. Bojanowski, E.R. Curticean, I. Wacker, R.R. Schröder, E. Blasco, and M. Wegener, *Nat. Photon*. **2021**, *15*, 932.

[129] S. Tibbits, *The emergence of "4D printing"*, https://www.ted.com/talks/skylar_tibbits_the_emergence_of_4d_printing (accessed: 08.02.2023; 20:00).

[130] Q. Ge, H. J. Qi, M. L. Dunn, *Appl. Phys. Lett.* **2013**, *103*, 131901.

[131] S. Tibbits, *Archit. Des.* **2014**, *84*, 116.

[132] D. Raviv, W. Zhao, C. McKnelly, A. Papadopoulou, A. Kadambi, B. Shi, S. Hirsch, D. Dikovsky, M. Zyracki, C. Olguin, *Sci. Rep.* **2015**, *4*, 7422.

[133] E. Pei, *Assem. Autom.* **2014**, *34*, 310.

[134] X. Kuang, D. J. Roach, J. Wu, C. M. Hamel, Z. Ding, T. Wang, M. L. Dunn, H. J. Qi, *Adv. Funct. Mater.* **2019**, *29*, 1805290.

[135] A. Andreu, P.-C. Su, J.-H. Kim, C. S. Ng, S. Kim, I. Kim, J. Lee, J. Noh, A. S. Subramanian, Y.-J. Yoon, *Addit. Manuf.* **2021**, *44*, 102024.

[136] S. Y. Hann, H. Cui, M. Nowicki, L. G. Zhang, *Addit. Manuf.* **2020**, *36*, 101567.

[137] C. de Marco, S. Pané, B. J. Nelson, *Sci. Robot.*, **2018**, *3*, eaau0449.

[138] Z. Guan, L. Wang, J. Bae, *Mater. Horiz.* **2022**, *9*, 1825.

[139] V. Mathur, P. Agarwal, V. Srinivasan, A. Panwar, K. S. Vasanthan, *J. Mater. Res* **2023**, *38*, 2.

[140] Y. Tang, B. Dai, B. Su, Y. Shi, Front. Mater. Sci. 2021, 8, 658046.

[141] K. Ntouanoglou, S. Panos, M. Dimitris, *Procedia Manuf.* **2018**, *18*, 120.

[142] Y. Xia, Y. He, F. Zhang, Y. Liu, J. Leng, *Adv. Mater.* **2021**, *33*, 2000713.

[143] K. M. Herbert, H. E. Fowler, J. M. McCracken, K. R. Schlafmann, J. A. Koch, T. J. White, *Nat. Rev. Mater.* **2022**, *7*, 23.

[144] Z. Li, Y. Zhou, T. Li, J. Zhang, H. Tian, *VIEW.* **2022**, *3*, 20200112.

[145] C. A. Spiegel, M. Hippler, A. Münchinger, M. Bastmeyer, C. Barner-Kowollik, M. Wegener, E. Blasco, *Adv. Funct. Mater.* **2020**, *30*, 1907615.

[146] D. Seliktar, *Science* **2012**, *336*, 1124.

[147] E. Caló, V. V. Khutoryanskiy, *Eur. Polym. J.* **2015**, *65*, 252.

[148] L. Ionov, *Adv. Funct. Mater.* **2013**, *23*, 4555.

[149] Z. Xiong, M.-L. Zheng, X.-Z. Dong, W.-Q. Chen, F. Jin, Z.-S. Zhao, X.-M. Duan, *Soft Matter* **2011**, *7*, 10353.

[150] M. R. Lee, I. Y. Phang, Y. Cui, Y. H. Lee, X. Y. Ling, *Small* **2015**, *11*, 740.

[151] L. D. Zarzar, P. Kim, M. Kolle, C. J. Brinker, J. Aizenberg, B. Kaehr, *Angew. Chem., Int. Ed.* **2011**, *50*, 9356.

[152] L. D. Zarzar, J. Aizenberg, *Acc. Chem. Res.* **2014**, *47*, 530.

[153] M. Hippler, K. Weißenbruch, K. Richler, E. D. Lemma, M. Nakahata, B. Richter, C. Barner-Kowollik, Y. Takashima, A. Harada, E. Blasco, M. Wegener, M. Tanaka, M. Bastmeyer, Sci. Adv. 2020, 6, eabc2648.

[154] G. Pasparakis, T. Constantinos, *Polymer* **2020**, *211*, 123146.

[155] T. Spratte, S. Geiger, F. Colombo, A. Mishra, M. Taale, L.-Y. Hsu, E. Blasco, C. Selhuber-Unkel, *Adv. Mater. Technol.* **2022**, *8*, 2200714.

[156] P.-G. de Gennes, *The Physics of Liquid Crystals*, Oxford University Press, London, UK **1974**.

[157] M. Warner, E. M. Terentjev, *Liquid Crystal Elastomers (International Series of Monographs on Physics)*, Vol. 120, Oxford University Press, Oxford, UK **2009**.

[158] A. Kotikian, R. L. Truby, J. W. Boley, T. J. White, J. A. Lewis, *Adv. Mater.* **2018**, *30*, 1706164.

[159] Z. Guan, L. Wang, J. Bae, *Mater. Horiz.*, **2022**, *9*, 1825.

[160] M. del Pozo, J. A. H. P. Sol, A. P. H. J. Schenning, M. G. Debije, *Adv. Mater.* **2022**, *34*, 2104390.

[161] C. P. Ambulo, J. J. Burroughs, J. M. Boothby, H. Kim, M. R. Shankar, T. H. Ware, *ACS Appl. Mater. Interfaces* **2017**, *9*, 37332.

[162] D. J. Roach, X. Kuang, C. Yuan, K. Chen, H. J. Qi, *Smart Mater. Struct.* **2018**, *27*, 125011.

[163] M. López-Valdeolivas, D. Liu, D. J. Broer, C. Sánchez-Somolinos, *Macromol. Rapid Commun.* **2018**, *39*, 1700710.

[164] M. Tabrizi, T. H. Ware, M. R. Shankar, *ACS Appl. Mater. Interfaces* **2019**, *11*, 28236.

[165] S. Li, H. Bai, Z. Liu, X. Zhang, C. Huang, L. W. Wiesner, M. Silberstein, R. F. Shepherd, *Sci. Adv.* **2021**, *7*, eabg3677.

[166] H. Zeng, P. Wasylczyk, G. Cerretti, D. Martella, C. Parmeggiani, D. S. Wiersma, Appl. *Phys. Lett.* **2015**, *106*, 111902.

[167] H. Zeng, D. Martella, P. Wasylczyk, G. Cerretti, J.-C. G. Lavocat, C.-H. Ho, C. Parmeggiani, D. S. Wiersma, *Adv. Mater.* **2014**, *26*, 2319.

[168] A. M. Flatae, M. Burresi, H. Zeng, S. Nocentini, S. Wiegele, C. Parmeggiani, H. Kalt, D. Wiersma, *Light: Sci. Appl.* **2015**, *4*, e282.

[169] D. Martella, S. Nocentini, D. Nuzhdin, C. Parmeggiani, D. S. Wiersma, *Adv. Mater.* **2017**, *29*, 1704047.

[170] S. Nocentini, F. Riboli, M. Burresi, D. Martella, C. Parmeggiani, D. S. Wiersma, *ACS Photonics* **2018**, *5*, 3222.

[171] F. J. Kahn, *Appl. Phys. Lett.* **1973**, *22*, 386.

[172] H. Zeng, P. Wasylczyk, C. Parmeggiani, D. Martella, M. Burresi, D. S. Wiersma, *Adv. Mater.* **2015**, *27*, 3883.

[173] C. C. Tartan, P. S. Salter, T. D. Wilkinson, M. J. Booth, S. M. Morris, S. J. Elston, *RSC Adv.* **2017**, *7*, 507.

[174] S. Nocentini, D. Martella, C. Parmeggiani, S. Zanotto, D. S. Wiersma, *Adv. Opt. Mater.* **2018**, *6*, 1800167.

[175] E. Sungur, L. Mager, A. Boeglin, M.-H. Li, P. Keller, K. D. Dorkenoo, *Appl. Phys. A* **2010**, *98*, 119.

[176] S. Zanotto, F. Sgrignuoli, S. Nocentini, D. Martella, C. Parmeggiani, D. S. Wiersma*, Appl. Phys. Lett.* **2019**, *114*, 201103.

[177] A. Münchinger, V. Hahn, D. Beutel, S. Woska, J. Monti, C. Rockstuhl, E. Blasco, M. Wegener, *Adv. Mater. Technol.* **2022**, *7*, 2100944.

[178] L.-Y. Hsu, P. Mainik, A. Münchinger, S. Lindenthal, T. Spratte, A. Welle, J. Zaumseil, C. Selhuber-Unkel, M. Wegener, E. Blasco, *Adv. Mater. Technol.* **2022**, *8*, 2200801.

[179] A. Münchinger, L. Hsu, F. Fürniß, E. Blasco, M. Wegener, *Mater. Today* **2022**, *59*, 9.

[180] A. Lendlein, S. Kelch, *Angew. Chem., Int. Ed.* **2002**, *41*, 2034.

[181] A. Lendlein, O. E. C. Gould, *Nat. Rev. Mater.* **2019**, *4*, 116.

[182] T. Chen, O. R. Bilal, R. Lang, C. Daraio, K. Shea, *Phys. Rev. Appl.* **2019**, *11*, 064069.

[183] V. L. Le, V. T. Le, N. S. Goo, *J. Intell. Mater. Syst. Struct.* **2019**, *30*, 2625.

[184] H. M. C. M. Herath, J. A. Epaarachchi, M. M. Islam, W. Al-Azzawi, J. Leng, F. Zhang, *Compos. Sci. Technol.* **2018**, *167*, 206.

[185] L. Santo, F. Quadrini, P. L. Ganga, V. Zolesi, *Aerosp. Sci. Technol.* **2015**, *40*, 109.

[186] F. Li, L. Liu, X. Lan, C. Pan, Y. Liu, J. Leng, Q. Xie, *Smart Mater. Struct.* **2019**, *28*, 075023.

[187] M. Champeau, D. A. Heinze, T. N. Viana, E. R. de Souza, A. C. Chinellato, S. Titotto, *Adv. Funct. Mater.* **2020**, *30*, 1910606

[188] Y. Zhang, Y. Li, W. Liu, *Adv. Funct. Mater.* **2015**, *25*, 471.

[189] Y. Liu, H. Du, L. Liu, J. Leng, *Smart Mater. Struct. 2014*, **23**, 023001.

[190] F. Li, Y. Liu, J. Leng, *Smart Mater. Struct.* **2019**, *28*, 103003.

[191] J. Delaey, P. Dubruel, S. Van Vlierberghe, *Adv. Funct. Mater.* **2020**, *30*, 1909047.

[192] H. Ramaraju, R. E. Akman, D. L. Safranski, S. J. Hollister, *Adv. Funct. Mater.* **2020**, *30*, 2002014.

[193] H. Gao, J. Li, F. Zhang, Y. Liu, J. Leng, *Mater. Horiz.* **2019**, *6*, 931.

[194] A. Lendlein, *Sci. Rob.* **2018**, *3*, eaat9090.

[195] T. Chen, O. R. Bilal, K. Shea, C. Daraio, *Proc. Natl. Acad. Sci. USA* **2018**, *115*, 5698.

[196] M. Gordon, J. S. Taylor, *J. Appl. Chem.* **1952**, *2*, 495.

[197] H. A. Schneider, J. Rieger, E. Penzel, *Polymer* **1997**, *38*, 1323.

[198] L. Weng, R. Vijayaraghavan, D. R. MacFarlane, G. D. Elliott, *Cryobiology* **2014**, *68*, 155.

[199] N. Inverardi, S. Pandini, F. Bignotti, G. Scalet, S. Marconi, F. Auricchio, *Macromol. Mater. Eng.* **2020**, *305*, 1900370.

[200] C. Pasini, N. Inverardi, D. Battini1, G. Scalet2, S. Marconi, F. Auricchio S. Pandini, *Smart Mater. Struct*. **2022**, *31*, 095021.

[201] M. Behl, K. Kratz, J. Zotzmann, U. Nöchel, A. Lendlein, *Adv. Mater.* **2013**, *25*, 4466.

[202] Y. Liu, K. Gall, M. L. Dunn, A. R. Greenberg, J. Diani, *Int. J. Plast.* **2006**, *22*, 279.

[203] Y.-C. Chen, D. C. Lagoudas, *J. Mech. Phys. Solids* **2008**, *56*, 1752.

[204] Y.-C. Chen, D. C. Lagoudas, *J. Mech. Phys. Solids* **2008**, *56*, 1766.

[205] H. Park, P. Harrison, Z. Guo, M.-G. Lee, W.-R. Yu, *Mech. Mater.* **2016**, *93*, 43.

[206] Y. Li, Z. Liu, *Polymer* **2018**, *143*, 298.

[207] X. Guo, L. Liu, B. Zhou, Y. Liu, J. Leng, *J. Intell. Mater. Syst. Struct.* **2016**, *27*, 314.

[208] International standard*, Plastics - Determination of dynamic mechanical properties - Part 11: Glass transition temperature*, ISO 6721-11:2019-06.

[209] N. Jung, H. Seo, D. Lee, C. Y. Ryu, S. Jeon, *Macromolecules* **2008**, *41*, 19, 6873.

[210] C. A. Spiegel, M. Hackner, V. P. Bothe, J. P. Spatz, E. Blasco, *Adv. Funct. Mater.* **2022**, *32*, 2110580.

[211] L. V. Elliott, E. E. Salzmann, J. R. Greer, *Adv. Funct. Mater.* **2021**, *31*, 2008380.

[212] M. Gastaldi, C. A. Spiegel, C. Vazquez-Martel, C. Barolo, I. Roppolo, E. Blasco, *Mol. Sys. Des. Eng.* **2023**, Advance Article.

[213] A. Cortés, A. Cosola, M. Sangermano, M. Campo, S. González Prolongo, C. F. Pirri, A. Jiménez-Suárez, A. Chiappone, *Adv. Funct. Mater.* **2021**, *31*, 2106774

[214] F. Zhang, L. Wang, Z. Zheng, Y. Liu, J. Leng, *Composites, Part A* **2019**, *125*, 105571.

[215] M. Herath, J. Epaarachchi, M. Islam, L. Fang, J. Leng, *Eur. Polym. J.* **2020**, *136*, 109912.

[216] E. Pantuso, G. D. Filpo, F. P. Nicoletta, *Adv. Opt. Mater.* **2019**, 7, 190025.

[217] R. Klajn, *Chem. Soc. Rev.* **2014**, 43, 148.

[218] H. Zhang, Y. Zhao, *ACS Appl. Mater. Interfaces* **2013**, *5*, 13069.

[219] N. Yenpech, V. Intasanta, S. Chirachanchai, *Polymer* **2019**, *182*, 121792.

[220] S. Ishii, K. Uto, E. Niiyama, M. Ebara, T. Nagao, *ACS Appl. Mater. Interfaces* **2016**, *8*, 5634.

[221] H. M. C. M. Herath, J. A. Epaarachchi, M. M. Islam, W. Al-Azzawi, J. Leng, F. Zhang, *Compos. Sci. Technol.* **2018**, *167*, 206.

[222] Y. Liu, G. Zhu, W. Liu, H. Liu, Y. Huo, T. Ren, X. Hou, *Smart Mater. Struct.* **2018**, *27*, 095008.

[223] P. Weis, W. Tian, S. Wu, *Chem. – Eur. J.* **2018**, *24*, 6494.

[224] M. Gastaldi, F. Cardano, M. Zanetti, G. Viscardi, C. Barolo, S. Bordiga, S. Magdassi, A. Fin, I. Roppolo, *ACS Mater. Lett.* **2021**, *3*, 1.

[225] A. Subash, B. Kandasubramanian, *Eur. Polym. J.* **2020**, *134*, 109771.

[226] S. Valvez, P. N. B. Reis, L. Susmel, F. Berto, *Polymers* **2021**, *13*, 701.

[227] W. Zhang, H. Wang, H. Wang, J. Y. E. Chan, H. Liu, B. Zhang, Y. F. Zhang, K. Agarwal, Y. Yang, A. S. Ranganath, H. Y. Low, Q. Ge, J. K. W. Yang, *Nat. Commun.* **2021**, *12*, 112.

[228] Q. Ge, A. H. Sakhaei, H. Lee, C. K. Dunn, N. X. Fang, M. L. Dunn, *Sci. Rep.* **2016**, *6*, 31110.

[229] M. Zarek, M. Layani, I. Cooperstein, E. Sachyani, D. Cohn, S. Magdassi, *Adv. Mater.* **2016**, *28*, 4449.

[230] M. Zarek, N. Mansour, S. Shapira, D. Cohn, *Macromol. Rapid Commun.* **2017**, *38*, 1600628.

[231] N. Maity, N. Mansour, P. Chakraborty, D. Bychenko, E. Gazit, D. Cohn, *Adv. Funct. Mater.* **2021**, *31*, 2108436.

[232] B. Zhang, H. Li, J. Cheng, H. Ye, A. H. Sakhaei, C. Yuan, P. Rao, Y.-F. Zhang, Z. Chen, R. Wang, X. He, J. Liu, R. Xiao, S. Qu, Q. Ge, *Adv. Mater.* **2021**, *33*, 2101298.

[233] J. Meurer, R. H. Kampes, T. Bätz, J. Hniopek, O. Müschke, J. Kimmig, S. Zechel, M. Schmitt, J. Popp, M. D. Hager, U. S. Schubert, *Adv. Funct. Mater*. **2022**, *32*, 46.

[234] N. Paunoví , J. Marbach, Y. Bao, V. Berger, K. Klein, S. Schleich, F. B. Coulter, N. Kleger, A. R. Studart, D. Franzen, Z. Luo, J.-C. Leroux, *Adv. Sci.* **2022**, *9*, 2200907.

[235] W. Peng, G. Zhang, Q. Zhao, T. Xie, *Adv. Mater.* **2021**, *33*, 2102473.

[236] B. Peng, Y. Yang, K. Gu, E. J. Amis, K. A. Cavicchi, *ACS Mater. Lett.* **2019**, *1*, 410.

[237] Y. Shi, G. Fang , Z. Cao, F. Shi, Q. Zhao, Z. Fang, T. Xie, *J. Chem. Eng.* **2021**, *426*, 131306.

[238] M. Invernizzi, S. Turri, M. Levi, R. Suriano, *Eur. Polym. J.* **2018**, *101*, 169.

[239] B. Zhang, W. Zhang, Z. Zhang, Y.-F. Zhang, H. Hingorani, Z. Liu, J. Liu, Q. Ge, *ACS Appl. Mater. Interfaces* **2019**, *11*, 10328.

[240] E. Rossegger, R. Höller, D. Reisinger, J. Strasser, M. Fleisch, T. Griesser, S. Schlögl, *Polym. Chem.* **2021**,*12*, 639.

[241] X. Li, R. Yu, Y. He, Y. Zhang, X. Yang, X. Zhao, W. Huang, *Polymer* **2020**, *200*, 122532.

[242] Z. Chen, M. Yang, M. Ji, X. Kuang, H. J. Qi, T. Wang, *Mater. Des.* **2021**, *197*, 109189.

[243] M. P. Jeske, W. Zhang, M. Anthamatten, *Adv. Mater. Technol.* **2022**, *7*, 2101725.

[244] G. Minnick, B. T. Safa, J. Rosenbohm, N. V. Lavrik, J. Brooks, A. M. Esfahani, A. Samaniego, F. Meng, B. Richter, W. Gao, R. Yang, *Adv. Funct. Mater.* **2023**, *33*, 2206739.

[245] M. Chen, Y. Gu, A. Singh, M. Zhong, A. M. Jordan, S. B., L. T. J. Korley, A. C. Balazs, J. A. Johnson, *ACS Cent. Sci.* **2017**, *3*, 124.

[246] F. A. Leibfarth, K. M. Mattson, B. P. Fors, H. A. Collins, C. J. Hawker, *Angew. Chem., Int. Ed.* **2013**, *52*, 199.

[247] M. Chen, M. J. Zhong, J. A. Johnson, *Chem. Rev.* **2016**, *116*, 10167.

[248] J. T. Trotta, B. P. Fors, *Synlett* **2016**, *27*, 702.

[249] N. Corrigan, S. Shanmugam, J. T. Xu, C. Boyer, *Chem. Soc. Rev.* **2016**, *45*, 6165.

[250] S. Dadashi-Silab, S. Doran, Y. Yagci, *Chem. Rev.* **2016**, *116*, 10212.

[251] A. Bagheri, C. M. Fellows, C. Boyer, *Adv. Sci.* **2021**, *8*, 2003701.

[252] N. Corrigan, K. Jung, G. Moad, C. J. Hawker, K. Matyjaszewski, C. Boyer, *Prog. Polym. Sci.* **2020**, *111*, 101311.

[253] J. Nicolas, Y. Guillaneuf, C. Lefay, D. Bertin, D. Gigmes, B. Charleux, *Prog. Polym. Sci.* **2013**, *38*, 63.

[254] F. Lorandi, M. Fantin, K. Matyjaszewski, *J. Am. Chem. Soc.* **2022**, *144*, 15413.

[255] S. Perrier, *Macromolecules* **2017**, *50*, 7433.

[256] G. Moad, E. Rizzardo, S. H. Thang, *Acc. Chem. Res.* **2008**, *41*, 1133.

[257] H. R. Lamontagne, B. H. Lessard, *ACS Appl. Polym. Mater.* **2020**, *2*, 5327.

[258] H. Fischer, *Chem. Rev.* **2001**, *101*, 3581.

[259] D. Leifert, A. Studer, *Angew. Chem. Int. Ed.* **2020**, *59*, 74.

[269] D. Benoit, V. Chaplinski, R. Braslau, C. J. Hawker, *J. Am. Chem. Soc.* **1999**, *121*, 3904.

[270] S. Grimaldi, J.-P. Finet, F. Le Moigne, A. Zeghdaoui, P. Tordo, D. Benoit, M. Fontanille, Y. Gnanou, *Macromolecules* **2000**, *33*, 1141.

[271] C. Wetter, J. Gierlich, C. A. Knoop, C. Müller, T. Schulte, A. Studer, *Chem. Eur. J.* **2004**, *10*, 1156.

[272] S. Miele, P. Nesvadba, A. Studer, *Macromolecules* **2009**, *42*, 2419.

[273] C. J. Kloxin, C. N. Bowman, *Chem. Soc. Rev.* **2013**, *42*, 7161.

[274] C. J. Kloxin, T. F. Scott, B. J. Adzima, C. N. Bowman, *Macromolecules* **2010**, *43*, 2643.

[275] M. Podgórski, B. D. Fairbanks, B. E. Kirkpatrick, M. McBride, A. Martinez, A. Dobson, N. J. Bongiardina, C. N. Bowman, *Adv. Mater.* **2020**, *32*, 1906876.

[276] J. M. Winne, L. Leibler, F. E. Du Prez, *Polym. Chem.* **2019**, *10*, 6091.

[277] L. Meher, D. Vidyasagar, S. Naik, *Renew. Sust. Energ. Rev.* **2006**, *10*, 248.

[278] R. A. Scheck, M. T. Dedeo, A. T. Iavarone, M. B. Francis, *J. Am. Chem. Soc.* **2008**, *130*, 11762.

[279] A. Rekondo, R. Martin, A. Ruiz de Luzuriaga, G. Cabañero, H. J. Grande, I. Odriozola, *Mater. Horiz.* **2014**, *1*, 237.

[280] H. Otsuka, S. Nagano, Y. Kobashi, T. Maeda, A. Takahara, *Chem. Commun.* **2010**, *46*, 1150.

[281] L. Li, X. Chen, J. M. Torkelson, *Macromolecules* **2019**, *52*, 8207.

[282] Y. Hou, G. Zhu, J. Cui, N. Wu, B. Zhao, J. Xu, N. Zhao*, J. Am. Chem. Soc.* **2022**, *144*, 436.

[283] W. Zou, J. Dong, Y. Luo, Q. Zhao, T. Xie, *Adv. Mater.* **2017**, *29*, 1606100.

[284] T. Maeda, H. Otsuka, A. Takahara, *Prog. Polym. Sci.* **2009**, *34*, 581.

[285] J.-T. Miao, M. Ge, S. Peng, J. Zhong, Y. Li, Z. Weng, L. Wu, L. Zheng, *ACS Appl. Mater. Interfaces* **2019**, *11*, 40642.

[286] Y. Jia, G. Delaittre, M. Tsotsalas, *Macromol. Mater. Eng.* **2022**, *307*, 2200178.

[287] Y. Amamoto, M. Kikuchi, H. Masunaga, S. Sasaki, H. Otsuka, A. Takahara, *Macromolecules* **2009**, *42*, 8733.

[288] K. Jin, L. Li, J. M. Torkelson, *Adv. Mater.* **2016**, *28*, 6746.

[289] Z. P. Zhang, Y. Lu, M. Z. Rong, M. Q. Zhang, *RSC Adv.* **2016**, *6*, 6350.

[290] Q. An, I. D. Wessely, Y. Matt, Z. Hassan, S. Bräse, M. Tsotsalas, *Polym. Chem.* **2019**, *10*, 672.

[291] Y. Jia, Y. Matt, Q.i An, I. Wessely, H. Mutlu, P. Theato, S. Bräse, A. Llevot, M. Tsotsalas, *Polym. Chem.* **2020**, *11*, 2502.

[292] S. Telitel, Y. Amamoto, J. Poly, F. Morlet-Savary, O. Soppera, J. Lalevée, K. Matyjaszewski, *Polym. Chem.* **2014**, *5*, 921.

[293] Z. Zhang, N. Corrigan, A. Bagheri, J. Jin, C. Boyer, *Angew. Chem., Int. Ed.* **2019**, *58*, 17954.

[294] Z. Zhang, N. Corrigan, C. Boyer, *Macromolecules* **2021**, *54*, 1170.

[295] X. Shi, J. Zhang, N. Corrigan, C. Boyer, *Mater. Chem. Front.* **2021**, *5*, 2271.

[296] A. Bagheri, C. W. A. Bainbridge, K. E. Engel, G. G. Qiao, J. Xu, C. Boyer, J. Jin, *ACS Appl. Polym. Mater.* **2020**, *2*, 782.

[297] C. W. A. Bainbridge, K. E. Engel, J. Jin, *Polym. Chem.* **2020**, *11*, 4084.

[298] A. Bagheri, H. Ling, C. W. A. Bainbridge, J. Jin, *ACS Appl. Polym. Mater.* **2021**, *3*, 2921.

[299] B. Zhao, J. Li, Y. Xiu, X. Pan, Z. Zhang, J. Zhu, *Macromolecules* **2022**, *55*, 1620.

[300] A. Bagheri, K. E. Engel, C. W. A. Bainbridge, J. Xu, C. Boyer, J. Jin, *Polym. Chem.* **2020**, *11*, 641.

[301] B. J. Green, C. A. Guymon, *Addit. Manuf.* **2019**, *27*, 20.

[302] K. Lee, N. Corrigan, C. Boyer, *Angew. Chem., Int. Ed.* **2021**, *60*, 8839.

[303] X. Shi, J. Zhang, N. Corrigan, C. Boyer, *Polym. Chem.* **2022**, *13*, 44.

[304] M. Asadi-Eydivand, T. C. Brown, A. Bagheri, *ACS Appl. Polym. Mater.* **2022**, *4*, 4940.

[305] V. A. Bobrin, K. Lee, J. Zhang, N. Corrigan, C. Boyer, *Adv. Mater.* **2022**, *34*, 2107643.

[306] V. A. Bobrin, Y. Yao, X. Shi, Y. Xiu, J. Zhang, N. Corrigan, C. Boyer, *Nat. Commun.* **2022**, *13*, 3577.

[307] K. Lee, Y. Shang, V. Bobrin, R. Kuchel, D. Kundu, N. Corrigan, C. Boyer, Adv. Mater. 2022, 34, 2204816.

[308] B. Zhao, J. Li, X. Pan, Z. Zhang, G. Jin, J. Zhu, *ACS Macro Lett.* **2021**, *10*, 1315.

[309] V. A. Bobrin, J. Zhang, N. Corrigan, C. Boyer, *Adv. Mater. Technol.* **2022**, 2201054.

[310] L. Qiao, M. Zhou, G. Shi, Z. Cui, X. Zhang, P. Fu, M. Liu, X. Qiao, Y. He, X. Pang, *J. Am. Chem. Soc.* **2022**, *144*, 9817.

[311] X. Wu, B. Gross, B. Leuschel, K. Mougin, S. Dominici, S. Gree, M. Belqat, V. Tkachenko, B. Cabannes-Boué, A. Chemtob, J. Poly, A. Spangenberg, *Adv. Funct. Mater*. **2022**, *32*, 2109446.

[312] M. Belqat, X. Wu, J. Morris, K. Mougin, T. Petithory, L. Pieuchot, Y. Guillaneuf, D. Gigmes, J.-L. Clément, A. Spangenberg, *Adv. Funct. Mater.* **2023**, 2211971.

[313] G. D. Zhu, Y. Hou, J. Xu, N. Zhao, *Adv. Funct. Mater.* **2021**, *31*, 2007173.

[314] W. Voit, T. Ware, R. R. Dasari, P. Smith, L. Danz, D. Simon, S. Barlow, S. R. Marder, K. Gall, *Adv. Funct. Mater.* **2010**, *20*, 162.

[315] E. G. Herbert, W. C. Oliver, G. M. Pharr, *J. Phys. D: Appl. Phys.* **2008**, *41*, 074021.

[316] W. C. Oliver, G. M. Pharr, *J. Mater. Res.* **2004**, *19*, 3.

[317] W. C. Oliver, G. M. Pharr, *J. Mater. Res.* **1992**, *7*, 1564.

[318] A. S. Alketbi, Y. Shi, H. Li, A. Raza, T. Zhang, *Soft Matter* **2021**, *17*, 7188.

[319] H. Jiang, G. Guo, W. Chen, Z. Cui, *Dyes Pigm.*, **2021**, *194*, 109555.

[320] E. Schab-Balcerzak, M. Siwy, M. Kawalec, A. Sobolewska, A. Chamera, A. Miniewicz, *J. Phys. Chem. A* **2009**, *113*, 8765.

[321] Q. Zhang, G. Vancoillie, M. A. Mees, R. Hoogenboom, *Polym. Chem*. **2015**, *6*, 2396.

[322] L. de Smet, G. Vancoillie, P. Minshall, K. Lava, I. Steyaert, E. Schoolaert, E. van de Walle, P. Dubruel, K. de Clerck, R. Hoogenboom, *Nat. Commun.* **2018**, *9*, 1123.